Ultra-cold Atoms in Optical Lattices: Simulating Quantum Spin Systems



Richard Walters
Keble College, Oxford

A thesis submitted to the Mathematical and Physical Sciences Division
for the degree of Doctor of Philosophy at the University of Oxford

Trinity Term, 2012

Atomic and Laser Physics
University of Oxford

To Jodie.

Ultra-cold Atoms in Optical Lattices: Simulating Quantum Spin Systems

Richard Walters, Keble College, Oxford
Trinity Term 2012

Abstract

Optical lattices provide ideal experimental tools for simulating a wide variety of physical systems. They exhibit excellent coherence properties, their microscopic dynamics are well-understood, and they can be dynamically controlled with great precision. Recent advances in cooling and trapping gases of dipolar molecules and Rydberg atoms have further increased the versatility of optical lattices as quantum simulators, particularly for solid state systems possessing long-range interactions.

In this thesis we further examine the microscopic properties of cold atoms trapped in an optical lattice, going beyond the case where the lattice axes are orthogonal. We present a transformation of the single-particle energy eigenstates to a complete, orthonormal basis of so-called 'generalised Wannier functions' that are localised to each lattice site. Generalised Wannier functions, as opposed to ordinary Wannier functions, are formed by mixing states between bands and are required when the bands are degenerate. We modify an algorithm devised by Marzari and Vanderbilt (Phys. Rev. B 56(20) 12847) for calculating maximally localised generalised Wannier functions, specifically to determine these functions for optical lattice systems of arbitrary geometry, including those with degenerate lower bands. Moreover, we overcome an issue with the initialisation of the original algorithm to find the maximally localised set without fail. We then present results for a variety of optical lattice systems in one- and two-dimensions, including hexagonal and Kagomé geometries. In each case we use the generalised Wannier functions to calculate the hopping and interaction parameters, and thus determine a reduced form of the system's Hamiltonian that contains only local interactions.

We also study two spin-1/2 systems with long-range interactions as paradigm examples of the models that can be simulated using optical lattices loaded with dipolar molecules. We first examine the critical properties of a 1D spin-1/2 Ising chain possessing exponentially decaying interactions as the range of the interactions is increased. Using the infinite density matrix renormalisation group method, we calculate the location of the critical point and observe a smooth approach to the classical mean-field result in the limit of infinite-ranged interactions. We go on to consider the quantum dynamics of a single spin-1/2 coupled to a bath of interacting spins as a model for decoherence in solid state quantum memories. The large degree of symmetry of the bath, described by the infinite-ranged Lipkin-Meshkov-Glick model, allows us to find parameter regimes where the initial qubit state is revived at well-defined times after the qubit preparation. We observe that these times may become independent of the bath size for large baths and thus enable faithful qubit storage even in the presence of strong coupling to the bath.

Acknowledgements

This thesis would not have been possible without the help and support of many people, who deserve my profound gratitude. Firstly, I would like to thank my supervisor Dieter Jaksch, and Stephen Clark. Both men invested a large amount of time and effort in me as their student, and I greatly appreciate the help and insight they offered. I have tremendous admiration for Dieter and Stephen and wish them continued success in their field. I must also thank my co-authors and colleagues in Dieter's group, in particular Tomi Johnson, Giovanni Cotugno, Javier Prior, Sarah Al-Assam and Simon Thwaite.

My time in Oxford was very special thanks to the numerous people I was fortunate to meet there. Matthew Baggaley, Daniel Norwick, Krishna Rao and Ed Stock are life-long friends who made my undergraduate years unforgettable. As a graduate I could not have hoped for better house-mates than John Lyle, Ross McAdam and Tom Ouldridge, who are extraordinary people for whom I have the utmost respect. I am tremendously grateful to everyone involved with the Oxford University Pool and Snooker Club, who are too many to list here, but with whom I shared some fantastic experiences. There are also the many people I met at Keble College who were a pleasure to spend time with, in particular James MacLaurin, Dan James and Chris Broadbent.

I reserve a special thank you to my parents, sister, and grandparents. Without their unquestioning love and support I would not be where am I now, and I am forever grateful.

Finally, I wish to thank my partner Jaclyn Rajsic. She is a constant source of inspiration and without her I doubt I would ever have been able to complete this thesis. Words cannot express how much Jaclyn's love and encouragement means to me.

Contents

Chapter 1. Introduction **1**
1.1 Ultra-cold atoms and optical lattices . . . 1
1.2 Quantum simulation with optical lattices . . . 3
1.3 Theoretical analysis . . . 5
1.4 Thesis overview . . . 7

Chapter 2. Ultra-cold atoms in optical lattices **11**
2.1 Formation of an optical lattice system . . . 12
2.1.1 The atom-light interaction . . . 12
2.1.2 The optical lattice potential . . . 16
2.1.3 Experimental considerations . . . 19
2.1.4 Lattice definitions . . . 19
2.2 Bosons in an optical lattice . . . 20
2.3 Single particle physics . . . 24
2.3.1 Fourier decompositions in the reciprocal lattice . . . 25
2.3.2 Brillouin zone sampling and symmetry . . . 27
2.4 The Wannier basis . . . 30
2.4.1 Generalised Wannier functions . . . 32
2.4.2 The spread functional . . . 34
2.4.3 Steepest-decent minimisation . . . 37
2.4.4 Isolated bands in systems with inversion symmetry . . . 40
2.4.5 Composite groups: 'disentangling' the bands . . . 42
2.4.6 Composite groups in systems with inversion symmetry . . . 47
2.5 The hopping matrix elements . . . 50
2.6 The tight-binding model . . . 51
2.A Appendix: Iterative minimisation of $\Omega_{\mathrm{I}}^{[n]}$ . . . 53

Chapter 3. Maximally localised generalised Wannier functions for one-dimensional optical lattices **55**
3.1 1D sinusoidal optical lattice . . . 56
3.1.1 Isolated bands as a composite group . . . 65
3.2 1D super-lattice, red-detuned . . . 71
3.3 1D super-lattice, blue-detuned . . . 77
3.4 Conclusions . . . 82
3.A Appendix: Convergence with Brillouin zone sampling density . . . 83

Chapter 4. Maximally localised generalised Wannier functions for two-dimensional optical lattices **87**
4.1 2D optical lattice configurations . . . 88
4.2 2D rhombic lattice . . . 90
4.3 2D equilateral triangular lattice . . . 96
4.4 2D hexagonal lattice . . . 100
4.5 2D Kagomé lattice . . . 104

Chapter 5. The Bose-Hubbard model **109**
5.1 Decoupled mean-field theory . . . 110
5.2 Mean-field phase diagram for 2D geometries . . . 116
5.3 Validity of the decoupled mean-field theory . . . 118

Chapter 6. Simulating quantum spin Hamiltonians with optical lattices **121**
6.1 Engineering spin Hamiltonians . . . 122
6.1.1 Direct mapping in the hard-core limit . . . 122
6.1.2 State-dependent optical lattices . . . 122
6.2 Dipolar gases in optical lattices . . . 127
6.2.1 The dipole-dipole interaction . . . 128
6.2.2 The extended Bose-Hubbard model . . . 129

Chapter 7. Approaching the classical limit of a quantum phase transition with long-range interactions **133**
7.1 Introduction . . . 133
7.2 Model . . . 135
7.3 Bounding approximations . . . 136
7.3.1 Mean-field theory . . . 136
7.3.2 Long-range fermionic model . . . 137
7.4 Renormalisation group approach . . . 139
7.4.1 Real-space renormalisation for $\alpha = 0$ . . . 140
7.4.2 Real-space renormalisation for $\alpha \geq 0$ . . . 141
7.4.3 Critical exponent . . . 145
7.5 infinite-DMRG approach . . . 147
7.5.1 infinite-DMRG results . . . 147
7.6 Conclusion . . . 150
7.A Energy spectrum for the long-range fermionic model . . . 152
7.B Real-space renormalisation . . . 154
7.B.1 Recursion relation for $\alpha = 0$ . . . 154
7.B.2 Extension to $\alpha \geq 0$ . . . 157

Chapter 8. Decoherence of a quantum memory coupled to a collective spin bath **159**
8.1 Introduction . . . 159
8.2 The Model . . . 162

8.2.1 The Lipkin-Meshkov-Glick bath . . . 162
8.2.2 Ising interaction . . . 168
8.2.3 LMG interaction . . . 168
8.2.4 Characterizing decoherence . . . 169
8.3 Results: Ising interaction . . . 170
8.3.1 Single link, $k = 1$ . . . 173
8.3.2 Completely connected, $k = N$ . . . 175
8.3.3 Multiple links . . . 178
8.4 Results: LMG interaction . . . 180
8.4.1 Single link, $k = 1$ . . . 181
8.4.2 Completely connected, $k = N$ . . . 183
8.4.3 Multiple links . . . 184
8.5 Conclusions . . . 186
8.A Quantum Operations Formalism and the Jamiolkowski Isomorphism 188
8.B The Loschmidt Echo for a single link and an isotropic bath . . . 190

Chapter 9. Conclusion **193**

Bibliography **197**

Chapter 1

Introduction

1.1 Ultra-cold atoms and optical lattices

In the mid 1990s a series of seminal discoveries, sparked in particularly by rapid advances in preparing, controlling and detecting many-body quantum systems, transformed the field of atomic and laser physics [1]. Laser cooling and evaporative cooling techniques [2] enabled experimenters to cool gases of atoms down to temperatures of the order of a few tens of nanoKelvin, which in 1995 resulted in the first realisations of a Bose-Einstein condensate (BEC) in a dilute, weakly-interacting gas of alkali atoms [3, 4]. This breakthrough shifted a focus on the study of single atoms to the exploration of particle statistics and their interactions. In particular, experiments involving BECs provided a new-found opportunity to explore the physics of coherent, macroscopically sized systems [5], leading to demonstrations of matter wave interference [6], long-range phase coherence [7], solitons [8], and quantised vortex lattices [9, 10]. Sympathetic cooling using BECs also allowed the realisation of degenerate Fermi gases, which exhibit the same high level of controllability as Bose gases resulting in a set of similar experiments with them [11, 12].

A feature common to all of the phenomena observed with BECs is that they are successfully described by the Gross-Pitaevskii equation and the well-known Bogoliubov mean-field theory of weakly interacting Bose gases [5]. As such, BECs have been highly valuable in the study of coherence properties, superfluidity, and further

concepts applicable to areas such as superconductivity. However, their importance more recently has been their use in investigating strongly correlated systems where the mean-field approach is no longer adequate. As originally proposed by Jaksch *et al.* [13] and later demonstrated by Greiner *et al.* [14], such strongly correlated systems can be engineered by adiabatically imposing an optical lattice, formed by standing waves of laser light, on a BEC of ultra-cold atoms. The resulting many-body systems can be described by Hubbard-type models, whose parameters can be manipulated using a variety of techniques to simulate a range of lattice and spin models that are of interest in condensed matter physics.

The engineering and investigation of these lattice and spin models is possible with optical lattice systems thanks to the unprecedented level of control they provide the experimenter over the microscopic parameters, which would not be the case with condensed matter systems. In addition, a range of measurement techniques are available, including, e.g. observation of the interference pattern following ballistic expansion [14] and coincidence detection for density-density correlation functions [15, 16]. A further differentiating and beneficial factor over condensed matter systems is the excellent isolation of the trapped atoms from their environment, allowing them to display coherent dynamics on timescales much greater than that of lattice manipulations [17]. This is not only ideal for employing these systems as quantum simulators, but also opens the possibility of them being employed for quantum information processing. Single atoms trapped within each well of an optical lattice provide a natural, scalable realisation of a quantum register, where the information can be encoded in the long-lived internal states of the atoms [18]. Gate operations can be achieved, for example, via controlled collisions [19, 20] or dipole-dipole interactions between Rydberg atoms [21, 22]. At present, there are some challenges to be overcome in implementing quantum computing with optical lattices such as single site addressability, however much progress has been made in recent years. For

a comprehensive overview of the current state of quantum information processing with optical lattices and other physical systems see the review paper by Ladd *et al.* [23].

1.2 Quantum simulation with optical lattices

As previously mentioned, a wide variety of techniques are available to control the dynamics of atoms in optical lattices for the purposes of quantum simulation and the study of strongly correlated systems. The primary techniques are as follows:[1]

- First of all, the depth of the lattice potential can be controlled by altering the intensity of the laser light. For example, in the original proposal by Jaksch *et al.* [13] the authors described how a BEC of ultra-cold atoms trapped in an optical lattice can realise the Bose-Hubbard model, where the ratio of the kinetic energy of the atoms to their interaction energy (caused by an on-site repulsion) is dependent on the lattice depth. By reducing this ratio via increasing the laser intensity they predicted that one would observe the transition from a superfluid to a Mott insulator [25], which was indeed confirmed in the seminal experiment by Greiner *et al.* using a BEC of ^{87}Rb atoms in a three-dimensional cubic optical lattice [14].

- By making the lattice very deep in one or more directions the system can be confined to two-dimensional planes or one-dimensional tubes, thus realising purely 1D and 2D models. This technique has led to the realisation of a Tonks-Girardeau gas in one dimension [26], while in two dimensions a Kosterlitz-Thouless crossover between a normal phase and one with quasi-long-range order has been observed [27].

[1] The following list is by no means exhaustive; for a more comprehensive overview see the review papers by Lewenstein *et al.* [1] and Bloch *et al.* [24].

- The geometry of the lattice can be altered by using different configurations of the lasers to achieve a variety of standing wave patterns [28]. For example, the superfluid-Mott insulator transition has been observed in a triangular optical lattice [29], a geometry that has since been employed to simulate a variety of magnetic phases, including ferromagnetic, antiferromagnetic, and even frustrated spin configurations [30]. More exotic geometries such as a Kagomé lattice, which has been predicted to exhibit novel Mott insulator phases with fractional filling, could also be created [31, 32]. The profiling of the microscopic parameters of optical lattices for arbitrary geometries forms a major part of this thesis.

- Superlattice techniques [33] can be employed to create non-uniform lattices, or to produce pseudo-random disorder. For example, the use of a double-well superlattice has been proposed as a method for the fast initialisation of a quantum register [34]. Disorder can also be controllably introduced through the use of an optical speckle field, which has allowed the observation of Anderson localisation [35, 36] and the realisation of the disordered Bose-Hubbard model [37]. Tilting the lattice is another tactic, through which Bloch oscillations have been observed in these systems [38, 39].

- The strength of the interactions in a gas of atoms can be tuned through the use of Feshbach resonances, which have been employed in experiments to observe the crossover from a diatomic molecular BEC to a BCS superfluid of weakly bound Cooper pairs [40, 41, 42]. When combined with other techniques, this greatly increases the versatility of optical lattices for simulating a range spin models [1]. In addition, recent advances in trapping and cooling dipolar molecules (for a review see Lahaye *et al.* [43]) opens the possibility of creating optical lattice systems with long-range interactions. These sys-

tems would be described by extended Hubbard models and could realise novel quantum phases, such as checkerboard and supersolid phases [44, 45, 46].

- Spin-dependent optical lattices can be produced by trapping two or more internal states of the same atomic species, which can be targeted by different polarisations of the laser light [17]. We discuss this in more depth in chapter 6. Other models can also be generated by including several atomic species and making the parameters species-dependent with different detunings of the laser light.

- Artificial magnetic fields can be introduced by engineering a complex hopping amplitude that induces a Peierls phase on atoms hopping between lattice sites. This could potentially allow for the observation of fractional quantum Hall physics in these systems [47, 48]. Optical lattices with artificial magnetic fields have recently been demonstrated in two experiments via different methods: Struck *et al.* used fast, off-resonant time-periodic potential modulations to drive the system [49]; while Jiménez-García *et al.* used a combination of Raman coupling and radio-frequency magnetic fields to derive the lattice potential [50]. Previous experiments have also realised artificial magnetic fields by rotating the optical lattice [51] and by using Raman-assisted tunneling in an optical superlattice [52].

1.3 Theoretical analysis

As we have seen, optical lattice systems can be employed as quantum simulators to investigate otherwise intractable many-body problems. Of course, this requires that the physics of optical lattice systems themselves is thoroughly understood. For example, one might wish to know the state after a certain time evolution under

the system's Hamiltonian so that it can be prepared for a particular experiment, or to predict various properties of a simulation experiment to compare with measurements. However, the theoretical analysis of optical lattice systems presents a considerable challenge; analytical solutions are available for just a handful of systems, while the exponential growth of the Hilbert space with system size poses difficulties for numerical calculations. Much progress has been made in recent years thanks to ingenious numerical methods such as the density matrix renormalisation group approach [53, 54] and the time-evolving-block-decimation algorithm [55, 56]. Regardless of the analytical or numerical methods employed, to provide meaningful results it is essential that the approach be based on a detailed microscopic knowledge of the system. Interestingly, while the microscopic parameters of optical lattice systems have been calculated for simple lattice structures, to our knowledge little work has been done for geometries that are even slightly more complex, e.g. with non-orthogonal axes. Moreover, studies of these systems have typically made assumptions about the microscopic description that are likely to prove inaccurate for some part of the parameter regime used in experiments.

In this thesis we focus on two aspects of quantum simulation using optical lattices. Firstly, we examine methods for calculating the microscopic properties of optical lattice systems for arbitrary lattice potentials. We then employ these methods to examine a variety of lattice geometries of notable recent interest. Secondly, we consider two quantum spin systems as paradigm examples of the models that can be simulated using optical lattices. The properties of these spin systems can be exploited to obtain accurate results for realistic numbers of spins, thus providing an understanding of the theoretically accessible properties of such models.

1.4 Thesis overview

This thesis is structured as follows:

- We begin in chapter 2 with a detailed review of the theory of optical lattices. After showing how the single-particle band-structure and energy eigenstates can be computed numerically, we introduce the concept of Wannier functions, which are localised to individual lattice sites and form a complete, orthonormal basis for the system. By determining the matrix elements of the many-body Hamiltonian within this basis one can neglect long-range terms, vastly reducing the Hamiltonian to a form both more appropriate for examining the physics and more amenable to numerical calculation. However, the transformation of the energy eigenbasis to the optimal Wannier basis is non-trivial and previously has only been achieved for simple optical lattice geometries where the bands are non-degenerate. A naive transformation results in Wannier functions with a large spatial variance and that do not retain the symmetry properties of the underlying lattice. Moreover, so-called 'generalised Wannier functions' are required when the bands are degenerate. We present an algorithm for calculating the maximally localised set of generalised Wannier functions, opening up a wide variety of optical lattice geometries for detailed investigation.

- In chapter 3 we focus on one-dimensional optical lattices of cold bosonic atoms. We use the well-studied sinusoidal optical lattice to introduce the reader to the key properties of Wannier functions, before presenting results for the interaction and hopping parameters. As was originally shown by Jaksch *et al.* [13], only nearest-neighbour terms are significant and thus the system can be reduced to a Bose-Hubbard model. We next consider the same system in addition to two types of super-lattice to examine band mixing and the use of generalised Wannier functions as a basis, even when the bands are not degener-

ate. We compare the interpolated bands deduced from the hopping parameters within a tight-binding model to the original single-particle band-structure, and observe that in certain scenarios generalised Wannier functions do improve the approximation to a reduced model containing only local interactions.

- In chapter 4 we consider a variety of two-dimensional optical lattices, including rhombic, equilateral triangular, hexagonal, and Kagomé geometries, where in the latter two cases the primitive unit cell has multiple potential minima and the lowest bands form a degenerate group. Our methods allow us to calculate in each case the maximally localised (generalised) Wannier functions, and therefore also the interaction and hopping parameters. For the rhombic lattice we do so as a function of the acute angle χ of the unit cell, and observe that for $\chi \neq 90^\circ$ hopping across the cell near-diagonal is introduced and becomes increasingly significant as χ is decreased. For the remaining geometries our results show that, as might be expected, the system's Hamiltonian can be reduced to that of a Bose-Hubbard model with only nearest-neighbour interactions between atoms in adjacent minima.

- In chapter 5 we briefly review the physics of the Bose-Hubbard model, discussing the mean-field phase diagram and the main features of the quantum phase transition. We calculate the critical point for the rhombic optical lattice as a function of the acute angle χ and show that the transition from the Mott phase to a superfluid is possible at a fixed lattice depth by altering the geometry of the lattice.

- In chapter 6 and the remaining chapters we turn our attention to quantum spin systems. We begin with an overview of a particular technique for simulating spin Hamiltonians using optical lattices. We also discuss optical lattices loaded with dipolar gases, which can potentially realise long-range spin sys-

tems thanks to the power-law decaying dipole-dipole interaction. This chapter provides the motivation for the two long-range spin systems investigated in the following chapters. Although these systems are not necessarily realisable themselves using optical lattices with current technology, their properties and dynamics can be calculated numerically to a high degree of accuracy, providing necessary intuition as to the behaviour of other systems with the potential for quantum simulation.

- In chapter 7 we consider the effect of quantum fluctuations on the critical properties of a quantum spin system. Specifically, we vary the range of exponentially decaying interactions in a one-dimensional spin-1/2 Ising chain with a transverse field, and calculate the shift in the critical point and critical exponent using the infinite density matrix renormalisation group method. We observe a diverging critical point in the limit of infinite-ranged interactions indicating that an infinite coordination number stabilises the ferromagnetic phase against any finite value of the transverse field. Moreover, our results also indicate a smooth approach to the classical mean-field critical properties in this limit.

- In chapter 8 we study the quantum dynamics of a single qubit coupled to a bath of interacting spins as a model for decoherence in solid state quantum memories. The spin bath is described by the infinite-ranged Lipkin-Meshkov-Glick model, whose permutational symmetry can be exploited to exactly solve its dynamics numerically for very large numbers of spins ($\sim$ 100-1000). We go beyond the usual 'central spin model' by examining the decoherence of the qubit as its exposure to the spin bath is varied from coupling to just one bath spin through to interacting with all bath spins. The large degree of symmetry of the bath allows us to find parameter regimes where highly non-Markovian

coherence properties are displayed within the quantum memory, and in these regimes our results show that the initial qubit state can be revived at well defined times after the qubit preparation. These times become independent of the bath size for large baths, thus enabling faithful qubit storage even in the presence of strong coupling to the bath.

- In chapter 9 we present our conclusions and discuss directions for future studies.

Chapter 2

Ultra-cold atoms in optical lattices

In this chapter we layout the theoretical framework for the study of a dilute gas of ultra-cold atoms in the presence of an optical lattice. We begin by outlining how it is possible to trap a gas of atoms using lasers and derive the conservative dipole force exerted on an atom via its interaction with the electromagnetic field. This force can be exploited to impose an optical lattice potential on the atoms using a set of lasers with carefully chosen intensity and frequency, and which produce a periodic intensity pattern. We discuss the Hamiltonian that describes this system and show how the single particle band-structure and Bloch eigenstates can be calculated numerically. We detail a transformation of the Bloch states that allows the bosonic field operators to be expanded in a complete, orthonormal basis of so-called 'generalised Wannier functions' localised on each lattice site. By computing the set of generalised Wannier functions with minimal spatial variance, the system's Hamiltonian can be reduced to a Bose-Hubbard-type model consisting of only local interactions, which is more amenable to numerical analysis.

2.1 Formation of an optical lattice system

2.1.1 The atom-light interaction

To derive the conservative dipole force experienced by an atom interacting with an electromagnetic field we consider the atom as an idealised two-level system with a free Hamiltonian given by

$$\hat{H}_{\mathrm{a}} = \frac{\hat{\mathbf{p}}^2}{2m_{\mathrm{a}}} + \tfrac{1}{2}\hbar\omega_{\mathrm{a}}(\mathbf{1} - \hat{\sigma}_z). \tag{2.1}$$

Here m_{a} is the mass of the atom, $\hat{\mathbf{p}}$ is the momentum operator, $\hbar\omega_{\mathrm{a}}$ is the energy separation of the internal ground state $|g\rangle$ and excited state $|e\rangle$, and $\hat{\sigma}_z = |g\rangle\langle g| - |e\rangle\langle e|$ is the Pauli z-operator. For later reference we also define the ladder operators $\hat{\sigma}_+ = |e\rangle\langle g|$ and $\hat{\sigma}_- = |g\rangle\langle e|$. We place the atom in a lossless cavity of volume V, which is illuminated by a monochromatic electromagnetic field with a frequency $\nu = \omega/2\pi$. The field is considered as being quantised and as such is described by the operator

$$\hat{\mathbf{E}}(\mathbf{r}) = \sqrt{\frac{\hbar\omega}{2\epsilon_0 V}} \sum_{\mathbf{k},\mu} \hat{a}_{\mathbf{k}}^{[\mu]} \mathbf{e}_{\mathbf{k}}^{[\mu]} e^{i\mathbf{k}\cdot\mathbf{r}} + H.c., \tag{2.2}$$

where $\hat{a}_{\mathbf{k}}^{[\mu]}$ is the photon annihilation operator for the mode $e^{i\mathbf{k}\cdot\mathbf{r}}$ with helicity $\mu = \pm 1$ and corresponding unit polarisation vector $\mathbf{e}_{\mathbf{k}}^{[\mu]}$, $\mathbf{r}$ is the real space coordinate vector, and ϵ_0 is the permittivity of free space [57]. The Hamiltonian for the field is described by

$$\hat{H}_{\mathrm{f}} = \hbar\omega \sum_{\mathbf{k},\mu} (\hat{a}_{\mathbf{k}}^{[\mu]\dagger} \hat{a}_{\mathbf{k}}^{[\mu]} + \tfrac{1}{2}). \tag{2.3}$$

In optical lattice experiments the typical wavelength $\lambda = c/\nu$ of the field is of the order of a few hundred nanometres, thus spatial variations of the field mode are significantly larger than the size of the atom (approximately the Bohr radius $a_0 \sim 53 \times 10^{-3}$ nm). The interaction between the atom and the field can therefore be

described using the dipole approximation [57], with interaction Hamiltonian $\hat{H}_{\rm int} = -\hat{\mathbf{d}} \cdot \hat{\mathbf{E}}(\mathbf{r})$. Here $\hat{\mathbf{d}} = \mathbf{d}_{eg}(\hat{\sigma}_+ + \hat{\sigma}_-)$ is the dipole operator of the atom, where $\mathbf{d}_{eg} = -q_{\rm e}\langle g|\hat{\mathbf{r}}|e\rangle$, $\hat{\mathbf{r}}$ is the position operator, and $q_{\rm e}$ is the charge of an electron. The full Hamiltonian for the atom-field system reads

$$\hat{H}_0 = \hat{H}_{\rm a} + \hat{H}_{\rm f} + \hbar(\hat{\sigma}_+ + \hat{\sigma}_-)\sum_{\mathbf{k},\mu}\left(\hat{a}^{[\mu]}_{\mathbf{k}}\Omega^{[\mu]}_{\mathbf{k}}e^{i\mathbf{k}\cdot\mathbf{r}} + H.c.\right), \tag{2.4}$$

where

$$\Omega^{[\mu]}_{\mathbf{k}} = \sqrt{\frac{\omega}{2\hbar\epsilon_0 V}}\mathbf{d}_{eg}\cdot\mathbf{e}^{[\mu]}_{\mathbf{k}} \tag{2.5}$$

is the Rabi frequency for the mode $\mathbf{k},\mu$ [2].[1]

To consider the time-evolution for the system it is useful to transform to the interaction picture using a time-dependent unitary operator $\hat{U}_1(t) = e^{i\omega_{\rm a}t(\mathbf{1}-\hat{\sigma}_z)/2}e^{i\hat{H}_{\rm f}t/\hbar}$. The Hamiltonian in the interaction picture is given by

$$\begin{aligned}\hat{H}_1(t) &= \hat{U}_1(t)\hat{H}_0\hat{U}_1^\dagger(t) - i\hbar\hat{U}_1(t)\dot{\hat{U}}_1^\dagger(t)\\ &= \frac{\hat{\mathbf{p}}^2}{2m_{\rm a}} + \hbar(e^{i\omega_{\rm a}t}\hat{\sigma}_+ + e^{-i\omega_{\rm a}t}\hat{\sigma}_-)\sum_{\mathbf{k},\mu}\left(\hat{a}^{[\mu]}_{\mathbf{k}}\Omega^{[\mu]}_{\mathbf{k}}e^{i\mathbf{k}\cdot\mathbf{r}}e^{-i\omega t} + H.c.\right).\end{aligned} \tag{2.6}$$

When the brackets in Eq. 2.6 are multiplied out we obtain terms with phases that have $\omega - \omega_{\rm a}$ or $\omega + \omega_{\rm a}$ time-dependence. If the detuning $\Delta = \omega - \omega_{\rm a}$ satisfies $|\Delta| \ll \omega_{\rm a}$, the terms with phase time-dependence $\omega+\omega_{\rm a}$ will vary much more rapidly than those with phase time-dependence $\omega-\omega_{\rm a}$. Therefore, we can make the rotating-wave approximation and neglect the rapidly oscillating terms [57]. When we then return to the Schrödinger picture using the unitary operator $\hat{U}_2(t) = e^{i\Delta t(\mathbf{1}-\hat{\sigma}_z)/2}$ the

[1] Many definitions of the Rabi frequency exist in the literature; the one used here is the real oscillation frequency of the population of the ground state $|g\rangle$ found by treating the field classically using a frequency $\omega = \omega_{\rm a}$.

Hamiltonian becomes

$$\begin{aligned}\hat{H}_2 &= \hat{U}_2(t)\hat{H}_1(t)\hat{U}_2^\dagger(t) - i\hbar\hat{U}_2(t)\dot{\hat{U}}_2^\dagger(t) \\ &= \frac{\hat{\mathbf{p}}^2}{2m_\mathrm{a}} - \tfrac{1}{2}\hbar\Delta(\mathbf{1}-\hat{\sigma}_z) + \hbar\sum_{\mathbf{k},\mu}\left(\hat{\sigma}_+\hat{a}_\mathbf{k}^{[\mu]}\Omega_\mathbf{k}^{[\mu]}e^{i\mathbf{k}\cdot\mathbf{r}} + H.c.\right). \end{aligned} \tag{2.7}$$

The terms in $\hat{H}_2$ describing the internal atomic and photon degrees of freedom form the well-known Jaynes-Cumming Hamiltonian [58], which couples pairs of 'bare' states $|g\rangle|n+1\rangle_\mathbf{k}^{[\mu]}$ to $|e\rangle|n\rangle_\mathbf{k}^{[\mu]}$, with $|n\rangle_\mathbf{k}^{[\mu]}$ an n photon Fock state for the mode $\mathbf{k},\mu$ (n is a positive integer). For a single mode with fixed n the number of excitations in the system is conserved, thus the dynamics of the internal atomic and photon degrees of freedom are confined to sets of two-dimensional subspaces. This allows the system to be solved analytically in terms of so-called 'dressed' states [57]. However, if we take the far-detuned limit

$$|\Delta| \gg |\Omega_\mathbf{k}^{[\mu]}|\sqrt{\langle n\rangle_\mathbf{k}^{[\mu]}} \;\forall\; \mathbf{k},\mu, \tag{2.8}$$

where $\langle n\rangle_\mathbf{k}^{[\mu]} = \langle\hat{a}_\mathbf{k}^{[\mu]\dagger}\hat{a}_{\mathbf{k}'}^{[\mu']}\rangle$ is the average photon number, the effect of the interaction may be treated using perturbation theory and one finds that the population of the electronic excited state $|e\rangle$ is negligible [59]. Consequently, we can derive an effective Hamiltonian (to lowest order in $\Omega_\mathbf{k}^{[\mu]}/\Delta$) for the ground state manifold by adiabatically eliminating the excited state manifold. This is achieved by applying the projection method

$$\hat{H}_\mathrm{eff} = \lim_{\varepsilon\to 0}\left[\mathbb{P}\hat{H}_2\mathbb{P} - \mathbb{P}\hat{H}_2\mathbb{Q}(\mathbb{Q}\hat{H}_2\mathbb{Q}+\varepsilon\mathbf{1})^{-1}\mathbb{Q}\hat{H}_2\mathbb{P}\right], \tag{2.9}$$

where $\mathbb{P} = |g\rangle\langle g|$ is the projector onto the ground state manifold, and $\mathbb{Q} = \mathbf{1} - \mathbb{P}$ is

the projector onto the orthogonal subspace [60]. The result is given by

$$\hat{H}_{\text{eff}} = \frac{\hat{\mathbf{p}}^2}{2m_{\text{a}}} + \frac{\hbar}{\Delta}|g\rangle\langle g| \sum_{\mathbf{k},\mathbf{k}'} \sum_{\mu,\mu'} \hat{a}_{\mathbf{k}}^{[\mu]\dagger} \hat{a}_{\mathbf{k}'}^{[\mu']} \Omega_{\mathbf{k}}^{[\mu]*} \Omega_{\mathbf{k}'}^{[\mu']} e^{-i\mathbf{k}\cdot\mathbf{r}} e^{i\mathbf{k}'\cdot\mathbf{r}}, \tag{2.10}$$

which demonstrates that the perturbing interaction induces a spatially dependent energy shift, or AC Stark shift, on the electronic ground state of the atom through the presence of the mode functions $e^{i\mathbf{k}\cdot\mathbf{r}}$. We also observe that $\hat{H}_{\text{eff}}$ does not entangle the state of the atom with the field.

We now consider each mode of the electromagnetic field to be of high intensity and described by a coherent state [57]

$$|\alpha_{\mathbf{k}}^{[\mu]}\rangle = \exp\left(-\tfrac{1}{2}|\alpha_{\mathbf{k}}^{[\mu]}|^2\right) \sum_{n=0}^{\infty} \frac{\alpha_{\mathbf{k}}^{[\mu]n}}{\sqrt{n!}} |n\rangle_{\mathbf{k}}^{[\mu]} \tag{2.11}$$

with an average photon number $\langle n\rangle_{\mathbf{k}}^{[\mu]} = |\alpha_{\mathbf{k}}^{[\mu]}|^2 \gg 1$. The Hamiltonian $\hat{h}$ describing the motional freedom of the atom is then found by taking the partial expectation value of $\hat{H}_{\text{eff}}$ with respect to the state $\sum_{\mathbf{k},\mu} |g\rangle|\alpha_{\mathbf{k}}^{[\mu]}\rangle$. Using $\langle\alpha_{\mathbf{k}}^{[\mu]}|\alpha_{\mathbf{k}'}^{[\mu']}\rangle = \alpha_{\mathbf{k}}^{[\mu]}\alpha_{\mathbf{k}'}^{[\mu']}\delta_{\mu,\mu'}$, one finds

$$\hat{h} = \frac{\hat{\mathbf{p}}^2}{2m_{\text{a}}} + V_{\text{d}}(\mathbf{r}), \tag{2.12}$$

where

$$V_{\text{d}}(\mathbf{r}) = \frac{\hbar}{\Delta} \sum_{\mu} \sum_{\mathbf{k},\mathbf{k}'} \Omega_{\mathbf{k}}^{[\mu]*} \Omega_{\mathbf{k}'}^{[\mu]} \alpha_{\mathbf{k}}^{[\mu]*} \alpha_{\mathbf{k}'}^{[\mu]} e^{-i\mathbf{k}\cdot\mathbf{r}} e^{i\mathbf{k}'\cdot\mathbf{r}} \propto \frac{I(\mathbf{r})}{\Delta} \tag{2.13}$$

is the effective, conservative potential experienced by the atom and $I(\mathbf{r})$ is the intensity within the cavity. The dipole force exerted on the atom by the field is $\mathbf{F}_{\text{d}} = -\nabla V_{\text{d}}(\mathbf{r})$, thus for blue-detuning $\omega > \omega_0$ ($\Delta > 0$) the atom is attracted to points of minimum light intensity, whereas for red-detuning $\omega < \omega_0$ ($\Delta < 0$) it is attracted to points of maximum light intensity. Typical values of the depth of the conservative potential for optical lattices is of the order of 100μK.

Finally, we note that the idealised two-level system used here is only an approximation to real atoms, which of course possess many internal energy levels. In general, the field will couple to more than two levels at the same time, and the potential given in Eq. 2.13 will be much more complicated. However, for optical lattice experiments using alkali atoms and optical frequencies there is typically a single dominant contribution to the interaction, and so the two-level idealisation provides a good description of the actual physics [2].

2.1.2 The optical lattice potential

From Eq. 2.13 we can see that an optical lattice potential can be formed by interfering a set of lasers to create a standing wave intensity pattern. For example, consider two counter-propagating laser beams, each of amplitude E_0 and described by plane-waves with wave-vectors $\mathbf{k}_1 = (0, 0, k)$ and $\mathbf{k}_2 = (0, 0, -k)$. Both beams are linearly polarised in the x-direction, i.e. $\mathbf{e}_1 = \mathbf{e}_2 = \mathbf{i}$ with $\mathbf{i} = (1, 0, 0)$. The sum of the fields is given by

$$\mathbf{E}(z,t) = E_0\mathbf{i}e^{i(\omega t+kz)} + E_0\mathbf{i}e^{i(\omega t-kz)}, \tag{2.14}$$

which has an intensity $I(z) = |\mathbf{E}(z)|^2 = 4|E_0|^2\cos^2(kz)$ that is independent of time. The potential experienced by the atom due to its interaction with the field is $V_\mathrm{d}(x) = V_\mathrm{OL}(x) \propto \cos^2(kx)$ (henceforth we denote V_d by V_OL for optical lattices). The exact value of the proportionality constant depends on the field amplitude, frequency, and detuning, all known quantities, however it also depends on the matrix element $\mathbf{d}_{eg}$, which is not easily calculated. Throughout this thesis we take the customary option of introducing a potential strength V_0 that is expressed in units of the recoil energy $E_\mathrm{R} = \hbar^2k^2/2m_\mathrm{a}$ [17]. We define the potential strength by setting it equal to the full energy range of the optical lattice potential, and further set the zero

of energy to the minimum of the optical lattice potential so that $V_0 = \max[V_{\rm OL}(\mathbf{r})]$ (for this reason we also refer to V_0 as the lattice depth). Typical values for the potential strength are 1-30$E_{\rm R}$ [14]. Returning to our example, the potential, which may now be expressed as $V_{\rm OL} = V_0 \cos^2(kx)$, is periodic in the z-direction with periodicity $\lambda/2$. If we use further pairs of beams in the orthogonal directions, a 3D cubic optical lattice can be formed as shown in Fig. 2.1 with a potential given by

$$V_{\rm OL} = V_0[V_x \cos^2(kx) + V_y \cos^2(ky) + V_z \cos^2(kz)], \tag{2.15}$$

where $\{V_i \mid i = x, y, z \mid \sum_i V_i = 1\}$ gives the ratio of the potential strengths in each lattice direction. To create this potential each pair of lasers must be independent of the others. Two pairs of lasers can be made independent by using orthogonal polarisations, but to make further pairs independent we require their frequencies to be detuned slightly from those of the others. For the potential given in Eq. 2.15 a frequency detuning that is negligible compared to the original field frequency is adequate to ensure independence, while to a good approximation the lattice remains cubic [14].

A wide variety of optical lattices can be constructed using different laser beam configurations, with the minimum number of beams required to generate a 3D optical lattice being four. A number of lattice potentials are studied in chapters 3 and 4 and we leave the details of each configuration until then. Here we note that 1D and 2D lattices can be realised by restricting the motion of the atoms in the orthogonal directions [61]. For example, a set of 1D lattices in the y-direction can be formed from the cubic potential of Eq. 2.15 by using high intensities in the x- and z-directions so that the depth of the potential in these directions is large (typically $\sim 100E_{\rm R}$). This prohibits tunnelling in the x- and z- directions and confines the atoms to sets of 1D tubes as shown in Fig. 2.1. The counter-propagating beams in the

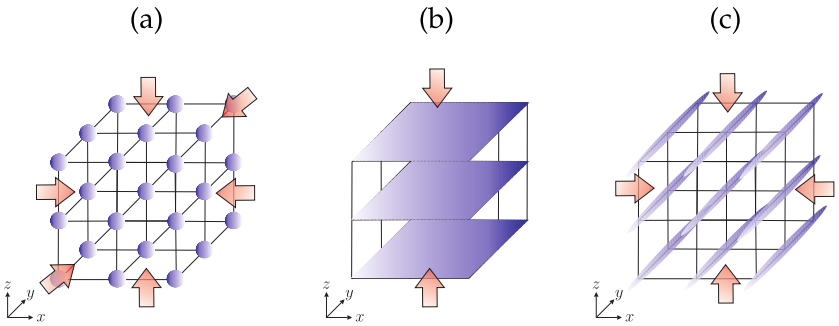


Figure 2.1. (a) Three independent, orthogonal pairs of counter-propagating laser beams produce a 3D cubic optical lattice potential. (b) If the pairs of beams in the x- and y-directions are of low intensity, while the pair in the z-direction are of high intensity, a large lattice depth will exist in the z-direction and the atoms will be constrained to one of a set of 2D planes. (c) Similarly, if the pair of beams in the x-direction are also of high intensity, the atoms will be constrained to one of a set of 1D tubes parallel to the x-axis. [Image courtesy of Stephen Clark]

y-direction can then be replaced by the set that create the particular 1D potential required. Similarly, 2D lattices can be formed by using a high intensity for just one of the beam pairs, which confines the atoms to sets of 2D planes that are normal to the direction of this pair.

The optical lattice potentials described thus far bear a close resemblance to conventional solid state crystals, although there are some differences. Perhaps the most important of these, highlighted in the discussion above, is that the lattice parameters may be controlled and even dynamically altered by varying the laser configuration [28, 62, 33, 63]. For example, the lattice depth may be altered by changing the intensity of the beams, while the geometry can be modified by changing the polarisation of the beams or their propagation direction. Secondly, the optical lattice is essentially defect free and does not possess lattice phonons.[2] Finally, the lattice spacing, determined by the wavelength of the beams, is several orders of magnitude greater than that found in solid state crystals.

[2]Phonon-like effects can occur in the quantum limit [64], however the classical limit is suitable for the typical intensities used in optical lattices.

2.1.3 Experimental considerations

A gas of atoms can be cooled to micro-Kelvin temperatures within a magneto-optical trap (MOT) using the optical molasses technique [2]. The density of the gas once equilibrium is reached is typically around 0.01 μm^{-3}, therefore the optical lattice will be sparsely populated if the atoms are loaded directly from the MOT (one atom per site within a cubic lattice of spacing $\lambda/2$ corresponds to a density of 64 μm^{-3} for $\lambda = 0.5$ μm). Filling factors (the number of atoms per potential well) of the order one or higher can be achieved by loading the optical lattice from a Bose-Einstein condensate of weakly-interacting alkali atoms [13, 14]. The optical lattice potential can then be imposed on the condensate by adiabatically ramping up the intensity of the laser beams, with the atoms going into the lowest vibrational modes of the potential wells.

The derivation of the dipole force given in Sec. 2.1.1 neglected incoherent scattering processes, which in a real system will lead to spontaneous emission of photons from atoms in the excited state $|e\rangle$. Spontaneous emission has a dissipative effect that will be a source of decoherence for the coherent dynamics of the many-body system within the lattice. However, for typical optical lattice experiments using alkali atoms and optical frequencies the spontaneous emission rate is $\Gamma \sim 10^{-2}$ s^{-1}, corresponding to a time scale on the order of minutes. Since the duration of experiments is usually shorter than one second [14, 62, 33] spontaneous emission does not play a significant role.

2.1.4 Lattice definitions

Henceforth, the term 'lattice' will describe an infinite set of lattice points $\{\mathbf{R}_j\}$ that together have the same translational symmetry as the optical lattice potential. The lattice is given by $\sum_j \delta(\mathbf{r} - \mathbf{R}_j)$ and is defined by a basis set of primitive translation

lattice vectors $\{\mathbf{T}_i \mid i = 1, \ldots, D\}$, where D is the dimension of the lattice. Any lattice point $\mathbf{R}_j$ can be reached from a chosen origin point $\mathbf{R}_0$ using a superposition of the primitive lattice vectors. We can also define a region of space as a primitive unit cell, which when associated with every lattice point completely fills all space [65]. The volume of the primitive unit cell is given by

$$\Upsilon = \begin{cases} |\mathbf{T}_1| & \text{for } D = 1, \\ |\mathbf{T}_1 \wedge \mathbf{T}_2| & \text{for } D = 2, \\ |\mathbf{T}_1 \cdot \mathbf{T}_2 \wedge \mathbf{T}_3| & \text{for } D = 3. \end{cases} \tag{2.16}$$

In addition to the lattice it is useful to introduce its Fourier transform, known as the reciprocal lattice. This may be denoted by $\sum_j \delta(\mathbf{k} - \mathbf{G}_j)$, where $\mathbf{k}$ is the conjugate variable to the real space position vector $\mathbf{r}$, and $\{\mathbf{G}_j\}$ are the set of reciprocal lattice points. The basis set of primitive lattice vectors that define the reciprocal lattice are given by $\{\mathbf{T}_i^* \mid i = 1, \ldots, D\}$, which satisfy $\mathbf{T}_i \cdot \mathbf{T}_j^* = 2\pi\delta_{i,j}$.

2.2 Bosons in an optical lattice

The Hamiltonian for a system of interacting bosons immersed in an optical lattice potential is given in second quantisation by

$$\hat{H} = \int d\mathbf{r}\ \hat{\Psi}^\dagger(\mathbf{r})\hat{h}_0\hat{\Psi}(\mathbf{r}) + \frac{g}{2}\int d\mathbf{r}\ \hat{\Psi}^\dagger(\mathbf{r})\hat{\Psi}^\dagger(\mathbf{r})\hat{\Psi}(\mathbf{r})\hat{\Psi}(\mathbf{r}), \tag{2.17}$$

where $\hat{h}_0 = \hat{\mathbf{p}}^2/(2m) + V_{\mathrm{OL}}(\mathbf{r})$ is the single particle Hamiltonian and $\hat{\Psi}(\mathbf{r})$ are the bosonic field operators obeying the usual commutation relations $[\hat{\Psi}(\mathbf{r}), \hat{\Psi}^\dagger(\mathbf{r}')] = \delta(\mathbf{r} - \mathbf{r}')$. The second term describes s-wave scattering between atoms, which is the dominant contribution to two-body collisions in the limit of low energies as used in optical lattice experiments [24]. Here the actual two-body inter-atomic potential

has been replaced by an effective pseudo-potential describing a contact interaction, given by

$$U_{\text{eff}}(\mathbf{r}-\mathbf{r}') = g\delta(\mathbf{r}-\mathbf{r}'), \tag{2.18}$$

where $g = 4\pi\hbar^2 a_{\text{s}}/m_{\text{a}}$ and a_{s} is the scattering length.

In the following sections we will use the physics of a single particle in an optical lattice to obtain a complete, orthonormal basis of 'Wannier' states [66], which are localised to individual lattice sites. The bosonic field operators can then be expanded in this basis as

$$\hat{\Psi}(\mathbf{r}) = \sum_{n,j} w_j^{[n]}(\mathbf{r})\hat{b}_j^{[n]}, \tag{2.19}$$

where $\hat{b}_j^{[n]}$ is an annihilation operator for a boson in the Wannier state $w_j^{[n]}(\mathbf{r})$ corresponding to band n and located at lattice site $\mathbf{R}_j$. Using the substitution in Eq. 2.19 the full many-body Hamiltonian reads

$$\hat{H} = \sum_{i,j}\sum_{m,n} J_{i-j}^{[mn]}\hat{b}_i^{[m]\dagger}\hat{b}_j^{[n]} + \frac{1}{2}\sum_{i,j,k,l}\sum_{m,n,p,s} U_{ijkl}^{[mnps]}\hat{b}_i^{[m]\dagger}\hat{b}_j^{[n]\dagger}\hat{b}_k^{[p]}\hat{b}_l^{[s]}. \tag{2.20}$$

The first term in Eq. 2.20 governs the tunnelling, or 'hopping', of a single particle between lattice sites with matrix elements

$$J_j^{[mn]} = \langle w_j^{[m]}|\hat{h}_0|w_0^{[n]}\rangle, \tag{2.21}$$

while the second term determines the strength of particle interactions with

$$U_{ijkl}^{[mnps]} = g\int d\mathbf{r}\; w_i^{[m]*}(\mathbf{r})w_j^{[n]*}(\mathbf{r})w_k^{[p]}(\mathbf{r})w_l^{[s]}(\mathbf{r}). \tag{2.22}$$

Examples of the various possible terms arising from particle interactions are shown in Fig. 2.2 for a pair of bands and neighbouring lattice sites. By choosing the

set of Wannier states with the least spatial variance, both hopping and interaction matrix elements involving particles that are not local will be negligible and the corresponding terms in Eq. 2.20 can be discarded. In chapters 3 and 4 we calculate the amplitudes of the matrix elements[3] for various lattice geometries to ascertain in each case the dominating terms in Eq. 2.20 resulting in a Bose-Hubbard-type Hamiltonian [25, 13]. Since the Bose-Hubbard Hamiltionian contains only local interactions, the many-body states of the system are more readily calculable than those of the original Hamiltonian in Eq. 2.20.[4]

An assumption that we have yet to address in this section is the use of the single particle band-structure to calculate the Wannier states for the substitution in Eq. 2.19. The assumption will be valid if the Wannier states do not change when more than one particle is loaded into the lattice potential. In general this will not be true and interactions between particles will play a role in forming the basis states in which the bosonic field operators are expanded [67, 68]. However, in the low-filling regime $n_o \sim 1$, the experimentally observed critical conditions for the quantum phase transition in a simple cubic optical lattice [14] are in good agreement with the predicted mean-field result [69] based on the Bose-Hubbard parameters calculated using the single particle physics [13]. In this thesis we consider a variety of lattices for which the single particle Wannier states have yet to be calculated, and leave more

[3] In chapters 3 and 4 we consider 1D and 2D systems respectively. For all of the results presented we treat the system as purely one- or two-dimensional and ignore the remaining orthogonal spatial dimensions. The terms corresponding to these orthogonal dimensions simply factorise out of the matrix elements given in Eq. 2.21 and Eq. 2.22, and therefore contribute a constant multiplicative factor that is the same for all of the geometries considered. For the hopping matrix elements this factor is unity for normalised Wannier functions. However, since the contact interaction constant g is given in terms of the scattering length, which is derived in three-dimensions, one must be careful in treating the interaction matrix elements in this way. In 1D we choose to present our results for the interaction matrix elements in terms of a new constant $\tilde{g}_1$ with units of J·m, and similarly in 2D in terms of a constant $\tilde{g}_2$ with units of J·m^2. One can always apply the multiplicative factor corresponding to the neglected spatial dimensions (calculated by obtaining the form of the Wannier states in these directions) to our results to determine them in terms of g.

[4] The Hamiltonian in Eq. 2.20 can only be diagonalised numerically for lattices with just a few sites.

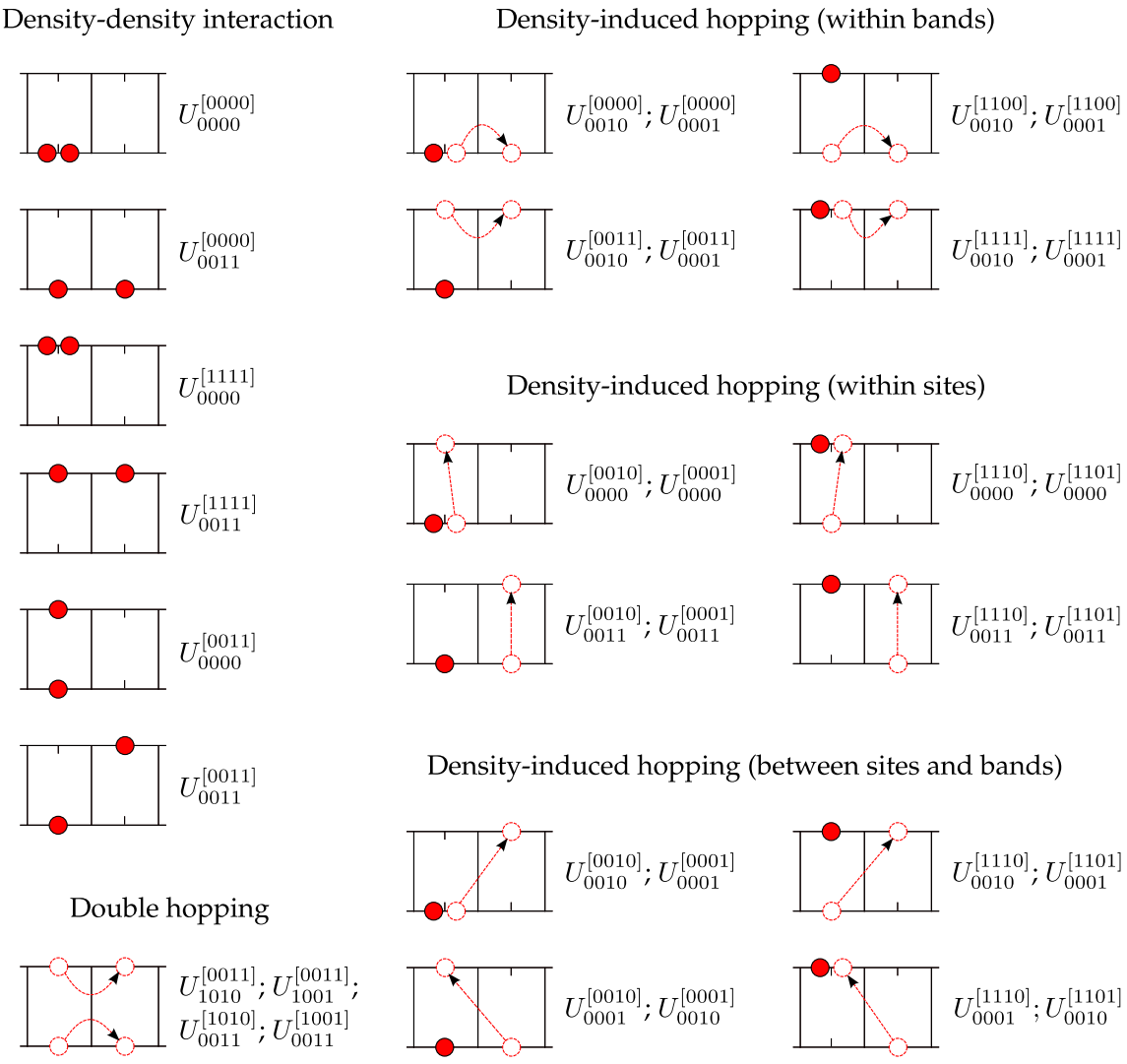


Figure 2.2. Schematic of the various possible interaction terms involving two bands and a pair of neighbouring sites. The left rectangle represents the home site $j = 0$, while the right rectangle represents the neighbouring site $j = 1$. The two bands are represented by the horizontal lines. Solid circles indicate the presence of a particle, i.e. $\hat{b}_j^{[n]\dagger}\hat{b}_j^{[n]}$, while dashed circles and the corresponding arrows represent hopping between sites and/or bands, e.g. $\hat{b}_i^{[m]\dagger}\hat{b}_j^{[n]}$.

complex approaches, e.g. as proposed in Ref. [67] or Ref. [68], to these systems for further work.

2.3 Single particle physics

A requirement of the translational invariance present in the optical lattice is that the single particle Hamiltonian $\hat{h}_0$ commutes with the lattice translation operator $\hat{T}_j f(\mathbf{r}) = f(\mathbf{r} + \mathbf{R}_j)$, leading to the well-known result that the eigenstates $\phi_{\mathbf{q}}(\mathbf{r})$, known in such systems as Bloch states, satisfy Bloch's theorem [65]

$$\phi_{\mathbf{q}}(\mathbf{r}) = e^{i\mathbf{q}\cdot\mathbf{r}} u_{\mathbf{q}}(\mathbf{r}). \tag{2.23}$$

A Bloch state describes a plane-wave with wave-vector $\mathbf{q}$ modulated by a periodic function $u_{\mathbf{q}}(\mathbf{r})$ that has the same translational symmetry as the underlying lattice, i.e. $\hat{T}_j u_{\mathbf{q}}(\mathbf{r}) = u_{\mathbf{q}}(\mathbf{r})$. By inserting the Bloch states into Schrödinger's equation $\hat{h}_0 \phi_{\mathbf{q}}(\mathbf{r}) = E_{\mathbf{q}} \phi_{\mathbf{q}}(\mathbf{r})$ we obtain the following for each wave-vector $\mathbf{q}$,

$$\hat{h}_{\mathbf{q}} u_{\mathbf{q}}(\mathbf{r}) = E_{\mathbf{q}} u_{\mathbf{q}}(\mathbf{r}), \text{ where } \hat{h}_{\mathbf{q}} = \frac{(\hat{\mathbf{p}} + \mathbf{q})^2}{2m} + V_{\mathrm{OL}}(\mathbf{r}). \tag{2.24}$$

The Bloch states are not unique but in fact form an infinite set of solutions, because each remains unchanged when the associated wave-vector $\mathbf{q}$ is translated by a reciprocal lattice vector.[5] We thus confine solutions of Eq. 2.24 to within the first Brillouin zone, which is the Wigner-Seitz unit cell [65] of the reciprocal lattice, and introduce a new quantum number n, called the band index, to label Bloch states with the same wave-vector $\mathbf{q}$. The Bloch states, now denoted by $\phi_{\mathbf{q}}^{[n]}(\mathbf{r})$, have

[5] The quantity $\hbar\mathbf{q}$ is often called the quasi-momentum or crystal momentum because of its interpretation as a quantum number of the momentum operator acting on the Bloch state. However, while the 'regular' momentum quantum number associated with a free particle is a conserved quantity, the result of the discrete translational invariance is that the quasi-momentum is only conserved to within a reciprocal lattice vector (multiplied by $\hbar$).

corresponding energies $E_{\mathbf{q}}^{[n]}$, which for an infinite lattice form a continuous function inside the first Brillouin zone called the band-structure [65], with n labelling the discrete set of bands.

2.3.1 Fourier decompositions in the reciprocal lattice

To calculate the band-structure at a given wave-vector we introduce the Fourier expansions of the potential and the Bloch periodic functions over a plane-wave basis set, with each Fourier component corresponding to a reciprocal lattice vector $\mathbf{G}_k$. These are respectively

$$V_{\mathrm{OL}}(\mathbf{r}) = \frac{1}{\sqrt{\Upsilon}} \sum_k v_k e^{i\mathbf{G}_k \cdot \mathbf{r}}, \tag{2.25}$$

$$u_{\mathbf{q}}^{[n]}(\mathbf{r}) = \frac{1}{\sqrt{\Upsilon}} \sum_k c_{\mathbf{q},k}^{[n]} e^{i\mathbf{G}_k \cdot \mathbf{r}}, \tag{2.26}$$

where $c_{\mathbf{q},k}^{[n]}$ are a set of coefficients satisfying $\sum_k (c_{\mathbf{q},k}^{[m]})^* c_{\mathbf{q},k}^{[n]} = \delta_{m,n}$, and Υ is the volume of the real space primitive unit cell. The factor $\Upsilon^{-0.5}$ in Eq. 2.26 ensures $u_{\mathbf{q}}^{[n]}(\mathbf{r})$ is normalised over the primitive unit cell. Since the function $V_{\mathrm{OL}}(\mathbf{r})$ for the potential is known the coefficients v_k can be calculated using

$$v_k = \frac{1}{\sqrt{\Upsilon}} \int_{\Upsilon} d\mathbf{r} V_{\mathrm{OL}}(\mathbf{r}) e^{-i\mathbf{G}_k \cdot \mathbf{r}}. \tag{2.27}$$

Inserting Eqs. 2.25 and 2.26 into Eq. 2.24 and equating coefficients leads to

$$\frac{1}{2m}(\mathbf{G}_k + \mathbf{q})^2 c_{\mathbf{q},k}^{[n]} + \frac{1}{\sqrt{\Upsilon}} \sum_l v_{k-l} c_{\mathbf{q},l}^{[n]} = E_{\mathbf{q}}^{[n]} c_{\mathbf{q},k}^{[n]}. \tag{2.28}$$

To proceed further we must truncate the Fourier expansions in order to deal with a finite number of coefficients. We do this by introducing a maximum cut-off frequency $G_{\max}$, including only those components satisfying $|\mathbf{G}_k| \leq G_{\max}$ as shown

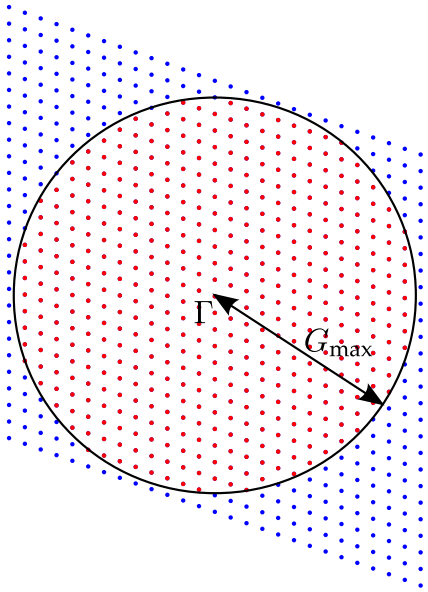


Figure 2.3. The reciprocal lattice points for a 2D oblique lattice. The black circle has a radius of $G_{\max}$ and is centred on Γ. Fourier components corresponding to reciprocal lattice points within the circle (red points) are included in the truncated basis set, while those outside (blue points) are not.

in Fig. 2.3. The cut-off frequency corresponds to a maximum kinetic energy for the plane-wave components given by $E_{\text{cut-off}} = G_{\max}^2/2m$, and introduces a minimum spatial resolution $\lambda_{\min} = \pi\sqrt{2/mE_{\text{cut-off}}}$ for describing real space functions in the system, namely, the potential and the Bloch periodic functions (and thereby the Wannier functions). The minimum spatial resolution must be smaller than the spatial variations in these functions in order for them to be accurately recreated using the truncated set of coefficients, therefore the cut-off energy must be at least as large as the highest energy Fourier component of the potential. The cut-off energy is then increased until the bands energies for each band under consideration have converged, at which point all non-zero coefficients $c_{\mathbf{q},k}^{[n]}$ describing the Bloch periodic functions $u_{\mathbf{q}}^{[n]}(\mathbf{r})$ will be included. Typically, this requires the cut-off energy to be an order of magnitude greater than the upper-end of the energy range of interest.[6]

[6]In our calculations a cut-off energy of 50 E_R is sufficient for band convergence and suitably limits the total number of coefficients such that even in three dimensions our numerics are not

The set of equations 2.28 can now be solved simultaneously by expressing them as a matrix equation

$$\mathtt{H}_{\mathbf{q}}\vec{c}_{\mathbf{q}}^{\,[n]} = E_{\mathbf{q}}^{[n]}\vec{c}_{\mathbf{q}}^{\,[n]}, \tag{2.29}$$

where $\vec{c}_{\mathbf{q}}^{\,[n]}$ is a vector containing a total of $\mathtt{R}$ coefficients $c_{\mathbf{q},k}^{[n]}$, and $\mathtt{H}_{\mathbf{q}}$ is an $\mathtt{R}\times\mathtt{R}$ matrix given by

$$\mathtt{H}_{\mathbf{q}}^{[k,l]} = \frac{1}{2m}(\mathbf{G}_k+\mathbf{q})^2\delta_{k,l} + \frac{1}{\sqrt{\Upsilon}}v_{k-l}, \tag{2.30}$$

with k,l denoting the rows and columns of $\mathtt{H}_{\mathbf{q}}$ respectively. High frequency Fourier components of the potential that connect Fourier components of the Bloch periodic functions with energies less than $E_{\text{cut-off}}$ to those with energies greater than $E_{\text{cut-off}}$ will not be important and can be ignored in $\mathtt{H}_{\mathbf{q}}$. Solving Eq. 2.29 yields the lowest $\mathtt{R}$ eigenvalues $E_{\mathbf{q}}^{[n]}$ labelled by the band index n, and their corresponding eigenvectors $\vec{c}_{\mathbf{q}}^{\,[n]}$ given in the plane-wave basis. The full band-structure is obtained by repeating for each wave-vector $\mathbf{q}$ in the Brillouin zone, with the Bloch periodic functions $u_{\mathbf{q}}^{[n]}(\mathbf{r})$, and thus the Bloch states $\phi_{\mathbf{q}}^{[n]}(\mathbf{r})$, determined by the eigenvectors $\vec{c}_{\mathbf{q}}^{\,[n]}$.

2.3.2 Brillouin zone sampling and symmetry

The methods described in the following sections require integrations of functions across the entirety of the Brillouin zone. With our numerical calculations we must approximate these functions using a discretised mesh of wave-vectors, which sample the functions across the zone. We choose a uniform mesh $\{\mathbf{q}\} = \sum_i \delta(\mathbf{k}-\mathbf{G}_i/N)$ that is bounded in each reciprocal lattice direction $i = 1,\ldots,D$ by the condition $-\mathbf{T}_i/2 \leq \mathbf{q} < \mathbf{T}_i/2$.[7] As shown in Fig. 2.4, with this choice of mesh some wave-vectors may lie outside the Brillouin zone in the case of non-orthogonal geometries, however, the corresponding Bloch states can always be translated into the Brillouin zone using a

computationally expensive.

[7] This corresponds to considering a finite real space lattice with periodic boundary conditions and N primitive unit cells in each lattice direction.

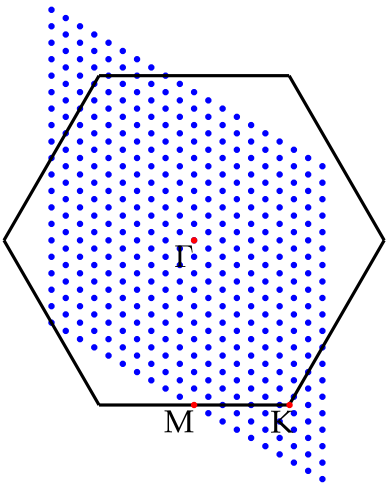


Figure 2.4. A mesh of wave-vectors $\{\mathbf{q}\}$ for a hexagonal 2D lattice used to sample the Brillouin zone, which is shown by the black hexagon. The mesh includes Γ but not necessarily other high symmetry points. Bloch states outside the Brillouin zone are unchanged when translated into the zone by a reciprocal lattice vector.

reciprocal lattice vector. Since the Hamiltonian obeys translational symmetry the energy will be unchanged by the translation, while the Fourier components of the Bloch periodic functions are shifted by the relation $u^{[n]}_{\mathbf{q}+\mathbf{G}_k} = e^{-i\mathbf{G}_k\cdot\mathbf{r}}u^{[n]}_{\mathbf{q}}$. Integrals can now be replaced by summations using

$$\frac{\Upsilon}{(2\pi)^D}\int d\mathbf{q} \to \frac{1}{N^D}\sum_{\mathbf{q}}. \tag{2.31}$$

The total number of band-structure calculations can be reduced from the maximum N^D by appealing to various additional symmetries present in the system. For example, consider the Hamiltonian $\hat{h}_0$ invariant under a particular symmetry operation $\hat{S}$; for any Bloch state $\phi^{[n]}_{\mathbf{q}}(\mathbf{r})$ there exists another solution $\hat{S}\phi^{[n]}_{\mathbf{q}}(\mathbf{r})$ to the time-independent Schödinger equation with the same energy eigenvalue. This solution may correspond to a Bloch state with phase factor $\mathbf{q}'\cdot\mathbf{r}$, in which case the Bloch states at $\mathbf{q}'$ and $\mathbf{q}$ are related by the symmetry operation allowing one

to be inferred from the other. If the symmetry operation keeps the wave-vector $\mathbf{q}$ fixed, i.e. $\mathbf{q}' = \mathbf{q}$, the bands will be at least two-fold degenerate at $\mathbf{q}$ if $u^{[n]}_{\mathbf{q}}(\mathbf{r})$ isn't simultaneously an eigenstate of $\hat{S}$, while if it is the invariance under the symmetry operation can impose some useful properties on the state.

Perhaps the most useful symmetry to exist in the system is time reversal symmetry [70]; the single particle Hamiltonian $\hat{h}_0$ commutes with a conventional time reversal operator $\hat{\mathcal{T}}$ defined by

$$t \xrightarrow{\hat{\mathcal{T}}} -t; \tag{2.32}$$

$$\hat{\mathcal{T}}\hat{x}\hat{\mathcal{T}}^{-1} = \hat{x}; \tag{2.33}$$

$$\hat{\mathcal{T}}\hat{p}\hat{\mathcal{T}}^{-1} = -\hat{p}; \tag{2.34}$$

$$\hat{\mathcal{T}}^2 = \pm 1, \tag{2.35}$$

where $\hat{x}$ and $\hat{p}$ are position and momentum operators respectively. In addition, $\hat{\mathcal{T}}$ is anti-unitary, i.e. for a pair of states ψ and ϕ,

$$\langle \hat{\mathcal{T}}\psi | \hat{\mathcal{T}}\phi \rangle = \langle \psi | \phi \rangle^* = \langle \phi | \psi \rangle. \tag{2.36}$$

For spinless particles the positive sign holds in Eq. 2.35 so that the action of $\hat{\mathcal{T}}$ on a state ψ is $\hat{\mathcal{T}}\psi = \pm\psi^*$ [70]. The consequence of time reversal symmetry, and in particular the fact that the operator is anti-unitary, is that for any Bloch state $\phi^{[n]}_{\mathbf{q}}(\mathbf{r})$ the transformed state, given by

$$\hat{\mathcal{T}}\phi^{[n]}_{\mathbf{q}}(\mathbf{r}) = \pm\phi^{[n]*}_{\mathbf{q}}(\mathbf{r}) = \pm e^{-i\mathbf{q}\cdot\mathbf{r}} u^{[n]*}_{\mathbf{q}}(\mathbf{r}), \tag{2.37}$$

corresponds to a Bloch state with phase factor $-\mathbf{q}\cdot\mathbf{r}$, and therefore $u^{[n]}_{-\mathbf{q}}(\mathbf{r}) = \pm u^{[n]*}_{\mathbf{q}}(\mathbf{r})$ is the solution of Eq. 2.24 at wave-vector $-\mathbf{q}$ with energy $E_{\mathbf{q}}$. Thus the

Fourier coefficients for half the mesh points with $\mathbf{q} \neq 0$ can be inferred from their inverted points using $c^{[n]}_{-\mathbf{q},k} = \pm c^{[n]*}_{\mathbf{q},-k}$, while at Γ the Bloch states are real disregarding a global phase[8] and the coefficients satisfy $c^{[n]}_{\mathbf{0},k} = \pm c^{[n]*}_{\mathbf{0},-k}$.[9]

Geometrical symmetries can also be present in the system, which can lead to additional gains in the computation of the band-structure. Consider now the operator $\hat{S}$ representing a crystallographic point group operation [65]. A Bloch state transforms as

$$\hat{S}\phi^{[n]}_{\mathbf{q}}(\mathbf{r}) = \pm e^{i\mathbf{q}\cdot\hat{S}\mathbf{r}} u^{[n]*}_{\mathbf{q}}(\hat{S}\mathbf{r}), \tag{2.38}$$

which corresponds to another Bloch state with phase factor $(\hat{S}^T\mathbf{q})\cdot\mathbf{r}$ and periodic function $u^{[n]}_{\hat{S}^T\mathbf{q}}(\mathbf{r}) = \pm u^{[n]}_{\mathbf{q}}(\hat{S}\mathbf{r})$. The transpose of a point group operation either preserves or inverts the operation, therefore in the case of reflections and rotations the Bloch states at the transformed Brillouin zone point can be inferred accordingly. In the case of inversion symmetry this implies $u^{[n]}_{-\mathbf{q}}(-\mathbf{r}) = \pm u^{[n]}_{\mathbf{q}}(\mathbf{r})$ and thus the Fourier coefficients must satisfy $c^{[n]}_{-\mathbf{q},k} = \pm c^{[n]}_{\mathbf{q},-k}$. In combination with the result of time reversal symmetry this means that the coefficients must be real disregarding a global phase and at Γ the Bloch states are real odd or even functions. Ensuring the origin is located at an inversion point reduces the number of real numbers involved in the computation by half.[10]

2.4 The Wannier basis

The previous section detailed how to efficiently compute the single particle eigenstates for an optical lattice potential, but the eigenbasis itself is not particularly useful for describing local interactions because the Bloch states have a spatial ex-

[8] Further discussion of the local and global phases of the Bloch states will be given in section 2.4.

[9] This is true even if there is degeneracy, which would arise because of the presence of a crystallographic point group symmetry.

[10] An arbitrary complex number requires two real numbers to be described numerically.

tent across the entire lattice. An alternative basis of states localised on each lattice site $\mathbf{R}_j$ is instead required; as previously stated such a basis exists and is comprised of so-called 'Wannier' states, denoted by $w_j^{[n]}(\mathbf{r})$. The Wannier states arise as the Fourier coefficients of the Bloch states when these are expanded, for fixed $\mathbf{r}$, over a plane-wave basis set associated to the real space lattice points, i.e.

$$\phi_{\mathbf{q}}^{[n]}(\mathbf{r}) = \sum_j w_j^{[n]}(\mathbf{r}) e^{i\mathbf{q}\cdot\mathbf{R}_j}. \tag{2.39}$$

In order for Eq. 2.39 to satisfy Bloch's theorem the Wannier states must be a function of $\mathbf{r}-\mathbf{R}_j$ as $w^{[n]}(\mathbf{r}-\mathbf{R}_j)$, thus for any band n the Wannier states associated to each lattice site are identical modulo a lattice vector. The Wannier states, or functions as we shall now refer to them, are defined from the inverse of Eq. 2.39 as

$$w^{[n]}(\mathbf{r}-\mathbf{R}_j) = \frac{\Upsilon}{(2\pi)^D} \int_{\mathrm{BZ}} d\mathbf{q} e^{-i\mathbf{q}\cdot\mathbf{R}_j} \phi_{\mathbf{q}}^{[n]}(\mathbf{r}), \tag{2.40}$$

where the integration is confined to the first Brillouin zone. By defining $u_{\mathbf{q}}^{[n]}(\mathbf{r}) = \langle \mathbf{r}|u_{\mathbf{q}}^{[n]}\rangle$ and $w^{[n]}(\mathbf{r}-\mathbf{R}_j) = \langle \mathbf{r}|w_j^{[n]}\rangle$, the orthonormality of the set of Wannier functions $\langle w_i^{[m]}|w_j^{[n]}\rangle = \delta_{i,j}\delta_{m,n}$ follows from that of the Bloch periodic functions $\langle u_{\mathbf{q}}^{[m]}|u_{\mathbf{q}'}^{[n]}\rangle = \delta_{\mathbf{q},\mathbf{q}'}\delta_{m,n}$, as does its completeness.[11]

A given set of Wannier functions is not unique due to a freedom in the choice of local phase of the Bloch states as a function of the wave-vector $\mathbf{q}$. For each Wannier function $w^{[n]}(\mathbf{r}-\mathbf{R}_j)$ associated with a single band n that contains no degeneracies, the corresponding Bloch states may be transformed using

$$|\phi_{\mathbf{q}}^{[n]}\rangle \rightarrow e^{i\theta_{\mathbf{q}}^{[n]}}|\phi_{\mathbf{q}}^{[n]}\rangle, \tag{2.41}$$

[11] For an infinite lattice the Bloch states form an orthogonal, complete set but are not normalised due to their infinite extent.

where $\theta_{\mathbf{q}}^{[n]}$ is a real function of $\mathbf{q}$ [71]. The centres of the Wannier functions $\bar{\mathbf{r}}_j^{[n]} = \langle w_j^{[n]}|\hat{\mathbf{r}}|w_j^{[n]}\rangle$ are preserved modulo a lattice vector, but the spatial variance $\Omega^{[n]} = \langle w_j^{[n]}|\hat{\mathbf{r}}^2|w_j^{[n]}\rangle - \bar{\mathbf{r}}_j^{[n]2}$ is not. Given an initial set of reference Bloch states, e.g. as determined from a band-structure calculation, a specific gauge transformation $U_{\mathbf{q}}^{[n]} = e^{i\theta_{\mathbf{q}}^{[n]}}$ exists that will result in a set of Wannier functions with a minimal spatial variance, or spread as this shall henceforth be called. The following sections detail the process of ascertaining this gauge transformation for both isolated bands and those that are degenerate, where in the latter case we follow the methods of Marzari and Vanderbilt in Ref. [71] and also Souza *et al.* in Ref. [72]. Firstly, we remark that the set of Wannier functions with minimal spread may not necessarily be the optimal choice for minimising terms beyond nearest-neighbour in the Hamiltonian in Eq. 2.17, although one would expect it to be close to optimal. Given the complexity of obtaining a maximally localised set that has been optimised with respect to a relatively simple measure in the spread, calculating a gauge transformation that directly minimises a variety of overlap terms would prove difficult. Please see Ref. [71] for a discussion on the use of the spread as a suitable functional for the localisation of Wannier functions.

2.4.1 Generalised Wannier functions

So far the discussion of Wannier functions has been limited to a set of isolated, non-degenerate bands. For a group of 'composite' bands that are degenerate amongst themselves but isolated from other bands, e.g. as shown in Fig. 2.5, we must allow further freedom in the choice of Bloch states to account for the degenerate subspaces. The extension is simply

$$|\phi_{\mathbf{q}}^{[n]}\rangle \rightarrow \sum_{m=1}^{K} U_{\mathbf{q}}^{[mn]}|\phi_{\mathbf{q}}^{[m]}\rangle, \tag{2.42}$$

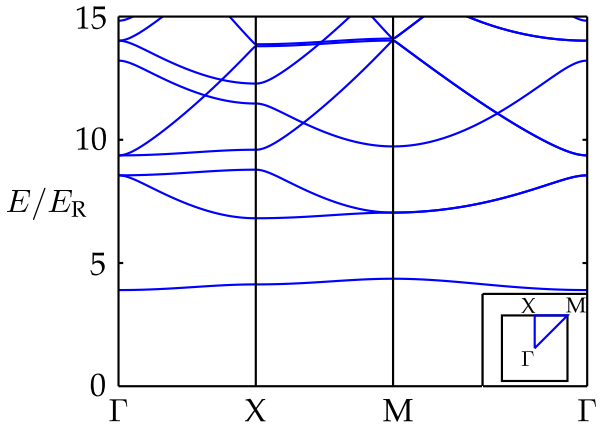


Figure 2.5. The band-structure for a 2D isotropic square optical lattice with a potential strength $V_0 = 10E_R$. The band energies are plotted along the path through the Brillouin zone shown in the inset. The lowest band is isolated from other bands, while the second and third lowest bands are degenerate amongst themselves but isolated from other bands, and therefore form a composite group.

where $U_{\mathbf{q}}$ is a unitary matrix that mixes the Bloch states of all bands in the composite group at $\mathbf{q}$, and K is the total number of bands. This freedom reduces to that described in Eq. 2.41 when the matrices $U_{\mathbf{q}}$ are diagonal. In the following we still refer to the Bloch states and Wannier functions as belonging to a particular band indexed by the band label n, but this is not strictly true and one can only consider them as corresponding to a particular 'mode' n of the composite group.

Starting with an initial set of reference Bloch states $\phi_{\mathbf{q}}^{[m](0)}(\mathbf{r})$, the 'generalised' Wannier functions are given by

$$w^{[n]}(\mathbf{r}-\mathbf{R}_j) = \frac{\Upsilon}{(2\pi)^D}\int_{\mathrm{BZ}} d\mathbf{q} e^{-i\mathbf{q}\cdot\mathbf{R}_j}\sum_{m=1}^{K} U_{\mathbf{q}}^{[mn]}\phi_{\mathbf{q}}^{[m](0)}(\mathbf{r}), \tag{2.43}$$

and form an orthonormal, complete set in the space spanned by the K bands since the matrices $U_{\mathbf{q}}$ are unitary. We wish to find the specific gauge that minimises the

total spread of a composite group of generalised Wannier functions, defined by

$$\Omega = \sum_{n=1}^{K} \Omega^{[n]} = \sum_{n=1}^{K} \left[\langle \hat{\mathbf{r}}^2 \rangle_0^{[n]} - \overline{\mathbf{r}}_0^{[n]2} \right], \tag{2.44}$$

where $\langle \hat{\mathbf{r}}^2 \rangle_j^{[n]} = \langle w_j^{[n]} | \hat{\mathbf{r}}^2 | w_j^{[n]} \rangle$. In the following we outline a procedure for achieving this, and detail the properties of generalised Wannier functions and their spread. Firstly, one further point to note is that one can of course allow the freedom described in Eq. 2.42 for a group of bands when one or more of its members is non-degenerate. The generalised Wannier functions obtained in this way for 1D optical lattices will be a topic of discussion in chapter 3.

2.4.2 The spread functional

A useful property of the spread is that it may be decomposed into two terms as $\Omega = \Omega_{\mathrm{I}} + \tilde{\Omega}$, where

$$\Omega_{\mathrm{I}} = \sum_{n} \left[\langle \hat{\mathbf{r}}^2 \rangle_0^{[n]} - \sum_{m,j} |\langle w_j^{[m]} | \hat{\mathbf{r}} | w_0^{[n]} \rangle|^2 \right] \tag{2.45}$$

is gauge invariant and positive definite, and

$$\tilde{\Omega} = \sum_{n} \sum_{(m,j) \neq (n,0)} |\langle w_j^{[m]} | \hat{\mathbf{r}} | w_0^{[n]} \rangle|^2, \tag{2.46}$$

which is also positive definite. The latter term may be decomposed further as $\tilde{\Omega} = \Omega_{\mathrm{D}} + \Omega_{\mathrm{OD}}$, where

$$\Omega_{\mathrm{D}} = \sum_{n} \sum_{j \neq 0} |\langle w_j^{[n]} | \hat{\mathbf{r}} | w_0^{[n]} \rangle|^2, \tag{2.47}$$

$$\Omega_{\mathrm{OD}} = \sum_{m \neq n} \sum_{j} |\langle w_j^{[m]} | \hat{\mathbf{r}} | w_0^{[n]} \rangle|^2, \tag{2.48}$$

are band-diagonal and band-off-diagonal terms respectively. By changing notation $|w_j^{[n]}\rangle \rightarrow |a\rangle$ and defining matrices $X_{ab} = \langle a|\hat{x}|b\rangle$, $X_{\mathrm{D},ab} = X_{ab}\delta_{a,b}$ and $X' = X - X_D$ for the x-component of the position operator $\hat{\mathbf{r}}$, and similarly for the y- and z-components, the variant part can be rewritten as

$$\tilde{\Omega} = \mathrm{tr}[X'^2 + Y'^2 + Z'^2]. \tag{2.49}$$

In 1D only X'^2 is present in the trace, and if we choose the generalised Wannier functions such that X is diagonal then $\tilde{\Omega}$ vanishes and the minimum spread is equal to the gauge invariant part Ω_{I}. Therefore, the maximally localised generalised Wannier functions in 1D are the eigenfunctions of X. In higher dimensions one requires that the matrices for each Cartesian component mutually commute for them to be simultaneously diagonalisable causing $\tilde{\Omega}$ to vanish. This is only possible if the single particle Hamiltonian $\hat{h}_0$ is separable in Cartesian coordinates, which is true only for lattices with orthogonal axes. For non-orthogonal geometries the problem, as stated in Ref. [71] for 3D, is to 'to find a set of Wannier functions that makes the best possible compromise in the attempt to diagonalise all three (matrices) simultaneously'.

The algorithm introduced by Marzari and Vanderbilt for achieving the above stated problem is a steepest-minimisation method using the gradient of the spread functional in reciprocal space. The derivations of definitions for the centres of the Wannier functions, their variances, and the total spread in reciprocal space are detailed in Ref. [71]. To summarise, one uses the discretised mesh of wave-vectors as described in Sec. 2.3.2, in conjunction with a finite-difference formula for calculating gradients in reciprocal space, to obtain the following for the Wannier centres and

variances respectively,

$$\bar{\mathbf{r}}^{[n]} = -\frac{1}{N^D}\sum_{\mathbf{q},\mathbf{b}} \omega_{\mathbf{b}} \mathbf{b} \mathrm{Im}[\ln M^{[nn]}_{\mathbf{q},\mathbf{b}}], \tag{2.50}$$

$$\langle \hat{\mathbf{r}}^2 \rangle^{[n]} = \frac{1}{N^D}\sum_{\mathbf{q},\mathbf{b}} \omega_{\mathbf{b}} \left\{ 1 - |M^{[nn]}_{\mathbf{q},\mathbf{b}}|^2 + (\mathrm{Im}[\ln M^{[nn]}_{\mathbf{q},\mathbf{b}}])^2 \right\}. \tag{2.51}$$

Here the vectors $\mathbf{b}$ connect each wave-vector $\mathbf{q}$ to its nearest-neighbours, $\omega_{\mathbf{b}}$ are associated weights [73], and the matrices $M_{\mathbf{q},\mathbf{b}}$ determine the overlaps of neighbouring Bloch periodic functions as

$$M^{[mn]}_{\mathbf{q},\mathbf{b}} = \langle u^{[m]}_{\mathbf{q}} | u^{[n]}_{\mathbf{q}+\mathbf{b}} \rangle. \tag{2.52}$$

Using Eqs. 2.50 and 2.51 we can formulate the reciprocal space definition of the spread functional $\Omega = \Omega_{\mathrm{I}} + \Omega_{\mathrm{D}} + \Omega_{\mathrm{OD}}$ as

$$\Omega_{\mathrm{I}} = \frac{1}{N^D}\sum_{\mathbf{q},\mathbf{b}} \omega_{\mathbf{b}} \left(K - \sum_{m,n} |M^{[mn]}_{\mathbf{q},\mathbf{b}}|^2 \right), \tag{2.53}$$

$$\Omega_{\mathrm{D}} = \frac{1}{N^D}\sum_{\mathbf{q},\mathbf{b}} \omega_{\mathbf{b}} \sum_{n} \rho^{[n]2}_{\mathbf{q},\mathbf{b}}, \tag{2.54}$$

$$\Omega_{\mathrm{OD}} = \frac{1}{N^D}\sum_{\mathbf{q},\mathbf{b}} \omega_{\mathbf{b}} \sum_{m \neq n} |M^{[mn]}_{\mathbf{q},\mathbf{b}}|^2, \tag{2.55}$$

where

$$\rho^{[n]}_{\mathbf{q},\mathbf{b}} = \mathrm{Im}[\ln M^{[nn]}_{\mathbf{q},\mathbf{b}}] + \mathbf{b} \cdot \bar{\mathbf{r}}^{[n]}. \tag{2.56}$$

By considering the first order change in the spread functional arising from an infinitesimal gauge transformation

$$U^{[mn]}_{\mathbf{q}} = \delta_{m,n} + dW^{[mn]}_{\mathbf{q}}, \tag{2.57}$$

where dW is an infinitesimal antiunitary matrix such that

$$|u_{\mathbf{q}}^{[n]}\rangle \rightarrow |u_{\mathbf{q}}^{[n]}\rangle + \sum_m dW_{\mathbf{q}}^{[mn]}|u_{\mathbf{q}}^{[m]}\rangle, \tag{2.58}$$

the gradient of the spread functional can be shown to be

$$G_{\mathbf{q}} = \frac{d\Omega}{dW_{\mathbf{q}}} = 4\sum_{\mathbf{b}} \omega_{\mathbf{b}} \left(A[V_{\mathbf{q},\mathbf{b}}] - S[T_{\mathbf{q},\mathbf{b}}]\right). \tag{2.59}$$

Here A and S are super-operators that act on an arbitrary matrix B as $A[B] = (B - B^\dagger)/2$ and $S[B] = (B + B^\dagger)/2i$, and

$$V_{\mathbf{q},\mathbf{b}}^{[mn]} = M_{\mathbf{q},\mathbf{b}}^{[mn]} M_{\mathbf{q},\mathbf{b}}^{[nn]*}, \tag{2.60}$$

$$T_{\mathbf{q},\mathbf{b}}^{[mn]} = \frac{M_{\mathbf{q},\mathbf{b}}^{[mn]}}{M_{\mathbf{q},\mathbf{b}}^{[nn]}} \rho_{\mathbf{q},\mathbf{b}}. \tag{2.61}$$

When the gradient in Eq. 2.59 is zero the spread will be at a minimum with respect to the gauge transformation of Eq. 2.42.

2.4.3 Steepest-decent minimisation[12]

The gradient can be reduced to zero by iteratively applying the infinitesimal gauge transformation in Eq. 2.57, setting

$$dW_{\mathbf{q}} = \epsilon G_{\mathbf{q}}, \tag{2.62}$$

[12]The steepest-descent algorithm summarised in this section is that introduced in Ref. [71]. The computer package Wannier90 (written in Fortran90), available under the GNU General Public Licence at http://www.wannier.org and documented in Ref. [73], implements the algorithm, taking as input the overlap matrices $M_{\mathbf{q},\mathbf{b}}$ and outputting the maximally localised generalised Wannier functions. We have written a Matlab program using our own implementation of the steepest-descent algorithm, which focusses on calculating maximally localised generalised Wannier functions for optical lattice potentials. This can be downloaded at http://ccpforge.cse.rl.ac.uk/gf/project/mlgws/.

where ϵ is a positive infinitesimal. To first order in ϵ the change in the spread functional is given by

$$d\Omega = \sum_{\mathbf{q}} \mathrm{tr}[G_{\mathbf{q}} dW_{\mathbf{q}}] \tag{2.63}$$

$$= -\epsilon \sum_{\mathbf{q}} \sum_{m,n} |G_{\mathbf{q}}^{[mn]}|^2, \tag{2.64}$$

where the second line is a result of the gradient matrices $G_{\mathbf{q}}$ being anti-unitary, i.e. $G_{\mathbf{q}}^{\dagger} = -G_{\mathbf{q}}$. Since $d\Omega$ is less than zero the gauge transformation reduces the total spread Ω. For a numerical implementation we use a finite fixed step $\epsilon \to \epsilon/4\omega$, where $\omega = \sum_{\mathbf{b}} \omega_{\mathbf{b}}$ and $\epsilon \sim 1$, so that $dW_{\mathbf{q}} \to \Delta W_{\mathbf{q}} = \epsilon G_{\mathbf{q}}/4\omega$. For an isolated band setting $\epsilon = 0.5$ will return the system to the solution at a minimum. Setting $\epsilon = 1$ is marginally unstable, however, in agreement with Ref. [71] we found this to be a safe choice for the majority of systems studied and the increased step size requires fewer iterations to reach a minimum.

The iterative procedure is as follows. We begin with the eigenvectors $\vec{c}_{\mathbf{q}}^{\,[n]}$ from the band-structure calculation, which may be used to define a reference set of Bloch states $\phi_{\mathbf{q}}^{[n](0)}(\mathbf{r})$, and also a set of cumulative transformation matrices initialised as $K \times K$ identity matrices,

$$U_{\mathbf{q}} = \mathbf{1}_K. \tag{2.65}$$

We compute the overlap matrices as

$$M_{\mathbf{q},\mathbf{b}}^{[mn]} = \vec{c}_{\mathbf{q}}^{\,[m]\dagger} \vec{c}_{\mathbf{q}+\mathbf{b}}^{\,[n]}, \tag{2.66}$$

and use these to calculate the initial spread and the transformation matrices $\exp[\Delta W_{\mathbf{q}}]$ for the first iteration (the transformation matrices are unitary since the $\Delta W_{\mathbf{q}}$ are anti-Hermitian). The overlap matrices and cumulative transformation matrices are

updated respectively as

$$M_{\mathbf{q},\mathbf{b}} \rightarrow (\exp[\Delta W_{\mathbf{q}}])^{\dagger} M_{\mathbf{q},\mathbf{b}} \exp[\Delta W_{\mathbf{q}+\mathbf{b}}], \tag{2.67}$$

$$U_{\mathbf{q}} \rightarrow U_{\mathbf{q}} \exp[\Delta W_{\mathbf{q}}]. \tag{2.68}$$

The updated overlap matrices are used to calculate a new set of spreads, gradients, etc. and the iterations are continued until the spread has converged. Thus we obtain a final set of cumulative transformation matrices $U_{\mathbf{q}}$, which may be used to calculate the maximally localised generalised Wannier functions from the reference set of Bloch states as in Eq. 2.43. The algorithm only requires matrix operations on a set of $K \times K$ matrices upon each iteration and is therefore relatively inexpensive to compute compared to progressively updating the Bloch states themselves.

The description of the steepest-descent algorithm has thus far neglected a crucial issue, which is the existence of local minima in the spread functional. In the original paper by Marzari and Vanderbilt [71] the authors state that the 'minimisation procedure can occasionally get trapped in local minimum' when using an arbitrary set of reference Bloch states or those output from a typical band-structure code. To account for this the authors describe a procedure for initialising the reference Bloch states by projecting onto a set of trial orbitals corresponding to some initial guess at the generalised Wannier functions. Using this method the authors claim to 'have never observed the system to become trapped in a false local minimum'. Unfortunately, in our experience with using this procedure to calculate Wannier functions for optical lattice potentials the system almost *always* becomes trapped in a local minimum. A further disadvantage is that a variety of trial orbitals are needed for different geometries. In Secs. 2.4.5 and 2.4.6 we propose an alternative approach to resolve this problem, but first we give an overview of a particular scenario–an isolated band in a system with inversion symmetry–for which the optimal gauge

transformation can be determined from the properties of the band.

2.4.4 Isolated bands in systems with inversion symmetry

For an isolated band the term Ω_{OD} is not present and one only needs to find a transformation of the form given in Eq. 2.41 that minimises Ω_{D}. From Eqs. 2.54 and 2.56 we can see that Ω_{D} will be zero if we can set $\rho_{\mathbf{q},\mathbf{b}} = 0 \ \forall \ \mathbf{q}, \mathbf{b}$ (we have omitted the band label when considering an isolated band). This will be true if, for every wave-vector $\mathbf{q}$, the phase of the overlaps between neighbouring Bloch periodic functions in each direction $\mathbf{b}$ is equal to $-\mathbf{b} \cdot \overline{\mathbf{r}}$. Interestingly, the expression for the Wannier centre $\overline{\mathbf{r}}$ in reciprocal space, given in Eq. 2.50, shows that it in turn is dependent on the sum of the phases of the overlaps in each direction $\mathbf{b}$. The quantity $\sum_{\mathbf{b}} \omega_{\mathbf{b}} \mathbf{b} \mathrm{Im}[\ln M_{\mathbf{q},\mathbf{b}}]$ is a finite-difference representation of the vector field $\vec{A}(\mathbf{q}) = i\langle u_{\mathbf{q}} | \nabla_{\mathbf{q}} | u_{\mathbf{q}} \rangle$, which is known as the Berry connection [74]. At the minimum of the spread functional $\nabla \cdot \vec{A}$ vanishes, while $\vec{B} = \nabla \times \vec{A}$, where $\vec{B}$ is known as the Berry curvature [74], is gauge-invariant and determines the minimum value of Ω_{D}.

In systems with inversion symmetry the Berry curvature is zero and therefore $\Omega_{\mathrm{D}} = 0$ at the minimum. The Berry connection is uniform at the minimum and its value is set by the Berry phase [75]

$$\vartheta_{\mathrm{C}_{\mathbf{b}}} = \sum_{\mathbf{q} \in \mathrm{C}_{\mathbf{b}}} \mathrm{Im}[\ln M_{\mathbf{q},\mathbf{b}}]. \tag{2.69}$$

The Berry phase is the geometric phase acquired in traversing a path $\mathrm{C}_{\mathbf{b}}$ across the full width of the Brillouin zone in the direction $\mathbf{b}$.[13] When the lattice potential possesses inversion symmetry the Berry phase of each isolated band is not only uniform across the Brillouin zone but also quantised [76]. The relationship between

[13] Any path across the full width of the Brillouin zone is automatically closed due to the torus topology of the zone.

the Berry connection and the Wannier centre implies that the latter is located at one of the symmetry centres of the lattice, known as the Wyckoff positions [65]. In Sec. 2.3.2 we have shown that if the system possesses inversion symmetry then the Fourier coefficients of the Bloch periodic functions are real up to a global phase. If the Berry phase is zero the Wannier centre resides at the origin; the Fourier coefficients can be chosen to be real, which results in $\mathrm{Im}[\ln M_{\mathbf{q},\mathbf{b}}] = 0 \ \forall \ \mathbf{q}, \mathbf{b}$, and thus $\Omega_{\mathrm{D}} = 0$. If the Berry phase is non-zero the Wannier centre will reside at a different Wyckoff position. The maximally localised Wannier function can be found by initially choosing all the Fourier coefficients to be real, then from one corner of the mesh progressively adjusting the phases of the neighbouring Bloch periodic functions such that $\mathrm{Im}[\ln M_{\mathbf{q},\mathbf{b}}] = \vartheta/N \ \forall \ \mathbf{q}, \mathbf{b}$. Once more Ω_D will vanish and the spread will be equal to the invariant part Ω_{I}. Further, the Wannier function will be symmetric under inversion and can be chosen to be real.

The issue with non-centro-symmetric systems is that the Berry curvature is non-zero and therefore the Berry phase along parallel paths through the Brillouin zone varies (the Berry connection is non-uniform). There is no straightforward method akin to that described above for determining the gauge transformation to the maximally localised Wannier state, with the exception of 1D to be described shortly. Fortunately, optical lattice potentials usually possess inversion symmetry since this is inherent from their creation using lasers, and super-lattice techniques are required to break the inversion symmetry. In this thesis we only consider optical lattices with inversion symmetry in 2D or 3D. If one is interested in systems lacking inversion symmetry one must resort to the steepest-descent minimisation algorithm of Sec. 2.4.3, with the gradient functional reducing to

$$G_{\mathbf{q}} = 4i \sum_{\mathbf{b}} \omega_{\mathbf{b}} \mathrm{Im}[\ln M_{\mathbf{q},\mathbf{b}}] \tag{2.70}$$

for an isolated band. However, one can use the 'progressive phase update' method described for centro-symmetric systems to initialise the Bloch periodic functions. The Fourier coefficients cannot be made real, but starting from one corner of the mesh one can adjust the phase of the neighbouring mesh point in one of the reciprocal lattice directions to set $\mathrm{Im}[\ln M_{\mathbf{q},\mathbf{b}}] = \vartheta_{\mathrm{C}_\mathbf{b}}/N$ for the pair. One then continues in the same direction, setting $\mathrm{Im}[\ln M_{\mathbf{q},\mathbf{b}}] = \vartheta_{\mathrm{C}_\mathbf{b}}/N$ for each pair until the penultimate mesh point at the end of the zone is reached. For a 1D system one then has $\rho_{\mathbf{q},\mathbf{b}} = 0 \; \forall \; \mathbf{q}, \mathbf{b}$, which as discussed is the condition for setting $\Omega_\mathrm{D} = 0$. In higher dimensions, the process is repeated for each path in the other reciprocal lattice directions as shown in Fig. 2.6. The Berry phase of each path will vary and thus $\rho_{\mathbf{q},\mathbf{b}} \neq 0 \; \forall \; \mathbf{q}, \mathbf{b}$, but the average value of $\rho_{\mathbf{q},\mathbf{b}}$, and therefore Ω_D, will in general be reduced to an extent that the steepest-descent minimisation can then be used to find the global minimum.

2.4.5 Composite groups: 'disentangling' the bands

Having discussed the minimisation of the spread for isolated bands we can now consider the more complex problem of composite groups. As previously stated, the requirement is to find an optimal gauge transformation, not just a phase transformation, to minimise the total spread of the group. The steepest-descent algorithm discussed in Sec. 2.4.3 provides a means of achieving this, but requires the initial gauge to be such that the term $\tilde{\Omega}$ is small enough (typically less than one) for the system to find the global minimum. Our approach is to take advantage of a second algorithm devised by Souza *et al.* in Ref. [72], which was initially proposed as a method for obtaining Wannier-like functions for a composite group of energy bands that is not isolated, but instead attached to other (usually higher) bands.

Consider the reciprocal space definition of the band-off-diagonal term Ω_OD given in Eq. 2.55. This term will be small whenever the inter-band overlaps between

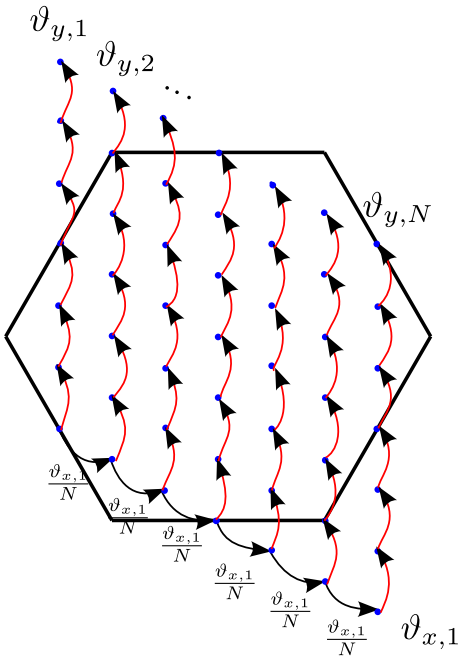


Figure 2.6. Progressive phase update method: starting from the bottom left corner of the Brillouin zone mesh (blue dots) the phase of the neighbour to the right (connected by the black arrow) is adjusted such that $\mathrm{Im}[\ln M_{\mathbf{q},\mathbf{b}}] = \vartheta_{x,1}/N$ for the pair, where $\vartheta_{x,1}$ is the Berry phase in this direction. The same adjustment is made for the next neighbour and so on until the end of the mesh is reached (lower-right corner). One then has $\mathrm{Im}[\ln M_{\mathbf{q},\mathbf{b}}] = \vartheta_{x,1}/N$ for all mesh points along this path. The process is repeated for each path in the next reciprocal lattice direction as shown by the red arrows. For an isolated band in a system with inversion symmetry the Berry phase along each path in this direction will be the same and the method will result in $\Omega_{\mathrm{D}} = 0$ for the band.

nearest-neighbour Bloch periodic functions are small, or alternatively, whenever the intra-band overlaps are large. Therefore, we require a means of choosing the reference Bloch periodic functions such that their 'character' is consistent across the Brillouin zone within each band, but differs between bands. It turns out that, heuristically, the gauge invariant part of the spread measures the uniformity of the character of a set of bands [71, 72]. This can be seen by rewriting Eq. 2.53 as

$$\Omega_{\mathrm{I}} = \frac{1}{N^D} \sum_{\mathbf{q},\mathbf{b}} \omega_{\mathbf{b}} \mathrm{tr}[\hat{P}_{\mathbf{q}} \hat{Q}_{\mathbf{q}+\mathbf{b}}], \tag{2.71}$$

where $\hat{P}_{\mathbf{q}} = \sum_{n=1}^{K} |u_{\mathbf{q}}^{[n]}\rangle\langle u_{\mathbf{q}}^{[n]}|$ is the projector onto the K-dimensional subspace $S(\mathbf{q})$ spanned by the Bloch periodic functions $u_{\mathbf{q}}^{[n]}(\mathbf{r})$, $\hat{Q}_{\mathbf{q}} = \mathbf{1} - \hat{P}_{\mathbf{q}}$ is the projector onto the orthogonal subspace, and again K is the number of bands in the composite group. The term $\mathrm{tr}[\hat{P}_{\mathbf{q}}\hat{Q}_{\mathbf{q}+\mathbf{b}}] = ||\hat{P}_{\mathbf{q}} - \hat{P}_{\mathbf{q}+\mathbf{b}}||^2/2$ defines a 'distance' between the spaces $S(\mathbf{q})$ and $S(\mathbf{q}+\mathbf{b})$, which vanishes when they are identical. Since Ω_{I} is invariant under transformations of the $u_{\mathbf{q}}^{[n]}(\mathbf{r})$ within each subspace $S(\mathbf{q})$,[14] it can be regarded as a functional of the set of spaces $S(\mathbf{q})$. By minimising Ω_{I} for a composite group under transformations within the set of larger spaces $F(\mathbf{q}) \subset S(\mathbf{q})$ one can obtain the set of spaces $S(\mathbf{q})$ with the greatest uniformity across the Brillouin zone. In Ref. [72] the invariant part of the spread for a group of bands is iteratively minimised to 'disentangle' the group from other bands that are connected to it. Here we apply the same technique, but minimise

$$\Omega_{\mathrm{I}}^{[n]} = \frac{1}{N^D} \sum_{\mathbf{q},\mathbf{b}} \omega_{\mathbf{b}} \left(1 - |M_{\mathbf{q},\mathbf{b}}^{[nn]}|^2\right) \tag{2.72}$$

for each band $n \in 1, \ldots, K$ in turn under transformations within the set of spaces $S(\mathbf{q}) \subset |u_{\mathbf{q}}^{[n]}\rangle$ in order to reduce Ω_{OD} for an isolated, composite group.

[14] The form for Ω_{I} given in Eq. 2.71 clearly shows that this is the case.

Our procedure for initialising the Bloch periodic functions is as follows. We once again begin with the eigenvectors $\vec{c}_{\mathbf{q}}^{\,[n]}$ from the band-structure calculation, which define a reference set of Bloch periodic functions $u_{\mathbf{q}}^{[n](0)}(\mathbf{r})$, and compute the initial overlap matrices $M_{\mathbf{q},\mathbf{b}}^{(0)}$ as in Eq. 2.66. We also have a set of transformation matrices $V_{\mathbf{q}}^{(0)}$, where at each $\mathbf{q}$ we take a $K \times K$ identity matrix and randomly permute its rows. Upon each iteration i we update the overlap matrices according to

$$M_{\mathbf{q},\mathbf{b}}^{(i)} = V_{\mathbf{q}}^{(i-1)\dagger} M_{\mathbf{q},\mathbf{b}}^{(i-1)} V_{\mathbf{q}+\mathbf{b}}^{(i-1)}, \tag{2.73}$$

thus for the first iteration the band labels of the Bloch periodic functions are randomised. This removes any initial uniformity of character across the Brillouin zone, which in almost all cases prevents the minimisation procedure from finding a local minimum in $\Omega_{\mathrm{I}}^{[n]}$. Even if this is not the case the algorithm can always be re-run with a new initial random configuration. Next, for each iteration $i \geq 1$ we calculate the Hermitian matrices

$$Z_{\mathbf{q}}^{[mp](i)} = \sum_{\mathbf{b}} \omega_{\mathbf{b}} M_{\mathbf{q},\mathbf{b}}^{[mn](i)} M_{\mathbf{q},\mathbf{b}}^{[pn](i)*}, \tag{2.74}$$

where m, p run over $n, \ldots, K$, and n, the current band for which $\Omega_{\mathrm{I}}^{[n]}$ is being minimised, is initially set to one. Equation 2.74 is derived in Ref. [72] for the multi-band case, while the single-band derivation is included in appendix 2.A. By choosing the transformation matrices as $V_{\mathbf{q}}^{(i)} = \mathbf{1}_{[n-1]} \otimes X_{\mathbf{q}}^{(i)}$, where $\mathbf{1}_{[k]}$ is a $k \times k$ identity matrix with $k = K - n + 1$ and $X_{\mathbf{q}}^{(i)}$ diagonalises $Z_{\mathbf{q}}^{(i)}$, i.e. $Z_{\mathbf{q}}^{(i)} = X_{\mathbf{q}}^{(i)} \Lambda_{\mathbf{q}}^{(i)} X_{\mathbf{q}}^{(i)\dagger}$, with $\Lambda_{\mathbf{q}}^{(i)}$ the diagonal form of $Z_{\mathbf{q}}^{(i)}$, one finds that

$$\Omega_{\mathrm{I}}^{[n](i+1)} = \sum_{\mathbf{b}} \omega_{\mathbf{b}} - \frac{1}{N^D} \sum_{\mathbf{q}} \Lambda_{\mathbf{q}}^{[11](i)}. \tag{2.75}$$

If the $X_{\mathbf{q}}^{(i)}$ are chosen at each $\mathbf{q}$ such that $\Lambda_{\mathbf{q}}^{[11](i)}$ is the largest eigenvalue of $Z_{\mathbf{q}}^{(i)}$, the overlaps $\langle u_{\mathbf{q}}^{[n](i+1)}|u_{\mathbf{q}+\mathbf{b}}^{[n](i)}\rangle$ between $|u_{\mathbf{q}}^{[n](i+1)}\rangle$ and its neighbours from the current iteration will be maximised, and thus $\Omega_{\mathrm{I}}^{[n](i+1)}$ will be minimised. Eventually, self-consistency will be achieved and $\Omega_{\mathrm{I}}^{[n]}$ will converge, in which case n is increased by one and the iterations are continued until $\Omega_{\mathrm{I}}^{[n]}$ has been minimised for each band in the group. On occasion the iterative procedure can become unstable, which may be prevented by replacing Eq. 2.74 with

$$Z_{\mathbf{q}}^{[mp](i)} = \sum_{\mathbf{b}} \omega_{\mathbf{b}} \Big\{ \alpha_{\mathrm{d}} M_{\mathbf{q},\mathbf{b}}^{[mn](i)} M_{\mathbf{q},\mathbf{b}}^{[pn](i)*} + (1-\alpha_{\mathrm{d}}) \left[V_{\mathbf{q}}^{(i-1)\dagger} M_{\mathbf{q},\mathbf{b}}^{(i-1)} \right]^{[mn]} \left[V_{\mathbf{q}}^{(i-1)\dagger} M_{\mathbf{q},\mathbf{b}}^{(i-1)} \right]^{[pn]*} \Big\}, \qquad (2.76)$$

where $0 < \alpha_{\mathrm{d}} \leq 1$ and a typical value is $\alpha_{\mathrm{d}} = 0.5$.[15] By using Eq. 2.76 we maximise the overlaps between $|u_{\mathbf{q}}^{[n](i+1)}\rangle$ and its neighbours, using a superposition from the current and previous iterations for the latter. Equation 2.76 is equivalent to Eq. 2.74 when $\Omega_{\mathrm{I}}^{[n]}$ has converged.

By cumulating the update matrices after each iteration we end up with a set of transformation matrices $U_{\mathbf{q}} = \prod_i V_{\mathbf{q}}^{(i)}$ for the entire disentangling procedure. With $\Omega_{\mathrm{I}}^{[n]}$ minimised for each band, the band-off-diagonal term Ω_{OD} will typically be less than one, but not necessarily at its minimum.[16] The disentangling procedure does not in general reduce the band-diagonal term Ω_{D} and thus a further step is necessary, which will be discussed in the next section. Once this further step has been implemented the final set of transformation and overlap matrices can be used as input for the steepest-descent algorithm instead of those given in Eqs. 2.65 and

[15] Equation 2.76 is not quite the same as Eq. 20 of Ref. [72], but is easier to compute with the same result.

[16] In general, the disentangling procedure minimises $\Omega_{\mathrm{I}}^{[n]}$ for each band n at the expense of the higher bands. When minimising Ω, the steepest-descent algorithm then increases $\Omega_{\mathrm{I}}^{[n]}$ for the lowest bands while decreasing it for the higher bands.

2.66.

The advantage of using the disentangling procedure for initialising the composite group is that one only needs to calculate a set of overlap matrices at the start of the procedure, after which all calculations involve only matrices of maximum size $K \times K$ and therefore are not computationally expensive. The procedure itself is quite robust when starting with a randomised set of Bloch periodic functions, and no other initialisation, e.g. as described in Ref. [72], is necessary.

2.4.6 Composite groups in systems with inversion symmetry

In Sec. 2.4.4 we stated that when the system is invariant under inversion the Berry curvature of an isolated band is zero. The band-diagonal term Ω_{D} can be made to vanish by adjusting the local phases of the Bloch periodic functions across the Brillouin zone according to the Berry phase in each reciprocal lattice direction. For a composite group of bands in multiple dimensions the Berry curvature is in general non-zero since the Bloch periodic functions can be mixed between bands using a gauge transformation.[17] However, in our results we observe that a specific gauge exists resulting in a set of highly localised generalised Wannier functions such that the Berry curvature of each band *is* zero, with $\Omega_{\mathrm{D}} = 0$. The generalised Wannier functions are then centred on the Wyckoff positions. This observation is hinted at in Ref. [77], but only a specific example in multiple dimensions is considered and no general derivation is given.[18] Similar to the isolated band case,

[17] In 1D this is not an issue because even in a composite group each band has a single, defined Berry phase. One can always adjust the phases of the Bloch periodic functions to set $\Omega_{\mathrm{D}} = 0$, and as a result the generalised Wannier functions can always be chosen to be real regardless of the presence of inversion symmetry or whether or not the band is isolated.

[18] In Ref. [77] the eigenvalues of a 'band-centre' operator are shown to be equal to the Wyckoff positions of the O_h^7 symmetry group for the valence band of Ge. The relationship between the eigenvalues of the band-centre operator, the Berry phase, and the Wannier centres [76] implies it would be possible to make the current observation for the valence band of Ge.

the generalised Wannier functions possess inversion symmetry and can be chosen to be real. In some cases the set of generalised Wannier functions will be the maximally localised set, while in others a further real gauge transformation that is uniform across the Brillouin zone is required to find the global minimum in Ω. Examples of both cases will be given in chapter 4. For the latter case, the transformation will break the inversion symmetry of each generalised Wannier function resulting in a finite Ω_{D}, but Ω_{OD} will be reduced such that $\Omega_{\mathrm{D}} + \Omega_{\mathrm{OD}}$ decreases. Since the transformation is real the resulting generalised Wannier functions will remain real even though inversion symmetry is broken. In Ref. [71] it is conjectured that optimally localised generalised Wannier functions are always real; our observations support this conjecture for systems with inversion symmetry.

In order to minimise Ω_{D} following the disentangling procedure we simply apply the progressive phase update method (as described in Sec. 2.4.4) followed by the steepest-descent minimisation of $\Omega_{\mathrm{D}}^{[n]}$ for each band in the composite group. In multiple dimensions we only consider inversion invariant lattice potentials, therefore the minimum value of Ω_{D} should be zero following the above discussion. In many cases the output of the disentangling procedure does have zero Berry curvature for each band and the progressive phase update method reduces Ω_{D} to zero. Even when this isn't the case, both Ω_{D} and Ω_{OD} are reduced significantly such that when the steepest-descent algorithm is applied to the entire composite group the global minimum of the spread functional is found.

The full procedure for calculating the maximally localised (generalised) Wannier functions from the output of the band-structure calculation is shown in Fig. 2.7. In one dimension, an alternative method for initialising a composite group of bands is detailed in Ref. [71]. Coined 'parallel transport', the procedure sweeps through the Brillouin zone, transforming each set of Bloch periodic functions under the constraint that the overlap between neighbours is Hermitian, before applying

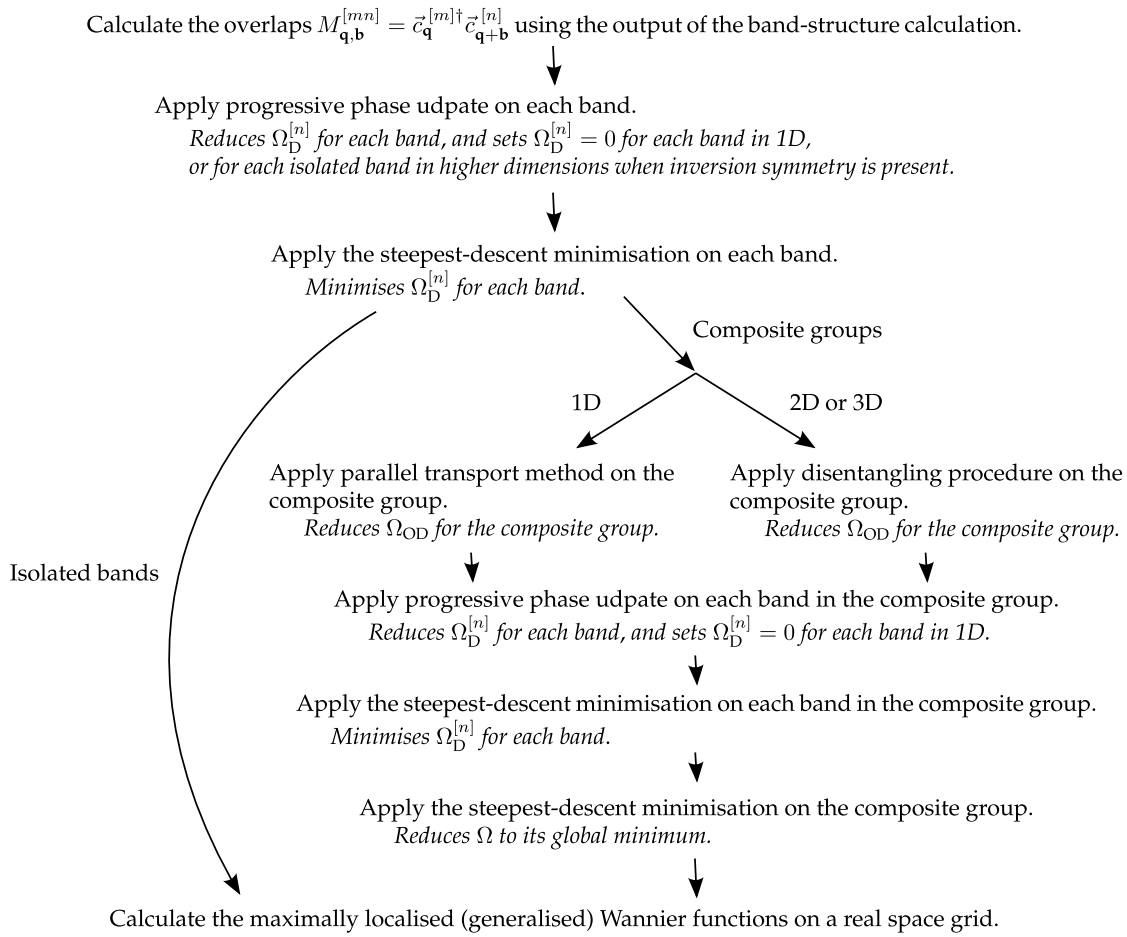


Figure 2.7. Flow diagram for calculating maximally localised (generalised) Wannier functions from the output of a band-structure calculation.

a further transformation that is uniform across the Brillouin zone. The result is a significant reduction in Ω_{OD} towards its minimum.[19] The parallel transport method has the advantage of taking only a single step, while typically resulting in the same gauge transformation as the disentangling procedure. However, the method does not generalise to higher dimensions.

[19] In Sec. 2.4.2 it was shown that Ω_{OD} vanishes at the minimum in 1D, but using a discrete mesh to sample the Brillouin zone restricts the minimum of Ω_{OD} to a finite value of atleast $O(b^2)$.

2.5 The hopping matrix elements

Once the generalised Wannier functions have been calculated we can compute the hopping and interaction matrix elements according to Eqs. 2.21 and 2.22 respectively. In the case of the hopping matrix elements it is useful to firstly substitute Eq. 2.43 into Eq. 2.21 and use $\hat{h}_0|\phi_{\mathbf{q}}^{[n](0)}\rangle = E_{\mathbf{q}}^{[n]}|\phi_{\mathbf{q}}^{[n](0)}\rangle$ to obtain

$$J_j^{[mn]} = \frac{\Upsilon}{(2\pi)^D}\int_{\mathrm{BZ}} d\mathbf{q}\; e^{i\mathbf{q}\cdot\mathbf{R}_j}\left[U_{\mathbf{q}}^{\dagger}D_{\mathbf{q}}U_{\mathbf{q}}\right]_{mn}, \tag{2.77}$$

where $D_{\mathbf{q}}$ is a diagonal matrix containing the energy eigenvalues at wave-vector $\mathbf{q}$. Equation 2.77 shows that the hopping matrix elements depend on the gauge transformation to the maximally localised set of generalised Wannier functions, as might be expected. However, since the $D_{\mathbf{q}}$ are diagonal the matrix elements are invariant with respect to transformations of the form given in Eq. 2.41, and thus are sensitive only to the mixing of bands required to minimise the band-off-diagonal term Ω_{OD}. Coupling between bands is allowed both on- and off-site because of band mixing, although it is disallowed on-site if there is a change in parity of the generalised Wannier functions. For the case of isolated bands, the unitary matrices are diagonal and the hopping matrix elements reduce to

$$J_j^{[mn]} = \frac{\Upsilon}{(2\pi)^D}\delta_{m,n}\int_{\mathrm{BZ}} d\mathbf{q}\; e^{i\mathbf{q}\cdot\mathbf{R}_j}E_{\mathbf{q}}^{[n]}, \tag{2.78}$$

and therefore are independent of the localisation properties of the Wannier functions. Inter-band coupling, both on- and off-site, is now disallowed by the orthogonality of the Bloch states because the bands are no longer mixed.

2.6 The tight-binding model

In a sufficiently deep lattice one would expect the wave-function of a single atom to be confined to a single potential minimum such that its spatial extent is much less than the lattice period. The Wannier function may then be approximated by this wave-function, which can be calculated by considering the potential only about its minimum. The tight-binding approach is a method for obtaining an approximate band-structure based on this assumption of well-localised wave-functions. We begin with the Hamiltonian

$$\hat{H}_{\min} = -\frac{\hat{\mathbf{p}}^2}{2m_{\mathrm{a}}} + V_{\min}(\mathbf{r}) \tag{2.79}$$

for an atom in a single potential minimum $V_{\min}(\mathbf{r})$, and then take into account a contribution $\Delta V(\mathbf{r}) = \sum_{j\neq 0} V_{\min}(\mathbf{r} - \mathbf{R}_j)$ for the potential at all other lattice sites. The tight-binding Hamiltonian is then given by $\hat{H}_{\mathrm{tb}} = \hat{H}_{\min} + \Delta V(\mathbf{r})$. A suitable choice of solution for the Schrödinger equation using this Hamiltonian is given by

$$\psi_{\mathbf{q}}^{[n]}(\mathbf{r}) = \sum_j c_{\mathbf{q},j}^{[n]} \varphi^{[n]}(\mathbf{r} - \mathbf{R}_j), \tag{2.80}$$

i.e. a linear superposition of atomic orbitals $\varphi^{[n]}(\mathbf{r})$ that satisfy $\hat{H}_{\min}\varphi^{[n]}(\mathbf{r}) = \epsilon^{[n]}\varphi^{[n]}(\mathbf{r})$. We require the solution to satisfy Bloch's theorem, which imposes the following condition on the coefficients,

$$c_{\mathbf{q},j}^{[n]} = e^{i\mathbf{q}\cdot\mathbf{R}_j} c_{\mathbf{q},0}^{[n]}. \tag{2.81}$$

Normalising the wave-function then sets $c_{\mathbf{q},0}^{[n]}$ as

$$|c_{\mathbf{q},0}^{[n]}|^2 = \frac{N_{\mathrm{T}}^{-1}}{1 + \sum_{j\neq 0} e^{-i\mathbf{q}\cdot\mathbf{R}_j}\alpha^{[n]}(\mathbf{R}_j)}, \tag{2.82}$$

where

$$\alpha^{[n]}(\mathbf{R}_j) = \int_{\text{lattice}} d\mathbf{r}\varphi^{[n]*}(\mathbf{r})\varphi^{[n]}(\mathbf{r}-\mathbf{R}_j) \tag{2.83}$$

are the atomic overlap integrals and N_{T} is the total number of real space unit cells (we assume a finite lattice with periodic boundary conditions). The atomic overlap integrals are assumed to be negligible resulting in

$$\psi_{\mathbf{q}}^{[n]}(\mathbf{r}) = \frac{1}{\sqrt{N_{\text{T}}}}\sum_j e^{i\mathbf{q}\cdot\mathbf{R}_j}\varphi^{[n]}(\mathbf{r}-\mathbf{R}_j). \tag{2.84}$$

Using these wave-functions we can derive an effective Hamiltonian for each wave-vector $\mathbf{q}$ given by

$$\begin{aligned}\hat{H}_{\mathbf{q}}^{[mn]} &= \int_{\text{lattice}} d\mathbf{r}\psi_{\mathbf{q}}^{[m]*}(\mathbf{r})\hat{H}_{\text{tb}}\psi_{\mathbf{q}}^{[n]}(\mathbf{r}) \\ &= \frac{1}{N_{\text{T}}}\sum_{i,j} e^{i\mathbf{q}\cdot(\mathbf{R}_i-\mathbf{R}_j)}\int_{\text{lattice}} d\mathbf{r}\varphi_{\text{at}}^{[m]*}(\mathbf{r}-\mathbf{R}_j)\hat{H}_{\text{tb}}\varphi_{\text{at}}^{[n]}(\mathbf{r}-\mathbf{R}_i) \\ &= \sum_j J_j^{[mn]} e^{i\mathbf{q}\cdot\mathbf{R}_j},\end{aligned} \tag{2.85}$$

where

$$J_j^{[mn]} = \int_{\text{lattice}} d\mathbf{r}\varphi^{[m]*}(\mathbf{r})\hat{H}_{\text{tb}}\varphi^{[n]}(\mathbf{r}-\mathbf{R}_j) \tag{2.86}$$

are the hopping integrals. If the hopping integrals are known, the Hamiltonian $\hat{H}_{\mathbf{q}}^{[mn]}$ can be diagonalised resulting in an approximate band-structure.

In chapters 3 and 4 we calculate the hopping matrix elements for a variety of optical lattice potentials. In each case we discard matrix elements of negligible magnitude to form the Bose-Hubbard-type Hamiltonian for the many-body system. By replacing the hopping integrals with the remaining matrix elements in Eq. 2.85 we can calculate an interpolated band-structure according to the tight-binding model. The legitimacy of our approximations can then be considered by determining the

accuracy of the interpolated band-structure to the original. Note that this only allows us to determine the accuracy of the hopping terms in the Bose-Hubbard-type Hamiltonian, and not the interaction terms when we also discard the negligible interaction matrix elements. For this one would need to compare the full spectrum of the Bose-Hubbard-type Hamiltonian to that of the original many-body Hamiltonian given in Eq. 2.20. However, the latter can only be calculated for lattices with only a few sites, which as previously stated is the reason for constructing a simplified local model.

2.A Appendix: Iterative minimisation of $\Omega_{\mathbf{I}}^{[n]}$

In this appendix we derive the Hermitian matrices in Eq. 2.74, which are diagonalised during the iterative procedure outlined in Sec. 2.4.5 for minimising $\Omega_{\mathrm{I}}^{[n]}$. We begin with Eq. 10 of Ref. [72], which is a stationarity condition at the ith iteration found by using Lagrange multipliers to enforce orthonormality. For a single band the stationarity condition reads

$$\frac{\delta\Omega_{\mathrm{I}}^{[n](i)}}{\delta u_{\mathbf{q}}^{[n](i)*}} + \lambda_{\mathbf{q}}^{[n](i)} \frac{\delta}{\delta u_{\mathbf{q}}^{[n](i)*}} \left[\langle u_{\mathbf{q}}^{[n](i)} | u_{\mathbf{q}}^{[n](i)} \rangle - 1\right] = 0, \tag{2.87}$$

where $\lambda_{\mathbf{q}}^{[n](i)} \in \mathbb{C}$. By expressing Eq. 2.75 as

$$\Omega_{\mathrm{I}}^{[n](i)} = \frac{1}{N^D} \sum_{\mathbf{q},\mathbf{b}} \omega_{\mathbf{b}} \left(1 - |\langle u_{\mathbf{q}}^{[n](i)} | u_{\mathbf{q}+\mathbf{b}}^{[n](i)} \rangle|^2\right) \tag{2.88}$$

we find that the first term in Eq. 2.87 is given by

$$\frac{\delta\Omega_{\mathrm{I}}^{[n](i)}}{\delta u_{\mathbf{q}}^{[n](i)*}} = \frac{2}{N^D} \left(\sum_{\mathbf{b}} \omega_{\mathbf{b}} |u_{\mathbf{q}+\mathbf{b}}^{[n](i)}\rangle\langle u_{\mathbf{q}+\mathbf{b}}^{[n](i)}|\right) |u_{\mathbf{q}}^{[n](i)}\rangle, \tag{2.89}$$

and thus the stationarity condition becomes

$$\left(\sum_{\mathbf{b}} \omega_{\mathbf{b}} \hat{P}^{[n](i)}_{\mathbf{q}+\mathbf{b}}\right) |u^{[n](i)}_{\mathbf{q}}\rangle = \tilde{\lambda}^{[n](i)}_{\mathbf{q}} |u^{[n](i)}_{\mathbf{q}}\rangle, \tag{2.90}$$

where $\hat{P}^{[n](i)}_{\mathbf{q}+\mathbf{b}} = |u^{[n](i)}_{\mathbf{q}+\mathbf{b}}\rangle\langle u^{[n](i)}_{\mathbf{q}+\mathbf{b}}|$ is the projector onto the band n at wave-vector $\mathbf{q}$, and $\tilde{\lambda}^{[n](i)}_{\mathbf{q}} = (N^D/2)\lambda^{[n](i)}_{\mathbf{q}}$. We wish to maximise the value of $\tilde{\lambda}^{[n]}_{\mathbf{q}}$ by applying a unitary transformation within the space $S(\mathbf{q}) \subset |u^{[n]}_{\mathbf{q}}\rangle$. This can be achieved by diagonalising $\sum_{\mathbf{b}} \omega_{\mathbf{b}} \hat{P}^{[n](i)}_{\mathbf{q}+\mathbf{b}}$ in the space $S(\mathbf{q})$ so that the largest resulting eigenvalue corresponds to band n. The matrix form of $\sum_{\mathbf{b}} \omega_{\mathbf{b}} \hat{P}^{[n](i)}_{\mathbf{q}+\mathbf{b}}$ is given by

$$\begin{aligned} Z^{[mp](i)}_{\mathbf{q}} &= \langle u^{[m](i)}_{\mathbf{q}}| \left(\sum_{\mathbf{b}} \omega_{\mathbf{b}} \hat{P}^{[n](i)}_{\mathbf{q}+\mathbf{b}}\right) |u^{[p](i)}_{\mathbf{q}}\rangle \\ &= \sum_{\mathbf{b}} \omega_{\mathbf{b}} M^{[mn](i)}_{\mathbf{q},\mathbf{b}} M^{[pn](i)*}_{\mathbf{q},\mathbf{b}}, \end{aligned} \tag{2.91}$$

which is the Hermitian matrix in Eq. 2.74. When we make the replacement given in Eq. 2.76 to prevent the iterative procedure from becoming unstable, we simply diagonalise a mixture of the projectors from the current and previous iterations, i.e.

$$Z^{[mp](i)}_{\mathbf{q}} = \langle u^{[m](i)}_{\mathbf{q}}| \left\{ \alpha_{\mathrm{d}} \sum_{\mathbf{b}} \omega_{\mathbf{b}} \hat{P}^{[n](i)}_{\mathbf{q}+\mathbf{b}} + (1-\alpha_{\mathrm{d}}) \sum_{\mathbf{b}} \omega_{\mathbf{b}} \hat{P}^{[n](i-1)}_{\mathbf{q}+\mathbf{b}} \right\} |u^{[p](i)}_{\mathbf{q}}\rangle. \tag{2.92}$$

Chapter 3

Maximally localised generalised Wannier functions for one-dimensional optical lattices[1]

In the next two chapters we apply the methods introduced in chapter 2 to consider optical lattice potentials in one- and two-dimensions. While 1D lattices have been widely studied in the literature because the Wannier functions are readily calculable, generalised Wannier functions have not been thoroughly examined. Our focus in this chapter is, therefore, to test the use of generalised Wannier functions as a basis for the system in 1D, before moving on in chapter 4 to consider a variety of 2D systems.[2] Specifically, in this chapter we investigate the suitability of treating a set of bands as a composite group, even when each band is isolated, in order to further localise the Wannier functions. When the many-body system within a super-lattice potential is reduced to include only local interactions between particles, we observe that mixing the bands can be beneficial in accurately recreating the single particle band-structure. However, for a simple 1D sinusoidal lattice mixing

[1] The results discussed in chapters 3 and 4 are presented in the publication 'Ab initio derivation of Hubbard models for cold atoms in optical lattices,' R. Walters, G. Cotugno, T.H. Johnson, S. R. Clark, and D. Jaksch, *Physical Review A* ***87***(4), 043613 (2013).

[2] We do not consider 3D systems in this thesis, although our methods would work equally well.

the bands does not improve the viability of a local model. For each system in this chapter we ignore the other real spatial dimensions since these can always be separated out in orthogonal geometries. The Brillouin zone mesh density is chosen such that the spreads of the Wannier functions have converged, as discussed in appendix 3.A.

3.1 1D sinusoidal optical lattice

The simplest 1D optical lattice is that formed using two counter-propagating laser beams producing a sinusoidal potential $V_{\mathrm{OL}} = V_0 \sin^2(\pi x/a)$, as discussed in Sec. 2.1.2. Here the lattice period a is equal to one half-wavelength. The single particle band-structure for this potential is plotted in Fig. 3.1 (a)-(c) for three different lattice depths. For $V_0 = 0$ the band-structure is the quadratic free particle spectrum mapped into the first Brillouin zone and therefore is continuous at the zone edges. As the potential is increased band gaps appear between the lower bands, which as a result become isolated, while higher bands of energies $E^{[n]} \gg V_0$ remain continuous. For $V_0 \gg E_R$ the lower bands have a narrow bandwidth and become cosinusoidal in shape, as shown in Fig. 3.1 (d)-(f).

The magnitudes of the hopping matrix elements for the case of isolated bands are plotted in Fig. 3.2 as a function of lattice depth. Hopping between bands is disallowed by the orthogonality of the Bloch states, as discussed in Sec. 2.5. For both the lowest and first excited bands the hopping matrix elements are shown to decrease almost exponentially with increasing lattice depth for $V_0 > 5E_R$. The rate of decrease is greater for elements involving more distant neighbours, such that the nearest-neighbour element $J_1^{[nn]}$ is more than an order of magnitude greater than that of the next-nearest-neighbour $J_2^{[nn]}$ (and further neighbours) at all but shallow lattice depths ($V_0 \lesssim 5E_R$). The hopping matrix elements for the first excited band

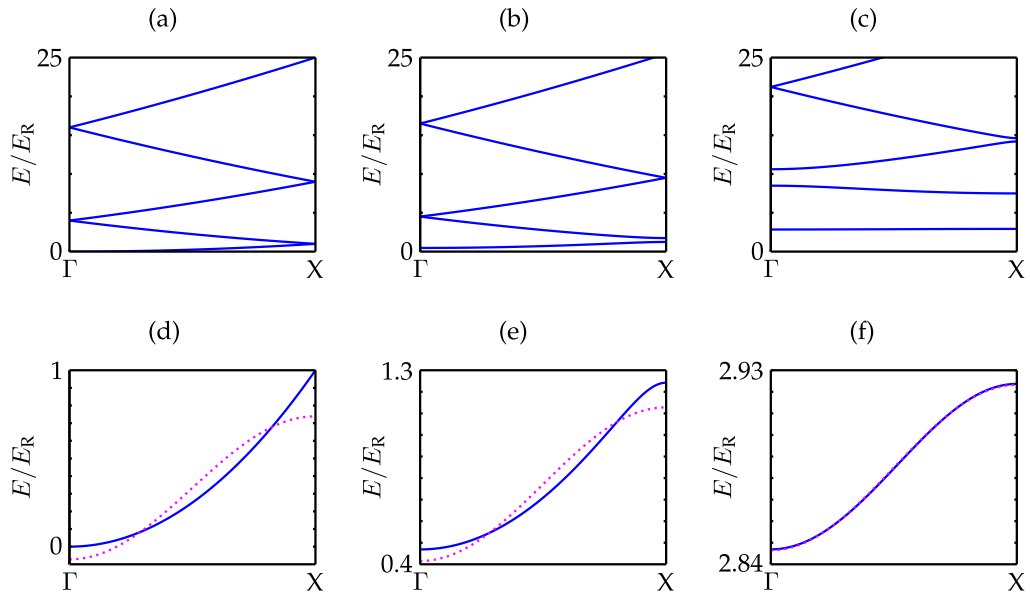


Figure 3.1. Figures (a)-(c) show the five lowest bands for a simple 1D optical lattice potential with lattice depth $V_0 = 0$, E_R, and $10E_R$ respectively. Figures (d)-(f) are, for each lattice depth V_0, zoomed in plots of the lowest band (solid line) and the interpolated band (dotted line) calculated using the local Hamiltonian in Eq. 3.1. Only half the Brillouin zone is shown since the other half is simply the mirror image and provides no further information. The point Γ is the zone-centre ($\mathbf{k} = 0$), while the point X is located at the zone boundary ($\mathbf{k} = \pi/a$).

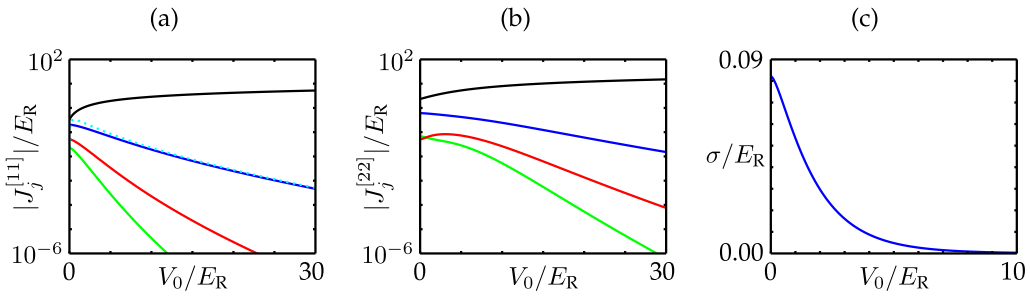


Figure 3.2. The magnitude of the hopping matrix elements for (a) the lowest band $n = 1$, and (b) the first excited band $n = 2$, for a 1D sinusoidal potential as a function of lattice depth V_0. The blue solid lines are the nearest-neighbour hopping matrix elements $|J_1^{[nn]}|$, while the red and green lines are next-nearest-neighbour $|J_2^{[nn]}|$, and third-neighbour $|J_3^{[nn]}|$, hopping elements respectively. The mean energy of the bands $|J_0^{[nn]}|$ is shown by the black solid lines. For the lowest band, the nearest-neighbour hopping calculated using the WBK approximation to the Mathieu equation is shown by the cyan dotted line. (c) The standard deviation of the interpolated lowest band, calculated using the local model discussed in the text, to the exact band.

are of greater magnitude than the corresponding elements for the lowest band; the next-nearest-neighbour element for the first excited band is shown to be of similar magnitude to the nearest-neighbour element for the lowest band.

Ignoring for the time-being many-body interactions, and considering only the lowest band, the Hamiltonian for the system can be approximated using only nearest-neighbour terms,

$$\hat{H} = \sum_j \left[J_0^{[1]} \hat{n}_j^{[1]} + J_1^{[11]} \hat{b}_j^{[1]\dagger} \left(\hat{b}_{j+1}^{[1]} + \hat{b}_{j-1}^{[1]} \right) \right], \tag{3.1}$$

where $\hat{n}_j^{[m]} = \hat{b}_j^{[m]\dagger} \hat{b}_j^{[m]}$. If we also considered the first excited band the next-nearest-neighbour term $\hat{b}_j^{[2]\dagger} \hat{b}_{j-1}^{[2]}$ would need to be included (in addition to the corresponding terms for the first excited band in Eq. 3.1). However, for the typical temperatures used in optical lattice experiments, and considering the large band gap between the bands, the lowest band suffices. The interpolated single-particle band energy for this

tight-binding Hamiltonian, calculated by inserting the values of the hopping matrix elements into Eq. 2.85, is cosinusoidal,

$$E^{[1]}(q) = J_0^{[11]} + 2J_1^{[11]}\cos(qa). \tag{3.2}$$

This interpolated band is plotted in Fig. 3.1 (d)-(f) and is shown to be increasingly accurate to the exact band as the lattice depth is increased. This is confirmed in Fig. 3.2 (c), which shows the standard deviation of the interpolated band to the exact band using a mesh density of $N = 1000$. By setting an acceptable standard deviation of $\sigma = 0.01E_{\mathrm{R}}$ for the accuracy of the interpolated band energy, this figure shows that the local model is restricted to lattice depths above $V_0 = 4E_{\mathrm{R}}$. For shallow lattices the tight-binding Hamiltonian would need to be extended to include longer-range hopping terms in order to accurately recreate the band-structure, and indeed the longer-range hopping matrix elements are not negligible in comparison to the nearest-neighbour element. In Sec. 3.1.1 we discuss whether mixing the bands to form generalised Wannier functions improves the limit on shallow lattices within a local model that includes only nearest-neighbour terms.

Qualitatively, the tight-binding Hamiltonian shows that the decreasing magnitude of the nearest-neighbour hopping matrix elements with lattice depth arises because of the decreasing bandwidths compared to the mean band energies. Similarly, the hopping matrix elements are greater for higher bands due to an increased bandwidth. The Schrödinger equation for the 1D sinusoidal potential in fact corresponds to the Mathieu equation [78], for which analytic solutions can be obtained in the deep lattice limit using the WKB approximation [79]. The solution for the lowest band results in a bandwidth given by

$$\Delta E^{[1]} \approx \frac{16}{\sqrt{\pi}}\left(\frac{V_0}{E_{\mathrm{R}}}\right)^{0.75} e^{-2\sqrt{V_0/E_{\mathrm{R}}}} E_{\mathrm{R}}. \tag{3.3}$$

The nearest-neighbour hopping matrix element calculated using the tight-binding Hamiltonian and this bandwidth is also plotted in Fig. 3.2 (a), and exemplifies the accuracy of the local model in the deep lattice limit.

The maximally localised Wannier functions for the two lowest bands and lattice depths of $V_0 = E_{\rm R}$ and $V_0 = 10E_{\rm R}$ are shown in Fig. 3.3 (a)(b). For these results we have treated each band as isolated. The Wannier functions exhibit an almost exponential localisation about their centres, as highlighted in Fig. 3.3 (c)(d), where they are plotted on a logarithmic scale. As a result of the periodicity of the lattice the tails of the Wannier functions are oscillatory, which is an essential feature for their orthogonality across pairs of sites.[3]

In the deep lattice limit one would expect an atom to be confined to a potential minimum of the sinusoidal lattice potential. By taking a Taylor expansion of a potential minimum about its centre we may obtain an approximate form given by a harmonic oscillator potential

$$V_{\rm ho}(x) = V_0 \frac{\pi^2 x^2}{a^2} = \tfrac{1}{2} m_{\rm a} \omega_{\rm ho}^2 x^2, \tag{3.4}$$

where $\omega_{\rm ho} = 2\sqrt{V_0 E_{\rm R}}$ is the harmonic oscillator frequency. Solutions for the wavefunction for such a potential are given by

$$\phi_{\rm ho}^{[n]}(x) = \frac{1}{\sqrt{2^n n!}} \left(\frac{m_{\rm a}\omega_{\rm ho}}{\pi}\right)^{1/4} e^{-m_{\rm a}\omega_{\rm ho}x^2/2} H_n(\sqrt{m_{\rm a}\omega_{\rm ho}}x), \tag{3.5}$$

where $H_n(x)$ are the Hermite polynomials. The ground and first excited states are

[3]The nodes of the Wannier functions do not necessarily occur at the neighbouring potential minima, and this is not required to ensure orthogonality.

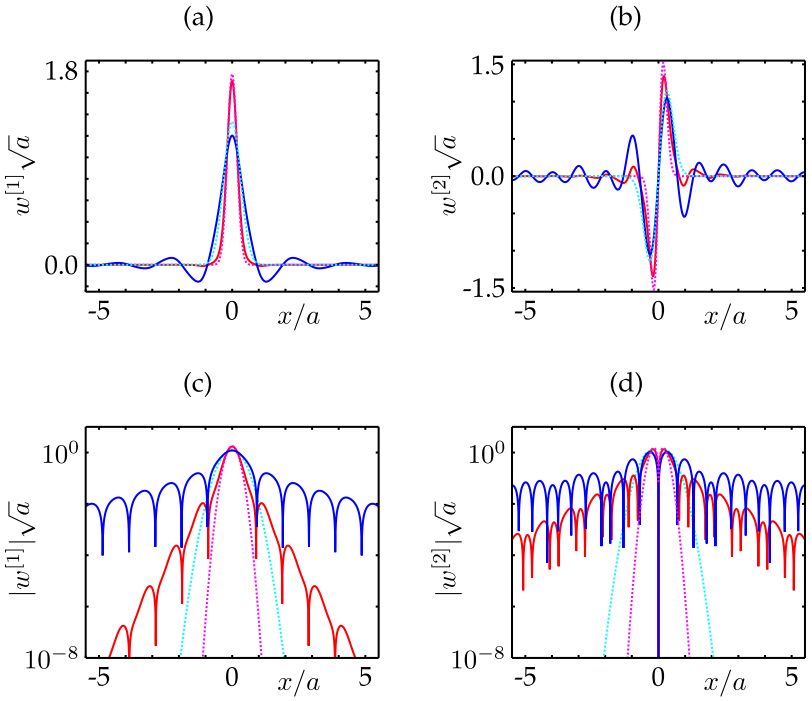


Figure 3.3. The maximally localised Wannier functions $w^{[1]}(x)$ and $w^{[2]}(x)$ for (a) the lowest band and (b) first excited band, for a 1D sinusoidal potential. The blue and red solid lines are for $V_0 = E_R$ and $V_0 = 10E_R$ respectively. The cyan and magenta dotted lines show, for each lattice depth V_0, the solutions for a tight-binding model using a harmonic oscillator potential. Figures (c) and (d) show the magnitude of the Wannier functions and the tight-binding solutions on a logarithmic scale. The minima of $|w^{[n]}(x)|$ indicate the nodes of the Wannier functions.

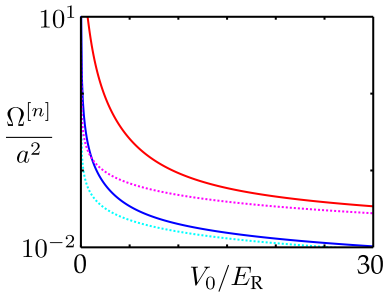


Figure 3.4. The spread $\Omega^{[n]}$ of the Wannier functions for the lowest band $n = 1$ (blue solid line) and first excited band $n = 2$ (red solid line), for a 1D sinusoidal potential. The cyan and magenta dotted lines show, respectively, the spreads of the corresponding harmonic oscillator wave-functions for each band.

given by

$$\begin{aligned}\phi_{\mathrm{ho}}^{[1]}(x) &= \left(\frac{1}{\pi a_{\mathrm{ho}}^2}\right)^{1/4} e^{-x^2/2a_{\mathrm{ho}}^2}, \\ \phi_{\mathrm{ho}}^{[2]}(x) &= \sqrt{2\pi}\left(\frac{1}{\pi a_{\mathrm{ho}}^2}\right)^{3/4} x e^{-x^2/2a_{\mathrm{ho}}^2},\end{aligned} \tag{3.6}$$

respectively. Here the ground state is a Gaussian with variance in the probability distribution $|\phi_{\mathrm{ho}}^{[1]}(x)|^2$ given by

$$\begin{aligned}a_{\mathrm{ho}}^2 &= \frac{1}{m\omega_{\mathrm{ho}}} \\ &= \left(\frac{a}{\pi}\right)^2 \sqrt{\frac{E_R}{V_0}}.\end{aligned} \tag{3.7}$$

The states in Eq. 3.6 are also plotted in Fig. 3.3. Within the central unit cell the harmonic oscillator states are a fair approximation to the Wannier functions, and become increasingly accurate with increasing lattice depth. Outside of the central unit cell the resemblance breaks down: the harmonic oscillator states of course do not have oscillatory tails, and, even in the deep lattice limit, the Gaussian decay of the harmonic oscillator states is much more rapid than the almost exponential decay of the Wannier functions. The spreads of the Wannier functions and harmonic oscillator states are plotted in Fig. 3.4 against lattice depth. The harmonic oscillator states have a smaller spread than their Wannier function counterparts at all lattice depths due to their smaller tails, but the difference becomes less significant in deeper lattices. We again observe that the Wannier functions become more localised with increasing lattice depth. Following this discussion we recognise that the harmonic oscillator states may be used instead of the Wannier functions to approximate on-site properties of the lattice, particularly in the deep lattice limit, but cannot be relied upon to approximate off-site properties involving states located at different

sites.

With the maximally localised Wannier functions calculated we may now consider the many-body interaction terms. In Fig. 3.5 we have plotted the magnitudes of the interaction matrix elements for the two lowest bands against lattice depth. Since we are considering a purely 1D system, we have introduced a '1D contact interaction constant' $\tilde{g}_1$ to replace the real contact interaction constant g used in 3D (*cf.* Sec. 2.2). The increasing localisation of the Wannier functions with increasing lattice depth causes off-site matrix elements, e.g. corresponding to the nearest-neighbour density-density interaction, $U_{0011}^{[mmnn]}$, or interaction induced hopping, $U_{0001}^{[mmnn]}$, to decay almost exponentially. The dominating matrix elements are therefore those corresponding to on-site density-density interactions, $U_{0000}^{[mmnn]}$. The magnitude of these elements increases relatively slowly with lattice depth due to the increased localisation of the Wannier functions, but does not converge to a finite value. The on-site matrix elements can be approximated using the harmonic oscillator states discussed above, and the results, also plotted in Fig. 3.5 (a)-(c), are shown to be in good agreement with the exact values in the deep lattice limit. For the lowest band the analytical expression for the on-site density-density interaction matrix element using the harmonic oscillator ground state is given by

$$U_{0000}^{[1111]} \approx \frac{\tilde{g}_1}{a}\sqrt{\frac{\pi}{2}}\left(\frac{V_0}{E_R}\right)^{0.25}. \tag{3.8}$$

Including only the on-site density-density interaction the tight-binding Hamiltonian in Eq. 3.1 can now be extended as

$$\hat{H} = \sum_j \left[J_0^{[11]}\hat{n}_j^{[1]} + J_1^{[11]}\hat{b}_j^{[1]\dagger}\left(\hat{b}_{j+1}^{[1]} + \hat{b}_{j-1}^{[1]}\right) + \tfrac{1}{2}U_{0000}^{[1111]}\hat{n}_j^{[1]}\left(\hat{n}_j^{[1]} - 1\right)\right], \tag{3.9}$$

which as is well-known is the Hamiltonian for the 1D Bose-Hubbard model. We note

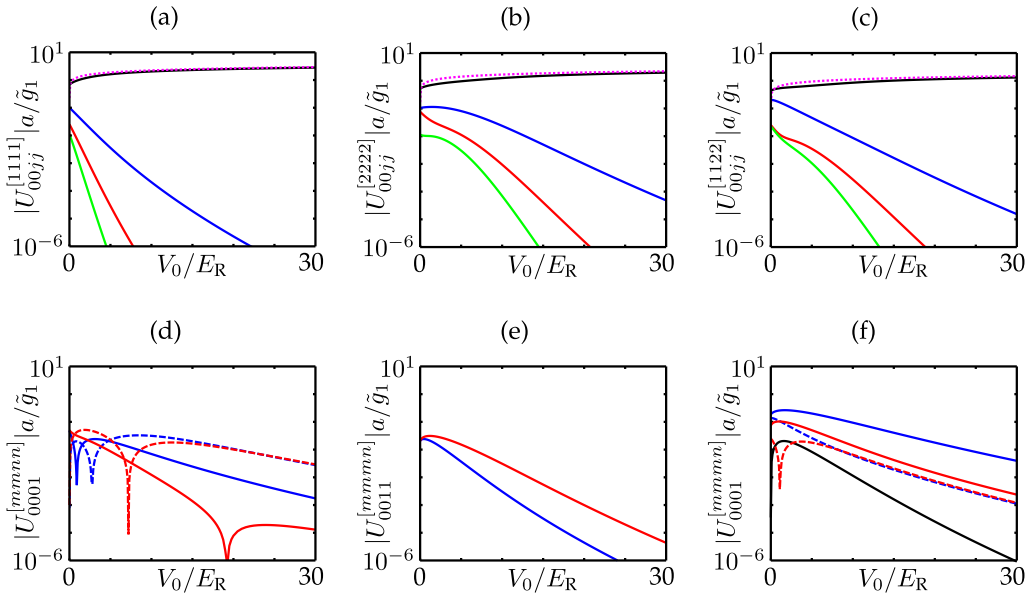


Figure 3.5. (a)-(c) The magnitude of the density-density interaction matrix elements $|U_{00jj}^{[mmnn]}|$ between a particle in site 0 and band m, and another in site j and band n, as a function of lattice depth V_0. Figure (a) is for the lowest band, $m = n = 1$; figure (b) is for the first excited band, $m = n = 2$; and figure (c) is for a particle in each band, $m = 1$ and $n = 2$. The on-site elements, $j = 0$ (black solid lines), dominate over nearest-neighbour, $j = 1$ (blue solid lines), next-nearest-neighbour, $j = 2$ (red solid lines), and third-neighbour, $j = 3$ (green solid lines), elements. The magenta dotted lines show the corresponding on-site density-density interaction elements as predicted using a tight-binding model with a harmonic oscillator potential. (d)-(f) The magnitude of the density-induced hopping matrix elements $|U_{00ij}^{[mmnp]}|$, as a function of lattice depth V_0. Blue and red lines indicate that the particle inducing the hopping is located in band $m = 1$ and $m = 2$ respectively. Figure (d) shows density-induced hopping within bands to the nearest-neighbour site, $|U_{0001}^{[mmnn]}|$. The solid and dashed lines indicate hopping within bands $n = 1$ and $n = 2$ respectively. Figure (e) shows density-induced hopping within sites but between bands, $|U_{00jj}^{[mmnp]}|$. Hopping between bands $n = 1$ and $p = 2$ is not allowed on-site due to symmetry, so only hopping within the nearest-neighbour site is visible. Figure (f) shows density-induced hopping between bands to the nearest-neighbour site, $|U_{0001}^{[mmmn]}|$, where $m = 1, 2$. The solid and dashed lines indicate hopping from and to the band containing the inducing particle respectively. Also shown is the double hopping term, e.g. $|U_{0101}^{[1122]}|$, by the black solid line.

that if we were to include the first excited band, more terms, such as the nearest-neighbour density-density interaction $\hat{n}_j^{[2]}\hat{n}_{j+1}^{[2]}$, may need to be included. The ratio of the hopping matrix element to the on-site density-density interaction matrix element can be determined from Eq. 3.3 and Eq. 3.8 as

$$\frac{U_{0000}^{[1111]}}{J_1^{[11]}} \approx \frac{\pi\tilde{g}_1}{4\sqrt{2}aE_{\mathrm{R}}}\left(\frac{V_0}{E_{\mathrm{R}}}\right)^{-0.5} e^{2\sqrt{V_0/E_{\mathrm{R}}}}. \tag{3.10}$$

As will be discussed in Chapter 5, this ratio determines the critical point of the quantum phase transition from a superfluid to a Mott insulator state. Its exponential dependence on lattice depth means that the system can easily be tuned to adiabatically pass from one phase to the other by altering the laser intensity, and it is for this reason that optical lattice systems play an important role in the study of quantum critical phenomena.

3.1.1 Isolated bands as a composite group

An interesting question posed by introducing the freedom to mix Bloch states to form generalised Wannier functions is can, by doing so, the approximation to a local model be improved? We have shown previously that the local model is accurate for a 1D sinusiodal potential for lattice depths above $V_0 \approx 4E_{\mathrm{R}}$. We now address whether this limit can be improved with band mixing, and consider the implications of using generalised Wannier functions instead of ordinary Wannier functions.

In Fig. 3.6 we have plotted the maximally localised generalised Wannier functions for the cases where the lowest two, and then lowest three, bands only are treated as a composite group. For the former case we observe that treating the bands as a composite group changes the character of the Wannier functions; namely, they no longer possess inversion symmetry and are centred away from the potential minimum. The generalised Wannier functions are images of each other through inversion

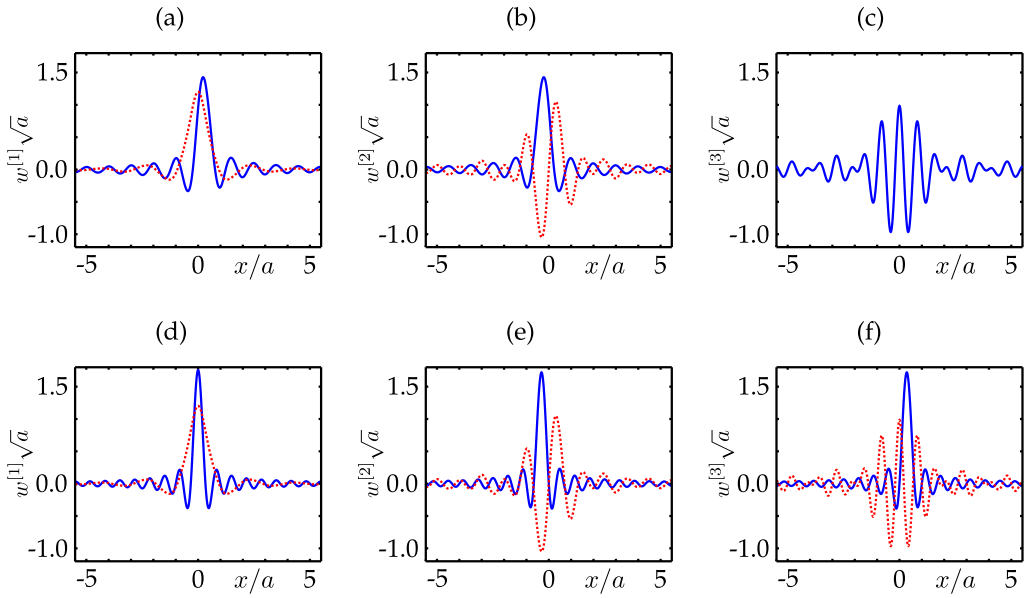


Figure 3.6. (a)-(c) The maximally localised generalised Wannier functions (blue solid lines) for a 1D sinusoidal lattice with the lowest and first excited bands treated as a composite group, and the second excited band treated as isolated. (d)-(f) The maximally localised generalised Wannier functions (blue solid lines) with all three lowest bands treated as a composite group. In each figure the Wannier function for an isolated band is shown by the red dotted line.

symmetry and therefore have equal spread. The result is that while the central peak of the generalised Wannier function for the lowest band has a narrower width than its isolated counterpart, the envelope function for its tail has a larger magnitude. Conversely, the envelope function for the first excited band has a smaller magnitude than its isolated counterpart. The minimisation procedure has reduced the spread for the first excited band (and total spread) at the expense of increasing the spread for the lowest band. We make similar observations for the case of treating the lowest three bands as a composite group. Here, the generalised Wannier function for the lowest band retains inversion symmetry, while the generalised Wannier functions for the first and second excited bands are images of each other with equal spread. Again, the magnitude of the tail for the lowest band is greater than the isolated version, but smaller for the excited bands.

Although not shown in a figure, we have calculated the generalised Wannier functions including higher bands into the composite group. For the case of even bands in the group the generalised Wannier functions labelled by mode indices $2n-1$ and $2n$, where n is a positive integer, are images of each other and have equal spread. For an odd number of bands the generalised Wannier functions labelled by $2n$ and $2n+1$ are images of each other, while the $n=0$ generalised Wannier function is centred at the origin and possesses inversion symmetry. In both cases the centres of each pair of generalised Wannier functions move further away from the potential minimum with increasing n, and as more bands are included in the group the spread of each generalised Wannier function decreases. We expect that in the limit of infinite bands included in the composite group a gauge transformation exists such that the Bloch periodic functions for each mode are uniform across the Brillouin zone, and take the form of a Dirac delta function. It would then follow that the generalised Wannier functions would also be Dirac delta functions, with centres spread evenly throughout the unit cell ensuring orthogonality is retained.

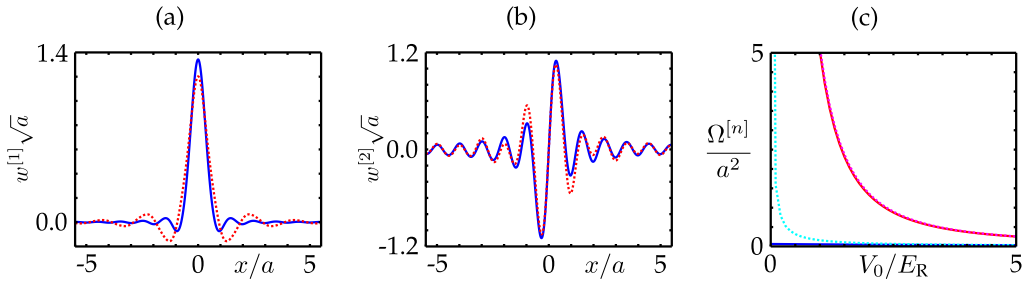


Figure 3.7. (a)-(b) The blue solid lines show the generalised Wannier functions for a sinusoidal optical lattice potential with $V_0 = E_R$, calculated by treating the lowest two bands as a composite group. Figure (a) is for the lower mode $n = 1$, while figure (b) is for the upper mode $n = 2$. The red solid lines are the original Wannier functions without band mixing. (c) The spreads of the generalised Wannier functions as a function of lattice depth V_0. The blue and red solid lines are for modes $n = 1$ and $n = 2$ respectively. The cyan and magenta dotted lines are the corresponding spreads of the original Wannier functions.

We now consider a local model including the two lowest bands only, which are treated as a composite group. The maximally localised generalised Wannier functions have a different character to the ordinary Wannier functions, therefore to consider the usefulness of mixing the bands we choose symmetric and anti-symmetric combinations of the former by applying a further transformation

$$U_{\mathrm{H}} = \frac{1}{\sqrt{2}} \begin{pmatrix} 1 & 1 \\ 1 & -1 \end{pmatrix} \tag{3.11}$$

at each mesh point $\mathbf{q}$. Since the unitary transformation U_{H} is uniform across the Brillouin zone the hopping matrices are themselves transformed using U_{H}, and it can easily be shown that there is no effect on the interpolated band-structure. The resulting generalised Wannier functions, shown in Fig. 3.7 (a)(b) for a lattice depth $V_0 = E_{\mathrm{R}}$, now possess inversion symmetry and are more localised than the original Wannier functions. The spreads of these generalised Wannier functions, now no longer with $\Omega_{\mathrm{OD}} = 0$ due to the additional transformation, are shown in Fig. 3.7

(c). In the limit $V_0 \to 0$ the spread for the lowest band is significantly less than that of the original Wannier function, however, for the first excited band the difference in spread is almost indistinguishable. As the lattice depth increases from zero the spreads for both bands converge to that of the original Wannier functions. This is likely due to the character of the Bloch states in the two bands becoming significantly different as the band gap increases, which implies that no mixing is possible that can reduce the total spread of the composite group.

The magnitudes of the hopping matrix elements for the symmetrised generalised Wannier functions are plotted in Fig. 3.8 (a)-(c). Hopping to neighbouring sites is reduced for shallow lattice depths within the lowest band compared to the original matrix elements, but greater for nearest and next-nearest neighbours within the first excited band. The matrix elements converge to those of the original Wannier functions in the deep lattice limit. The major impact of mixing the bands is that there is now inter-band hopping with a magnitude that is between that of hopping within the upper and lower bands. On-site hopping between bands is disallowed due to the change in parity of the generalised Wannier functions.

In Fig. 3.8 (d) we have plotted the standard deviation between the interpolated band energies of a local model using the generalised Wannier functions to the exact band energies. We remind the reader that the interpolated band-structure is the same for both the maximally localised generalised Wannier functions and their symmetrised combinations. Mixing of the bands to form generalised Wannier functions improves the accuracy of the interpolated lowest band at shallow lattice depths, but this is at the expense of the accuracy of the upper band. The standard deviation for both bands combined shows that the net result is an overall decrease in the accuracy of the local model, and therefore generalised Wannier functions should not be used for a 1D sinusoidal potential.

For completeness, we have plotted the magnitudes of the interaction matrix el-

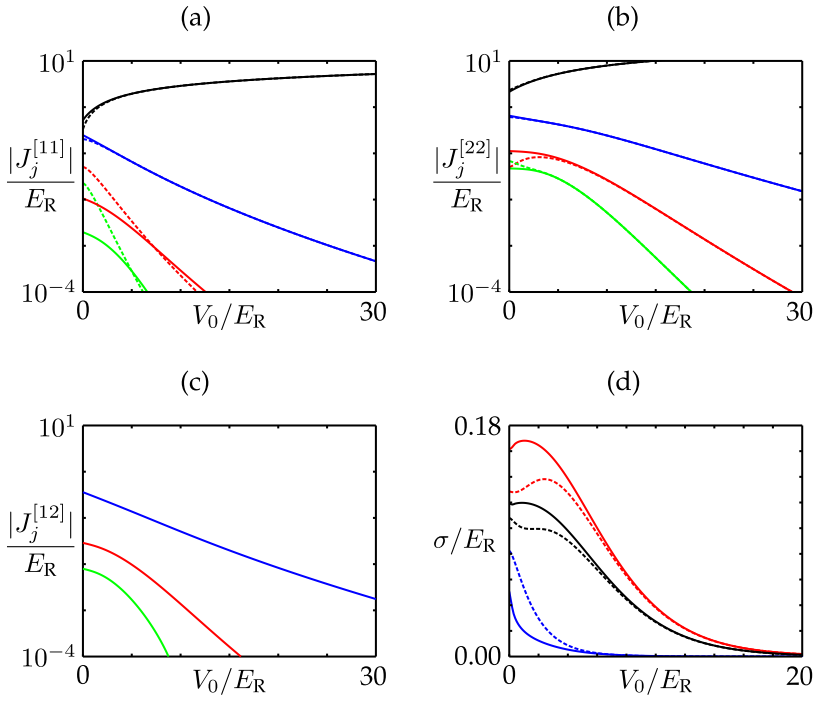


Figure 3.8. (a)-(c) The solid lines show the magnitude of the hopping matrix elements $|J_j^{[mn]}|$ for hopping (a) within the lowest mode $m = n = 1$, (b) within the upper mode $m = n = 1$, and (c) between modes $m \neq n$, for a 1D sinusoidal potential using maximally localised generalised Wannier functions. The dotted lines show the same terms using the original Wannier functions. The black lines are for on-site matrix elements $|J_0^{[mn]}|$, while the blue, red, and green lines are for nearest-neighbour $|J_1^{[mn]}|$, next-nearest-neighbour $|J_2^{[mn]}|$, and third-neighbour $|J_3^{[mn]}|$, matrix elements respectively. Hopping between modes is allowed in the case of generalised Wannier functions because of band mixing. (d) The standard deviation between the interpolated bands, calculated using the local model discussed in the text, to the exacts bands. The blue and red lines are for the lowest and first excited bands respectively, while the black lines are for both bands combined. The solid lines are for a local model with generalised Wannier functions, whereas the dotted lines are for a local model with ordinary Wannier functions.

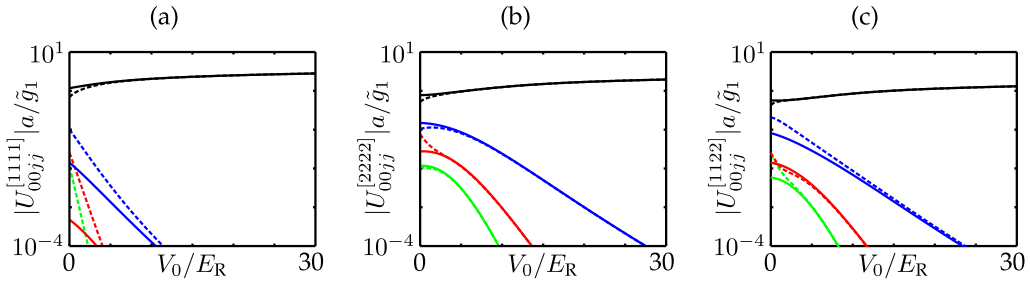


Figure 3.9. The magnitude of the density-density interaction matrix elements $|U_{00jj}^{[mmnn]}|$ between a particle in site 0 and band m, and another in site j and band n, as a function of lattice depth V_0, using generalised Wannier functions (solid lines). Figure (a) is for the lowest mode $m = n = 1$, figure (b) is for the upper mode $m = n = 2$, and figure (c) is for a particle in each mode, $m = 1$ and $n = 2$. The black lines are for on-site terms $j = 0$, the blue lines for nearest-neighbour terms $j = 1$, the red lines for next-nearest-neighbour terms $j = 2$, and the green lines for third-neighbour terms $j = 3$. The dotted lines are the corresponding terms using the original Wannier functions.

ements using the symmetrised generalised Wannier functions in Fig. 3.9. There is a small increase in the magnitude of the on-site density-density matrix elements at shallow lattice depths due to the greater localisation of the generalised Wannier functions compared to the original Wannier functions. As expected, this also implies a decrease in the magnitude of off-site terms due to the reduced overlap of neighbouring generalised Wannier functions.

3.2 1D super-lattice, red-detuned

Super-lattice potentials can be produced in one dimension by using two or more independent pairs of laser beams. The lattice parameter for each pair of beams can be controlled by directing the pair at an angle to each other, as shown in Fig. 3.10 (a). In this section we consider two pairs of red-detuned beams, which individually produce potentials with lattice parameters $\lambda/2$ and λ respectively. The combined

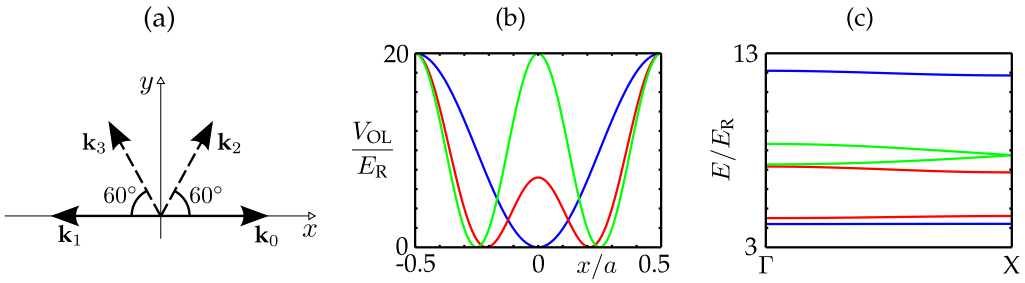


Figure 3.10. (a) The laser configuration to produce the super-lattice potential shown in figure (b). One pair of beams is counter-propagating along the x-axis generating a potential with lattice parameter $\lambda/2$. A second, independent pair of beams, aligned at a 60° angle to the x-axis, imposes an additional potential with lattice parameter λ. (b) The 1D super-lattice potential for red-detuning as a function of position for $s = 0$ (blue solid line), $s = 0.5$ (red dotted line) and $s = 1$ (green dashed line). (c) The band-structure for the corresponding potentials in figure (b).

super-lattice potential is given by

$$V_{\mathrm{OL}}(x, s) = V_0 \left[(1 - s)\sin^2(\pi x/a) + s\sin^2(2\pi x/a)\right], \tag{3.12}$$

where s is a parameter that can be varied between 0 and 1 by altering the relative intensity of each pair of beams. The total intensity is also altered accordingly to ensure the lattice depth is held fixed at $V_0 = 20E_{\mathrm{R}}$. For $s = 0$ the potential is that of a sinusoidal lattice with parameter a. By increasing s we introduce a double-well structure such that when $s = 1$ the potential corresponds to a lattice with parameter $a/2$ (see Fig. 3.10 (b)). This system has been experimentally realised in Ref. [80] and Ref. [33], and was proposed in Ref. [34] as a method for initialising a quantum register on a time-scale that is an order of magnitude smaller than the conventional quantum-freezing of a superfluid to a Mott insulator state [14, 13]. Here we carry out a more thorough analysis of the generalised Wannier functions and resulting matrix elements than was presented in Ref. [34] for the potential in Eq. 3.12, before considering blue-detuning for the same configuration in Sec. 3.3.

The band-structure for the system is shown in Fig. 3.10 (c) for the cases $s = 0$, 0.5 and 1. We observe that the band gap between the lowest two bands decreases with increasing s until for $s = 1$ the X point becomes degenerate. For this last scenario the two lowest bands correspond to the single lowest band of the $a/2$ sinusoidal lattice wrapped within a zone that is half the size of the actual Brillouin zone. Because of the diminishing band gap in the limit $s \to 1$ we must consider both lowest bands to describe the system, and in the following we shall analyse the scenarios where these bands are treated as isolated and as a composite group.

The Wannier functions and generalised Wannier functions for the case $s = 0.999$ are presented in Fig. 3.11 (a)(b). Once again we use symmetrised combinations of the maximally localised generalised Wannier functions to compare to the original Wannier functions since the local model produces the same interpolated band-structure. While the Wannier function for the excited band remains largely unaltered as s is increased from zero, the Wannier function for the lowest band inherits a dual peak structure, with the centre of the peaks located at the potential minima. This arises because the maximally localised generalised Wannier functions, shown in Fig. 3.11 (c), separate into the two potential wells as s increases. The spreads of the generalised Wannier functions, shown in Fig. 3.11 (d), are almost equal to those of the original Wannier functions up to $s = 0.5$, but then become more than a magnitude smaller for both bands in the limit $s \to 1$.

The magnitudes of the hopping matrix elements for both the original Wannier functions and symmetrised generalised Wannier functions are shown in Fig. 3.12. Hopping to the neighbouring sites is shown to increase significantly with s for the original Wannier functions due to the increased spread. While the nearest-neighbour elements for the generalised Wannier functions are similar to those of the original Wannier functions, the elements for further neighbours are significantly less as s increases towards one, and it would appear that these could be safely neglected in

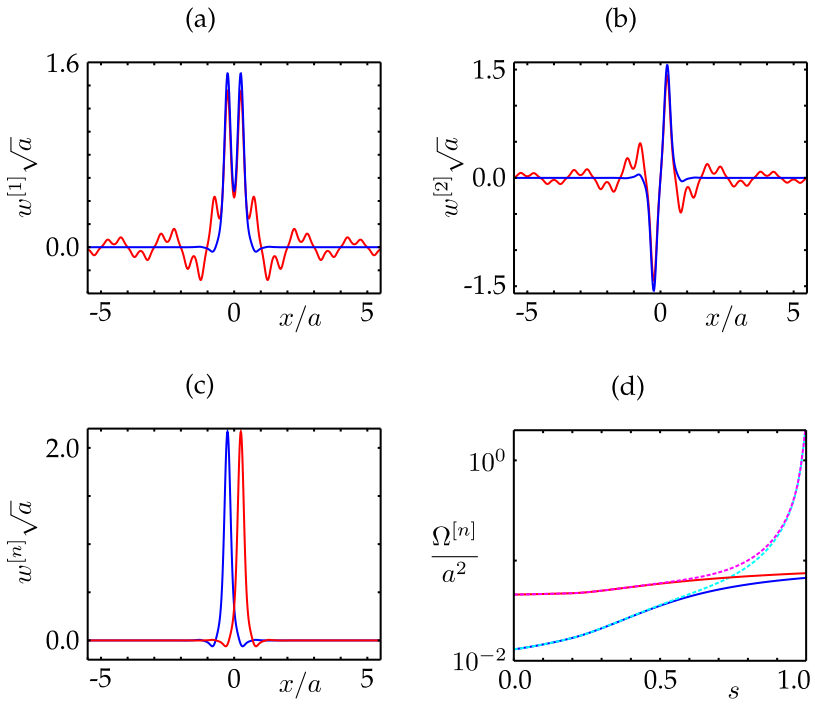


Figure 3.11. (a)-(b) The blue solid lines show the generalised Wannier functions for a red-detuned super-lattice potential with $V_0 = 20E_R$ and $s = 0.999$, calculated by treating the lowest two bands as a composite group. Figure (a) is for the lower mode $n = 1$, while figure (b) is for the upper mode $n = 2$. The red solid lines are the original Wannier functions without band mixing. (c) The maximally localised generalised Wannier functions from which the generalised Wannier functions in figures (a) and (b) are formed using symmetric and anti-symmetric super-positions. (d) The spreads of the generalised Wannier functions as a function of the parameter s. The blue and red solid lines are for modes $n = 1$ and $n = 2$ respectively. The cyan and magenta dotted lines are the corresponding spreads of the original Wannier functions.

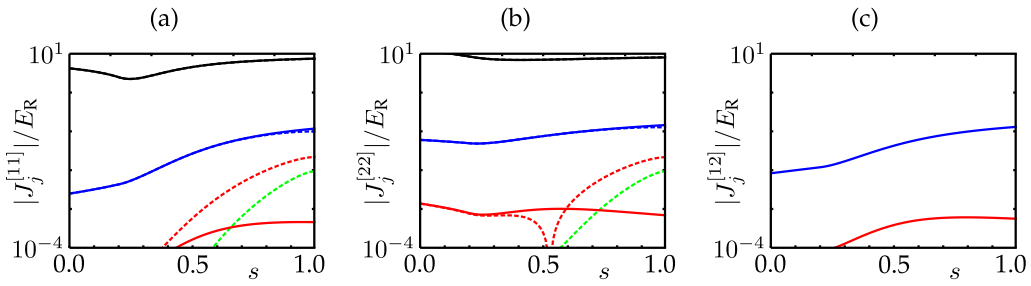


Figure 3.12. The hopping matrix elements for a red-detuned super-lattice potential as a function of the parameter s. Each term is represented for the cases of generalised Wannier functions and the original Wannier functions in identical fashion to Fig. 3.8 (a)-(c) and are labelled accordingly.

a local model. Once again, mixing the bands allows inter-band hopping to occur to the nearest-neighbour site with a magnitude between that of the elements for hopping within bands.

The interpolated bands for a local model including only nearest-neighbour hopping terms and with parameter $s = 0.999$ are shown in Fig. 3.13 (a) alongside the exact bands for the cases of ordinary and generalised Wannier functions. The interpolated bands calculated using generalised Wannier functions are almost indistinguishable from the exact bands, while those calculated using ordinary Wannier functions differ significantly and do not merge at the X point. The standard deviation between the interpolated bands and exact bands, shown in Fig. 3.13 (b), confirms that the accuracy of the local model using generalised Wannier functions is significantly better than that using ordinary Wannier functions. In the limit $s \to 1$ the lattice unit cell contains two primitive unit cells of the $a/2$ lattice, but the local model using ordinary Wannier functions does not include a term that describes on-site inter-mode hopping between bands, i.e. between the the two primitive unit cells of the $a/2$ lattice. This local model therefore cannot fully describe the system. In contrast, the local model using maximally localised generalised Wannier functions (leading to the equivalent interpolated band-structure as the symmetrised gener-

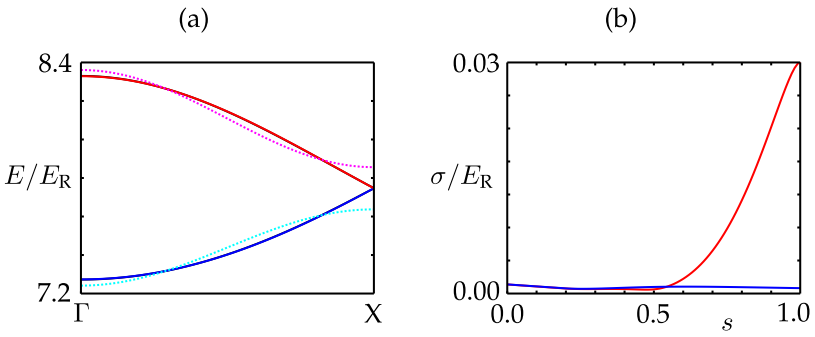


Figure 3.13. (a) The black solid lines show the lowest and first excited bands for a red-detuned super-lattice potential with $V_0 = 20E_R$ and $s = 0.999$. The blue and red solid lines show the interpolated lowest and first excited bands respectively for a tight-binding model using the maximally localised generalised Wannier functions, while the cyan and magenta dotted lines are the corresponding bands using the original Wannier functions. For the case of maximally localised generalised Wannier functions the interpolated bands are almost indistinguishable from the exact bands on this scale. (b) The standard deviation between the exact bands and the interpolated bands as a function of the super-lattice parameter s. The blue line is for the case of generalised Wannier functions, while the red line is for the original Wannier functions.

alised Wannier functions) does include this term and therefore accurately recreates the exact band-structure.

Finally, the magnitudes of the interaction matrix elements are shown in Fig. 3.14. For $s > 0.5$ the magnitudes of the nearest-neighbour density-density interaction ma-

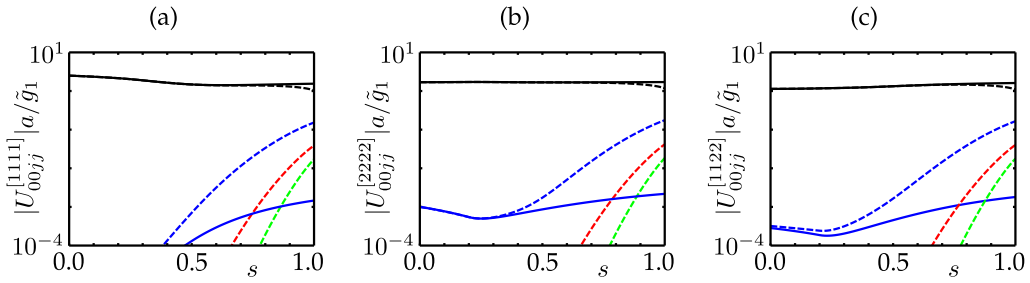


Figure 3.14. The interaction matrix elements for a red-detuned super-lattice potential as a function of the parameter s. Each term is represented for the cases of generalised Wannier functions and the original Wannier functions in identical fashion to Fig. 3.9 and are labelled accordingly.

trix elements are significantly reduced for the case of generalised Wannier functions compared to the case of ordinary Wannier functions, which is a result of the reduced spread. The on-site density-density interaction dominates all other terms for the case of generalised Wannier functions, allowing us to express the tight-binding Hamiltonian for the local model as

$$\hat{H} = \sum_j \sum_{m=1}^{2} \Bigg\{ J_0^{[mm]} \hat{n}_j^{[m]} + J_1^{[mm]} \hat{b}_j^{[m]\dagger} \left(\hat{b}_{j+1}^{[m]} + \hat{b}_{j-1}^{[m]} \right) + \tfrac{1}{2} U_{0000}^{[mmmm]} \hat{n}_j^{[m]} \left(\hat{n}_j^{[m]} - 1 \right) + \sum_{p \neq m} \left[J_1^{[mp]} \hat{b}_j^{[m]\dagger} \left(\hat{b}_{j+1}^{[p]} + \hat{b}_{j-1}^{[p]} \right) + \tfrac{1}{2} U_{0000}^{[mmpp]} \hat{n}_j^{[m]} \hat{n}_j^{[p]} \right] \Bigg\}. \tag{3.13}$$

3.3 1D super-lattice, blue-detuned

The same laser configuration as was used in the last section, but with blue detuning, produces the potential

$$V_{\mathrm{OL}}(x, s) = V_0 \left[1 - (1 - s) \sin^2(\pi x/a) - s \sin^2(2\pi x/a) \right], \tag{3.14}$$

where once again the intensities of the lasers can be altered to vary the parameter s between 0 and 1. This potential is shown in Fig. 3.15 (a) for the cases $s = 0$, 0.5 and 1. Since the opposite detuning reverses the maxima and minima, increasing s introduces a local minimum within the potential barrier, until for $s = 1$ the potential is again a sinusoidal lattice with lattice parameter $a/2$. The band-structure for the cases $s = 0$, 0.5 and 1 is shown in Fig. 3.15 (b). Since the potential is the same for both types of detuning for $s = 0$ and 1, the band-structure is the same as was shown in Fig. 3.10 (c), and therefore the lowest bands become degenerate at the X point for $s = 1$. However, for $s = 0.5$ the first excited band of the blue-detuned super-lattice has a larger mean energy due to the smaller width of the potential.

The Wannier functions and symmetrised generalised Wannier functions for the

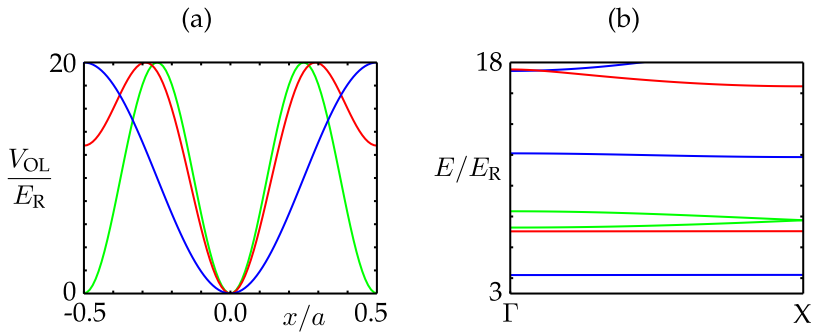


Figure 3.15. (a) The 1D super-lattice potential for blue-detuning as a function of position for $s = 0$ (blue solid line), $s = 0.5$ (red dotted line) and $s = 1$ (green dashed line). (b) The band-structure for the corresponding potentials in figure (a).

case $s = 0.999$ are presented in Fig. 3.16 (a)(b). The symmetrised generalised Wannier functions are the same as the red-detuned versions but centred at $x = -0.25a$ due to the shifted potential minima within the unit cell. Interestingly, the original Wannier functions are vastly different to those of the red-detuned lattice, with the Wannier function for the lowest band centred on $x = 0$ and that for the first excited band now centred at $x = 0.5/a$. In fact the form of the Wannier functions exhibits an abrupt change as the parameter s is increased through a value $s_c = 0.47$, as shown in Fig. 3.16 (d). At s_c the spread of the Wannier function for the first excited band reaches a peak, while the centre shifts to $x = 0.5/a$. The point s_c is approximately the value of s at which the mean energy of the first excited band coincides with the potential minimum of the upper well. It is also the point at which the Berry phase of the first excited band changes from zero to π. This potential therefore exemplifies the connection between the Berry phase and the Wannier centre, highlighted here by the Wannier function of the first excited band shifting from one potential minimum to another as the second minimum is lowered. Since the generalised Wannier functions are a mixture of both bands, the symmetrised generalised Wannier function for the lower band also shifts at s_c,

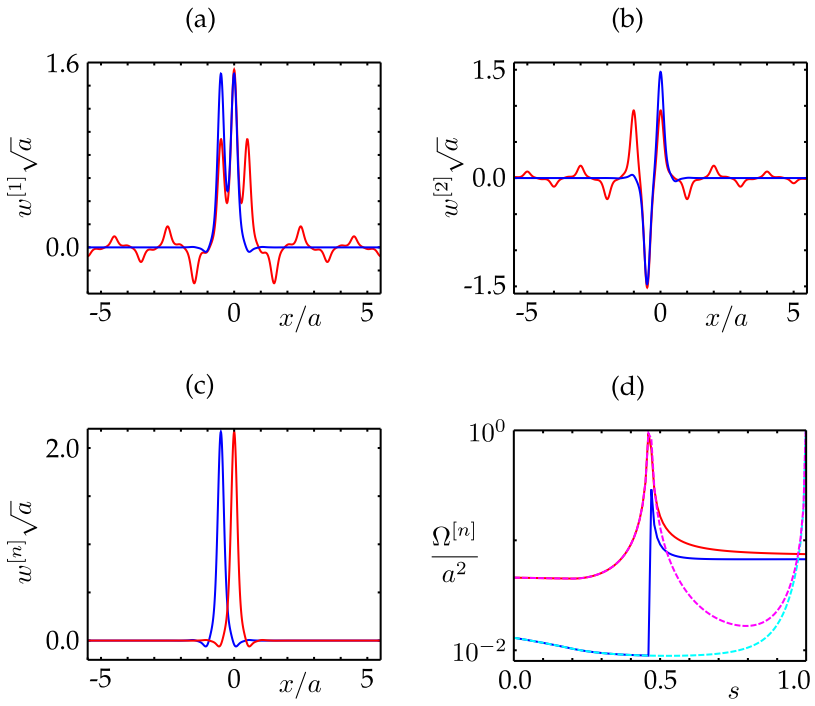


Figure 3.16. (a)-(b) The blue solid lines show the symmetrised generalised Wannier functions for a blue-detuned super-lattice potential with $V_0 = 30E_R$ and $s = 0.999$, calculated by treating the lowest two bands as a composite group. Figure (a) is for the lower mode $n = 1$, while figure (b) is for the upper mode $n = 2$. The red solid lines are the original Wannier functions without band mixing. (c) The maximally localised generalised Wannier functions from which the generalised Wannier functions in figures (a) and (b) are formed using symmetric and anti-symmetric super-positions. (d) The spreads of the symmetrised generalised Wannier functions as a function of the parameter s. The blue and red solid lines are for modes $n = 1$ and $n = 2$ respectively. The cyan and magenta dotted lines are the corresponding spreads of the original Wannier functions.

and this is also observable in the spread. Finally, notice that the spread of both symmetrised generalised Wannier functions is almost an order of magnitude greater than that of the original Wannier functions above s_c, except in the limit $s \to 1$, where it is less.

The magnitudes of the hopping matrix elements are shown in Fig. 3.17 (a)-(c). The hopping matrix elements for the lowest band using symmetrised generalised Wannier functions exhibit a sharp increase in magnitude at s_c as a result of the change in form of the Wannier functions. Once again, hopping to the nearest-neighbour site dominates all other terms. Inter-mode hopping has a slightly different magnitude in opposite directions above s_c due to the generalised Wannier functions being located away from the centre of the unit cell. The standard deviation between the interpolated bands for a local model including only nearest-neighbour interactions and the exact bands is shown in Fig. 3.17 (d). For both the original and generalised Wannier functions the standard deviation peaks at s_c, coinciding with the maxima in the hopping matrix elements, and hinting that more terms would need to be included in the local model to more accurately recreate the band-structure. The local model using generalised Wannier functions is only significantly more accurate than that using the original Wannier functions for $s > 0.9$, but is no worse within the rest of the parameter range.

The magnitudes of the interaction matrix elements for this potential are shown in Fig. 3.18. As expected there is an abrupt change at s_c due to the change in form of the Wannier functions. The on-site density-density matrix elements dominate above all others, leading to the same tight-binding Hamiltonian as given in Eq. 3.13 but with the matrix elements shown in Fig. 3.17 and Fig. 3.18.

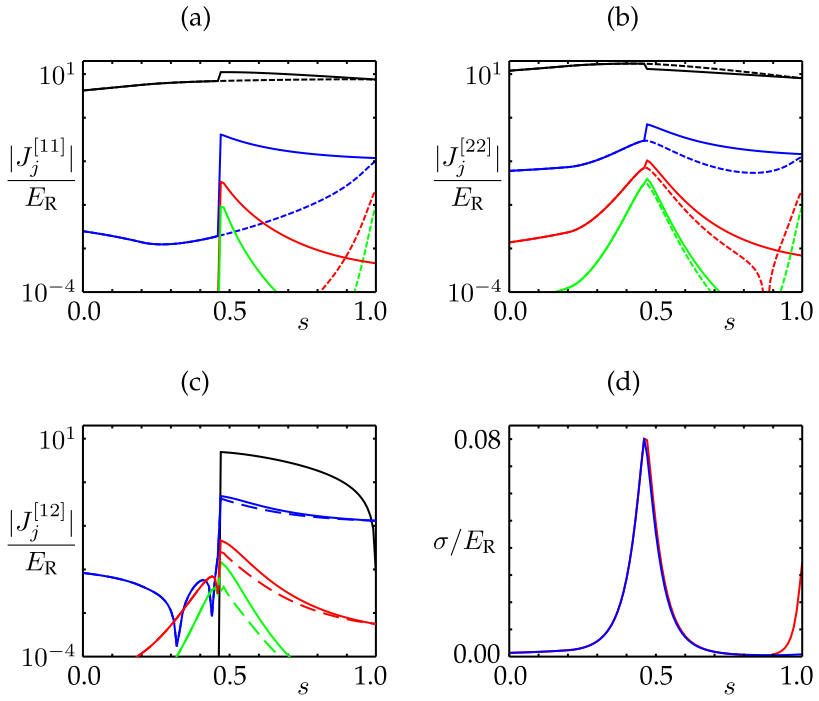


Figure 3.17. (a)-(c) The solid lines show the magnitude of the hopping matrix elements $|J_j^{[mn]}|$ for hopping (a) within the lowest mode $m = n = 1$, (b) within the upper mode $m = n = 1$, and (c) between modes $m \neq n$, for a blue-detuned super-lattice potential using maximally localised generalised Wannier functions. The dashed lines in figure (c) are the corresponding terms for hopping in the opposite lattice direction. The dotted lines show the same terms using the original Wannier functions. The black lines are for on-site matrix elements $|J_0^{[mn]}|$, while the blue, red, and green lines are for nearest-neighbour $|J_1^{[mn]}|$, next-nearest-neighbour $|J_2^{[mn]}|$, and third-neighbour $|J_3^{[mn]}|$, matrix elements respectively. (d) The standard deviation between the interpolated bands, calculated using the local model discussed in the text, to the exacts bands. The blue line is for a local model with generalised Wannier functions, whereas the red line is for a local model with ordinary Wannier functions.

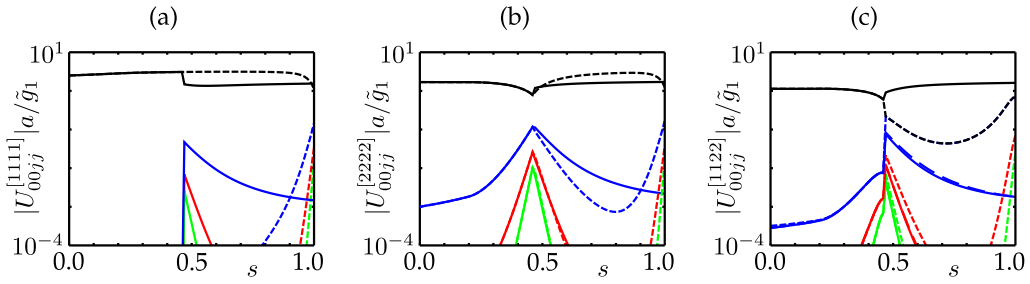


Figure 3.18. The interaction matrix elements for a blue-detuned super-lattice potential as a function of the parameter s. Each term is represented for the cases of generalised Wannier functions and the original Wannier functions in identical fashion to Fig. 3.9 and are labelled accordingly. In addition, the dashed lines in figure (c) show the magnitude of the density-density interaction matrix elements between modes for neighbours in the opposite lattice direction.

3.4 Conclusions

In this chapter we have considered the use of generalised Wannier functions for describing the many-body system of three 1D optical lattice potentials within a local model including only nearest-neighbour interactions. For the simple sinusoidal lattice the generalised Wannier functions offered no improvement over the original Wannier functions for this purpose. However, for the two super-lattice potentials the accuracy of the interpolated band-structure increased as the potential approached that of a sinusoidal lattice with two identical potential minima per unit cell. Mixing the bands introduced an inter-mode hopping term to allow hopping between all adjacent minima (i.e. between on-site minima), which was not possible when treating the bands as isolated. We surmise that mixing the bands is useful, and indeed necessary, when the bands are isolated and the potential exhibits multiple minima of similar depths per unit cell. This should be expected since mixing the bands is necessary when degeneracies are present, which can be caused by, e.g. identical local minima present within a single unit cell. One might expect that an improved accuracy from band mixing is observed in such systems when the band gaps between

isolated bands are less than or of the order of the band widths, however we do not prove this here.

3.A Appendix: Convergence with Brillouin zone sampling density

In Sec. 2.3.2 we discussed the use of a finite mesh of points for sampling the Brillouin zone in order to perform numerical integrations. In this appendix we briefly address the consequences that the use of a finite mesh has on our calculations, using the 1D sinusoidal optical lattice as an example.

The first, and most notable, consequence of using a finite Brillouin zone mesh is that the computed Wannier functions are of course periodic across the real space lattice, because the integral over Bloch states has been replaced with a finite summation. The situation corresponds to calculating Wannier functions for a finite lattice with N unit cells (in 1D) and periodic boundary conditions, where N is the Brillouin zone density. This is shown in Fig. 3.19 (a), where the Wannier function $w_0^{[1]}(x)$ for the lowest band and a lattice depth $V_0 = 0.5E_{\mathrm{R}}$ is plotted from calculations using $N = 100$ and $N = 10$. The Wannier functions are plotted across thirty-one unit cells, thus in the latter case three periods are visible. The implication for computing quantities such as the interaction matrix elements using these periodic Wannier functions is that one is restricted to work within one real space period–essentially, within the confines of the corresponding finite lattice. If the tails of the Wannier functions have not decayed to a negligible magnitude at the periodic boundary calculations for an infinite lattice when confined to a single period will be inaccurate. This will arise firstly due to the fact that we have neglected a non-zero contribution outside the period, but moreover because the Wannier functions themselves are in-

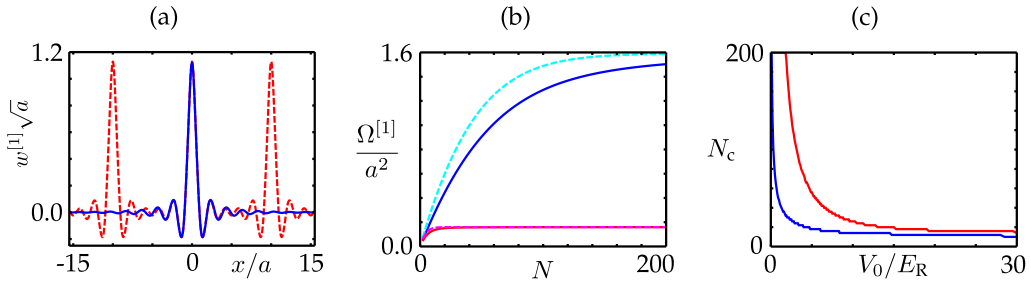


Figure 3.19. (a) The solid and dotted lines show the maximally localised Wannier function for the lowest band and a lattice depth $V_0 = 0.5E_R$, calculated using Brillouin zone densities of $N = 100$ and $N = 10$ respectively. On this scale the periodicity in the latter as a result of the finite density is visible. (b) The spread of the maximally localised Wannier function for the lowest band as a function of Brillouin zone density. The blue (and cyan) and red (and magenta) lines are for lattice depths $V_0 = 0.1E_R$ and $V_0 = E_R$ respectively. The solid lines show the spread calculated using Eq. 2.72, while the dotted lines show the spread as calculated directly from the Wannier functions using $\Omega^{[1]} = \langle w^{[1]}|\hat{\mathbf{r}}^2|w^{[1]}\rangle - \bar{\mathbf{r}}^{[1]2}$ over a lattice of N unit cells. (c) The Brillouin zone density N_c at which the spreads of the lowest band (blue solid line) and first excited band (red solid line) have converged, as a function of lattice depth. Here, convergence is quantified as the Brillouin zone density at which the percentage change in the spread, as N is increased by two (N is always even), is less than 0.1%.

accurate within the period. Figure 3.19 (a) provides an example of this; there is an observable difference in tails of the two types of Wannier function within $|x| < 5a$.

Following the discussion above we must choose the Brillouin zone density such that the corresponding real space period is large enough to completely contain the Wannier functions. This is measurable by considering the convergence of the spread of the Wannier functions with Brillouin zone density. For example, in Fig. 3.19 (b) we have plotted the spread for the lowest band against N for lattice depths $V_0 = 0.1E_R$ and $V_0 = E_R$. The solid lines show the spread calculated using the reciprocal space definition given in Eq. 2.72, while the dotted lines show the spread calculated by numerically integrating over the real space period, i.e. over a lattice of N unit cells, using $\Omega^{[1]} = \langle w^{[1]}|\hat{\mathbf{r}}^2|w^{[1]}\rangle - \bar{\mathbf{r}}^{[1]2}$. The two forms differ because the reciprocal space definition is an approximation resulting from the use of a finite-difference

formula [73], but both converge to the same value. For each lattice depth the spread is underestimated at low mesh densities due to neglecting the non-zero contribution outside the real space period.[4] The spread converges rapidly for $V_0 = E_\mathrm{R}$, but does not converge within $N < 200$ for the shallow lattices.

In Fig. 3.19 (c) we have plotted the Brillouin zone density at which convergence is reached against lattice depth for the lowest two bands. The convergence density is shown to rapidly increase as the lattice depth decreases towards zero. For the lowest band, the spread converges below a density of $N = 100$ for lattice depths above $V_0 = 0.4E_\mathrm{R}$, and below a density of $N = 20$ for lattice depths above $V_0 = 4E_\mathrm{R}$. Since the spread of the Wannier function for the first excited band is greater, a density of $N = 100$ is only suitable for this band for lattices with $V_0 > 3E_\mathrm{R}$, while the lattice depth must be greater than $13E_\mathrm{R}$ for a density as low as $N = 20$. In 1D a mesh density of a few hundred does not pose a problem for numerical computations, therefore results with good convergence in the spread of the Wannier functions can be obtained at all but very low lattice depths. However, in higher dimensions we must use N Brillouin zone mesh points in each reciprocal lattice direction, which significantly increases the total number of points. In 3D we typically cannot use mesh densities above $N = 20$ because of memory constraints. If we consider only the lowest band (or lowest manifold) we are restricted to lattice depths above $V_0 \approx 4E_\mathrm{R}$, while for higher bands this will increase due to the greater spread of the Wannier functions.

[4] The slow convergence of the spread was noted in the Ref. [71]. The authors contemplated whether a higher-order finite difference method would improve the convergence, however, as shown here, the slow convergence is primarily due to the periodic boundary cut-off.

Chapter 4

Maximally localised generalised Wannier functions for two-dimensional optical lattices

In the previous chapter we studied three one-dimensional optical lattice potentials as a test-bed for considering band mixing and the use of generalised Wannier functions. In each case the chosen bands were isolated because of a fundamental lack of symmetry (excluding inversion symmetry). In more than one dimension this is not generally the case; the presence of a crystallographic point group symmetry can lead to degeneracies amongst a group of bands, and in such cases generalised Wannier functions must be used (see Sec. 2.3.2). Because of the difficulties in calculating the maximally localised generalised Wannier functions, previous studies of these systems have typically assumed Gaussian functions for the localised states (see e.g. Ref. [81] or Ref. [31]), while thorough descriptions of the Bose-Hubbard parameters have been restricted to systems where the lowest band is isolated (see e.g. Ref. [82]). Using the methods discussed in chapter 2 we now calculate the maximally localised generalised Wannier functions and Bose-Hubbard parameters for a variety of two-dimensional optical lattice potentials of particular recent interest, including

rhombic, triangular, hexagonal, and Kagomé geometries.

4.1 2D optical lattice configurations

A laser configuration for creating a 2D optical lattice potential is shown in Fig. 4.1 (a), and consists of four beams contained within the x-y plane, which are linearly polarised in the z-direction.[1] The beams have wave-vectors $\mathbf{k}_0$, $\mathbf{k}_1$, $\mathbf{k}_2$, and $\mathbf{k}_3$, respectively, and each are of magnitude $k = 2\pi/\lambda$. Beams 0 and 1 form an independent pair, as do beams 3 and 4, and we define the angles θ_i between beam 0 and beams $i = 1, 2, 3$. The potential produced by this configuration is given by

$$V_{\mathrm{OL}}(\mathbf{r}) = \frac{V_0}{2}\left[\sin^2\left(\frac{\mathbf{T}_1^* \cdot \mathbf{r}}{2}\right) + \sin^2\left(\frac{\mathbf{T}_2^* \cdot \mathbf{r}}{2}\right)\right], \tag{4.1}$$

where

$$\mathbf{T}_1^* = \mathbf{k}_0 - \mathbf{k}_1, \tag{4.2}$$

$$\mathbf{T}_2^* = \mathbf{k}_2 - \mathbf{k}_3, \tag{4.3}$$

are the reciprocal lattice vectors. The potential has one minimum per primitive unit cell, and is unchanged (aside from a translation) if the detuning is switched from red to blue. When $\mathbf{T}_1^*$ and $\mathbf{T}_2^*$ are orthogonal the optical lattice potential formed is rectangular, with lattice parameters

$$a_1 = \frac{\lambda}{2}\csc\left(\frac{\theta_1}{2}\right), \tag{4.4}$$

$$a_2 = \frac{\lambda}{2}\csc\left(\frac{\theta_3 - \theta_2}{2}\right), \tag{4.5}$$

[1] Throughout this chapter we treat each 2D lattice as purely two-dimensional since the trapping potential in the z-direction can always be separated out.

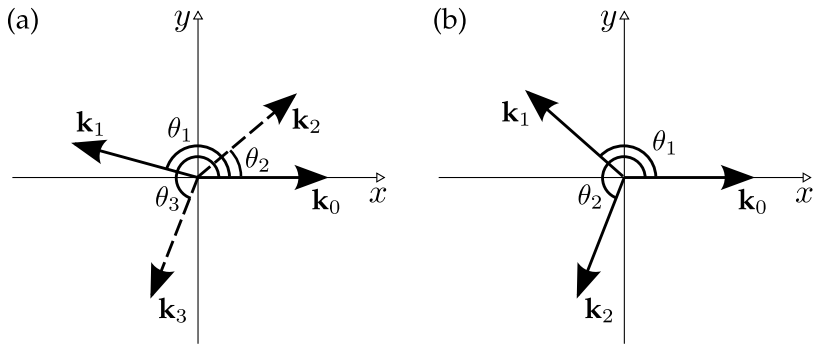


Figure 4.1. The wave-vectors for two laser configurations for generating 2D optical lattice potentials. The beams are contained within the x-y plane and linearly polarised in the z-direction. In figure (a) beams 0 and 1 form an independent pair, as do beams 2 and 3. In figure (b) all beams have the same frequency.

which can be altered between $\lambda/2$ and infinity by changing the angles between the beams. In Ref. [82] this setup was used to investigate the hopping and interaction parameters within a square optical lattice as a function of the lattice parameter. Oblique optical lattice potentials are formed when the reciprocal lattice vectors are non-orthogonal; these potentials will be considered in Sec. 4.2.

Another configuration, shown in Fig. 4.1 (b), involves three beams (the minimum number for creating a 2D optical lattice), which are again contained in the x-y plane and linearly polarised in the z-direction. As opposed to the previous configuration all beams have the same frequency and interfere with one another, resulting in the potential

$$V_{\mathrm{OL}}(\mathbf{r}) \propto \tfrac{3}{2} + \cos(\mathbf{T}_1^* \cdot \mathbf{r}) + \cos(\mathbf{T}_2^* \cdot \mathbf{r}) + \cos([\mathbf{T}_1^* - \mathbf{T}_2^*] \cdot \mathbf{r}). \tag{4.6}$$

The reciprocal lattice vectors are defined by

$$\mathbf{T}_1^* = \mathbf{k}_1 - \mathbf{k}_0, \tag{4.7}$$

$$\mathbf{T}_2^* = \mathbf{k}_2 - \mathbf{k}_0, \tag{4.8}$$

where $\mathbf{k}_i$ are the wave-vectors for the beams $i = 0, 1, 2$. If the beams are red-detuned the potential in Eq. 4.6 forms a general triangular lattice with one potential minimum per primitive unit cell, whereas if the beams are blue-detuned the primitive unit cell contains two minima and the lowest two bands are degenerate. In the former case, the crystallography of the potential was considered in Ref. [28] for its use in the laser cooling of atoms, while the Bose-Hubbard parameters for a variety of geometries were investigated in Ref. [82]. In Ref. [29] the superfluid-Mott insulator quantum phase transition was observed experimentally for the first time using an equilateral triangular geometry, and in Sec. 4.3 we determine the Bose-Hubbard parameters for this system. We then consider a blue-detuned hexagonal optical lattice in Sec. 4.4, which requires generalised Wannier functions for the two lowest bands.

In Sec. 4.5 we consider a further beam configuration for creating a Kagomé optical lattice, and leave the discussion of this until then. Firstly, we note that in any configuration if the wave-vectors do not sum to zero there will be a net radiation pressure in the resultant direction. However, the reactive part of the atom-field coupling is greater than the dissipative part, which includes radiation pressure, by a factor of the order of Δ/Γ. Typically $\Delta/\Gamma \gg 1$, and therefore the net radiation pressure can be ignored to a good approximation [28].

4.2 2D rhombic lattice

In this section we examine the Bose-Hubbard parameters for a rhombic optical lattice as it is transformed from being square. The geometries can be generated by using two independent pairs of counter-propagating beams as shown in Fig. 4.2. The acute angle of the rhombic unit cell, which we denote by χ, is equal to the angle between the beam pairs and can therefore be varied from ninety degrees to a limit

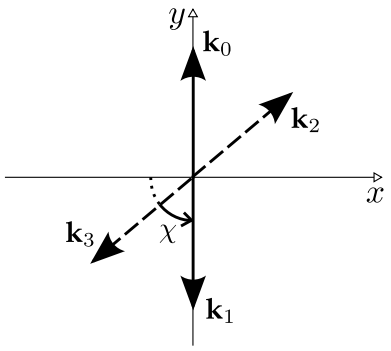


Figure 4.2. The beam configuration for generating a 2D rhombic optical lattice. The beams with wave-vectors $\mathbf{k}_0$ and $\mathbf{k}_1$ are counter-propagating and held fixed along the y-axis. The beams with wave-vectors $\mathbf{k}_2$ and $\mathbf{k}_3$, also counter-propagating and independent from the first pair, can be rotated through $0° < \chi \leq 90°$ to create a rhombic lattice with acute angle χ.

of zero degrees by rotating one pair relative to the other. The potential is given as a function of χ by

$$V_{\mathrm{OL}}(x, y, \chi) = \frac{V_0}{2}\left[\sin^2(ky) + \sin^2(kx\sin\chi - ky\cos\chi)\right], \tag{4.9}$$

which has a lattice parameter $a = 0.5\lambda\csc\chi$. The potentials for $\chi = 90°$, $60°$, and $30°$ are shown in Fig. 4.3 (a)-(c) respectively; one can clearly observe the increase in lattice parameter with decreasing χ. In each lattice direction there exists a saddle-point half-way between every pair of sites with a potential strength $V_0/2$. The potential maxima occur at the corners of the conventional primitive unit cell (if centred on the potential minimum) and therefore lie in between any lattice site and its nearest 'diagonal' neighbour.

The band-structures for the scenarios $\chi = 90°$, $60°$, and $30°$, using a lattice depth $V_0 = 20E_{\mathrm{R}}$, are shown in Fig. 4.3 (d)-(e). The lowest band in each case is isolated since there is only one potential minimum per unit cell. For the square lattice the first and second excited bands are degenerate along the path $\Gamma \rightarrow \mathrm{M}$. As is well-known, the square lattice potential is separable in x and y, therefore these bands are

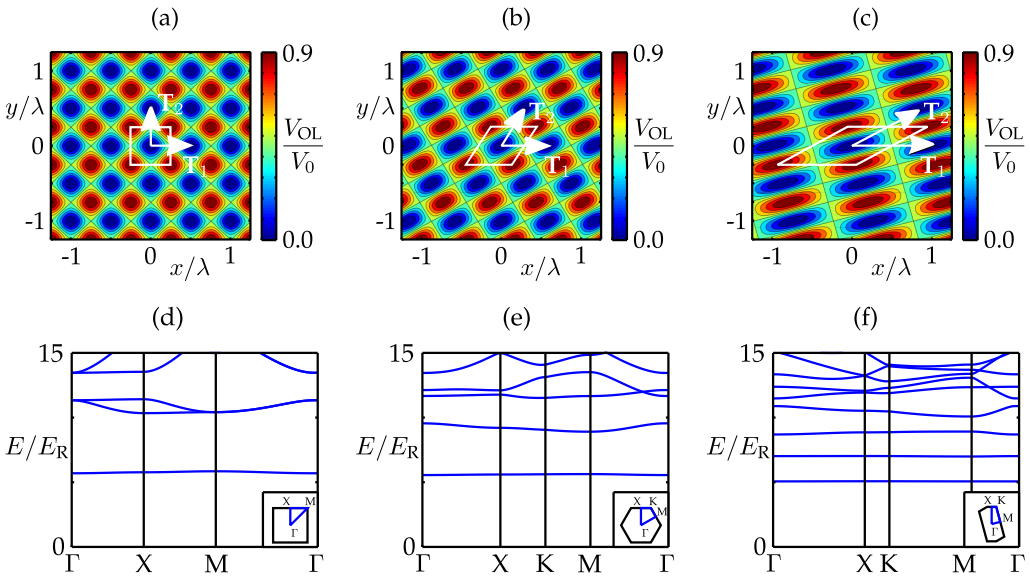


Figure 4.3. (a)-(c) Contour plots of a 2D rhombic optical lattice potential for acute lattice angle $\chi = 90°$ (a), $\chi = 60°$ (b), and $\chi = 30°$ (c). (d)-(e) The corresponding band-structures for the potentials in figures (a)-(c). For each figure the band energies are displayed along the path through the Brillouin zone shown in the inset.

the sum of the lowest band of a 1D lattice in the x-direction and first excited band in the y-direction, and vice versa. For $\chi \neq 90°$ the four-fold rotational symmetry is broken causing the first and second excited bands to separate. The mean energy of the first excited band decreases with χ, reducing the band gap to the lowest band, while the mean energy of the second excited band increases causing it to become degenerate with higher bands. In general, we observe that bands associated with Bloch states that have high frequency components in the direction $\mathbf{T}_2 - \mathbf{T}_1$ increase in energy with decreasing χ due to the narrowing of the on-site potential in this direction. Bands associated with Bloch states that have only low frequency components in the direction $\mathbf{T}_2 - \mathbf{T}_1$ decrease in energy due to the increasing width of the on-site potential in the direction $\mathbf{T}_1 + \mathbf{T}_2$. In the limit $\chi \to 0°$ the lattice parameter tends to infinity and therefore the band gaps between the lowest bands diminish to zero.

The maximally localised (generalised) Wannier functions for a square lattice and a rhombic lattice with acute angle $\chi = 60°$ are shown in Fig. 4.4. A lattice depth of $V_0 = 5E_\mathrm{R}$, shallower than considered in the rest of this section, is used for these plots to enhance the visibility of the tails. The first notable feature of the Wannier functions for the isolated bands is that they possess the same symmetry properties as the lattice potential. The generalised Wannier functions for the excited bands of the square lattice do not individually possess four-fold rotational symmetry, but are instead images of each other through a rotation of ninety degrees. Since the square optical lattice potential is separable in x and y, the 2D Wannier functions are products of the 1D Wannier functions for the 1D potentials associated with each Cartesian direction.[2] Consequently, the variant part of the total spread $\tilde{\Omega} = \Omega_\mathrm{D} + \Omega_\mathrm{OD}$ for the set of maximally localised generalised Wannier functions (i.e. for the two excited bands) is zero, as expected following our discussion in Sec. 2.4.2. For $\chi \neq 90°$ we observe that the maximally localised Wannier function for the first excited band is reminiscent of the superposition of $w^{[1]}(\mathbf{r})$ and $w^{[2]}(\mathbf{r})$ for the square lattice, but aligned in the direction $\mathbf{T}_1 + \mathbf{T}_2$. However, this Wannier function cannot be derived from separable 1D Wannier functions. In the limit $\chi \to 90°$ the first and second excited bands are isolated but have a diminishing band gap. Following the conclusions drawn in chapter 3 one might expect that generalised Wannier functions could be used for these bands to improve the viability of a Bose-Hubbard-type model containing only nearest-neighbour terms. However, due to the large band gap between the lowest and excited bands we next exclude all but the lowest band for examining the Bose-Hubbard parameters of the rhombic optical lattice, and leave this for future study.

The magnitudes of the hopping and interaction matrix elements for the lowest

[2]The plots shown in Fig. 4.4 (a)-(c) were obtained using our algorithm for obtaining maximally localised (generalised) Wannier functions in 2D.

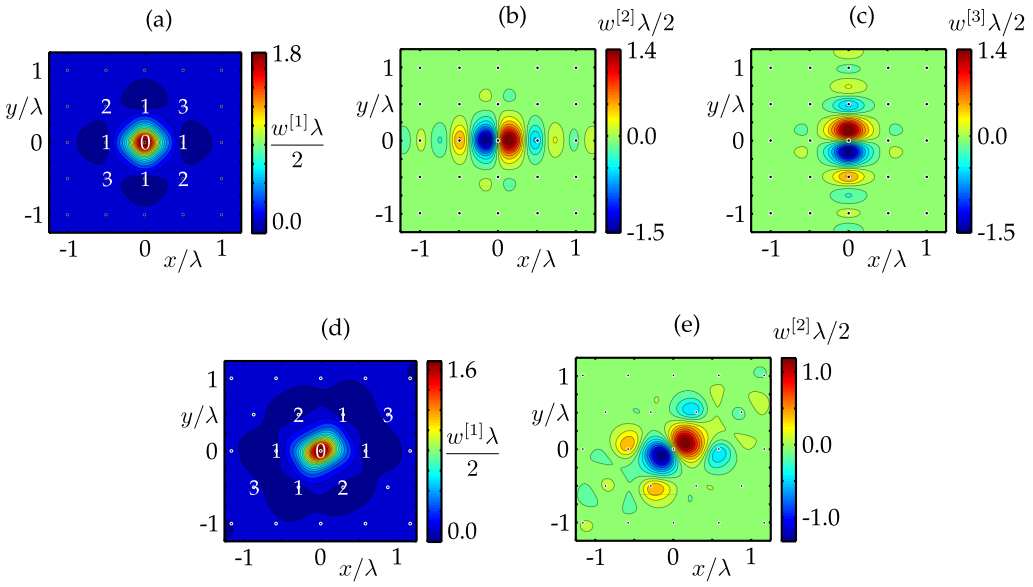


Figure 4.4. Contour plots of the maximally localised (generalised) Wannier functions for a rhombic optical lattice with a lattice depth $V_0 = 5E_\mathrm{R}$. Figure (a) shows the Wannier function for the lowest band of a square optical lattice ($\chi = 90°$), while figures (b)(c) show the generalised Wannier functions for the first and second excited bands. Figures (d)(e) show the Wannier functions for the lowest and first excited bands respectively of a rhombic lattice with acute angle $\chi = 60°$. In figures (a) and (d) we have labelled sites with equal hopping matrix elements from the 'home' site to neighbouring sites by $j = 0, 1, 2, 3$.

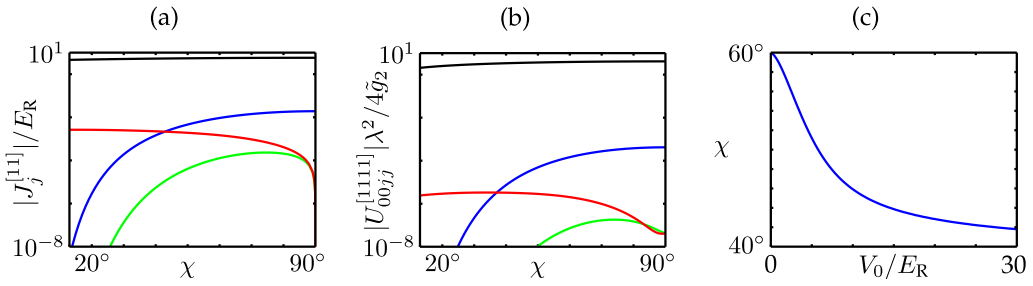


Figure 4.5. The magnitudes of (a) the hopping matrix elements, and (b) the density-density interaction matrix elements, for a rhombic optical lattice as a function of the acute angle χ. The blue, red, and green lines correspond to matrix elements involving the nearest-neighbour site $j = 1$, the near-diagonal site $j = 2$, and the far-diagonal site $j = 3$, respectively, while the black lines are for on-site terms ($j = 0$). (c) The value of χ at which $|J_2| = |J_1|$, as a function of lattice depth V_0.

band of a rhombic optical lattice are plotted in Fig. 4.5 (a)(b) respectively as a function of the acute angle χ (henceforth in this section we remove the band labels since we now consider the lowest band only). As was done in chapter 3, here we have introduced a '2D contact interaction constant' $\tilde{g}_2$ to replace the real contact interaction constant g used in 3D (*cf.* Sec. 2.2). For a square optical lattice it can be shown that hopping is allowed only in the lattice directions as a result of the separability of the potential in x and y, therefore the magnitudes of the matrix elements for hopping to 'diagonal' neighbours are zero for $\chi = 90°$. In the opposite regime, $\chi \to 0°$, the lattice parameter tends to infinity causing the hopping matrix element J_1 to reduce to zero. Similarly, hopping across the far-diagonal to site $j = 3$, which is zero for $\chi = 90°$ but finite otherwise, also diminishes in the limit $\chi \to 0°$. Meanwhile, the magnitude of the matrix element for hopping across the near-diagonal to site $j = 2$ increases from zero as χ is decreased from ninety degrees, and surpasses the magnitude of J_1 for $\chi < 42.853°$ due to the smaller distance between sites. The angle at which $|J_2| = |J_1|$ is shown as a function of lattice depth in Fig. 4.5 (c). Finally, while the on-site density-density interaction matrix element U_{0000} dominates for all values of χ, we observe that the magnitude of the density-density matrix element U_{0022} is greater than that of U_{0011} for $\chi < 37.070°$, again due to the reduced distance between sites $j = 0$ and $j = 2$ compared to the lattice parameter.

We can now express the Hamiltonian for the rhombic lattice as

$$\hat{H} = \sum_{i,j} \Big[J_0 \hat{n}_{i,j} + J_1 \hat{b}^\dagger_{i,j} \left(\hat{b}_{i+1,j} + \hat{b}_{i-1,j} + \hat{b}_{i,j+1} + \hat{b}_{i,j-1} \right) + J_2 \hat{b}^\dagger_{i,j} \left(\hat{b}_{i+1,j-1} + \hat{b}_{i-1,j+1} \right) + \tfrac{1}{2} U_{0000} \hat{n}_{i,j} \big(\hat{n}_{i,j} - 1 \big) \Big]. \tag{4.10}$$

Here we have continued to label the hopping matrix elements according to Fig.

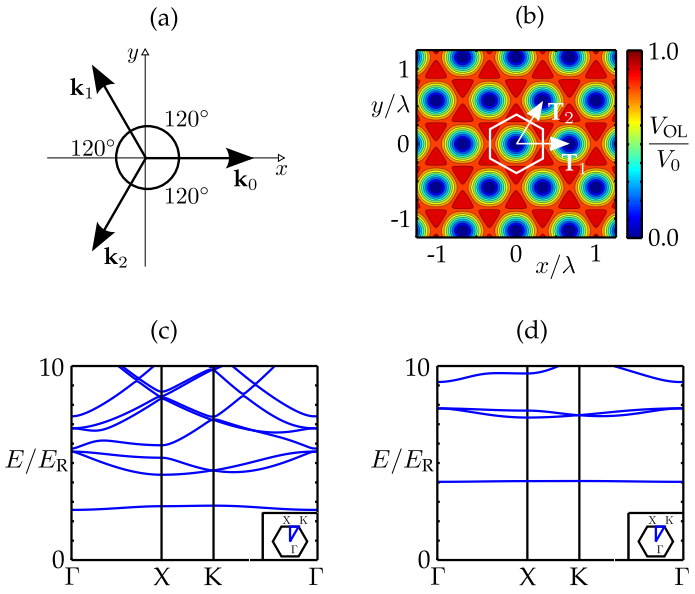


Figure 4.6. (a) The beam configuration for generating a 2D equilateral triangular optical lattice. The beam wave-vectors are aligned at 120° to each other, with one beam parallel to the x-axis. (b) A contour plot of the 2D equilateral triangular optical lattice potential. (c)(d) The band-structure for this potential with lattice depths $V_0 = 5E_{\rm R}$ and $10E_{\rm R}$ respectively. For each figure the band energies are displayed along the path through the Brillouin zone shown in the inset.

4.4 (a) and (d), but have introduced a 2D grid to label the the bosonic operators according to the site i in the direction $\mathbf{T}_1$ and site j in the direction $\mathbf{T}_2$. Notably, the coordination number of this Hamiltonian is four for $\chi = 90°$, then increases to six as χ is decreased, and is reduced to two in the limit $\chi \to 0°$.

4.3 2D equilateral triangular lattice

We now consider the three beam configuration introduced earlier, which for red-detuning generates a triangular optical lattice potential. Specifically, we align the beams at 120° to one another as shown in Fig. 4.6 (a) to create an equilateral

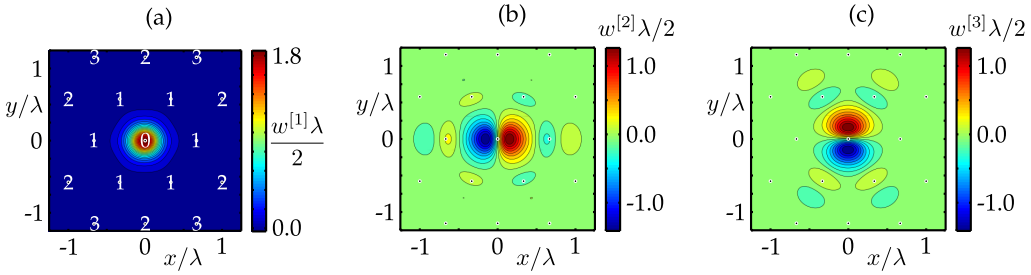


Figure 4.7. Contour plots of the maximally localised (generalised) Wannier functions for an equilateral triangular optical lattice with a lattice depth $V_0 = 5E_\mathrm{R}$. Figure (a) shows the Wannier function for the lowest band, while figures (b)(c) show the generalised Wannier functions for the first and second excited bands. In figure (a) we have labelled sites with equal hopping matrix elements from the 'home' site and within the lowest band by $j = 0, 1, 2, 3$.

triangular lattice.[3] The potential is given by

$$V_{\mathrm{OL}}(\mathbf{r}) = \frac{V_0}{9}\left[6 - 2\cos\left(\sqrt{3}ky\right) - 4\cos\left(\frac{3kx}{2}\right)\cos\left(\frac{\sqrt{3}ky}{2}\right)\right], \tag{4.11}$$

which is plotted in Fig. 4.6 (b).[4] The Wigner-Seitz unit cell is hexagonal and the underlying potential retains the six-fold rotational symmetry. Each lattice site has six nearest-neighbours spaced by the lattice parameter $a = 2\lambda/3$, which is larger than that of the rhombic lattice by a factor 3/2. A saddle point exists half-way between each pair of neighbouring lattice sites with a potential strength $8V_0/9$, while the potential maxima are positioned at the vertices of the Wigner-Seitz unit cell (if centred on the potential minimum). Thus, the potential barrier between each lattice site is comparable to the full lattice depth, contrary to the situation in the rhombic lattice for which the potential barrier is half the lattice depth.

The band-structure for the equilateral triangular lattice is shown in Fig. 4.6

[3]The Bravais lattice type is hexagonal, but we denote the lattice potential as equilateral triangular. The hexagonal optical lattice potential to be introduced in Sec. 4.4 also uses the hexagonal Bravais lattice.

[4]Here we have set V_0 as positive and adjusted the zero of energy such that the potential minima occur where $V_{\mathrm{OL}} = 0$ and the maxima where $V_{\mathrm{OL}} = V_0$. The red-detuning then causes the coefficients of the cosine terms from Eq. 4.6 to be negated.

(c)(d) for the cases $V_0 = 5E_{\mathrm{R}}$ and $V_0 = 10E_{\mathrm{R}}$ respectively. Once again the lowest energy band is isolated because there is one potential minimum per primitive unit cell, while the first and second excited bands form a composite group and are degenerate at the Γ and K points (the K points are the vertices of the hexagonal Brillouin zone). As expected, the band-width of each band decreases with increasing lattice depth, while the band gaps increase. The maximally localised (generalised) Wannier functions for these bands are shown in Fig. 4.7 for a lattice depth $V_0 = 5E_{\mathrm{R}}$. The maximally localised Wannier function for the lowest band (Fig. 4.7 (a)) is located at the potential minimum and possesses the same symmetry as the optical lattice potential. For a lattice depth of $V_0 = 5E_{\mathrm{R}}$ the Wannier function is well-localised on its lattice site and has little overlap with neighbouring sites. The maximally localised generalised Wannier functions for the first and second excited bands (Fig. 4.7 (b)(c)) each possess only two-fold rotational symmetry, and, contrary to the corresponding generalised Wannier functions for the square optical lattice, are not images of each other through a rotation. Within the central unit cell, i.e. ignoring the tails, these generalised Wannier functions are reminiscent of the wave-functions for a 2D harmonic oscillator potential. As such, their form, consisting of a single, central anti-node corresponding to a low energy wave-function, is only possible if the six-fold rotational symmetry is broken. The fact that they are not images of each other through a rotation of ninety degrees, as is the case with the corresponding functions for the square optical lattice, is to ensure orthogonality.

Figure 4.8 (a)(b) shows the magnitudes of the hopping and interaction matrix elements for the lowest band of the equilateral triangular lattice as a function of lattice depth. Due to the six-fold rotational symmetry of the maximally localised Wannier function the magnitudes of the hopping matrix elements, and also interaction matrix elements, are equal between sites with equal distance, as labelled in Fig. 4.7 (a). Similar to the situation for a 1D sinusoidal lattice, the hopping matrix ele-

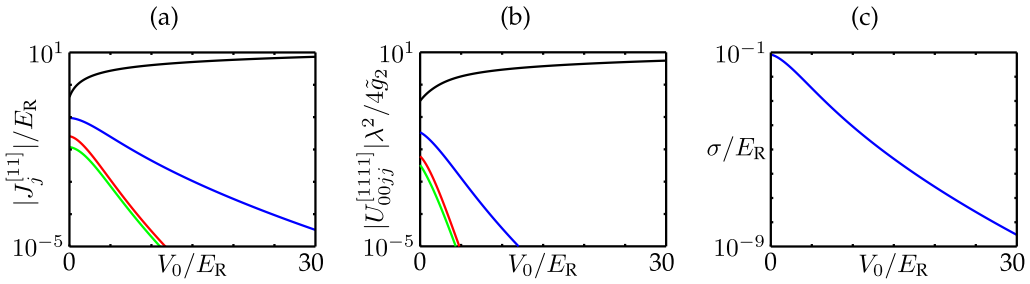


Figure 4.8. (a)(b) The magnitudes of the hopping and density-density interaction matrix elements respectively for an equilateral triangular lattice as a function of lattice depth V_0. The blue, red, and green lines are for matrix elements involving the 'home' site and sites $j = 1, 2, 3$ respectively, while the black lines are for on-site terms ($j = 0$). The labelling of the minima is shown in Fig. 4.7. (c) The standard deviation between the exact lowest band and the interpolated tight-binding band as a function of lattice depth.

ments decrease almost exponentially with lattice depth, while the nearest-neighbour element is at least an order of magnitude greater than other hopping elements at all but very shallow lattice depths. In addition, the on-site density-density interaction matrix element dominates over all other interaction matrix elements. This leads us to the following Hamiltonian for the equilateral triangular lattice, labelled in the same fashion as with the rhombic lattice,

$$\hat{H} = \sum_{i,j} \Big[J_0 \hat{n}_{i,j} + J_1 \hat{b}_{i,j}^\dagger \left(\hat{b}_{i+1,j} + \hat{b}_{i-1,j} + \hat{b}_{i,j+1} + \hat{b}_{i,j-1} + \hat{b}_{i+1,j-1} + \hat{b}_{i-1,j+1} \right) + \tfrac{1}{2} U_{0000} \hat{n}_{i,j} \left(\hat{n}_{i,j} - 1 \right) \Big]. \tag{4.12}$$

In agreement with the experimental observation in Ref. [29], this Hamiltonian is the equivalent version of that for the square lattice, but with a coordination number of six. We have inserted the hopping matrix elements included in this Hamiltonian into Eq. 2.85 to calculate the energy of the lowest band according to a tight-binding model. The standard deviation between the interpolated band and the exact band is plotted in Fig. 4.8 (c) as a function of lattice depth. It decreases

almost exponentially with increasing lattice depth, highlighting the accuracy of the included hopping terms in recreating the single-particle lowest band for all but shallow lattices.

4.4 2D hexagonal lattice

The laser configuration used for the equilateral triangular lattice produces a hexagonal optical lattice potential when the lasers are blue-detuned. The potential is simply the negation of that given in Eq. 4.11,

$$V_{\mathrm{OL}}(\mathbf{r}) = \frac{V_0}{9}\left[3 + 2\cos\left(\sqrt{3}ky\right) + 4\cos\left(\frac{3kx}{2}\right)\cos\left(\frac{\sqrt{3}ky}{2}\right)\right], \tag{4.13}$$

and is shown in Fig. 4.9 (a). Here we have adjusted the zero of energy such that the potential minima occur when $V_{\mathrm{OL}} = 0$. The Wigner-Seitz unit cell is identical to that of the previous section because the Bravais lattice type remains hexagonal, however, the potential now exhibits two minima per unit cell, which are positioned at the cell vertices forming the hexagonal (or honeycomb) structure. A saddle point with a potential strength $V_0/9$ exists inbetween each pair of minima, which are separated by a distance $2\lambda/3\sqrt{3}$. The minima therefore form shallow wells in a region of low potential strength surrounding the relatively large potential maxima. The consequence of there being two potential minima per unit cell is that the two lowest bands are degenerate at the K points of the Brillouin zone, as shown in Fig. 4.9 (b)(c) for lattice depths $V_0 = 10E_{\mathrm{R}}$ and $V_0 = 30E_{\mathrm{R}}$ respectively. The mean energy of the bands is greater than the saddle point between potential minima, but less than the full lattice depth. The band-width of the lowest bands is comparable to the band gap to higher bands for $V_0 = 10E_{\mathrm{R}}$; since we can only legitimately ignore higher bands when the band gap is larger than the band-width, this places a limit

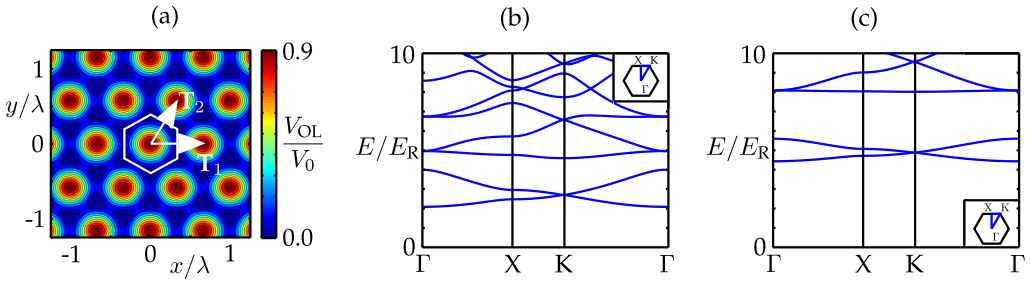


Figure 4.9. (a) A contour plot of the 2D hexagonal optical lattice potential. (b)(c) The band-structure for this potential with lattice depths $V_0 = 10E_{\mathrm{R}}$ and $30E_{\mathrm{R}}$ respectively. For each figure the band energies are displayed along the path through the Brillouin zone shown in the inset.

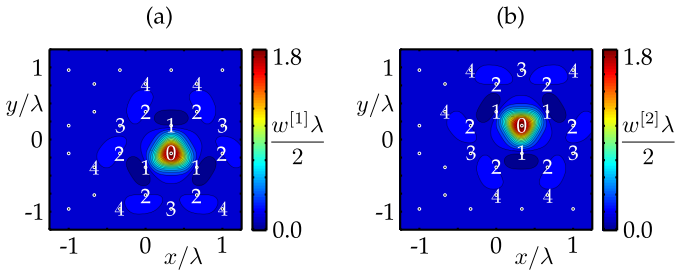


Figure 4.10. Contour plots of the maximally localised generalised Wannier functions for the two lowest bands of a hexagonal optical lattice with a lattice depth $V_0 = 10E_{\mathrm{R}}$. We have labelled the potential minima with equal hopping matrix elements from the 'home' minimum by $j = 0, 1, 2, 3, 4$.

of $V_0 \sim 10E_{\mathrm{R}}$ on the lattice depth for which a Bose-Hubbard-type model (including the lowest two bands only) can be used. This lower limit is greater than that of the previously studied lattices because of the relatively shallow saddle point between potential minima.

The maximally localised generalised Wannier functions for the two lowest bands are shown in Fig. 4.10 for a lattice depth $V_0 = 10E_{\mathrm{R}}$. Both functions possess three-fold rotational symmetry about their centres and are images of one another through a rotation of sixty degrees about the centre of the Wigner-Seitz unit cell. The functions are less well-localised than was the case for the previous lattices due to the larger area where the potential is shallow. Neither generalised Wannier

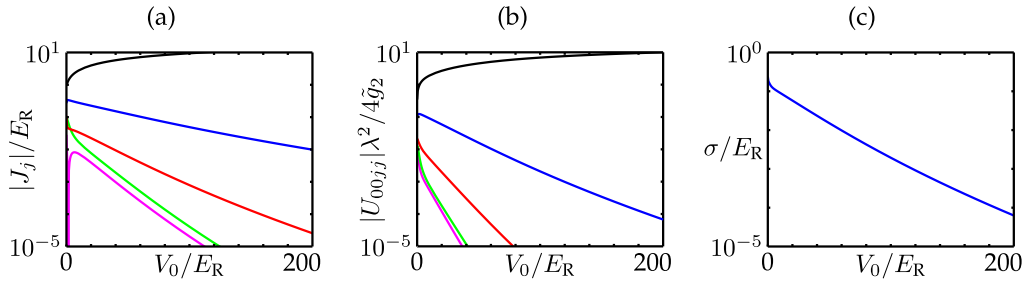


Figure 4.11. (a)(b) The magnitudes of the hopping and density-density interaction matrix elements respectively for a hexagonal optical lattice as a function of lattice depth V_0. The blue, red, green, and magenta lines are for matrix elements involving the 'home' minimum and minima $j = 1, 2, 3, 4$ respectively, while the black lines are for on-site terms ($j = 0$). The labelling of the minima is shown in Fig. 4.10. (c) The total standard deviation between the exact lowest bands and the interpolated tight-binding bands as a function of lattice depth.

function possesses inversion symmetry because the potential minima are not located at Wyckoff positions (centres of inversion). As a result $\Omega_D \neq 0$ for the pair although the total spread is minimised and the functions are real. Since inversion symmetry is broken it is clear that a Gaussian function would not adequately describe these generalised Wannier functions even in the deep lattice limit. As was the case for the 1D super-lattice, one can choose a symmetric and anti-symmetric combination to form new generalised Wannier functions that are centred on a Wyckoff position and have greater total spread but with $\Omega_D = 0$. However, we continue with the maximally localised generalised Wannier functions for examining the Bose-Hubbard parameters of the system.

The magnitudes of the hopping and density-density interaction matrix elements for the two lowest bands of the hexagonal optical lattice are shown in Fig. 4.11. Since the maximally localised generalised Wannier functions are related through a symmetry operation the matrix elements within each mode are identical. We therefore label the matrix elements not by site and mode, but by the distance between potential minima, as shown in Fig. 4.10. Matrix elements involving minimum $j = 0$

and minima $j = 0, 2$ are intra-mode, while those involving minimum $j = 0$ and minima $j = 1, 3, 4$ are inter-mode. The decay in the magnitude of the hopping and off-site density-density interaction matrix elements with lattice depth is considerably less than observed with the previous lattices due to the larger spread of the generalised Wannier functions. We therefore calculate these matrix elements up to a lattice depth of $V_0 = 200E_{\mathrm{R}}$. We observe that the significant matrix elements are the 'on-site' density-density interaction element U_{0000} and the hopping matrix element J_1, therefore the Hamiltonian for the hexagonal optical lattice can be given by

$$\begin{aligned}\hat{H} = \sum_{i,j} \Bigg[\sum_m J_0 \hat{n}_{i,j}^{[m]} + J_1 \hat{b}_{i,j}^{[1]\dagger} \left(\hat{b}_{i,j}^{[2]} + \hat{b}_{i,j-1}^{[2]} + \hat{b}_{i+1,j-1}^{[2]} \right) \\ + J_1 \hat{b}_{i,j}^{[2]\dagger} \left(\hat{b}_{i,j}^{[1]} + \hat{b}_{i,j+1}^{[1]} + \hat{b}_{i-1,j+1}^{[1]} \right) \\ + \sum_m \tfrac{1}{2} U_{0000} \hat{n}_{i,j}^{[m]} \left(\hat{n}_{i,j}^{[m]} - 1 \right) \Bigg]. \end{aligned} \tag{4.14}$$

The hopping terms included in this Hamiltonian are inter-mode only, however, because the system is invariant under a rotation of 180° about the point equi-distant from the two Wannier centres, the two modes are equivalent, and one can express the Hamiltonian in the general form

$$\hat{H} = \sum_i J_0 \hat{n}_i + \sum_{\langle i,j \rangle} J_1 \hat{b}_i^\dagger \hat{b}_j + \sum_i \tfrac{1}{2} U_{0000} \hat{n}_i (\hat{n}_i - 1), \tag{4.15}$$

where the sum is taken over potential minima (we have now dropped the mode index and labelled the minima by the index i), each with three nearest-neighbours.

We once again insert the hopping matrix elements included in the Hamiltonian in Eq. 4.14 into a tight-binding model to recreate the single particle band-structure. The standard deviation between the interpolated bands and the exact bands is shown

in Fig. 4.11 (c) as a function of lattice depth. This is larger than was observed for the equilateral triangular optical lattice potential due to the greater band-width of the lowest bands, but again decreases exponentially with lattice depth indicating the good accuracy of the model at all but shallow depths.

4.5 2D Kagomé lattice

An optical lattice geometry that has received a large degree of interest in recent years is the Kagomé lattice because it realises a many-body system with a high degree of frustration [31, 32, 81, 83]. In this section we consider the particular implementation proposed in Ref. [83], which is shown schematically in Fig. 4.12 (a). The geometry is formed by first creating an equilateral triangular lattice with parameter $2\lambda/3$ as discussed in Sec. 4.3, and then overlaying an independent hexagonal lattice potential with parameter $4\lambda/3$. The maxima of the hexagonal potential, which themselves form an equilateral triangular structure, cancel out one quarter of the potential minima of the triangular lattice, thus creating the Kagomé potential shown in Fig. 4.12 (b). In Ref. [83] the larger lattice parameter of the hexagonal potential is achieved by using long-wavelength beams of double the transition wavelength, however, this could also be achieved using the same wavelength by aligning the three beams at a sixty degree angle[5] to the x-y plane as shown in Fig. 4.12 (a).

The Kagomé potential is given in terms of the real space coordinates by

$$\begin{aligned} V_{\mathrm{OL}}(\mathbf{r}) \propto &- \cos\left(\sqrt{3}ky\right) - 2\cos\left(\frac{3kx}{2}\right)\cos\left(\frac{\sqrt{3}ky}{2}\right) \\ &+ \cos\left(\frac{\sqrt{3}ky}{2}\right) + 2\cos\left(\frac{3kx}{4}\right)\cos\left(\frac{\sqrt{3}ky}{4}\right). \end{aligned} \tag{4.16}$$

[5]The opposite detuning of the two sets of beams means the two potentials are not perfectly commensurate with a sixty degree angle, but the angle can always be adjusted to ensure this is the case.

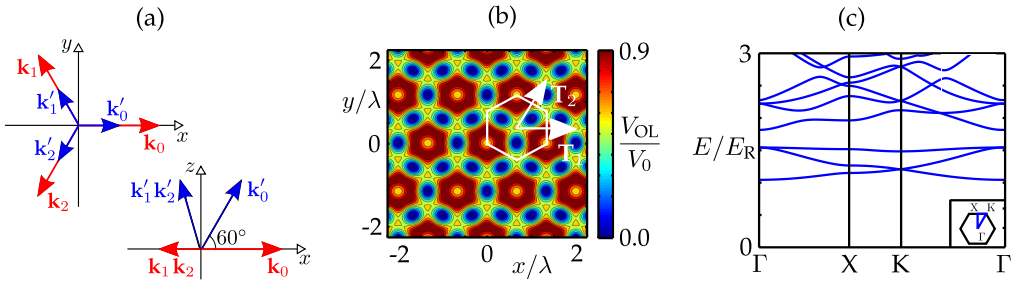


Figure 4.12. (a) The beam configuration for generating a Kagomé optical lattice potential. The projections of the beam wave-vectors are shown in the x-y and x-z planes. The red-detuned beams lie in the x-y plane and generate an equilateral triangular lattice potential, while the blue-detuned beams are at a 60° angle to the x-y plane, overlaying a hexagonal lattice potential of twice the lattice parameter. (b) A contour plot of the 2D Kagomé optical lattice potential. (c) The band-structure for this potential with lattice depth $V_0 = 2E_{\mathrm{R}}$. The band energies are displayed along the path through the Brillouin zone shown in the inset.

We once again scale the potential such that the full lattice depth is V_0. The Bravais lattice type is hexagonal with the lattice parameter determined by the larger of the two superimposed potentials, i.e. $a = 4\lambda/3$. The primitive unit cell possesses three potential minima as shown in Fig. 4.12 (b). The saddle points between each pair of minima in the trimer have a potential strength $0.62V_0$, thus the potential wells are deeper relative to the full lattice depth than was the case for the hexagonal lattice. A fourth local minima is also present within each unit cell with a potential strength of $0.62V_0$. It is separated from the trimer by a barrier of height V_0, and as we shall observe has no particular significance for the low-energy states. The band-structure is plotted in Fig. 4.12 (c) for a lattice depth $V_0 = 2E_{\mathrm{R}}$. The lowest three bands form a composite group; two of the bands are degenerate at the K points and are reminiscent of the lowest bands of the hexagonal lattice, while the highest energy band is almost flat and is degenerate at the Γ point.

The three maximally localised generalised Wannier functions for the lowest bands of the Kagomé lattice are plotted in Fig. 4.13 for a lattice depth $V_0 = 2E_{\mathrm{R}}$. Since the

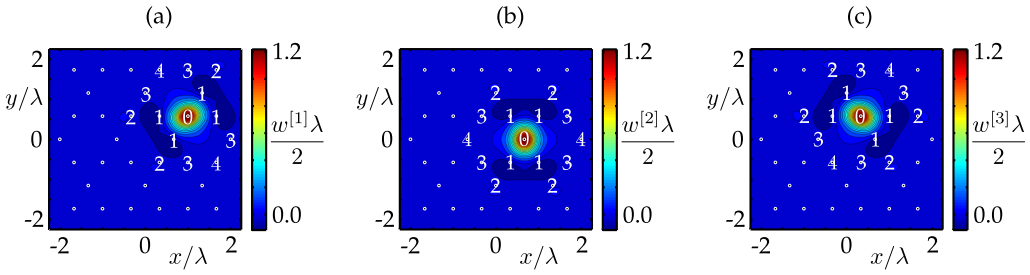


Figure 4.13. Contour plots of the maximally localised generalised Wannier functions for the lowest three bands of a Kagomé optical lattice with a lattice depth $V_0 = 2E_\mathrm{R}$. We have labelled the potential minima with equal hopping matrix elements from the 'home' minimum by $j = 0, 1, 2, 3, 4$.

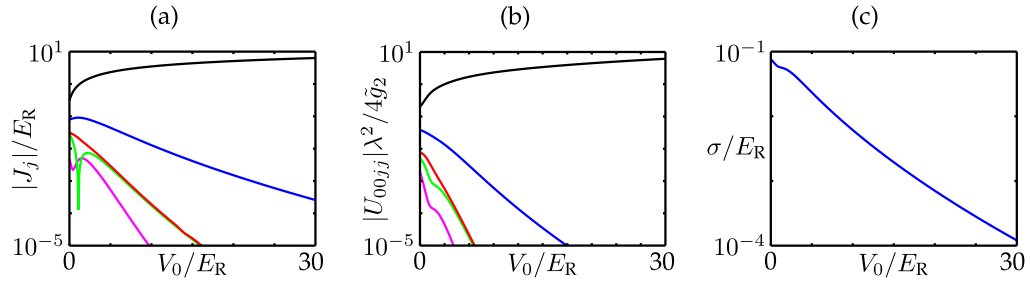


Figure 4.14. (a)(b) The magnitudes of the hopping and density-density interaction matrix elements respectively for a Kagomé optical lattice as a function of lattice depth V_0. The blue, red, green, and magenta lines are for matrix elements involving the 'home' minimum and minima $j = 1, 2, 3, 4$ respectively, while the black lines are for on-site terms ($j = 0$). The labelling of the minima is shown in Fig. 4.13. (c) The total standard deviation between the exact lowest bands and the interpolated tight-binding bands as a function of lattice depth.

potential minima are located at Wyckoff positions the generalised Wannier functions possess inversion symmetry and therefore $\Omega_\mathrm{D} = 0$ for the composite group. Each function is only two-fold symmetric under rotation in accordance with the point-symmetry of the Wyckoff position it is centred on. The functions are images of each other through a rotation of 120° about the centre of a trimer. Because of this the magnitudes of the matrix elements between equivalent neighbouring potential minima are equal, as was observed with the hexagonal lattice; we once again use the same labelling system, as shown in Fig. 4.13.

The magnitudes of the hopping and density-density interaction matrix elements are plotted in Fig. 4.14 as a function of lattice depth. The scenario is similar to the case of a hexagonal lattice; the 'on-minimum' density-density interaction matrix elements dominate while the matrix elements corresponding to hopping between adjacent minima decay almost exponentially. The nearest-neighbour density-density interaction matrix elements are at least an order of magnitude smaller than the on-minimum elements except at very low lattice depths, which we do not consider because of the narrow band gap to higher bands. This leads us to the following Hamiltonian for the Kagomé lattice,

$$\begin{aligned}\hat{H} = \sum_{i,j} \Bigg[& \sum_m J_0 \hat{n}_{i,j}^{[m]} + J_1 \hat{b}_{i,j}^{[1]\dagger} \left(\hat{b}_{i,j}^{[2]} + \hat{b}_{i,j-1}^{[2]} + \hat{b}_{i,j-1}^{[3]} + \hat{b}_{i+1,j-1}^{[3]} \right) \\ & + J_1 \hat{b}_{i,j}^{[2]\dagger} \left(\hat{b}_{i,j}^{[1]} + \hat{b}_{i,j+1}^{[1]} + \hat{b}_{i,j}^{[3]} + \hat{b}_{i+1,j-1}^{[3]} \right) \\ & + J_1 \hat{b}_{i,j}^{[3]\dagger} \left(\hat{b}_{i,j+1}^{[1]} + \hat{b}_{i-1,j+1}^{[1]} + \hat{b}_{i,j}^{[2]} + \hat{b}_{i-1,j+1}^{[2]} \right) \\ & + \sum_m \tfrac{1}{2} U_{0000} \hat{n}_{i,j}^{[m]} \left(\hat{n}_{i,j}^{[m]} - 1 \right) \Bigg]. \end{aligned} \tag{4.17}$$

Due to symmetry the modes are equivalent and therefore this Hamiltonian also reduces to the form given in Eq. 4.15, where the sum is taken over potential minima. We have once more calculated the single-particle band-structure of this system according to a tight-binding model using the included hopping matrix elements. The standard deviation between the interpolated bands and the exact bands, shown in Fig. 4.14 (c), decreases exponentially with lattice depth and is significantly smaller than the exact band-width, indicating good accuracy.

Chapter 5

The Bose-Hubbard model

In the previous chapters we discussed the physics of a gas of atoms trapped in an optical lattice potential. We began with the atom-light interaction, then examined the single-particle physics, and ultimately derived an effective description of the system in terms of the Bose-Hubbard model. Importantly, we have shown how to calculate the Bose-Hubbard parameters in terms of the lattice properties, and have presented results for a variety of interesting geometries. To complete this discussion we now briefly examine the physics of the Bose-Hubbard model itself, and consider the well-known phase diagram for the geometries studied in chapter 4.

The Bose-Hubbard Hamiltonian for a system with identical nearest-neighbours is given by [25]

$$\hat{H} = J \sum_{\langle i,j \rangle} \hat{b}_i^\dagger \hat{b}_j + \tfrac{1}{2} U \sum_i \hat{n}_i(\hat{n}_i - 1). \tag{5.1}$$

Here we have dropped the term $J_0 \sum_i \hat{n}_i$ since it gives a constant contribution for each site, and have removed the subscripts from the hopping and interaction parameters. The Hamiltonian is invariant under the transformation $\hat{b}_j \to \hat{b}_j e^{i\phi}$ and therefore possesses $U(1)$ symmetry. Consequently, it also commutes with the operator $\hat{N} = \sum_j \hat{n}_j$ and thus the total number of bosons is a conserved quantity. The Hamiltonian is composed of a kinetic energy term describing the hopping of

bosons between nearest-neighbour sites with amplitude J, and a repulsive on-site interaction with amplitude U, which makes it energetically unfavourable for any site to have multiple occupancies. Competition between the two terms results in a quantum phase transition between two parameter regimes: for $U \ll J$ the system has a gapless spectrum and is in a superfluid state characterised by on-site number density fluctuations; for $U \gg J$ the spectrum is gapped, the system is incompressible,[1] and on-site density fluctuations are suppressed. In the latter case the state is called a Mott insulator.

5.1 Decoupled mean-field theory

The Bose-Hubbard model is not exactly solvable in finite dimensions with any currently known analytical technique, except in the limits $J = 0$ and $U = 0$ [84, 85, 86]. However, considerable insight into the system can be gained by introducing a mean-field approximation that decouples the kinetic energy terms of the Hamiltonian as [87, 88]

$$\hat{b}_i^\dagger \hat{b}_j = \langle \hat{b}_i^\dagger \rangle \hat{b}_j + \hat{b}_i^\dagger \langle \hat{b}_j \rangle - \langle \hat{b}_i^\dagger \rangle \langle \hat{b}_j \rangle = \Phi \hat{b}_i^\dagger + \Phi^* \hat{b}_j - |\Phi|^2. \tag{5.2}$$

Here $\langle \cdot \rangle$ indicates the average over the ground state at temperature $T = 0$, and we have introduced an order parameter $\Phi = \langle \hat{b}_j \rangle$, which we assume to be non-zero and homogeneous. The order parameter acts as a mean-field describing the influence of hopping in the system between nearest-neighbours. Our assumption that it is non-zero implies that states with indefinite total particle number will exist, and therefore the $U(1)$ symmetry of the original Bose-Hubbard Hamiltonian will be broken. The

[1] The definition of compressibility used here arises from the term 'electron compressibility', used to describe the metallic-insulator transition in solid-state systems.

approximation results in an effective Hamiltonian $\hat{H}_{\mathrm{MF}} = \sum_j \hat{h}_{\mathrm{MF}}$, where

$$\hat{h}_{\mathrm{MF}} = -zJ(\Phi\hat{b}^\dagger + \Phi^*\hat{b}) + zJ|\Phi|^2 + \tfrac{1}{2}U\hat{n}(\hat{n}-1) \tag{5.3}$$

is the single-site Hamiltonian, identical across the entire lattice,[2] and z is the co-ordination number denoting the number of nearest-neighbours per site. Since the interaction terms are treated exactly the method is exact for $J = 0$. The ground state of $\hat{H}_{\mathrm{MF}}$ is a site-wise product of the ground state $|\psi_{\mathrm{MF}}(\Phi)\rangle$ of $\hat{h}_{\mathrm{MF}}$, which we determine in the grand-canonical ensemble by introducing an appropriate occupancy cut-off [87] and diagonalising $\hat{h}_{\mathrm{MF}} - \mu\hat{n}$ in the number basis, with μ representing the chemical potential. The value of Φ is determined self-consistently by minimising the single-site ground state energy $E_{\mathrm{MF}}(\Phi)$ with respect to Φ.

Before we consider the phase diagram obtained using the above described method we note that the ground state $|\psi_{\mathrm{MF}}\rangle$ of $\hat{H}_{\mathrm{MF}}$ is a Gutzwiller state of the form [89, 90, 91]

$$|\Psi_{\mathrm{GW}}\rangle = \prod_j \left(\sum_{n=0}^{\infty} c_n |n\rangle_j \right), \tag{5.4}$$

where c_n are the complex amplitudes of the on-site number states $|n\rangle$. An alternative method for determining the ground state would be to start with Eq. 5.4 as an ansatz (this is typically called the Gutzwiller ansatz), and minimise the energy of this state with respect to the set of variational parameters $\{c_n\}$ using the original Bose-Hubbard Hamiltonian,

$$\begin{aligned} E_{\mathrm{GW}}(\{c_n\}) &= \langle\Psi_{\mathrm{GW}}|\hat{H} - \mu\sum_j \hat{n}_j|\Psi_{\mathrm{GW}}\rangle \\ &= N^D \left\{ -zJ|\phi|^2 + \sum_n \left[\tfrac{1}{2}Un(n-1) - \mu n\right]|c_n|^2 \right\}. \end{aligned} \tag{5.5}$$

[2]For this reason we have dropped the subscript labelling the sites.

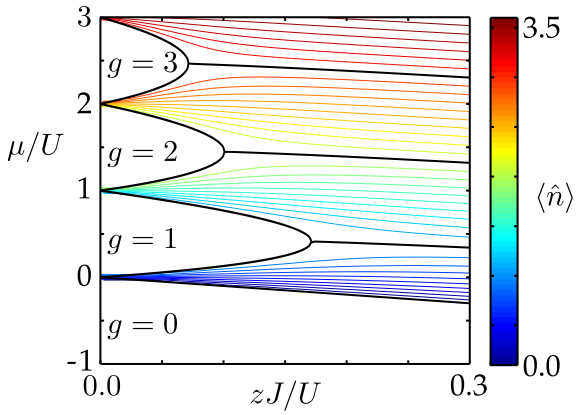


Figure 5.1. The mean-field phase diagram of the Bose-Hubbard model as calculated using decoupled mean-field theory. The Mott insulator phase is confined to lobes (the white regions), which are enumerated by the integer filling factor $\langle \hat{n}_i \rangle = g$. The black solid lines bounding the lobes are determined analytically in the text. In the superfluid phase the coloured lines are lines of constant fractional density, while the black solid lines extending from the tips of the lobes are lines of constant integer density.

The order parameter is now given by

$$\phi = \langle \Psi_{\mathrm{GW}} | \hat{b}_j | \Psi_{\mathrm{GW}} \rangle = \sum_n \sqrt{n} c^*_{n-1} c_n. \tag{5.6}$$

This minimisation can be carried out either analytically, see e.g. Ref. [89] or Ref. [90], or numerically as in Ref. [92]. However, since $|\psi_{\mathrm{MF}}\rangle$ is a Gutzwiller state one could instead use the decoupled mean-field Hamiltonian to calculate the ground state energy $\langle \Psi_{\mathrm{GW}} | \hat{H}_{\mathrm{MF}} - \mu \sum_j \hat{n}_j | \Psi_{\mathrm{GW}} \rangle$, and one finds that this is identical to the energy function in Eq. 5.5. This shows that the self-consistent diagonalisation of the decoupled mean-field Hamiltonian in the number basis is entirely equivalent to the minimisation of the ground state energy of the Bose-Hubbard Hamiltonian within the Gutzwiller ansatz [87].

The mean-field phase diagram for the Bose-Hubbard model as calculated using decoupled mean-field theory is shown in Fig. 5.1. The theory correctly predicts a

quantum phase transition between a superfluid and a Mott insulator state, where the critical point $(zJ/U)_{\mathrm{c}}$ is defined by an abrupt change in the order parameter from exactly zero in the Mott phase to a non-zero value in the superfluid phase. As noted, for $J = 0$ the mean-field approximation is exact (or more accurately, nullified) and the ground state is given by a site-wise product of Fock states, i.e.

$$|\mathrm{GS}\rangle = |g, g, \cdots, g\rangle, \tag{5.7}$$

where g is an integer function of μ/U,

$$g(\mu/U) = \begin{cases} 0 \quad \text{for} \quad \mu/U < 0, \\ 1 \quad \text{for} \quad 0 < \mu/U < 1, \\ 2 \quad \text{for} \quad 1 < \mu/U < 2, \\ \quad \vdots \\ g \quad \text{for} \quad g - 1 < \mu/U < g. \end{cases} \tag{5.8}$$

The exception occurs when μ/U is a positive integer, where there is a discontinuous jump in the on-site number density. Here the ground state is degenerate and therefore the system is gapless, which is highlighted in the phase diagram by the superfluid phase extending down to $zJ/U = 0$ for $\mu/U \in \mathbb{Z}^+$. Outside of these points, for $J = 0$, the density does not change with variations in the chemical potential, i.e.

$$\frac{\partial \langle \hat{N} \rangle}{\partial \mu} = 0, \tag{5.9}$$

implying that the state is incompressible. For non-integer μ/U the Mott phase, characterised by the incompressibility property,[3] is shown to persist out to non-zero

[3]Within the Gutzwiller ansatz the only possible states possessing a definite total particle are those that are a site-wise product of Fock states. Therefore, to maintain continuity with the $J = 0$ limit the decoupled mean-field theory predicts that the entire Mott phase is described by a site-wise product of Fock states, corresponding to vanishing on-site number density fluctuations. This is in

zJ/U and is confined to regions known as 'lobes' enumerated by the integer filling factor $\langle \hat{n}_i \rangle = g$ [25]. Outside of the lobes, in the superfluid phase, the density can take a fractional value as highlighted by the density contours.

An expression for the phase boundary depicted in Fig. 5.1 can be determined within the mean-field theory by using perturbation theory. The order parameter Φ is taken to be real (without loss of generality) and the mean-field hopping terms are treated as the perturbation,

$$\hat{H}_{\mathrm{MF}} - \mu\hat{n} = \hat{H}^{(0)} + \Phi\hat{H}_{\mathrm{pert}}, \tag{5.10}$$

where

$$\hat{H}^{(0)} = zJ\Phi^2 + \tfrac{1}{2}U\hat{n}(\hat{n}-1) - \mu\hat{n}, \tag{5.11}$$

$$\hat{H}_{\mathrm{pert}} = -zJ(\hat{b}^\dagger + \hat{b}). \tag{5.12}$$

Since $\hat{H}^{(0)}$ is diagonal in the number basis the zeroth order eigenstates are Fock states $|n\rangle$ with energy $E_n^{(0)} = \frac{1}{2}Un(n-1) - \mu n$. Meanwhile, the perturbation is off-diagonal in the number basis, therefore the first order correction to the ground state energy is zero. The second order correction to the energy is given by [88]

$$E_{\mathrm{GS}}^{(2)} = \frac{zJg}{U(g-1)-\mu} + \frac{zJ(g+1)}{\mu - Ug}, \tag{5.13}$$

leading to an expansion of the ground state energy in Φ of the form

$$E_{\mathrm{GS}} = a_0(g,U,\mu) + a_2(g,U,\mu)\Phi^2 + O(\Phi^4). \tag{5.14}$$

fact a failing of the mean-field theory; on-site number density fluctuations are non-zero to second order in the Mott phase [59], which is characterised by its incompressibility property and not the emergence of a site-wise product of Fock states [24].

By following the Landau procedure for second order phase transitions and minimising this function with respect to Φ one finds that $\Phi = 0$ when $a_2(g, U, \mu) > 0$ and $\Phi \neq 0$ when $a_2(g, U, \mu) < 0$. Therefore $a_2(g, U, \mu) = 0$ signifies the boundary between the superfluid and Mott phases. Solving this equality leads to the following expression for the boundary [88],

$$(\mu/U)_{\pm} = \tfrac{1}{2}\left[2g - 1 - (zJ/U) \pm \sqrt{1 - 2(2g+1)(zJ/U) + (zJ/U)^2}\right], \qquad (5.15)$$

where $\pm$ denotes the monotonic upper and lower branches confining the Mott phase. The boundary is shown in Fig. 5.1 by the black solid line. Equating the expressions for the individual branches determines the position of the tip of each lobe as

$$(J/U)_{\mathrm{c}} = \frac{1}{z(2g + 1 + 2\sqrt{g(g+1)}}. \qquad (5.16)$$

Fig. 5.1 shows that the positions of the tips are located at the intersections of the phase boundary with the lines of constant integer density extending into the superfluid phase. This fact reveals that there are two types of phase transition occurring within the Bose-Hubbard model: across the upper and lower branches of the boundary the density changes continuously to a fractional value above and below g respectively, while at the tip the transition occurs at constant integer density. In the Mott phase the lowest energy excited states, which are N^D-fold degenerate, are those with one more or one less particle, and therefore referred to as containing particle and hole excitations respectively [25]. Away from the tip the phase transition occurs because the state with one particle excitation (upper branch) or the state with one hole excitation (lower branch) becomes degenerate with the ground state. The kinetic energy gained by the addition of a particle or hole excitation balances the on-site interaction and potential energies resulting in the on-set of superfluidity.

In contrast, at the lobe tip the transition from a Mott insulator to a superfluid is caused solely by the increase in kinetic energy due to the increase in the relative strength of the hopping parameter J. As a result, at the tip the transition belongs to the universality class of the $(D+1)$-dimensional XY model, whereas elsewhere it does not [25].

5.2 Mean-field phase diagram for 2D geometries

The phase diagram of the Bose-Hubbard model is customarily presented as a function of the generic variable zJ/U, which allows it to represent a large range of geometries and dimensions. The dependence on the coordination number z implies that the phase boundary depends significantly on both geometry and dimension, with the height of the lobes in terms of J/U decreasing with increasing z. In chapter 4 we presented results detailing the Bose-Hubbard parameters for a variety of optical lattice geometries, and with the exception of the rhombic lattice showed that each system's Hamiltonian is of the form given in Eq. 5.1, and therefore represented by the mean-field diagram shown in Fig. 5.1. Using our results for J and U one could easily recalculate the phase diagram for each geometry to be displayed as a function of the lattice depth V_0. This would allow, e.g. the lobe tips to be calculated directly in terms of the laser parameters.

As an example we consider the rhombic optical lattice, whose Hamiltonian within the decoupled mean-field theory is also of the form $\hat{H}_{\mathrm{MF}} = \sum_j \hat{h}_{\mathrm{MF}}$ but with

$$\hat{h}_{\mathrm{MF}}(V_0, \chi) = -(zJ)_{\mathrm{eff}}(\Phi\hat{b}^\dagger + \Phi^*\hat{b}) + (zJ)_{\mathrm{eff}}|\Phi|^2 + \tfrac{1}{2}U\hat{n}(\hat{n}-1), \tag{5.17}$$

where $(zJ)_{\mathrm{eff}} = 2[2J_1(V_0,\chi) + J_2(V_0,\chi)]$ is the effective mean-field strength experienced at each site. We remind the reader that one can form the rhombic optical

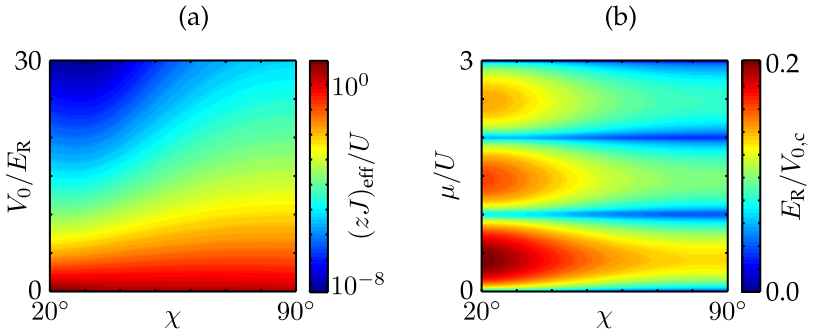


Figure 5.2. (a) A contour diagram showing the value of the mean-field variable $(zJ)_{\text{eff}}/U$ (see text) as a function of lattice depth V_0 and angle χ for a rhombic optical lattice. (b) A contour diagram showing the reciprocal value of the lattice depth at which criticality occurs in a rhombic optical lattice within the decoupled mean-field theory.

lattice potential using two independent pairs of counter-propagating laser beams, with the rhombic angle χ determined by the angle between the beams. Thus J_1, J_2 and U are all functions of χ in addition to the lattice depth V_0. The value of $(zJ)_{\text{eff}}/U$ calculated using our previous results is shown in Fig. 5.2 (a) as a function of V_0 and χ. As χ is reduced from ninety degrees (a square lattice) there is a general increase in the decay rate of $(zJ)_{\text{eff}}/U$ with lattice depth V_0. This is due primarily to the decrease in the hopping parameter J_1 along the lattice axes resulting from an increasing lattice parameter, even though diagonal hopping increases resulting in a larger effective coordination number (see Fig. 4.5 (a)). As χ approaches twenty degrees the decay rate of $(zJ)_{\text{eff}}/U$ with lattice depth decreases slightly because of a decrease in U at any given V_0 (see Fig. 4.5 (b)), while J_2 is almost constant and J_1 is insignificant. The reciprocal value of the lattice depth V_0^{-1} at which criticality occurs within this model is shown in Fig. 5.2 (b) as a function of χ. The lobe structure of the generic mean-field phase diagram of course remains, but now the height of the Mott insulator lobes in terms of V_0^{-1} is shown to increase with decreasing χ. Here the increase in the decay rate of the effective on-site mean-field strength $(zJ)_{\text{eff}}$ caused by the increasing lattice parameter stabilises the Mott insulator phase at

shallower lattice depths, which corresponds to the Mott insulator lobes extending out to higher values of V_0^{-1}. This result implies that the transition from a Mott insulator to a superfluid could be achieved in a rhombic optical lattice at constant lattice depth by adiabatically increasing the rhombic angle χ.

5.3 Validity of the decoupled mean-field theory

In this chapter we have studied the salient properties of the Bose-Hubbard model using decoupled mean-field theory. We shall now briefly address the validity of this approach and give an overview of results found using more accurate methods. Firstly, we recall the Ginzburg criterion, which states that mean-field calculations will be accurate if fluctuations in the order parameter are significantly less than than its value in the vicinity of a critical point [93]. It is well known that in all systems as the dimensionality increases mean-field results become more accurate, which can be interpreted by considering the fact that as more degrees of freedom are introduced into the interaction the relevant observables will fluctuate less about their mean value. The Bose-Hubbard model is no exception; in table 5.1 we compare the value of J/U at tip of the first Mott insulator lobe as calculated using decoupled mean-field theory to results reported using more precise methods. We see that the accuracy of the mean-field value for a 1D Bose-Hubbard system is unsatisfactory, but improves as the dimensionality is increased. In three dimensions the value of $(J/U)_{\mathrm{c}} = 0.0341$ was reported in Ref. [94] to an accuracy of 0.1% using quantum Monte Carlo calculations. The result of $(J/U)_{\mathrm{c}} = 0.062$ in two-dimensions was earlier found also using quantum Monte Carlo calculations [95], while in one-dimension the value of $(J/U)_{\mathrm{c}} = 0.297$ was reported using Density Matrix Renormalisation Group calculations [96]. Previous studies in three dimensions have also used perturbative expansions to improve upon the mean-field results [97]. We note that the

D	z	$(J/U)_{\mathrm{MF}}$	$(J/U)_{\mathrm{c}}$	Error
1	2	0.0862	0.297	70.3%
2	4	0.0431	0.062	29.3%
3	6	0.0287	0.034	15.6%

Table 5.1. A comparison of the critical point at the tip of the first Mott insulator lobe as calculated by decoupled mean-field theory $(J/U)_{\mathrm{MF}}$ and by more precise methods $(J/U)_{\mathrm{c}}$ (see text). The three systems compared, labelled by their dimensionality D, are a simple 1D optical lattice, a 2D square lattice, and a 3D cubic lattice.

mean-field theory for the Bose-Hubbard model has been shown to be exact in the limit of infinite dimensions [25], and in finite dimensions in the limits $J/U = 0$ and $U/J = 0$.

While the mean-field theory does capture the qualitative structure of the Bose-Hubbard phase diagram, there are some failures. Firstly, the theory fails to account for non-trivial correlation functions between different sites [91]. For example, employing the Gutzwiller ansatz for the ground state implies that the one-particle density matrix is independent of the distance between sites, whereas in reality the correlations would become long-ranged at the phase transition. Secondly, table 5.1 shows that the mean-field critical point occurs at a lower value of J/U than expected. Quantum fluctuations, which are more significant in lower dimensions, cause the transition from the superfluid phase to the Mott insulator phase at higher values of the kinetic energy than accounted for in the mean-field theory. Thirdly, more accurate methods have shown that the lobes, in addition to having a greater extension into J/U, are much narrower towards the tip. In addition, the lower branch of each lobe is not monotonic, but instead curves downwards towards the tip resulting in a 're-entrance' phenomenon [98, 96, 99]. As J/U is increased at constant μ/U from a low value in the Mott insulator phase the usual transition to a superfluid occurs when the lower branch is crossed, with the density decreasing from its initial integer value. However, as J/U is then increased further it is possible to

once again cross the lower branch where it curves downwards and transition back to the Mott insulator phase. The outcome, rather counter-intuitively, is that the Mott insulator state can be re-established at certain values of the chemical potential μ by increasing the kinetic energy.

Our observations have shown that while the mean-field theory gives a qualitative picture of the Bose-Hubbard model, its quantitative accuracy is in general unsatisfactory, particularly in one- and two-dimensions. In this chapter we used the mean-field theory as an example to show how our methods discussed in the previous chapters can be used to obtain the Bose-Hubbard properties directly in terms of the optical lattice parameters. While using mean-field theory to generate quantitative data in this way is not necessarily useful, the same process can of course be used for more precise methods such as those referred to in this section.

Chapter 6

Simulating quantum spin Hamiltonians with optical lattices

In chapters 7 and 8 we investigate the properties and dynamics of two quantum spin systems with long-range interactions. In this short chapter we motivate these studies in the context of optical lattices, which can be employed as quantum simulators of various models found in solid state physics. We outline a particular method for engineering spin Hamiltonians with optical lattices, which exploits dipole selection rules to create state-dependent potentials for multi-component atoms.[1] We then go on to describe an extended Bose-Hubbard model that could be realised using an ultra-cold dipolar gas in an optical lattice. The dipole-dipole interaction, which decays as r^{-3}, introduces a long-range term into the standard Bose-Hubbard model discussed in chapter 5. This can lead to novel quantum phases in these systems [44, 45, 46], and in combination with the other techniques described in this chapter could allow for the simulation of spin systems with long-range interactions.

[1] For an overview of other techniques for engineering spin Hamiltonians with optical lattices, see the review paper by Lewenstein *et al.* [1]

6.1 Engineering spin Hamiltonians

6.1.1 Direct mapping in the hard-core limit

Before discussing the use of state-dependent optical lattices for engineering spin Hamiltonians, we note that a straightforward method of realising the XX spin-1/2 Hamiltonian is to take the hard-core limit of the Bose-Hubbard model. Specifically, one starts with the Bose-Hubbard Hamiltonian for single-component bosons, including the term for the chemical potential so that the total particle number is not fixed (*cf.* Eq. 5.1),

$$\hat{H} = J \sum_{\langle i,j \rangle} \hat{b}_i^\dagger \hat{b}_j + \tfrac{1}{2} U \sum_i \hat{n}_i(\hat{n}_i - 1) - \mu \sum_i \hat{n}_i. \tag{6.1}$$

One then takes the limit $U \gg J, \mu$ so that there is at most one boson per lattice site, which causes the interaction term to disappear. The spin-1/2 states $|\uparrow\rangle_i$ and $|\downarrow\rangle_i$ may be encoded as the presence and absence of a boson at site i respectively, where the bosonic annihilation operators transform as $\hat{b}_i \rightarrow (\hat{\sigma}_i^x + i\hat{\sigma}_i^y)/2$. Here $\hat{\sigma}^\gamma$ ($\gamma = x, y, z$) are the Pauli operators. Through this mapping the Hamiltonian reduces to that of the XX model in a transverse field,

$$\hat{H} = \tfrac{1}{2} J \sum_{\langle i,j \rangle} \left(\hat{\sigma}_i^x \hat{\sigma}_j^x + \hat{\sigma}_i^y \hat{\sigma}_j^y \right) + \tfrac{1}{2} \mu \sum_i (1 - \hat{\sigma}_i^z). \tag{6.2}$$

6.1.2 State-dependent optical lattices

In this section we show how dipole selection rules can be exploited to create independent potentials that target different internal atomic states, and that can be used to engineer spin Hamiltonians. As an example, consider an atom with nuclear spin $I = \frac{3}{2}$, such as ^{23}Na or ^{87}Rb as commonly used in optical lattice experiments (see e.g. Ref. [14] or Ref. [62]), which is interacting with left (σ^-) and right (σ^+) circularly polarised laser beams. The fine structure for such an atom is shown in Fig. 6.1 (a),

in which we also depict the electric dipole transitions from the $S_{1/2}$ level induced by the circularly polarised light. The σ^+ polarised beam couples the $S_{1/2}$ level with $m_j = -\frac{1}{2}$ to both the $P_{1/2}$ level and $P_{3/2}$ level, but couples the $S_{1/2}$ level with $m_j = \frac{1}{2}$ to the $P_{3/2}$ level only. In the former case there are two contributions to the AC Stark shift acquired by the atom. If the laser frequency satisfies $\omega_1 < \omega < \omega_2$, where ω_1 and ω_2 are the resonant frequencies for the transitions from the $S_{1/2}$ level to the $P_{1/2}$ and $P_{3/2}$ levels respectively, the two contributions will have opposite detunings and can cancel exactly at a frequency $\omega = \omega_c$ [17] as shown in Fig. 6.1 (b). Meanwhile, the $S_{1/2}$ level with $m_j = \frac{1}{2}$ receives only a single contribution to its AC Stark shift, which is therefore finite at $\omega = \omega_c$. Similarly, for the σ^- polarised beam the net AC Stark shift of the $S_{1/2}$ level with $m_j = \frac{1}{2}$ is zero at $\omega = \omega_c$, while that of the $S_{1/2}$ level with $m_j = -\frac{1}{2}$ is finite. Therefore, at $\omega = \omega_c$ the AC Stark shifts of the $S_{1/2}$ level with $m_j = \pm\frac{1}{2}$ are purely due to the $\sigma^\pm$ polarised beams resulting in separate potentials $V_\pm(\mathbf{r})$. The potentials $V_{F,m_f}(\mathbf{r})$ corresponding to the hyperfine levels of the $S_{1/2}$ manifold, which are also shown in Fig. 6.1 (a), are related to $V_\pm(\mathbf{r})$ by the Clebsch-Gordan coefficients as [17]

$$\begin{aligned} V_{2,2}(\mathbf{r}) &= V_+(\mathbf{r}), \quad \text{for} \quad |F=2, m_f=2\rangle, \\ V_{1,1}(\mathbf{r}) &= \tfrac{3}{4}V_+(\mathbf{r}) + \tfrac{1}{4}V_-(\mathbf{r}), \quad \text{for} \quad |F=1, m_f=1\rangle. \end{aligned} \tag{6.3}$$

Before showing how one can engineer spin Hamiltonians with this technique, we briefly discuss how two overlapping optical lattices potentials for the $|F=2, m_f=2\rangle$ and $|F=1, m_f=1\rangle$ hyperfine states can be shifted with respect to one another. Consider two linearly polarised counter-propagating laser beams with wave-vectors $\mathbf{k}_1 = (k, 0, 0)$ and $\mathbf{k}_2 = -(k, 0, 0)$ respectively and an angle 2θ between their corre-

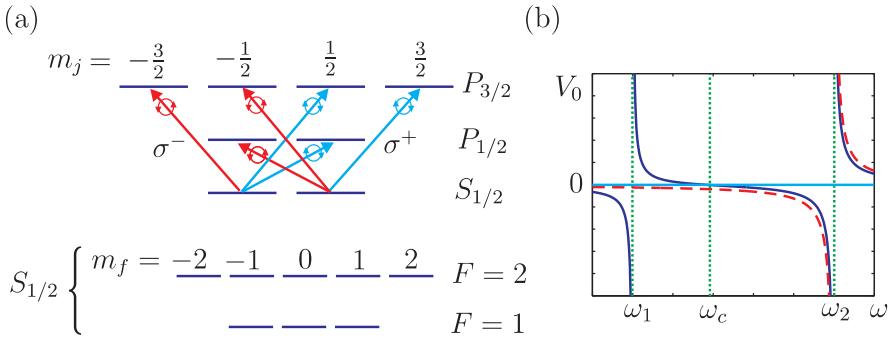


Figure 6.1. (a) The atomic fine (upper) and hyperfine (lower) structure of the $S_{1/2}$ manifold for an alkali atom with nuclear spin $I = \frac{3}{2}$. The blue and red arrows indicate electric dipole transitions from the $S_{1/2}$ level induced by left (σ^-) and right (σ^+) circularly polarised light respectively. (b) A schematic of the AC Stark shift of the $S_{1/2}$ level with $m_j = -\frac{1}{2}$ (solid lines) and $m_j = \frac{1}{2}$ (dashed lines) as a function of the frequency ω of the σ^+ polarised light. Here ω_1 and ω_2 are the resonant frequencies for the transitions to the $P_{1/2}$ and $P_{3/2}$ levels respectively. For a laser frequency $\omega = \omega_c$ the net AC Stark shift of the $S_{1/2}$ level with $m_j = -\frac{1}{2}$ as a result of coupling to both $P_{1/2}$ and $P_{3/2}$ levels is zero. [Image courtesy of Stephen Clark]

sponding electric fields,

$$\begin{aligned}\mathbf{E}_1(\mathbf{r},t) &= E_0[\mathbf{e}_y\cos\theta + \mathbf{e}_z\sin\theta]e^{i(\omega t+\mathbf{k}_1\cdot\mathbf{r})},\\ \mathbf{E}_2(\mathbf{r},t) &= E_0[\mathbf{e}_y\cos\theta - \mathbf{e}_z\sin\theta]e^{i(\omega t+\mathbf{k}_2\cdot\mathbf{r})}.\end{aligned} \tag{6.4}$$

Here E_0 is the amplitude of each beam and $\{\mathbf{e}_x, \mathbf{e}_y, \mathbf{e}_z\}$ are the standard Cartesian unit vectors. The sum of the two electric fields $\mathbf{E}(\mathbf{r},t) = \mathbf{E}_1(\mathbf{r},t) + \mathbf{E}_2(\mathbf{r},t)$ can be expressed as a superposition of left and right circularly polarised standing waves [17],

$$\mathbf{E}(\mathbf{r},t) = E_0[\mathbf{e}_-\cos(\mathbf{k}\cdot\mathbf{r}-\theta) + \mathbf{e}_+\cos(\mathbf{k}\cdot\mathbf{r}+\theta)]e^{i\omega t}, \tag{6.5}$$

where $\mathbf{e}_\pm = \mathbf{e}_z \pm i\mathbf{e}_y$. The resulting optical lattice potentials are given by $V_\pm \propto \cos^2(kx \pm \theta)$. By varying the angle θ one can shift the nodes of the two potentials in opposite directions to one another. As previously shown, the two standing waves

can act as state-dependent potentials for the $|F = 2, m_f = 2\rangle$ and $|F = 1, m_f = 1\rangle$ hyperfine states at a frequency $\omega = \omega_c$, therefore atoms trapped in the optical lattice can be shifted according to their atomic state. When combined with collisional interactions of the atoms [62, 19] this technique can be used to implement two-qubit quantum gates and create entangled states between atoms [17].

We now return to engineering spin Hamiltonians with state-dependent optical lattices. As an example, consider using the state-dependent technique to trap two hyperfine states of a gas of bosonic atoms in an optical lattice, where the states are now denoted by $|a\rangle$ and $|b\rangle$, and the corresponding atoms by a and b. We assume a sufficiently low temperature such that the atoms are restricted to the lowest energy band of their respective potentials. The generalisation of the Bose-Hubbard Hamiltonian for the two-species optical lattice is then given by [100, 101]

$$\hat{H} = \sum_{\langle i,j \rangle} \left(J^a \hat{a}_i^\dagger \hat{a}_j + J^b \hat{b}_i^\dagger \hat{b}_j \right) + \sum_i \left[\tfrac{1}{2} U^a \hat{n}_i^a (\hat{n}_i^a - 1) + \tfrac{1}{2} U^b \hat{n}_i^b (\hat{n}_i^b - 1) + U^{ab} \hat{n}_i^a \hat{n}_i^b \right], \quad (6.6)$$

where $\hat{a}_i(\hat{b}_i)$ is the bosonic annihilation operator and $\hat{n}_i^a(\hat{n}_i^b)$ is the number density operator for an atom with hyperfine state $|a\rangle(|b\rangle)$ in site i. We see that in addition to the standard Bose-Hubbard Hamiltonians for each species the full Hamiltonian also contains a term corresponding to the on-site interaction between species.[2] The hopping matrix elements J^a and J^b can be calculated using the methods discussed in chapter 2 and will depend on the corresponding strengths of the potentials for each species. Therefore, state-dependent tunnelling can be controlled by the intensity of the laser beams [100, 101]. Similarly, the interaction matrix elements can be calculated from the generalised Wannier functions, which depend crucially on the lattice depth. As discussed in Sec. 2.2 the interaction matrix elements also depend

[2] We have dropped the on-site energy shifts since, although the two species will have different contributions, these can easily be compensated by applying a homogeneous external magnetic field.

on the scattering length, which is species dependent, and can be controlled using an external magnetic field sweeping through a Feshbach resonance [102]. In addition, the interaction matrix element U^{ab} can be varied by shifting the two state-dependent potentials by a fractional amount of the lattice spacing as discussed previously, which will vary the overlap of the Wannier functions between different species.

We now take the limit $U^a, U^b, U^{ab} \gg J^a, J^b$ so that multiple occupancies of any site are energetically suppressed, and consider the system as being commensurately filled, i.e. $\langle \hat{n}_i^a \rangle + \langle \hat{n}_i^b \rangle = 1$. The Hilbert space of the system is spanned by two-species Fock states $|(n_1^a, n_1^b), (n_1^a, n_2^b), \cdots, (n_M^a, n_M^b)\rangle$, where (n_i^a, n_i^b) are the occupancies of site i corresponding to the species a and b and subject to the constraint $\sum_i (n_i^a + n_i^b) = M$, and M is the total number of lattice sites. We consider two particular subspaces of the full Hilbert space: (i) the subspace S_s of size 2^M spanned by the occupancy pairs $(n_i^a, n_i^b) = \{(1,0),(0,1)\}\ \forall\ i$, which therefore excludes all double occupancies; (ii) the subspace S_e containing the remaining states not included in S_s. The states in subspace S_e are separated from those in S_s by a significant energy gap in the insulating limit, and therefore have negligible amplitude in the full state of the system at the low temperatures used in experiments. We can therefore employ a projection method [60] to obtain an effective Hamiltonian for the system in the subspace S_s, with the result [100, 101],

$$\hat{H}_\mathrm{s} = \sum_{\langle i,j \rangle} \left[\lambda^{zz} \hat{\sigma}_i^z \hat{\sigma}_j^z - \lambda^{xy} (\hat{\sigma}_i^x \hat{\sigma}_j^x + \hat{\sigma}_i^y \hat{\sigma}_j^y) \right] + \sum_i \lambda^z \hat{\sigma}_i^z, \tag{6.7}$$

This is exactly the Hamiltonian for the anisotropic Heisenberg (XXZ) spin-1/2 model in a transverse field. Here the spin states are encoded as $|\uparrow\rangle_i \equiv |a\rangle_i$ and $|\downarrow\rangle_i \equiv |b\rangle_i$, and the corresponding Pauli operators are given by $\hat{\sigma}_i^x = \hat{a}_i^\dagger \hat{b}_i + \hat{b}_i^\dagger \hat{a}_i$, $\hat{\sigma}_i^y = -i(\hat{a}_i^\dagger \hat{b}_i - \hat{b}_i^\dagger \hat{a}_i)$ and $\hat{\sigma}_i^z = \hat{a}_i^\dagger \hat{a}_i - \hat{b}_i^\dagger \hat{b}_i$, which act exclusively on the subspace S_s.

The couplings in Eq. 6.7 are given by [100, 101]

$$\begin{aligned}\lambda^{zz} &= \frac{(J^a)^2 + (J^b)^2}{2U^{ab}} - \frac{(J^a)^2}{U^a} - \frac{(J^b)^2}{U^b}, \\ \lambda^{xy} &= \frac{J^a J^b}{U^{ab}}, \\ \lambda^{z} &= 4\left[\frac{(J^a)^2}{U^a} - \frac{(J^b)^2}{U^b}\right].\end{aligned} \tag{6.8}$$

The system can reduce to further spin models by suitably engineering these couplings. For example, by choosing a lattice depth for species a that is significantly greater than that of species b the hopping parameter J^b will be negligible while J^a will remain finite. In this situation the Hamiltonian in Eq. 6.7 reduces to that of the Ising model,

$$\hat{H}_{\mathrm{s}} = \sum_{\langle i,j \rangle} \lambda^{zz} \hat{\sigma}_i^z \hat{\sigma}_j^z + \sum_i \lambda^z \hat{\sigma}_i^z, \tag{6.9}$$

where $\lambda^{zz} = (J^a)^2(1/2U^a b - 1/U^a)$ and $\lambda^z = 4(J^a)^2/U^a$.

Note that at no point have we made any assumptions about the geometry or dimensionality of the optical lattice potential for each species. The versatility in designing optical lattices, discussed chapter 4, can be exploited in combination with this technique to engineer spin Hamiltonians with a wide variety of geometries.

6.2 Dipolar gases in optical lattices

In recent years ultra-cold dipolar gases have garnered much attention thanks to the successful realisation a Bose-Einstein condensate of ^{52}Cr atoms [103, 104] and the remarkable progress in cooling and trapping dipolar molecules [105, 43]. In anticipation of experiments realising optical lattice systems loaded with dipolar gases, much has been done on the theoretical side, with studies showing that the addition of long-range interactions in optical lattices can lead to novel quantum phases and

the appearance of states with long-range order [43, 44, 46, 106]. In this section we outline the derivation of the extended Bose-Hubbard model that could be realised with dipolar gases in optical lattices, and show how the dipole-dipole interaction can allow for the simulation of spin systems with long-range interactions.

6.2.1 The dipole-dipole interaction

Before we consider the many-body Hamiltonian for an optical lattice system of dipolar atoms or molecules, we briefly discuss the dipole-dipole interaction itself. The interaction energy of two particles separated in space by the vector $\mathbf{r}$ and possessing dipole moments $\mathbf{d}_1$ and $\mathbf{d}_2$ respectively is given by

$$U_{\mathrm{d}}(\mathbf{r}) = \frac{C_{\mathrm{d}}}{4\pi} \frac{(\mathbf{d}_1 \cdot \mathbf{d}_2) r^2 - 3(\mathbf{d}_1 \cdot \mathbf{r})(\mathbf{d}_2 \cdot \mathbf{r})}{r^5}, \tag{6.10}$$

where $r = |\mathbf{r}|$. The dipolar coupling constant is $C_{\mathrm{d}} = \mu_0 \mu^2$ and $C_{\mathrm{d}} = d^2/\varepsilon_0$ for particles with a permanent magnetic dipole moment μ and permanent electric dipole moment d respectively, where μ_0 is the vacuum permeability and ε_0 is the vacuum permittivity. This interaction is long-range in nature, decaying at large distances as $U_{\mathrm{d}} \sim r^{-3}$, compared to the van der Waals interaction between two atoms which decays rapidly as r^{-6}. It is also anisotropic; for example, consider the dipole moments aligned in the same direction, in which case the interaction energy reduces to

$$U_{\mathrm{d}}(\mathbf{r}) = \frac{C_{\mathrm{d}}}{4\pi} \frac{1 - 3\cos^2\phi}{r^3}, \tag{6.11}$$

where ϕ is the angle between the dipole moment and the vector separating the dipoles. For $\phi = 0$ the interaction is attractive, while for $\phi = \pi/2$ it is repulsive. If the dipole moments are aligned in opposite directions then the opposite is true. Because of the long-range nature and anisotropy of the interaction energy, it cannot

be replaced by an effective pseudo-potential as is the case for s-wave scattering describing collisions between atoms, and it must be treated by explicitly using the expression in Eq. 6.10 [107].

6.2.2 The extended Bose-Hubbard model

The many-body Hamiltonian of a bosonic dipolar gas is as given in Eq. 2.17 with the addition of a new term representing the dipolar interaction,

$$\hat{H}_{\mathrm{d}} = \tfrac{1}{2} \iint d\mathbf{r}_1 d\mathbf{r}_2 \; \hat{\Psi}^\dagger(\mathbf{r}_1)\hat{\Psi}^\dagger(\mathbf{r}_2)U_{\mathrm{d}}(\mathbf{r}_1 - \mathbf{r}_2)\hat{\Psi}(\mathbf{r}_1)\hat{\Psi}(\mathbf{r}_2). \tag{6.12}$$

As we described in chapter 2, the bosonic field operators can be expanded in the Wannier basis, which here results in the following,

$$\hat{H}_{\mathrm{d}} = \tfrac{1}{2} \sum_{i,j,k,l} \sum_{m,n,p,s} V_{ijkl}^{[mnps]} \hat{b}_i^{[m]\dagger} \hat{b}_j^{[n]\dagger} \hat{b}_k^{[p]} \hat{b}_l^{[s]}, \tag{6.13}$$

where the matrix elements $V_{ijkl}^{[mnps]}$ are given by

$$V_{ijkl}^{[mnps]} = \iint d\mathbf{r}_1 d\mathbf{r}_2 \; w_i^{[m]*}(\mathbf{r}_1) w_j^{[n]*}(\mathbf{r}_2) U_{\mathrm{d}}(\mathbf{r}_1 - \mathbf{r}_2) w_k^{[p]}(\mathbf{r}_1) w_l^{[s]}(\mathbf{r}_2). \tag{6.14}$$

To understand the physics behind Eq. 6.14 we consider that for a deep optical lattice the spread of the Wannier functions Ω will be much smaller than the lattice spacing a, i.e. $\Omega \ll a$. In such cases, we can see from the results of chapters 3 and 4 that the only significant elements will be when $i = k$ and $j = l$. These can be divided into two categories: (i) the off-site matrix elements $V_{ijij}^{[mnps]}$ corresponding to $i = k \neq j = l$; (ii) the on-site matrix elements $V_{iiii}^{[mnps]}$ for which $i = j = k = l$. We discuss these in more detail below:

- Off-site matrix elements $V_{ijij}^{[mnps]}$ – Within the limit $\Omega \ll a$ the dipolar potential

varies slowly across the width of a Wannier function, therefore we may take it to be constant and replace it with $U_{\rm d}(\mathbf{r}_i - \mathbf{r}_j)$, where $\mathbf{r}_i$ is the position of site i. The integral in Eq. 6.14 then reduces to

$$V_{ijkl}^{[mnps]} \approx U_{\rm d}(\mathbf{r}_i - \mathbf{r}_j) \int d\mathbf{r}_1 \; w_i^{[m]*}(\mathbf{r}_1) w_i^{[p]}(\mathbf{r}_1) \int w_j^{[n]*}(\mathbf{r}_2) w_j^{[s]}(\mathbf{r}_2). \qquad (6.15)$$

For a single band only, e.g. for a cubic optical lattice at sufficiently low temperature such that only the lowest band is occupied, the corresponding term in Eq. 6.13 reduces to

$$\hat{H}_{\rm d}^{\text{off-site}} = \tfrac{1}{2} \sum_{i \neq j} V_{ij} \hat{n}_i \hat{n}_j, \qquad (6.16)$$

where $V_{ij} = U_{\rm d}(\mathbf{r}_i - \mathbf{r}_j)$. This describes an interaction between bosons at sites i and j with a strength proportional to the distance between the sites.

- On-site matrix elements $V_{iiii}^{[mnps]}$ – At the same lattice site $|\mathbf{r}_1 - \mathbf{r}_2|$ is of the order of Ω, and therefore the dipolar potential varies rapidly across the width of a Wannier function. We cannot take the approximation as above and must explicitly calculate the integral

$$V_{iiii}^{[mnps]} = \iint d\mathbf{r}_1 d\mathbf{r}_2 \; w_i^{[m]*}(\mathbf{r}_1) w_i^{[n]*}(\mathbf{r}_2) U_{\rm d}(\mathbf{r}_1 - \mathbf{r}_2) w_i^{[p]}(\mathbf{r}_1) w_i^{[s]}(\mathbf{r}_2). \qquad (6.17)$$

For a single band this becomes

$$V^{\text{on-site}} = \iint d\mathbf{r}_1 d\mathbf{r}_2 \; |w(\mathbf{r}_1)|^2 U_{\rm d}(\mathbf{r}_1 - \mathbf{r}_2) |w(\mathbf{r}_2)|^2, \qquad (6.18)$$

with the corresponding term

$$\hat{H}_{\rm d}^{\text{on-site}} = \tfrac{1}{2} V^{\text{on-site}} \sum_i \hat{n}_i (\hat{n}_i - 1). \qquad (6.19)$$

By adding the terms in Eq. 6.16 and Eq. 6.19 to the standard Bose-Hubbard model as derived in previous chapters we obtain an extended Bose-Hubbard model incorporating the effect of the dipole-dipole interaction between bosons,

$$\hat{H} = J \sum_{\langle i,j \rangle} \hat{b}_i^\dagger \hat{b}_j + \tfrac{1}{2}\tilde{U} \sum_i \hat{n}_i(\hat{n}_i - 1) + \tfrac{1}{2} \sum_{i \neq j} V_{ij} \hat{n}_i \hat{n}_j. \tag{6.20}$$

Here the effective on-site interaction $\tilde{U}$ contains a contribution from both the contact potential and the dipole-dipole interaction,

$$\tilde{U} = g \int d\mathbf{r} |w(\mathbf{r})|^4 + \iint d\mathbf{r}_1 d\mathbf{r}_2 \; |w(\mathbf{r}_1)|^2 U_{\mathrm{d}}(\mathbf{r}_1 - \mathbf{r}_2) |w(\mathbf{r}_2)|^2. \tag{6.21}$$

Importantly, Eq. 6.20 is the standard Bose-Hubbard model with the addition of a long-range term corresponding to an interaction between bosons at different sites, which has a strength depending on the distance r between sites as r^{-3}. This term could be exploited when engineering spin Hamiltonians to introduce long-range interactions. As a simple example, consider the hard-core boson limit for mapping the Bose-Hubbard model to an XX spin model as discussed in Sec. 6.1.1. The extended Bose-Hubbard Hamiltonian transforms as

$$\hat{H} = \tfrac{1}{2} J \sum_{\langle i,j \rangle} \left(\hat{\sigma}_i^x \hat{\sigma}_j^x + \hat{\sigma}_i^y \hat{\sigma}_j^y \right) + \tfrac{1}{2} \mu \sum_i (1 - \hat{\sigma}_i^z) + \tfrac{1}{8} \sum_{i \neq j} V_{ij} (1 - \sigma_i^z - \sigma_j^z + \sigma_i^z \sigma_j^z), \tag{6.22}$$

which now contains a long-range $\sigma^z \sigma^z$ interaction.

Chapter 7

Approaching the classical limit of a quantum phase transition with long-range interactions[1]

7.1 Introduction

The study of quantum critical phenomena has long revealed the acute sensitivity of whether particular phases of interacting many-body systems are stable to the nature of the fluctuations present. These fluctuations in turn are known to depend crucially on the dimensionality of the system, the range of the interactions, and the presence of symmetries [108]. One dimensional (1D) systems such as spin-1/2 chains with nearest-neighbour interactions typically exhibit strong zero-point quantum fluctuations that can prevent ordering at $T = 0$ causing the onset of a quantum phase transition. In the opposite regime of an infinitely coordinated interacting system, the Ginzburg criterion tells us that the fluctuations are diminished allowing the system to be accurately described using mean-field theory [93]. Of fundamental interest is exactly how a low-dimensional quantum system negotiates the transition

[1]The work presented in this chapter is to be included in a publication authored by Richard Walters, Javier Prior, Dieter Jaksch, and Stephen R. Clark, which is currently in preparation.

to this classical limit through variations in the magnitude of the fluctuations, e.g. as caused by an increasing coordination number.

In this paper we examine the approach of the ferromagnetic 1D spin-1/2 Ising chain at $T = 0$ to its classical limit by increasing the decay length of exponentially decaying interactions between the spins. While the Ising spin chain is perhaps one of the most well studied of systems, to our knowledge little work has been conducted in studying the influence of long-range interactions on the fluctuations. In Ref. [109] a mean-field analysis of the ferromagnetic quantum Ising and rotor models with power-law decaying interactions suggested that the critical properties have a non-trivial dependence on the interaction exponent when the interaction is long-range. The influence of power-law decaying interactions has also been studied in Refs. [110, 111, 112, 113], and more recently examined in the context of frustrated systems [114, 115]. We now complement these studies by using the infinite density matrix renormalisation group (iDMRG) method to calculate the shift in the critical point and critical exponent of the Ising chain from the exact values for the nearest-neighbour system to the expected mean-field values in the limit of infinite-ranged interactions.

Our motivation for considering exponentially decaying interactions is two-fold. Firstly, from a practical perspective, this form of interaction is extremely straightforward to handle using iDMRG, which importantly can approximate the thermodynamic limit and permits similar accuracies to the nearest-neighbour case. Secondly, commonly found screened interactions such as a Yukawa-type potential often possess an exponential component that dominates their long-range behaviour [116, 117, 118, 119]. With recent advances in cooling and trapping gases of dipolar molecules [103, 104, 120, 121, 122], in addition to proposals for realising tunable spin chains with dipolar interactions [123, 124], the physics of long-ranged interactions is becoming increasingly experimentally accessible. While our results will not be

quantitatively correct for systems possessing the power-law decaying dipole-dipole interaction, they do provide valuable insight contributing to this expanding field of study.

This paper is organised as follows. In Sec. 7.2 we introduce the model and the form of the exponentially decaying long-range interactions. We then consider a mean-field analysis of the system in Sec. 7.3 in addition to an analytic approach to obtain two approximate solutions for the position of the critical point, which turn out to bound our iDMRG result. In Sec. 7.4 we use real-space renormalisation to examine the critical properties, from which we conjecture an exponential-type function that accurately fits the iDMRG data. The numerical iDMRG results for the critical point and critical exponent are presented in Sec. 7.5, and conclusions are drawn in Sec. 7.6.

7.2 Model

We consider an infinite 1D spin-1/2 chain embedded in a transverse field g, which is described by the following Ising type Hamiltonian,

$$\hat{H}(\alpha) \;=\; -\sum_i \sum_{j>i} J_{ij} \hat{\sigma}_i^x \hat{\sigma}_j^x - g \sum_i \hat{\sigma}_i^z, \tag{7.1}$$

where $\hat{\sigma}^\gamma$ ($\gamma = x, y, z$) are the Pauli operators. Here the interaction strength J_{ij} is exponentially decaying as $J(r) = J\alpha^{r-1}$, where $0 \leq \alpha \leq 1$, $r = j - i$ is the separation, and J is the nearest-neighbour strength. The limits $\alpha = 0$ and $\alpha = 1$ correspond to the standard nearest-neighbour and infinite-ranged Ising models respectively. The nearest-neighbour model is analytically soluble [125] and exhibits a critical point at $g_c = J$ between a ferromagnetic phase ($g < g_c$) and a paramagnetic phase ($g > g_c$). The order parameter $\langle \hat{\sigma}^x \rangle$ in the ferromagnetic phase is known to decay in the

vicinity of g_c with a critical exponent of $\beta = 1/8$.

7.3 Bounding approximations

In this section we introduce the mean-field solution for the position of the critical point as a function of the interaction parameter α, before obtaining an approximate analytic solution by extending the exact method for solving the nearest-neighbour model. These solutions provide some intuition as to the expected behaviour of the critical point as the range of the interactions is increased, and in fact bound our iDMRG result from below and above (see Fig. 7.4 of Sec. 7.5). For this reason we refer to them as bounding approximations.

7.3.1 Mean-field theory

The standard mean-field approach comprises of replacing each spin operator by its corresponding component in a classical vector, i.e. $\hat{S}^\gamma = \hat{\sigma}^\gamma/2 \mapsto \vec{S}^\gamma$, where

$$\vec{S} = \frac{1}{2}\left[\sin(\theta)\cos(\phi), \sin(\theta)\sin(\phi), \cos(\theta)\right], \tag{7.2}$$

and (θ, ϕ) are the polar and azimuthal vector angles. This replacement is expected to be accurate in the limit $\alpha \to 1$ due to the large coordination number of the interactions of any single spin. Following the Ginzburg criterion [126] the larger the coordination number of the interactions the less single site quantities fluctuate about their mean value, therefore treating the effect of the surrounding spins as a mean-field becomes more justified. Assuming the ground state of the system is given by a uniform configuration (θ, ϕ), we are led to the following classical energy density

function per spin

$$E(\theta,\phi) = -\frac{J}{1-\alpha}\sin^2(\theta)\cos^2(\phi) - g\cos(\theta). \tag{7.3}$$

Upon minimizing it is found that $\phi = \{0,\pi\}$ and $\theta = \arccos[g(1-\alpha)/2J]$. The latter only has a real solution when $g \leq 2J/(1-\alpha)$ and so $g_\alpha = 2J/(1-\alpha)$ is the mean-field critical point. This is twice the known result of $g_c = J$ for $\alpha = 0$ and diverges as $\alpha \to 1$, where we expect the mean-field approximation to be accurate. Notice that g_α is identical to the coordination number of the interactions regardless of the dimension. Here we have an effective coordination number dependent on α that characterises the number of spins significantly interacting with any single spin on the chain.

7.3.2 Long-range fermionic model

We next consider an extension to the exact analysis of Pfeuty for the nearest-neighbour problem [125], which proceeds by employing the Jordan-Wigner transformation (JWT) [108] to map the Hilbert space of the Ising system to that of spinless fermions hopping between sites with single orbitals. The spin-1/2 operators transform as

$$\begin{aligned}\hat{\sigma}_i^x &= \prod_{j<i}(1-2\hat{c}_j^\dagger\hat{c}_j)(\hat{c}_i+\hat{c}_i^\dagger),\\ \hat{\sigma}_i^z &= 1-2\hat{c}_i^\dagger\hat{c}_i,\end{aligned} \tag{7.4}$$

where $\hat{c}_i$ is the fermionic annihilation operator for the ith site. The nearest-neighbour Ising Hamiltonian is quadratic in the fermionic operators,

$$\begin{aligned}\hat{H}(0) = &- J\sum_i (\hat{c}_{i+1}^\dagger \hat{c}_i + \hat{c}_i^\dagger \hat{c}_{i+1} + \hat{c}_i^\dagger \hat{c}_{i+1}^\dagger + \hat{c}_{i+1}\hat{c}_i) \\ &- g\sum_i (1 - 2\hat{c}_i^\dagger \hat{c}_i),\end{aligned} \tag{7.5}$$

and as is well-known can be diagonalised analytically by first using a Fourier transform to momentum space and then employing a Boguliobov transformation. However, with the introduction of long-range interactions this is no longer the case because the fermionic Hamiltonian is complicated by the presence of many-fermion Jordan Wigner string operators. Specifically, after applying the JWT to the Hamiltonian of Eq. (7.1) we obtain

$$\begin{aligned}\hat{H}(\alpha) = &-J\sum_i \sum_r \alpha^{r-1}(\hat{c}_i^\dagger - \hat{c}_i) \\ &\times \prod_{j=i+1}^{i+r-1} (1 - 2\hat{c}_j^\dagger \hat{c}_j)(\hat{c}_{i+r}^\dagger + \hat{c}_{i+r}) \\ &- g\sum_i (1 - 2\hat{c}_i^\dagger \hat{c}_i).\end{aligned} \tag{7.6}$$

Progress can be made with a crude approximation consisting of replacing the intervening terms $1 - 2\hat{c}_j^\dagger \hat{c}_j = \hat{\sigma}_i^z$ by unity [127], which is motivated somewhat by the fact that deep in the paramagnetic phase for $\alpha = 0$ we have $\langle \hat{\sigma}_i^z \rangle \approx 1$. This results in the following Hamiltonian that is again quadratic in its fermionic operators,

$$\begin{aligned}\hat{H}(\alpha) = &-J\sum_i \sum_r \alpha^{r-1}(\hat{c}_i^\dagger - \hat{c}_i)(\hat{c}_{i+r}^\dagger + \hat{c}_{i+r}) \\ &- g\sum_i (1 - 2\hat{c}_i^\dagger \hat{c}_i).\end{aligned} \tag{7.7}$$

The fermionic system described by this Hamiltonian can be solved exactly using the methods of Ref. [128]. The energy spectrum, derived in appendix 7.A, is given by

$$\varepsilon_k = 2J\left[\left(\frac{g}{J}\right)^2 + \frac{1}{1-\alpha^2} + 2\left(\frac{\alpha}{1-\alpha^2} - \frac{g}{J}\right)\frac{\cos k - \alpha}{1+\alpha^2-2\alpha\cos k}\right]^{\frac{1}{2}}, \tag{7.8}$$

where k is the quasi-momentum of the plane-wave normal modes. This function is non-negative and has a global minimum in the interval $[-\pi, \pi]$ for any positive g located at $k = 0$. The energy gap between the ground and first excited state is given by

$$\Delta = 2J\left|\frac{1}{1-\alpha} - \frac{g}{J}\right|. \tag{7.9}$$

The critical point, determined by a vanishing gap, is therefore predicted to depend on α as $g_\alpha = J/(1-\alpha)$ by this approximation. Remarkably, this approach has yielded a divergence at $\alpha = 1$ and the reciprocal of the critical point is exactly half the mean-field result.

7.4 Renormalisation group approach

In this section we use real-space renormalisation [129, 130] to examine the influence of decaying long-range interactions in the Ising chain. While the method produces a solution for the critical point that is in disagreement with the later iDMRG results (see Fig. 7.4 of Sec. 7.5), it does allow us to obtain a function in α that accurately fits the iDMRG data.

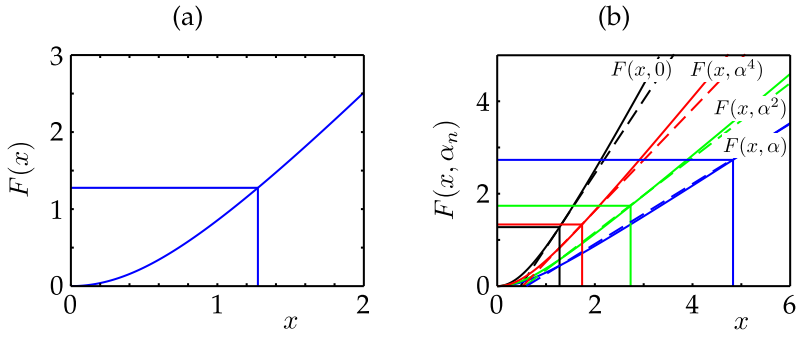


Figure 7.1. (a) The iteration function $F(x)$ for the $\alpha = 0$ RG scheme. The finite point x_c where $F(x) = x$ is highlighted by the horizontal and vertical lines. Notice that $F(x)$ becomes increasingly linear for $x > 1$. (b) The solid curves show the iteration functions $F(x, \alpha)$, $F(x, \alpha^2)$, $F(x, \alpha^4)$ and $F(x, 0)$ for $\alpha = 0.7$, which has a critical point $x_\alpha \sim 4.83$. If we follow the iterations over each function $F(x, \alpha^{2^n})$ in succession starting from x_α, we see that we rapidly converge on x_c. The dashed lines represent a linear approximation (discussed in the text) to each curve and can be seen to accurately reproduce the behaviour of each function in the region sampled by the iteration sequence.

7.4.1 Real-space renormalisation for $\alpha = 0$

The particular real-space renormalisation group scheme employed here is that of Drell *et al.* [131], which we extend to consider long-range interactions. The scheme involves spin-blocking pairs of lattice sites in each step and is included in appendix 7.B.1 for completeness. The following recursion relation for the rescaling of the ratio $x = g/J$ upon the nth iteration is obtained,

$$\begin{aligned} x_{n+1} &= \frac{2(\sqrt{1+4x_n^2}-1)(1+4x_n^2-2x_n\sqrt{1+4x_n^2})}{(1+\sqrt{1+4x_n^2}-2x_n)^2} \\ &= F(x_n). \end{aligned} \tag{7.10}$$

The behaviour of the renormalisation group (RG) is entirely contained within the iteration function $F(x)$ and how it behaves when it is compounded. Notice in Fig. 7.1 (a) that $F(x)$ is a monotonically increasing function, which at large x becomes linear with an asymptotic gradient of two. Fixed points of the iteration are limited

values that are obtained from the function $R(x) = F(\dots F(F(x)))$ composed of an infinite repeated application of $F(\cdot)$. Two trivial fixed points are clear: since $F(0) = 0$ and $F(\infty) = \infty$ we have $R(0) = 0$ and $R(\infty) = \infty$ respectively. From the shape of $F(x)$ there exists one finite fixed point x_c where $F(x) = x$ so that $R(x) = x$. Since $F(x)$ is a monotonically increasing function this point x_c separates values of $F(x)$ where $F(x) < x$ and $F(x) > x$. Thus any input $x < x_c$ will flow to $R(x) = 0$ while inputs $x > x_c$ will flow to $R(x) = \infty$. Only $x = x_c$ flows to the finite value $R = x_c$ and so this is an unstable fixed point. The trivial fixed points $R = 0$ and $R = \infty$ correspond to driving the Hamiltonian to the weak and strong transverse field limits respectively. The unstable fixed point $R(x) = x_c$ implies that here the Hamiltonian remains unchanged under successive RG transformations (up to an overall scale factor), i.e. it is scale-invariant. This point is of course the critical point of the model as predicted by the scheme and is found by solving $F(x)$ numerically, giving a solution $x_c = 1.277$ (to 4 s.f.). This is in disagreement with the known value of $x_c = g_c/J = 1$ and shows the inaccuracy of the RG scheme. However, we shall see in later sections that, when extended to include the $\alpha > 0$ case, the RG approach results in a solution whose functional form gives a very good description of the numerical iDMRG critical point.

7.4.2 Real-space renormalisation for $\alpha \geq 0$

We show in appendix 7.B.2 that when the RG scheme is applied to the full model including exponentially decaying long-range interactions the recursion relation is modified to

$$x_{n+1} = \frac{2(\sqrt{1+4x_n^2}-1)(1+4x_n^2-2x_n\sqrt{1+4x_n^2})}{(1+\alpha_n)^2(1+\sqrt{1+4x_n^2}-2x_n)^2}, \tag{7.11}$$

where $\alpha_n = \alpha^{2^n}$. Note that when $\alpha = 1$ the iteration function $F(x) \to F(x)/4$, which results in $F(x) < x$ for all finite x. There is no finite point where $F(x) = x$, therefore

$R(x) = 0$ for all x, i.e. all finite transverse field inputs flow to the ferromagnetic fixed point. This agrees with our intuition that an infinite coordination number for the interaction stabilises the ferromagnetic phase against any finite transverse field g, corresponding to a diverging critical point.

The iteration function is iteration dependent for $0 < \alpha < 1$ through the α_n appearing in the denominator. We denote this function by $F(x, \alpha) = F(x)/(1+\alpha)^2$ and obtain a new composite function

$$R_\alpha(x) = F(\cdots F(F(F(x, \alpha), \alpha^2), \alpha^4, \cdots, 0), \tag{7.12}$$

in which we have embedded the successive squaring of the α for each iteration. Since $\alpha < 1$ this implies that the iterations exponentially converge to the $\alpha = 0$ function $F(x)$. To determine the finite fixed point of this function we consider that after some large but finite number of iterations M we have $\alpha_{M+1} = 0$, and so for the remaining number of iterations the function $F(x)$ is used. Since the finite fixed point of the final infinite composition of $F(x)$ is simply x_c, the finite fixed point x_α of $R_\alpha(x)$ is given by

$$F(\cdots F(F(F(x_\alpha, \alpha), \alpha^2), \alpha^4, \cdots, \alpha^{2^M}) = x_c. \tag{7.13}$$

Thus $R_\alpha(x_\alpha) = x_c$ and is finite, while $R_\alpha(x < x_\alpha) = 0$ and $R_\alpha(x > x_\alpha) = \infty$. The exact solution for x_α is in principle obtained by solving $R_\alpha(x) = x_c$ for infinite M. However, this is unlikely to yield an analytical solution since the composite function will be an extremely complicated function of x, and even solving $F(x) = x$ was not possible analytically.

In Fig. 7.2 we have plotted numerical results for the position of the critical point x_α, which we determined by evaluating the flow of many inputs x across the expected position using $M = 1000$ RG iterations. The results show that the critical point moves smoothly from x_c at $\alpha = 0$ to a diverging value at $\alpha = 1$. To obtain

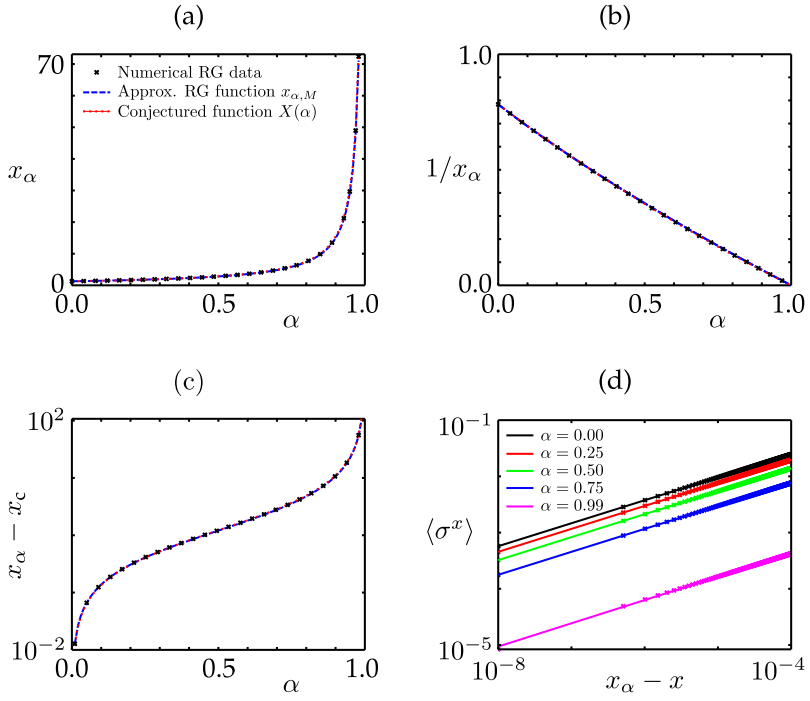


Figure 7.2. (a) shows the critical point x_α as calculated numerically by the RG method (crosses). The blue dashed line is the function $x_{\alpha,M}$ with $M = 1000$, while the red dotted line is the conjectured function $X(\alpha)$. (b) is the same plot but for the inverse of x_α, while (c) shows $x_\alpha - x_c$ with a logarithmic y-axis. Notice that in plot (b) the functions do not intersect the y-axis at unity because the RG calculation does not reproduce the correct $\alpha = 0$ critical point. The purpose of this variety of plots is to show the quality of the fit over inverse and logarithmic scales by the approximate RG solution and the conjectured function (given in the text) to the exact RG critical points. (d) The order parameter $\langle\sigma^x\rangle$ in the vicinity of the critical point (in the ferromagnetic phase) for a range of α as calculated numerically by the RG method (crosses). As expected $\langle\sigma^x\rangle$ obeys a power-law for all α (lines), however the exponent is found to be independent of α as $\beta \sim 0.409$.

some analytical understanding of this shifting critical point we exploit the fact that $F(x)$ is nearly linear for $x > 1$, and since the shift obeys $x_\alpha > x_c$ we remain in this regime. We replace the iteration function $F(x, \alpha)$ by the following linear function

$$f(x, \alpha) = \frac{x_c + d(\alpha)(x - x_c)}{(1 + \alpha)^2}, \tag{7.14}$$

since a linear function has the advantage of only ever generating other linear functions when compounded. Ideally the function $d(\alpha)$ gives the gradient of $F(x)$ at the sequence of inputs x_n that the finite fixed point traverses during the iterations. A suitable approximation is to choose $d(\alpha) = b + (c - b)\alpha$, where $b = 1.596$ (to 4 s.f.) is the gradient of $F(x)$ at $x = x_c$ and $c = 2$ is the asymptotic limit of the derivative of $F(x)$. In comparing $f(x, \alpha)$ to $F(x, \alpha)$ for each α_n we find (see Fig. 7.1 (b)) that $f(x, \alpha)$ for this choice of $d(\alpha)$ accurately reproduces the value of $F(x, \alpha_n)$ at precisely the points sampled by the iteration sequence. Solving

$$R_\alpha(x) = f(\cdots f(f(f(x, \alpha), \alpha^2), \alpha^4, \cdots, \alpha^{2^M}) = x_c, \tag{7.15}$$

then yields

$$x_{\alpha,M} \approx x_c \left\{ 1 + \frac{1}{(1 - \alpha)^2} \sum_{n=0}^{M} \frac{2\alpha^{2^n} - 3\alpha^{2^{n+1}} + \alpha^{2^{n+2}}}{\prod_{m=0}^{n} d(\alpha^{2^m})} \right\}. \tag{7.16}$$

As required this gives $x_{0,M} = x_c$ and in the limit $M \to \infty$ we find $x_{1,M}$ diverges. In Fig. 7.2 it is found that $x_{\alpha,M}$ evaluated for $M = 1000$ produces a near perfect fit of the numerically found RG critical points. Interestingly, by making the gradient function d constant and taking the limit $M \to \infty$ the solution simplifies to the

power-series

$$x_\alpha \approx \frac{x_c}{(1-\alpha)^2}\left\{1-(d-1)\alpha+\frac{(d-1)(d-2)}{d}\sum_{n=0}^{\infty}\frac{\alpha^{2^n}}{d^n}\right\}. \tag{7.17}$$

For $d = 2$ this becomes $x_\alpha = x_c/(1-\alpha)$, which is the function obtained in our previous mean-field and truncated fermionic analyses, while for $d = 1$ the solution simplifies to $x_\alpha = x_c/(1-\alpha)^2$.

Curiously, one can conjecture a reasonable function that also reproduces the behaviour of x_α. Specifically, one such form is

$$X(\alpha) = \frac{x_c}{(1+x_c\gamma_0)e^{-\alpha/\xi} - x_c\gamma_0}, \tag{7.18}$$

where γ_0 is the single fit parameter and $\xi = -1/\ln[x_c\gamma_0/(1+x_c\gamma_0)]$ such that $X(0) = x_c$ and $X(1)$ diverges as required. In fact we do not need to fit this function, by simply setting $\gamma_0 = b$ we find the curves shown in Fig. 7.2. The quality of this curve without any fitting seems to suggest that it accurately captures all of the essential dependency on α of the critical point as predicted by the RG calculation. However, it is not exactly identical to the approximate RG function of Eq. (7.16) and we have been unable to find an appropriate simplification of the RG scheme that yields this function naturally.

7.4.3 Critical exponent

In addition to finding the critical point the RG scheme can be used to compute the order parameter $\langle\hat{\sigma}^x\rangle$ and extract the critical exponent β. After a sufficiently large number of iterations n the ratio x_n will tend to one of two trivial fixed points $x = 0$ or $x = \infty$ (assuming we are not exactly at the unstable critical fixed point). For $x < x_c$ the $x = 0$ fixed point gives doubly degenerate ground states $|++\cdots+\rangle$

and $|--\cdots-\rangle$, where $|\pm\rangle = (|\tilde{\uparrow}\rangle \pm |\tilde{\downarrow}\rangle)/\sqrt{2}$ are spin states for each fictitious block spin (see Ref. [131] or appendix 7.B.1). We may assume that symmetry breaking chooses one of these states and, since the operator $\tilde{\sigma}^x$ maps to itself up to rescaling, this means we need only calculate

$$\langle \hat{\sigma}^x \rangle = \lim_{n\to\infty} \langle \tilde{\uparrow} | \tilde{\sigma}^x | \tilde{\downarrow} \rangle_n, \tag{7.19}$$

where the subscript n on the term in the limit implies that this is the diagonal element of $\tilde{\sigma}^x$ following n successive RG transformations. The result is simply

$$\langle \hat{\sigma}^x \rangle = \prod_{n=1}^{\infty} \eta_n(x), \tag{7.20}$$

where the scale factor for the nth iteration of $\tilde{\sigma}^x$ is

$$\eta_n(x) = \frac{1 + \sqrt{1+4x_n^2} - 2x_n}{2(1+4x_n^2 - 2x_n\sqrt{1+4x_n^2})^{1/2}}. \tag{7.21}$$

Notice that the form of the order parameter in Eq. (7.20) is independent of α. Any possible α dependence arises only from the modified values of x_n in the scale factor η_n for each iteration n. Numerical data for the order parameter in the vicinity of the critical point is shown in Fig. 7.2 (d) for a range of α. As expected, for $\alpha = 0$ the order parameter obeys $\langle \hat{\sigma}^x \rangle \sim (x_c - x)^\beta$ in this region but the RG calculation yields $\beta_{RG} = 0.4086$ (to 4 s.f.), which deviates substantially from the exact result $\beta = 0.125$. With the introduction of a non-zero α we still observe a power-law decay of $\langle \hat{\sigma}^x \rangle$ at the shifted critical point, but no change in the exponent from the $\alpha = 0$ value. Therefore, while the RG calculation agrees with our intuition that the critical point tends towards its mean-field value as $\alpha \to 1$, its prediction for the critical exponent is inconsistent with our expectation that this should approach the mean-field value $\beta_{MF} = 0.5$.

7.5 infinite-DMRG approach

We now present the central result of this paper: the position of the quantum critical point $x_\alpha = g_\alpha/J$ of the 1D Ising model in a transverse field, which includes exponentially decaying long-range interactions, as calculated by the iDMRG algorithm. Specifically, we follow the recently developed matrix product operator formulation of the algorithm, which offers some significant advantages over the conventional approach [132]. Importantly for our work, this formulation provides a straightforward representation of the operator for the exponentially decaying interaction in terms of a lower triangular matrix, which is preserved under standard matrix product manipulations. We iterate the iDMRG algorithm until a fixed point is reached, which represents the matrix product approximation to the infinite translationally invariant system. This is in contrast with most past uses of iDMRG where it provides an initialisation step to the finite DMRG algorithm [53, 54]. Importantly, in order to extract results for the truly infinite-sized limit the central pair of sites in the iDMRG iterations are used to form an infinite two-site periodic matrix product state. After explicitly orthonormalising this state it is then used to compute expectation values in the thermodynamic limit [133]. The results obtained are often many orders of magnitude more accurate than those obtained from the iDMRG iterations directly, which instead represents a matrix product state of a large but finite-sized system.

7.5.1 infinite-DMRG results

Numerical data obtained using the iDMRG algorithm with a value of $\chi = 200$ for the dimension of the MPOs is plotted in Fig. 7.3. As expected we find that the inverse of x_α is a smooth monotonic function between the two exact limits $1/x_\alpha = 1/x_c = 1$ for $\alpha = 0$ and $1/x_\alpha = 0$ for $\alpha = 1$. We find from a least-squared fitting to the numerical data that the conjectured function $X(\alpha)$ has a fit parameter of $\gamma_0 = 0.4507$ (to 4

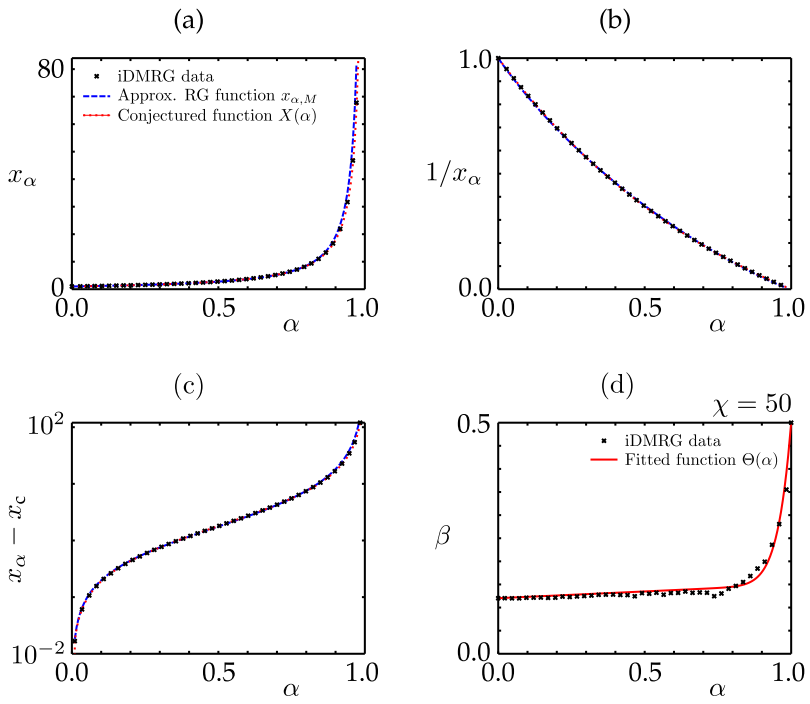


Figure 7.3. (a) shows the critical point x_α as calculated numerically by the iDMRG method (crosses). As expected the exact $\alpha = 0$ critical point is reproduced. The blue dashed line is the fitted RG function $x_{\alpha,M}$ of Sec. 7.4 with $M = 1000$ and $x_c = 1$, while the red dotted line is the fitted conjectured function $X(\alpha)$. (b) is the same plot but for the inverse of x_α, while (c) shows $x_\alpha - x_c$ with a logarithmic y-axis. Once again, these variety of plots show the excellent quality of the fit over inverse and logarithmic scales by the conjectured function, whereas now the approximate RG function deviates from the numerical data as α approaches unity. (d) Numerical iDMRG data for the critical exponent β (crosses) fitted by the function $\Theta(\alpha)$ (red dotted line) given in the main text. The iDMRG result $\beta = 0.1202$ for the $\alpha = 0$ critical exponent deviates slightly from the known result $\beta = 0.125$.

s.f.). The various plots of Fig. 7.3 show that the quality of the fit is excellent over both inverse and logarithmic scales. We also perform a two-parameter fit of the approximate RG function $x_{\alpha,M}$ for b and c with $M = 1000$ RG iterations, giving $b = 1.101$ and $c = 1.812$ (to 4 s.f.). This fit is very good for small α but deviates slightly from the numerical data for α approaching unity. Therefore, while the approximate RG solution gives an accurate description of the RG approach, it is the conjectured exponential-type function $X(\alpha)$ that fully describes both the RG and iDMRG numerical data.

In Fig. 7.4 we have plotted the iDMRG data for the inverse of x_α along with the approximate solutions from the previous sections. The iDMRG data is bounded from below and above by the mean-field and fermionic solutions respectively. Notice that in the limit $\alpha \to 1$ the iDMRG data converges towards the mean-field solution indicating a smooth approach to the classical limit. By making a Taylor expansion of $X(\alpha)$ about $\alpha = 1$ we find $1/x_\alpha \approx \gamma_0(1-\alpha)/\xi$ in comparison with the mean-field solution $1/x_\alpha = (1-\alpha)/2$. Using the value of $\gamma_0 = 0.4507$ for the fit to the iDMRG data we find $\gamma_0/\xi = 0.5269$, which is in reasonable agreement with the mean-field value of 0.5.

Finally, we also use the iDMRG approach to calculate the critical exponent $\beta(\alpha)$, with the data plotted in Fig. 7.3 (d). In contrast to the RG approach the iDMRG data shows that the critical exponent smoothly increases from a value of $\beta(0) = 0.1202$ at $\alpha = 0$ towards the mean-field value of $\beta_{MF} = 0.5$ at $\alpha = 1$. Notice that the iDMRG method has not quite reproduced the known nearest-neighbour critical exponent of $\beta = 0.125$. Also shown in Fig. 7.3 (d) is a least-squared fit using two parameters γ_1 and γ_2 of the function

$$\Theta(\alpha) = u + \gamma_1(v-u)\alpha + \gamma_2(v-u)e^{-\kappa/\alpha}, \tag{7.22}$$

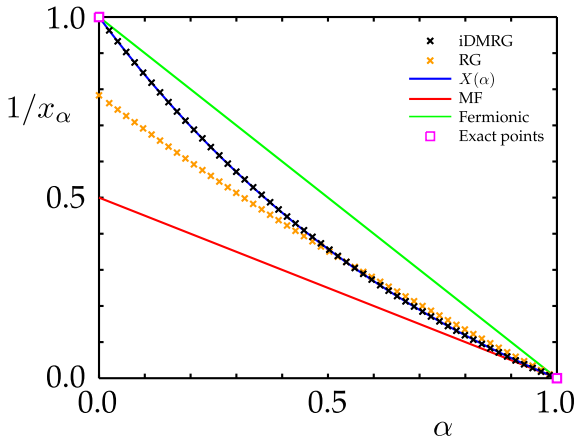


Figure 7.4. For the iDMRG data fitted by the conjectured function $X(\alpha)$ and the various approximations we plot the inverse of x_α against α. The exact $\alpha = 0$ and $\alpha = 1$ points are also included.

where $\kappa = \ln[\gamma_2/(1-\gamma_1)]$, and we have set $u = \beta(0) = 0.1202$ and $v = \beta_{MF} = 0.5$. The fit parameters are $\gamma_1 = 0.0771$ and $\gamma_2 = 3.620 \times 10^9$. This function deviates from the numerical data for large α but nevertheless shows the critical exponent increases linearly for small α before an almost exponential increase to the mean-field value at large α. This is yet another indication of the smooth approach of the Ising model to its classical limit by increasing the range of the interactions.

7.6 Conclusion

We have investigated the shift in the critical point of the 1D spin-1/2 Ising chain as the range of the interactions are increased beyond nearest-neighbour. To gain some intuition as to the expected behaviour of this shift, we calculated the critical properties of the model, firstly within mean-field theory, and then by extending the method of Pfeuty in Ref. [125] with a suitable approximation to obtain an analytical solution. At $\alpha = 0$, corresponding to nearest neighbour interactions only, the mean-field result for the critical point was calculated as twice that of the known exact

result. In the opposite limit of infinite-range interactions, $\alpha = 0$, both solutions predict a diverging critical point indicating that the long-range interactions stabilise the ferromagnetic phase against all values of the transverse field.

We next explored the critical properties of the system using a real space renormalisation group (RG) analysis. While this method did not reproduce the exact $\alpha = 0$ result for the critical point, the solution was found to lie between those of the two prior solutions in the full range of α, and was again shown to diverge in the limit $\alpha \to 1$. Importantly, this method allowed us to obtain an analytic series in α to approximate the shift in the critical point, and to further conjecture an exponential-type function that was found to accurately fit the later iDMRG result. We also used the RG analysis to calculate the order parameter, which as expected obeyed a power-law decay for all α. However, the critical exponent $\beta_{\mathrm{RG}} = 0.4086$ was independent of α and therefore inconsistent with both the exact result of $\beta = 0.125$ at $\alpha = 0$ and the expected mean-field result of $\beta = 0.5$ in the limit $\alpha \to 1$.

Finally, we presented the critical properties of the system using the more accurate iDMRG calculations. The critical point g_α was found to shift smoothly from the exact result of $g_c = J$ for the nearest-neighbour model to a diverging value in the limit of infinite-ranged interactions. Moreover, the value of $x_\alpha = J/g_\alpha$ converged towards the mean-field solution for $\alpha \to 1$ indicating a smooth approach to the classical limit. In agreement, the critical exponent was found to exponentially increase from a value of $\beta = 0.1202$ at $\alpha = 0$ towards the expected mean-field value in the limit $\alpha \to 1$. As stated, the conjectured function $X(\alpha)$ obtained empirically from the RG analysis was an accurate fit to the iDMRG critical point. However, it not at all obvious why the shifting of the critical point appears to follow so well such a simple, exponential-type function. Indeed, all of our attempts to understand this behaviour analytically yield an algebraic divergence, and we therefore leave this open to further investigation.

Acknowledgments

This work was supported by the UK EPSRC through projects QIPIRC (GR/S82176/01) and EuroQUAM (EP/E041612/1).

7.A Energy spectrum for the long-range fermionic model

The Hamiltonians of Eq. (7.5) and (7.7) are specific cases of a more general canonical form of quadratic fermionic Hamiltonian [128], namely,

$$\hat{H} = -\sum_{ij}\left[\hat{c}_i^\dagger \mathbf{A}_{ij}\hat{c}_j + \tfrac{1}{2}(\hat{c}_i^\dagger \mathbf{B}_{ij}\hat{c}_j^\dagger + \hat{c}_j \mathbf{B}_{ij}\hat{c}_i)\right]. \tag{7.23}$$

Here $\mathbf{A}$ and $\mathbf{B}$ are real symmetric and real anti-symmetric matrices respectively, which can always be chosen to be the case by trivial phase transformations on the fermionic operators. We can determine numerically, and in some cases analytically, a linear transformation of the form

$$\begin{aligned}\hat{b}_k &= \sum_i \left[\tfrac{1}{2}(\phi_{ki}+\psi_{ki})\hat{c}_i + (\phi_{ki}-\psi_{ki})\hat{c}_i^\dagger\right],\\ \hat{b}_k^\dagger &= \sum_i \left[\tfrac{1}{2}(\phi_{ki}+\psi_{ki})\hat{c}_i^\dagger + (\phi_{ki}-\psi_{ki})\hat{c}_i\right].\end{aligned} \tag{7.24}$$

The coefficients ϕ_{ki} and ψ_{ki} are real, which ensures the transformation is canonical so that $\hat{b}_k$ and $\hat{b}_k^\dagger$ continue to satisfy fermionic anticommutation relations. Importantly, the transformation must diagonalise $\hat{H}$ as

$$\hat{H} = \sum_k \varepsilon_k \hat{b}_k^\dagger \hat{b}_k + \tfrac{1}{2}\left(\sum_i \mathbf{A}_{ii} - \sum_k \varepsilon_k\right), \tag{7.25}$$

which implies that $\hat{b}_k$ is a lowering operator of $\hat{H}$ satisfying $[\hat{b}_k, \hat{H}] = \varepsilon_k \hat{b}_k$. The second term in Eq. (7.25) is a constant, which is determined by the invariance of the trace of $\hat{H}$. The diagonalisation is achieved if the row vectors $\vec{\phi}_k$ and $\vec{\psi}_k$ satisfy the coupled matrix equations

$$\begin{aligned} \vec{\phi}_k(\mathbf{A} - \mathbf{B}) &= \varepsilon_k \vec{\psi}_k, \\ \vec{\psi}_k(\mathbf{A} + \mathbf{B}) &= \varepsilon_k \vec{\phi}_k. \end{aligned} \tag{7.26}$$

We can choose to eliminate $\vec{\psi}_k$ and solve the eigenvalue equation

$$\vec{\phi}_k(\mathbf{A} - \mathbf{B})(\mathbf{A} + \mathbf{B}) = \varepsilon_k^2 \vec{\phi}_k \tag{7.27}$$

to obtain the energy spectrum ε_k. The Hamiltonian of Eq. (7.7) yields a band diagonal $(\mathbf{A} - \mathbf{B})(\mathbf{A} + \mathbf{B})$ matrix with corner elements, of the form

$$(\mathbf{A} - \mathbf{B})(\mathbf{A} + \mathbf{B}) = 4J^2 \begin{pmatrix} a & d_1 & d_2 & d_3 & \cdots & d_2 & d_1 \\ d_1 & a & d_1 & d_2 & \cdots & d_3 & d_2 \\ d_2 & d_1 & a & d_1 & \cdots & d_4 & d_3 \\ d_3 & d_2 & d_1 & a & \cdots & d_5 & d_4 \\ \vdots & \vdots & \vdots & \vdots & \ddots & \vdots & \vdots \\ d_2 & d_3 & d_4 & d_5 & \cdots & a & d_1 \\ d_1 & d_2 & d_3 & d_4 & \cdots & d_1 & a \end{pmatrix}. \tag{7.28}$$

For the moment let us take the system as having size N so that this matrix is $N \times N$ and the number of long-range terms beyond the nearest-neighbour is finite and equal to R. We assume $N \geq 2R + 3$ so that the corner and band diagonal elements do

not intersect. The matrix elements in terms of g, J, and α are given by

$$\begin{aligned} a &= \left(\frac{g}{J}\right)^2 + \sum_{j=0}^{R} \alpha^{2j}, \\ d_n &= \begin{cases} \alpha^n \left(\sum_{j=0}^{R-n} \alpha^{2j} - \dfrac{g}{\alpha J} \right) & \text{for } 1 \leq n \leq (R+1), \\ 0 & \text{for } n > (R+1). \end{cases} \end{aligned} \tag{7.29}$$

This matrix is exactly of the kind that arises for a single-particle tight-binding Hamiltonian with periodic boundary conditions and hopping up to $R+1$ sites. Therefore, it can readily be shown that the spectrum is given by (c.f. band-structure for a tight-binding lattice)

$$\varepsilon_k^2 = 4J^2 \left[a + 2 \sum_{n=1}^{R+1} d_n \cos(nk) \right], \tag{7.30}$$

which in the limit $N \to \infty$ and $R \to \infty$ can be evaluated exactly as

$$\begin{aligned} \varepsilon_k = 2J \Bigg[&\left(\frac{g}{J}\right)^2 + \frac{1}{1-\alpha^2} \\ &+ 2 \left(\frac{\alpha}{1-\alpha^2} - \frac{g}{J} \right) \frac{\cos k - \alpha}{1 + \alpha^2 - 2\alpha \cos k} \Bigg]^{\frac{1}{2}}. \end{aligned} \tag{7.31}$$

7.B Real-space renormalisation

7.B.1 Recursion relation for $\alpha = 0$

Consider the nearest-neighbour spin-1/2 Ising chain with a finite number of spins N and periodic boundary conditions described by

$$\hat{H} = -\sum_{i=1}^{N} (J \hat{\sigma}_i^x \hat{\sigma}_{i+1}^x + g \hat{\sigma}_i^z). \tag{7.32}$$

Eigenstate	Energy
$\|\varepsilon_0\rangle = (\|\uparrow\uparrow\rangle + \lambda\|\downarrow\downarrow\rangle)/\sqrt{1+\lambda^2}$	$-\sqrt{J^2+4g^2}$
$\|\varepsilon_1\rangle = (\|\uparrow\downarrow\rangle + \|\downarrow\uparrow\rangle)/\sqrt{2}$	$-J$
$\|\varepsilon_2\rangle = (\|\uparrow\downarrow\rangle - \|\downarrow\uparrow\rangle)/\sqrt{2}$	$+J$
$\|\varepsilon_3\rangle = (-\lambda\|\uparrow\uparrow\rangle + \|\downarrow\downarrow\rangle)/\sqrt{1+\lambda^2}$	$+\sqrt{J^2+4g^2}$

Table 7.1. The eigenstates and energies of the block Hamiltonian discussed in the text.

We apply a real-space renormalisation group scheme where we group pairs of lattice sites into blocks and express the Hamiltonian as

$$\hat{H} = \sum_{j=1}^{N/2} (\hat{H}_j^B + \hat{H}_j^R), \tag{7.33}$$

where $\hat{H}_j^B$ includes all the terms that act within a block and $\hat{H}_j^R$ contains the inter-block terms. Specifically, for the jth block we have

$$\begin{aligned} \hat{H}_j^B &= -J\hat{\sigma}_{2j-1}^x\hat{\sigma}_{2j}^x - g(\hat{\sigma}_{2j-1}^z + \hat{\sigma}_{2j}^z), \\ \hat{H}_j^R &= -J\hat{\sigma}_{2j}^x\hat{\sigma}_{2j+1}^x. \end{aligned} \tag{7.34}$$

We diagonalise the block Hamiltonian and, defining $\lambda = \sqrt{1+4x^2}-2x$ with $x = g/J$, obtain the eigenstates and energies listed in table 7.1. We now make an approximation by allowing the lowest two eigenstates $|\varepsilon_0\rangle$ and $|\varepsilon_1\rangle$ to represent the spin states $|\tilde{\uparrow}\rangle$ and $|\tilde{\downarrow}\rangle$ of a new fictitious spin-1/2 for the two-site block. A reduced set of basis states is defined for the entire system as the products

$$|\Psi_{\mathbf{s}}\rangle = \prod_{\text{blocks } j} |\tilde{\mathbf{s}}_j\rangle, \tag{7.35}$$

where $\tilde{\mathbf{s}} = \{\tilde{\uparrow}, \tilde{\downarrow}\}$ [2]. The resulting truncated Hamiltonian for any single block in the reduced basis is then

$$\tilde{H}^B = -\tfrac{1}{2}(\sqrt{J^2+4g^2}+J)\tilde{\mathbf{1}} - \tfrac{1}{2}(\sqrt{J^2+4g^2}-J)\tilde{\sigma}^z. \tag{7.36}$$

We next find a mapping for the inter-block terms by evaluating the action of the operators $\mathbf{1}\otimes\hat{\sigma}^x$ and $\hat{\sigma}^x\otimes\mathbf{1}$ on the spin block in the reduced basis. It turns out that both operators map with the same prefactor to the $\tilde{\sigma}^x$ operator for the fictitious spin-1/2 such that the inter-block terms become

$$\tilde{H}^R_j = -J\frac{(1+\lambda)^2}{2(1+\lambda^2)}\tilde{\sigma}^x_j\tilde{\sigma}^x_{j+1}. \tag{7.37}$$

The total truncated Hamiltonian is then

$$\tilde{H}_1 = -\sum_{j=1}^{N/2}(J_1\tilde{\sigma}^x_j\tilde{\sigma}^x_{j+1} + g_1\tilde{\sigma}^z_i + c_1\tilde{\mathbf{1}}_j), \tag{7.38}$$

where the coefficients are given by

$$\begin{aligned} c_1 &= \tfrac{1}{2}(\sqrt{J^2+4g^2}+J), \\ g_1 &= \tfrac{1}{2}(\sqrt{J^2+4g^2}-J), \\ J_1 &= -J\frac{(1+\lambda)^2}{2(1+\lambda^2)}. \end{aligned} \tag{7.39}$$

Importantly, we see that the truncated Hamiltonian has precisely the same form as the original one except that it describes a system of half the size and with renormalised coefficients. We repeat the procedure n times yielding a Hamiltonian

$$\tilde{H}_n = -\sum_j(J_n\tilde{\sigma}^x_j\tilde{\sigma}^x_{j+1} + g_n\tilde{\sigma}^z_i + c_n\tilde{\mathbf{1}}_j), \tag{7.40}$$

[2] We have halved the total number of states by thinning the degrees of freedom.

Term	Renormalised coupling
$\tilde{\sigma}^x \otimes \tilde{\mathbf{1}} \otimes \tilde{\sigma}^x$	$\alpha^2 J_1$
$\tilde{\sigma}^x \otimes \tilde{\mathbf{1}} \otimes \tilde{\mathbf{1}} \otimes \tilde{\sigma}^x$	$\alpha^4 J_1$
$\vdots$	$\vdots$
$\tilde{\sigma}^x \otimes (\tilde{\mathbf{1}})^{\otimes n} \otimes \tilde{\sigma}^x$	$\alpha^{2n} J_1$

Table 7.2. The renormalised couplings for the long-range interaction terms during each iteration of the RG scheme.

with coefficients

$$\begin{aligned} c_{n+1} &= \tfrac{1}{2}(J_n\lambda_n + 2g_n + J_n), \\ g_{n+1} &= \tfrac{1}{2}(J_n\lambda_n + 2g_n - J_n), \\ J_{n+1} &= -J\frac{(1+\lambda_n)^2}{2(1+\lambda_n^2)}, \\ d_{n+1} &= c_{n+1} + 2d_n, \end{aligned} \tag{7.41}$$

where $g_0 = g,\ J_0 = J$, and $d_0 = 0$. With some algebra one obtains the recursion relation

$$\begin{aligned} x_{n+1} &= \frac{2(\sqrt{1+4x_n^2}-1)(1+4x_n^2-2x_n\sqrt{1+4x_n^2})}{(1+\sqrt{1+4x_n^2}-2x_n)^2} \\ &= F(x_n). \end{aligned} \tag{7.42}$$

7.B.2 Extension to $\alpha \geq 0$

We now apply the RG scheme above to the $\alpha \geq 0$ case. Since no finite block can ever encompass all the interactions we make the simplest choice of continuing to use a two-spin blocking procedure. In this way only the nearest-neighbour interaction is ever included in the block diagonalisation step. The effect of spin-blocking when long-range terms are present is to map four different interactions terms to the same spin-blocked interaction term $\tilde{\sigma}_j^x \tilde{\sigma}_{j+1}^x$. To see this consider four spins making up

two adjacent spin-blocks j and $j+1$. The inter-block term is now composed of the nearest-neighbour term $-J(\mathbf{1}\otimes\sigma^x\otimes\sigma^x\otimes\mathbf{1})$, two next-nearest-neighbour terms $-J\alpha(\sigma^x\otimes\mathbf{1}\otimes\sigma^x\otimes\mathbf{1})$ and $-J\alpha(\mathbf{1}\otimes\sigma^x\otimes\mathbf{1}\otimes\sigma^x)$, and one next-next-nearest-neighbour term $-J\alpha^2(\sigma^x\mathbf{1}\otimes\otimes\mathbf{1}\otimes\sigma^x)$. From the $\alpha=0$ case we know that the operators $\mathbf{1}\otimes\sigma^x$ and $\sigma^x\otimes\mathbf{1}$ within any spin-block are renormalised identically and so the nearest-neighbour spin-block interaction $\tilde{\sigma}_j^x\tilde{\sigma}_{j+1}^x$ acquires a coupling

$$J_1 = J\frac{(1+\lambda)^2}{2(1+\lambda^2)}(1+2\alpha+\alpha^2). \tag{7.43}$$

For long-ranged terms the couplings are modified as shown in table 7.2. It is evident after renormalisation that the Hamiltonian remains in identical form, now with not only renormalised J and g but also $\alpha\rightarrow\alpha^2$ corresponding to a halving of the interaction length scale. This is a sensible consequence of spin-blocking. The result is that the recursion relation obtained for the $\alpha=0$ case is modified by the presence of exponentially decaying long-range interactions to

$$x_{n+1} = \frac{2(\sqrt{1+4x_n^2}-1)(1+4x_n^2-2x_n\sqrt{1+4x_n^2})}{(1+\alpha_n)^2(1+\sqrt{1+4x_n^2}-2x_n)^2}, \tag{7.44}$$

where $\alpha_{n+1}=\alpha_n^2$ and thus $\alpha_n=\alpha^{2^n}$.

Chapter 8

Decoherence of a quantum memory coupled to a collective spin bath[1]

8.1 Introduction

The transfer and storage of quantum information between different physical systems is of crucial importance to quantum communication and distributed quantum computing [134]. Experimentally, quantum communication is one of the most advanced areas of quantum technology with promising commercial applications being a realistic possibility in the near future [135]. However, for its full potential to be realized over relevant distances, limitations caused by noisy transmission lines, e.g. the exponential scaling of photon losses in an optical fiber with its length, need to be overcome.

Several promising proposals to solve this problem exist. The most well studied is the use of quantum repeaters which segment the transmission line into shorter pieces [136, 137]. By applying sophisticated entanglement purification schemes and entanglement swapping at these repeater units, high-fidelity entangled pairs can be

[1]The results discussed in this chapter are presented in the publication 'Decoherence of a quantum memory coupled to a collective spin bath,' R. Walters, S. R. Clark, and D. Jaksch, *Int. J. Quant. Info.* **8**, 271 (2010).

established over much larger distances than direct transmission could feasibly permit. A recent alternative method has been proposed that is based on the idea of entanglement percolation in a quantum network. Given nodes that are initially connected by partially entangled pure states [138] or mixed states [139], schemes based on classical bond percolation have been shown to enable the creation of maximally entangled singlet states between arbitrary points in the network with a probability independent of the distance between them [140]. Both quantum repeater and percolation schemes require that quantum information is stored locally at the repeaters or nodes of the network and crucially their operation degrades in the presence of decoherence in these memories.

In this work we investigate the quantum dynamics of a single qubit quantum memory coupled to an environment of interacting spin-1/2 particles [141]. Such a model of decoherence has relevance for solid-state quantum memories involving the nuclear spin [142, 143], electron spin in a semiconducting quantum dot [144] and nitrogen vacancy centers in diamond [145]. Previous studies examining the decoherence induced by spin baths have mostly considered the so-called 'central spin model' in which the qubit is coupled isotropically to all spins in the bath. Early work has analyzed the decoherence due to independent bath spins [146, 147, 148, 149], whilst most studies since have investigated 1D models with nearest-neighbor couplings [150, 151, 152, 153, 154, 155]. The effect of an infinite-range interaction amongst bath spins has also been studied within the central spin model [156, 157, 158, 159]. However, as pointed out by Rossini *et al.* in Ref. [160], the assumption of a central spin may not be valid for many physical systems. Thus, in their work [160] the authors depart from the central spin model and consider just a few links between the qubit and a 1D spin chain. Here we consider the spin bath as being described by the Lipkin-Meshkov-Glick (LMG) model (see Eq. 8.3), which possesses infinite-range interactions, and similarly go beyond the central spin model by examining the

decoherence of a single qubit as its exposure to the spin bath is varied from coupling to just one bath spin through to interacting with all bath spins.

The LMG spin bath represents an ideal benchmark for investigating the effects of the varying qubit interactions with a non-trivial spin bath. Firstly, it possesses permutational symmetry, which can be exploited to exactly solve its dynamics numerically for very large number of spins ($\sim$ 100-1000). This in itself is a rare property for many-body quantum systems. The large degree of symmetry in the bath also allows us to identify parameter regimes where highly non-Markovian [148] coherence properties are displayed within the quantum memory. We quantify this by its rephasing time and periodic entanglement breaking, which are found to be independent of the bath size. Secondly, the LMG model has also attracted much attention [161, 162, 163, 164, 165] for exhibiting either first- or second-order equilibrium quantum phase transitions dependent on the type of intra-bath coupling. As is now well known the entanglement properties of the ground state are strongly affected at criticality [166, 167, 168, 169] and this in turn can have a profound effect on the induced decoherence of a coupled qubit [150]. We explore the effects of criticality and in a similar fashion to H. T. Quan *et al.* in Ref. [150] our findings point to a possible use of a coupled quantum memory as an apparatus for the dynamical measurement of a QPT through its coherence properties.

The structure of this paper is as follows. In Sec. 8.2 we introduce the model and the bath Hamiltonian, and describe the ground state properties of the bath under various parameter regimes. We also introduce the dephasing Ising interaction and dissipative XY interaction terms and discuss the measures used to quantify decoherence in our system. The results are presented in Sec. 8.3 and 8.4 for dephasing and dissipative interactions respectively, with conclusions drawn in Sec. 8.5.

8.2 The Model

The model under consideration is that of a single spin-1/2 (qubit) Q interacting with a spin bath R. The purpose of the investigation is two-fold: the primary focus is to study how the interaction with the bath affects the evolution of Q, however in doing so we also use Q as a probe to study the bath dynamics across criticality. The Hamiltonian of the global system, depicted schematically in Fig. 8.1, is of the standard form

$$H_T = H_Q + H_R + H_I, \tag{8.1}$$

where H_Q and H_R are the free Hamiltonians of the qubit and the bath respectively, and H_I is the interaction term. For the qubit we assume

$$H_Q = -\omega \varsigma^z, \tag{8.2}$$

where ς^z is the Pauli z-operator and ω is the energy difference between the ground and excited states; we work in units with $\hbar = 1$. In the following subsections, we will introduce the bath Hamiltonian $H_R = H_{LMG}$ and the two different interaction terms under consideration. Throughout this work, the subsystems Q and R will be initiated at time $t = 0$ in a product state, with the bath in its ground state.

8.2.1 The Lipkin-Meshkov-Glick bath

The bath is described by the Lipkin-Meshkov-Glick model, which was originally proposed in nuclear physics to describe shape phase transitions in nuclei [170]. We note that it has since found relevance in describing the Josephson effect in two-mode Bose-Einstein condensates [171] and a dissipative implementation of it has also recently been proposed in optical cavity QED [172]. The model involves a system of N spins-1/2 mutually interacting in the x-y plane and embedded in a

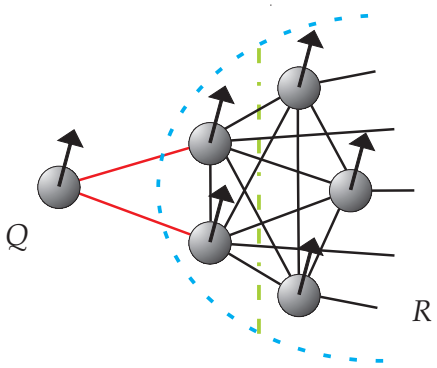


Figure 8.1. (Color on line) A schematic of the model under investigation. A single spin-1/2 is coupled via k links (red lines) to a completely connected spin bath R. Note that the lengths of the lines do not correspond to the strength of the interactions. The green dash-dotted line indicates a particular bath partition.

transverse magnetic field. The Hamiltonian is given by

$$\begin{aligned} H_{LMG} &= -\frac{\lambda}{N}\sum_{i<j}^{N}(\sigma_i^x\sigma_j^x + \gamma\sigma_i^y\sigma_j^y) - h\sum_{i=1}^{N}\sigma_i^z \\ &= -\frac{2\lambda}{N}(S_x^2 + \gamma S_y^2) - 2hS_z + \frac{\lambda}{2}(1+\gamma), \end{aligned} \tag{8.3}$$

where $S_\alpha = \sum_{i=1}^{N}\sigma_i^\alpha/2$ is the collective spin operator for the direction $\alpha = x, y, z$; and the σ^α are the Pauli operators for spins in the bath. The quantities λ, h, and γ characterize the interaction strength between bath spins, the magnetic field strength, and the anisotropy in the x-y plane, respectively. The above Hamiltonian describes an infinite-ranged XY model, with the prefactor $1/N$ on the first term necessary to ensure a finite free energy per spin in the thermodynamical limit. The cases $\gamma = 1$ and $\gamma = 0$ correspond to infinite-ranged XX and transverse Ising models respectively. In the following, we consider only ferromagnetic interactions $\lambda > 0$ within the bath for anisotropy values $0 \leq \gamma \leq 1$.

The mutual coupling of all spins described by H_{LMG} results in the energy eigenstates of the free bath being invariant under particle exchange. Furthermore, H_{LMG}

commutes with the total spin operator $\mathbf{S}^2 = S_x^2 + S_y^2 + S_z^2$, and so the energy eigenstates are divided into symmetric subspaces $\mathbb{S}_S$ defined by the spin quantum number S of $\mathbf{S}^2$ and each of dimensionality $2S + 1$. This symmetry vastly reduces the complexity of studies of the ground state (GS) of the bath. For ferromagnetic intra-bath couplings the GS lies in the maximal spin subspace $\mathbb{S}_{N/2}$, and so its calculation is an eigenvalue problem scaling as just $N + 1$.

For isotropic intra-bath coupling ($\gamma = 1$) H_{LMG} also commutes with S_z and is thus diagonal in the symmetric eigenbasis spanned by Dicke states $|S, M\rangle$ [173] (M is the quantum number for S_z). Dicke states are degenerate except for those belonging to the maximal spin subspace $\mathbb{S}_{N/2}$. For an ensemble of N spins, Dicke states in the subspace $\mathbb{S}_{N/2}$ are entangled states except for the two spin-polarized states $|N/2, N/2\rangle$ and $|N/2, -N/2\rangle$.

Ground state properties

The ground state of the ferromagnetic bath lies in the maximal spin subspace $\mathbb{S}_{N/2}$ for all γ and $\lambda > 0$. A mean-field approach [174, 175] predicts a second-order quantum phase transition in the thermodynamical limit at the critical point $\lambda = h$ for all $\gamma \geq 0$.

For a finite, isotropic bath there is a crossing of the lowest energy levels at $\lambda_c = hN/(N-1)$. This is shown in Fig. 8.2(a), where we have plotted the energies $E = \langle H_{LMG} \rangle$ of the lowest levels for $\gamma = 1$. The GS is the separable, spin-polarized state $|N/2, N/2\rangle$ for $0 \leq \lambda \leq \lambda_c$ (normal phase), and an entangled state $|N/2, \lfloor hN/2\lambda \rceil\rangle$ for $\lambda > \lambda_c$ (broken phase), where the function $\lfloor x \rceil$ rounds x to the nearest integer. For both phases the GS is non-degenerate for any bath size. Note that the critical point depends on h, thus the bath can be directed to either phase by setting the magnetic field strength correspondingly greater or less than the intra-bath coupling strength.

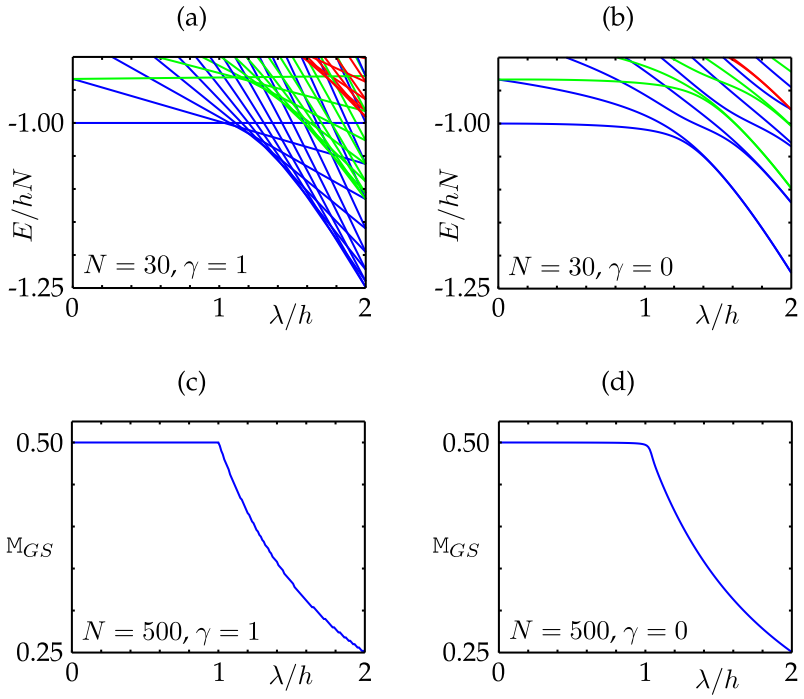


Figure 8.2. (Color on line) Upper: the energy spectrum for isotropic (a) and anisotropic (b) ferromagnetically coupled baths of $N = 30$ spins. Blue lines indicate levels in the subspace $\mathbb{S}_{N/2}$, green lines the subspace $\mathbb{S}_{(N/2)-1}$, and red lines the subspace $\mathbb{S}_{(N/2)-2}$. Lower: GS magnetization (per spin) in the z-direction for isotropic (c) and anisotropic (d) ferromagnetically coupled baths of $N = 500$ spins.

The GS of an anisotropic bath is a superposition over all Dicke states in the maximal spin subspace $\mathbb{S}_{N/2}$, but tends to the spin-polarized state $|N/2, N/2\rangle$ in the limit $\lambda \to 0$. The GS is non-degenerate for the normal phase, but becomes doubly degenerate in the thermodynamical limit for the broken phase. This is demonstrated in Fig. 8.2(b), which shows that the energies of the lowest levels are almost identical for an anisotropic bath of just $N = 30$ spins. In the thermodynamical limit, the GS magnetization (per spin) in the z-direction is given by

$$\mathtt{M}_{GS} = \frac{1}{N}\langle S_z \rangle = \begin{cases} 1/2 & \text{for} \quad 0 \leq \lambda \leq h \\ h/2\lambda & \text{for} \quad \lambda \geq h \end{cases}, \tag{8.4}$$

for all γ. See Figs. 8.2(c) and 8.2(d) for the magnetization of a large but finite bath with $\gamma = 1$ and $\gamma = 0$ respectively.

Analytical calculations with a partitioned LMG bath

The high symmetry of the LMG bath allows us to easily compute exact solutions of the system dynamics for a large number of spins, since the GS can be expressed in a reduced subspace $\mathbb{S}_S$ scaling at most as $N+1$. However, this representation of the GS is limited in that we can only consider operators that are symmetric across the entire bath ensemble. Fortunately, the LMG model provides some flexibility since we can make partitions of the bath, as shown in Fig. 8.1, without significantly increasing the scaling with system size, and thus can also consider non-symmetric operators. As an example, consider an operator that acts on, and is symmetric across, a total of k bath spins. We make a bipartite split of the bath into subsystems A and B

with k and $N-k$ spins respectively, and transform the original Dicke states as

$$|(s_A, s_B)S, M\rangle = \sum_{m_A, m_B} |s_A, m_A\rangle \otimes |s_B, m_B\rangle \times \langle s_A, m_A| \otimes \langle s_B, m_B|S, M\rangle, \tag{8.5}$$

where $|s_A, m_A\rangle$ and $|s_B, m_B\rangle$ are Dicke states for subsystems A and B; $s_A \leq k/2$; and $s_B \leq (N-k)/2$. We denote the tensor product space by $\mathbb{S}^k_{s_A} \otimes \mathbb{S}^{N-k}_{s_B}$, where the superscripts indicate the corresponding number of spins. On the LHS of Eq. 8.5 we specify s_A and s_B because, in general, there are a range of allowed values these quantum numbers can take when coupling to form $|S, M\rangle$. However, for the case where S is maximal, which is our only concern, we have $s_A = k/2$, $s_B = (N-k)/2$ and $s_A + s_B = S$, reducing the Clebsch-Gordan coefficients in Eq. 8.5 from the general form in Ref. [176] to

$$\langle k/2, m_A| \otimes \langle (N-k)/2, m_B|N/2, M\rangle = \sqrt{\frac{F_{m_A+k/2}(k) F_{m_B+(N-k)/2}(N-k)}{F_{M+N/2}(N)}} \times \delta_{m_A+m_B,M}, \tag{8.6}$$

where $F_b(a) = a!/[b!(a-b)!]$ are binomial coefficients. From Eqs. 8.5 and 8.6 we can construct a transformation operator that maps the subspace $\mathbb{S}_{N/2}$ to the tensor product space $\mathbb{S}^k_{k/2} \otimes \mathbb{S}^{N-k}_{(N-k)/2}$, given by

$$T_{N/2 \to k/2,(N-k)/2} = \sum_{M=-N/2}^{N/2} \sum_{m_A=-k/2}^{k/2} \sum_{m_B=-(N-k)/2}^{(N-k)/2} \delta_{m_A+m_B,M} \times \sqrt{\frac{F_{m_A+k/2}(k) F_{m_B+(N-k)/2}(N-k)}{F_{M+N/2}(N)}} \times |k/2, m_A\rangle \otimes |(N-k)/2, m_B\rangle\langle N/2, M|. \tag{8.7}$$

We apply this transformation operator to the representations in $\mathbb{S}_{N/2}$ of both the GS and H_{LMG}, allowing us to consider operators that are symmetric across just k spins without needing to revert to the full Hilbert space $\mathbb{C}_2^{\otimes N}$.

8.2.2 Ising interaction

The first interaction term we consider is of the Ising type

$$H_I = \frac{\epsilon}{\sqrt{k}} \varsigma^z \otimes \sum_{i=1}^{k} \sigma_i^z, \tag{8.8}$$

where ϵ is the interaction strength. This commutes with the free qubit Hamiltonian (i.e. $[H_I, H_Q] = 0$) and thus there will be no energy exchange between the qubit and the bath; the evolution will affect the off-diagonal terms of the state of Q only. The term above describes a situation involving a total of k out of N bath spins interacting with the qubit. By using the transformation operator in Eq. 8.7 we can vary the value of k to study any scenario from a single coupled bath spin ($k = 1$) to a completely coupled bath (i.e. the central spin model, $k = N$), allowing us to evaluate how the evolution of the qubit changes as it is exposed to varying numbers of bath spins. We have introduced the factor $1/\sqrt{k}$ so as not to artificially increase the interaction strength as we increase the number of links, effectively normalizing the interaction term.

8.2.3 LMG interaction

With the second interaction we allow energy exchange between the qubit and the bath and thus introduce dissipation into the subsystem Q. A natural way of doing this is to consider the qubit interacting with the bath spins in the same way the

bath spins do with each other, i.e.

$$H_I = \frac{\epsilon}{\sqrt{k}} \sum_{i=1}^{k} (\varsigma^x \otimes \sigma_i^x + \gamma \varsigma^y \otimes \sigma_i^y). \tag{8.9}$$

The anisotropy parameter γ used here is the same as that in the LMG Hamiltonian in Eq. 8.3. Once again, we vary k from 1 to N in order to consider different levels of exposure of the qubit to the bath.

8.2.4 Characterizing decoherence

The main aim of this work is to characterize how the coupling to an LMG spin bath affects the decoherent evolution of the qubit Q. In the following subsections we introduce two measures that allow us to do this; namely, the average purity, and whether the induced decoherence is 'entanglement breaking'. Their calculation requires the use of an ancilla qubit and exploits the Jamiolkowski isomorphism [177], which is detailed in appendix 8.A. Importantly, all the information pertaining to the decoherent evolution of the single qubit is mapped via the Jamiolkowski isomorphism to a two-qubit state ρ^Λ for Q and the ancilla. From ρ^Λ we can ascertain if and when the evolution is entanglement breaking, and also deduce the Kraus operators for the evolution to obtain the average purity.

Average purity

We use the purity of the reduced quantum state $\rho(t)$ of the qubit, defined as $P[\rho] \equiv \mathrm{Tr}(\rho^2)$, as a measure of its decoherent evolution in the presence of the bath. The qubit state at time t will be pure iff $P(t) = 1$, and mixed for $P(t) < 1$. We initialize the qubit in a pure state at $t = 0$ so that any mixing of the state, i.e. decoherence, can be observed in its subsequent evolution described by the unital map $\varepsilon\{\rho(0)\}$. In general, the purity depends on the exact details of the state at $t = 0$ and thus we

average over all possible initial pure states $|\psi\rangle$ to obtain the average purity. This can be achieved once the Kraus operators A_i for the evolution are known via [178]

$$\begin{aligned}\overline{P} &= \overline{\mathrm{Tr}[\varepsilon\{|\psi\rangle\langle\psi|\}^2]}^{\psi} \\ &= \frac{1}{d(d+1)}\left(\sum_{ij=1}^{d^2}\left|\mathrm{Tr}[A_i^\dagger A_j]\right|^2 + d\right),\end{aligned} \tag{8.10}$$

where $d = 2$ is the dimension of the quantum subsystem.

Entanglement breaking

A useful property to determine environmentally induced decoherence is whether it destroys any entanglement the primary subsystem Q has with an external subsystem. The superoperator Λ (see appendix 8.A) describing the effect of the interaction is 'entanglement breaking' [179] if, when acting on a subsystem b of dimension d_b, the final state $\rho_{ab}^{fin} = \mathbf{1} \otimes \Lambda_a(\rho_{ab}^{ini})$ is separable for every (possible entangled) initial state ρ_{ab}^{ini} of the composite system of b and an external subsystem a of dimension d_a (not necessarily a copy of b). Importantly, when the state ρ^Λ obtained as described in appendix 8.A is separable, the superoperator Λ will be entanglement breaking since this implies the corresponding quantum operation ε has a Kraus representation composed entirely of projectors. Separability can be determined, using the positive partial transposition (PPT) criterion [180, 181], by computing the minimum eigenvalue $\mu(t)$ of the matrix $(\rho^\Lambda)^{T_a}$. The induced decoherence will be entanglement breaking iff $\mu(t) \geq 0$.

8.3 Results: Ising interaction

In this section we present results for the single spin decoherence induced by the Ising interaction with the LMG bath spins. Before doing so, it is useful to discuss exactly

how decoherence arises in this system.

Consider the qubit initially prepared in a generic superposition of its ground and excited states, such that the global state at time $t = 0$ is

$$|\Psi(0)\rangle = \big(a_0|0\rangle + a_1|1\rangle\big) \otimes |GS\rangle, \tag{8.11}$$

where the coefficients a_0 and a_1 satisfy $|a_0|^2 + |a_1|^2 = 1$. The subsequent evolution under H_T for times $t > 0$ is described by

$$\begin{aligned} |\Psi(t)\rangle = a_0 e^{-i\omega t}|0\rangle \otimes e^{-iH_+ t}|GS\rangle \\ + a_1 e^{i\omega t}|1\rangle \otimes e^{-iH_- t}|GS\rangle, \end{aligned} \tag{8.12}$$

where $S_z^k = \sum_{i=1}^k \sigma_i^z/2$, and $H_\pm = H_R \pm 2\epsilon S_z^k/\sqrt{k}$ are perturbed bath Hamiltonians. In general, the bath evolves to different states dependent on whether the qubit was initially in the state $|0\rangle$ or $|1\rangle$, and therefore Eq. 8.12 is an entangled state of the two subsystems. After tracing out the bath we obtain the reduced density matrix for the qubit (in the eigenbasis $\{|0\rangle, |1\rangle\}$)

$$\rho(t) = \mathrm{Tr}_R\{|\Psi(t)\rangle\langle\Psi(t)|\} = \begin{pmatrix} |a_0|^2 & \rho_{12}(t) \\ \rho_{12}^*(t) & |a_1|^2 \end{pmatrix}, \tag{8.13}$$

where

$$\rho_{12}(t) = a_0 a_1^* e^{-2i\omega t} D^*(t). \tag{8.14}$$

The relative populations of the ground and excited states of the qubit are conserved, but dephasing noise is introduced through the decoherence factor

$$D(t) = \langle GS|e^{iH_+ t} e^{-iH_- t}|GS\rangle. \tag{8.15}$$

Note that the induced decoherence is independent of ω. The purity of the state in Eq. 8.13 is

$$P[\rho(t)] = 1 - 2|a_0|^2|a_1|^2\left[1 - L(t)\right], \tag{8.16}$$

where $L(t) \equiv |D(t)|^2$ is a real quantity taking the form of a Loschmidt Echo (LE) [182] for the bath. Unlike the purity, $L(t)$ is independent of the initial state of the qubit, aside from the fact that it is undefined for $a_0 = 0, 1$. Thus, the average purity is trivially related to the LE via $\overline{P(t)} = [2 + L(t)]/3$.

By the term Loschmidt Echo we mean that $L(t)$ quantifies the distance between the two bath states that have evolved from the GS under the two perturbed bath Hamiltonians $H_{\pm}$. When the distance between these states is small, the entanglement between the qubit and the bath is low and the average purity is close to one. Conversely, when the LE is zero the two time-evolved bath states are orthogonal and the qubit is maximally entangled with the bath. In such cases, the qubit undergoes total dephasing to a completely mixed state and the average purity takes its minimum value of 2/3. Also, this type of dephasing noise is entanglement breaking iff $L(t) = 0$ [179].

A useful quantity to consider that will give insight into how the decoherence varies with link number k is the Fourier Transform of the decoherence factor in Eq. 8.15, given by

$$\chi(E) = \sum_{i,j} \langle GS|\phi_i^+\rangle\langle\phi_i^+|\phi_j^-\rangle\langle\phi_j^-|GS\rangle\ \delta(E - E_j^- + E_i^+), \tag{8.17}$$

where $|\phi_i^{\pm}\rangle$ are eigenvectors of the perturbed bath Hamiltonians $H_{\pm}$, and $E_i^{\pm}$ their eigenenergies. Contributions to $\chi(E)$ occur at energy differences $E_j^- - E_i^+$ corresponding to eigenstates $|\phi_j^-\rangle$ and $|\phi_i^+\rangle$ that simulaneously connect to (i.e. are not distant from) each other and the bath GS.

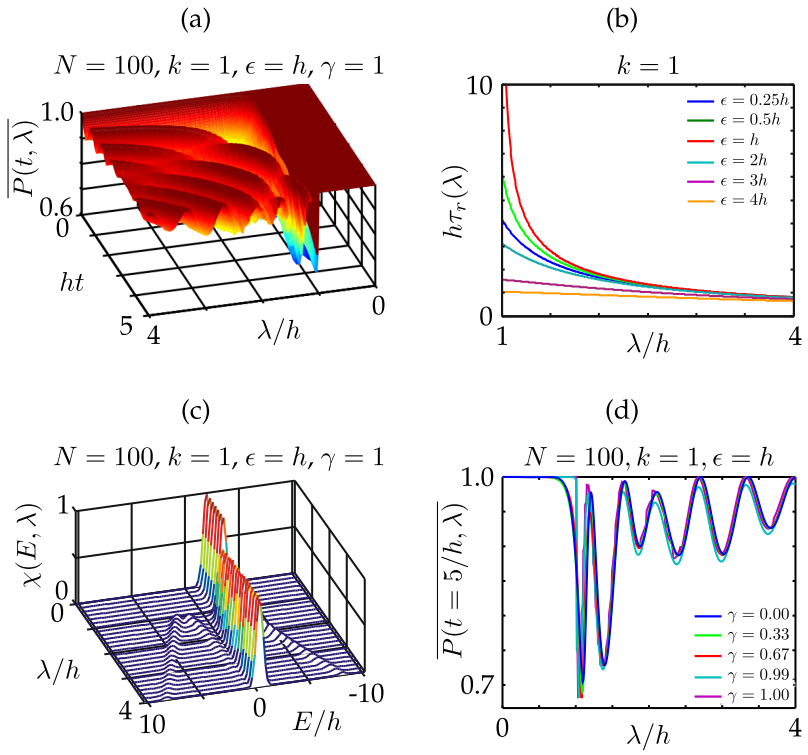


Figure 8.3. Ising interaction, single link ($k = 1$): (a) the average purity plotted against λ and t. (b) The approximate rephasing time τ_r plotted against λ for various values of ϵ. (c) The Fourier Transform of the decoherence factor as a function of energy and λ. We have used Gaussian envelopes at each Fourier component for ease of viewing. (d) The average purity plotted against λ, at $t = 5/h$, for various values of γ.

8.3.1 Single link, $k = 1$

The simplest case to consider first is that of a single link between the qubit and the bath. In particular, for an isotropic bath ($\gamma = 1$) the GS in the normal phase ($\lambda < h$) is the spin-polarized state $|N/2, N/2\rangle$, which is an eigenstate of both perturbed bath Hamiltonians $H_{\pm}$. The bath remains in the GS for the entirety of the evolution and simply induces an additional z-rotation on the initial qubit state through an angle $2\epsilon t$, thus there is zero dephasing.

In the broken phase ($\lambda > h$) we observe a loss of qubit coherence and find that the average purity has an oscillatory behavior with time, as shown in Fig. 8.3(a).

For an isotropic bath, we show in appendix 8.B that the GS in the broken phase decomposes into two terms when we move to the bipartite subspace $\mathbb{S}^1_{1/2} \otimes \mathbb{S}^{N-1}_{(N-1)/2}$. The evolution of the bath under $H_\pm$ is further confined to a subspace comprising only the two states of the decomposition, allowing us to describe the bath propagators $e^{-iH_\pm t}$ by 2 x 2 matrices (see Eq. 8.33). The resulting expression for the purity is too complicated to be given explicitly, however, we can extract the salient behavior from the form of the two propagators. The off-diagonal matrix elements of $e^{-iH_- t}$ vary sinusoidally such that it periodically becomes equal to the identity matrix with a frequency $\eta_- = 2\sqrt{\lambda^2 + \epsilon(\epsilon + 2h)}$ that is independent of bath size N. Similarly, $e^{-iH_+ t}$ varies periodically with a frequency $\eta_+ = 2\sqrt{\lambda^2 + \epsilon(\epsilon - 2h)}$. When both propagators are the identity at the same time, the LE becomes unity and there is a revival of full qubit coherence. This 'coherence time' τ_c must simultaneously satisfy $\eta_- \tau_c = 2l_-\pi$ and $\eta_+ \tau_c = 2l_+\pi$, where l_- and l_+ are integers. In general, we observe fast oscillations of the average purity determined by the higher frequency η_-, which are contained within an envelope function that is periodic with a frequency η_+. High average purities of $\overline{P(t,\lambda)} > 0.98$ are obtained at times $t = l\tau_r$ (l an integer), where $\tau_r = \pi/\eta_+$ is the approximate 'rephasing time' corresponding to the first maximum of the envelope function. This is plotted in Fig. 8.3(b) for various values of the interaction strength ϵ. In the limit $\epsilon \ll h$, the frequencies $\eta_\pm$ are approximately equal and a full revival of qubit coherence occurs at a time $\tau_c \sim \tau_r = \pi/\lambda$. For $\epsilon = h$ the rephasing time is asymptotic at $\lambda = h$, and thus its sensitivity to small changes in the magnetic field allows for an observation of criticality. However, criticality should be avoided if one wishes to use the system for storage of the qubit state so that rephasing can occur on short-time scales.

The behavior described above for the coupling to an isotropic bath is independent of bath size N. Thus, the revivals of qubit coherence are not a finite size effect and occur in the thermodynamical limit. This independence with N arises because

the bath Hamiltonian takes a particularly simple form for $\gamma = 1$ that is diagonal in the eigenbasis spanned by Dicke states $|S, M\rangle$, ultimately restricting the evolution to just a two-dimensional subspace. As a result, the decoherence factor has a maximum of four Fourier components, as shown in Fig. 8.3(c); there is only a single component in the normal phase where no dephasing occurs. Interestingly, when we consider anisotropic baths such that the evolution utilizes the entire $\mathbb{S}^1_{1/2} \otimes \mathbb{S}^{N-1}_{(N-1)/2}$ subspace, we find there are still only $n = 4$ significant Fourier components to the decoherence factor. Significant Fourier components are defined here as those of greatest amplitude that reproduce 98% of the signal. Also, we observe a rapid convergence of the average purity to the isotropic bath result with increasing bath size. In Fig. 8.3(d) we have plotted the average purity across criticality at time $t = 5/h$ for various bath anisotropies and a bath of $N = 100$ spins. Away from criticality, the average purity for all bath anisotropies is within 5% of the isotropic result for a bath of this size. Close to criticality the convergence is slower, and we observe oscillations in the average purity in the normal phase that disappear in the thermodynamical limit.

8.3.2 Completely connected, $k = N$

We now consider the opposite extreme where the qubit is coupled to all spins in the bath, i.e. the central spin model. For an isotropic bath the average purity is trivially equal to one for all λ; the interaction term commutes with the bath Hamiltonian and thus the qubit and the bath cannot become entangled. The qubit experiences a z-rotation through an angle $\epsilon N t$ in addition to that of its free evolution[2].

Figure 8.4(a) shows a color map of the average purity against λ and t for an anisotropic bath ($\gamma = 0$) with $\epsilon = 0.25h$. At this low interaction strength the

[2]The scaling with bath size N of the induced phase may make it difficult for one to keep track of this for large baths.

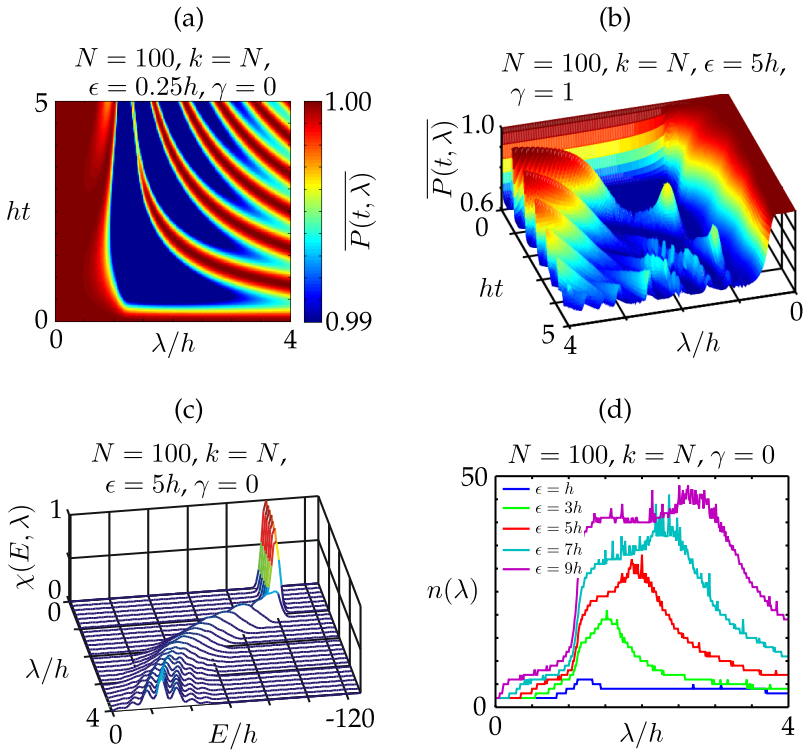


Figure 8.4. Ising interaction, completely connected ($k = N$): (a) a colour map of the average purity plotted against λ and t for $\epsilon = 0.25h$. The map has a threshold at $\overline{P} = 0.99$ to improve clarity. (b) The average purity plotted against λ and t for $\epsilon = 5h$. (c) The Fourier transform of the decoherence factor as a function of energy and λ for $\epsilon = 5h$; again, we have used Gaussian envelopes at each Fourier component. (d) The number of Fourier components n of greatest amplitude that reproduce 98% of the signal, plotted against λ, and for various values of ϵ.

average purity is qualitatively similar to the single link scenario; there is almost zero dephasing in the normal phase, whilst oscillations occur within an envelope function in the broken phase. The rephasing time τ_r is asymptotic at criticality but contrary to the single link scenario we find it is independent of ϵ. As would be expected for this description the Fourier Transform of the decoherence factor for low interaction strengths is qualitatively similar to that shown in Fig. 8.3(c); there is one Fourier component with a large amplitude accompanied by a few ($n < 15$) of smaller amplitude.

As the interaction strength is increased above $\epsilon = h$ the behavior becomes markedly different. The maxima in the average purity are suppressed and, as shown in Fig. 8.4(b) for $\epsilon = 5h$, high average purities are no longer achieved on short-time scales, except in the limit $\lambda \to 0$. In addition, away from the maxima the LE is close to zero indicating that the evolution is almost entanglement breaking. The Fourier Transform of the decoherence factor for $\epsilon = 5h$, shown in Fig. 8.4(c), contains a large number n of significant components but no single one of high amplitude, resulting in the suppression of the maxima. In Fig. 8.4(d) we have plotted n across criticality for various values of ϵ. The number of significant Fourier components increases rapidly as we move from the normal to the broken phase, and contrary to the single link scenario increases at all intra-bath coupling strengths with ϵ.

Interestingly, for any ϵ the energy spread and number of components rapidly converge to finite values with increasing bath size. Thus, although at high interaction strengths there is a decay of qubit coherence on short-time scales, full revivals will eventually occur for any ϵ even in the thermodynamical limit, with the coherence time τ_c independent of N for large baths, $N \gtrsim 100$. Finally, we note that the behavior described in this subsection is only qualitatively the same for different bath anisotropies and does not tend to the isotropic behavior in the limit $\gamma \to 1$.

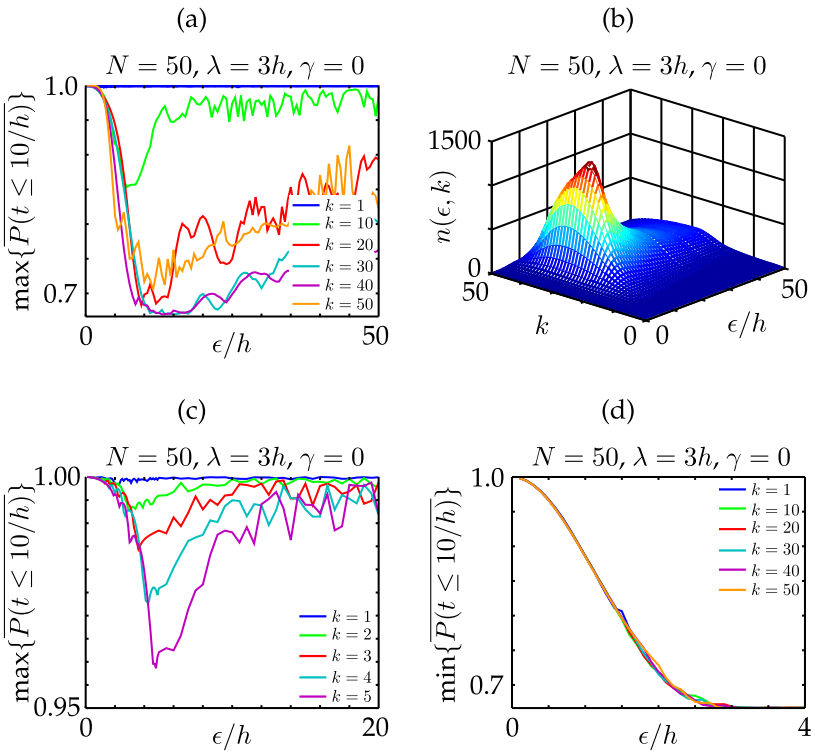


Figure 8.5. Ising interaction: (a) the maximum value of the Loschmidt Echo at $\lambda = 3h$ for rephasing within a time $t \leq 10/h$, as a function of ϵ, and for a range of k. (b) The number of Fourier components n of greatest amplitude that reproduce 98% of the signal, as a function of ϵ and k. (c) same as (a) but for only a few links. (d) The minimum value of the Loschmidt Echo within $t \leq 10/h$ at $\lambda = 3h$, plotted against ϵ.

8.3.3 Multiple links

In the previous two subsections we have seen approximate rephasing occurs on short-time scales for any interaction strength when the qubit is connected via a single link to the bath, whilst for a completely connected qubit rephasing is suppressed at high interaction strengths. We now examine how this transition occurs as we gradually increase the number of links from the scenario $k = 1$ to $k = N$. We consider an intra-bath coupling strength of $\lambda = 3h$ such that we are away from criticality and rephasing is possible on short-time scales for any link number.

In Figs. 8.5(a) and 8.5(c) we have plotted the maximum value of the average

purity for rephasing within a time $t \leq 10/h$, as a function of the interaction strength ϵ, and for a range of link numbers k. The bath size is $N = 50$. High average purities of $\overline{P} > 0.98$ are achieved for any link number below $\epsilon \sim 4h$, whilst above this interaction strength a high average purity is only guaranteed for $k < 3$. At higher link numbers we observe the suppression of maxima up to $\epsilon \sim 10h$ as discussed in Sec. 8.3.2 for a completely connected bath. Interestingly, above $\epsilon = 10h$ the maxima in the average purity increase back towards one, with the rate of increase slowest for link numbers $k \sim$ 30-40. This behavior is prevalent when we consider the number of significant Fourier components n as a function of link number and interaction strength, shown in Fig. 8.4(b). For a few link numbers, we have $n < 10$ for all ϵ allowing approximate rephasing to occur. For higher link numbers, the number of components increase with ϵ up to a maximum value at $\epsilon \sim 10h$, before decreasing once more at higher interaction strengths. The number of components also has a maximum at $k \sim 35$ and therefore decreases with large k, but albeit is still relatively large for a completely connected qubit.

The restriction of the number of significant Fourier components can be explained by considering the form of the perturbed bath Hamiltonians $H_\pm = H_R \pm 2\epsilon S_z^k/\sqrt{k}$. At low interaction strengths $\epsilon < h$, the perturbing terms are small and the eigenstates of the two Hamiltonians are similar. There are approximately $(k+1)(N-k+1)$ terms $\langle \phi_i^+ | \phi_j^- \rangle$ that are non-zero, but only a few of these will connect to the GS and thus $\chi(E)$ will have only a few components. As the interaction strength is increased above $\epsilon = h$, the two sets of eigenstates differ meaning that there are now $(k+1)^2(N-k+1)^2$ non-zero-terms $\langle \phi_i^+ | \phi_j^- \rangle$, each of which will be of similar magnitude. There is a larger set of pairs of eigenstates to connect to the GS leading to many more components. When the interaction strength is increased further such that the second terms dominate in $H_\pm$, the eigenstates again become similar and the number of components asymptotically decreases to one in the limit $\epsilon \to \infty$.

The maximum in the number of components with link number arises because the subspace $\mathbb{S}^k_{k/2} \otimes \mathbb{S}^{N-k}_{(N-k)/2}$ is largest for $k = N/2$, however the maximum is skewed towards $k = N$ so that a completely connected qubit still has a relatively large number of components compared to the case $k = 1$.

Finally, we note that although the maxima in the average purity depend on link number, the minima do not, as shown in figure 8.5(d). The minima decrease towards, but do not reach, the minimum value of 2/3 (corresponding to an LE of zero) with increasing interaction strength and so the interaction is never formally entanglement breaking.

8.4 Results: LMG interaction

We now present the results for the qubit interacting with the bath spins via the dissipative LMG interaction. Contrary to the Ising interaction, the relative populations of the ground and excited states of the qubit can vary in time in addition to the coherence. This implies the average purity can take a minimum value of 1/2, but more significantly it is now dependent on the energy difference ω between the two levels of the qubit. In the following, we consider the scenario[3] in which the qubit is subject to an identical external field as the bath spins, thereby setting $\omega = h$. In tests where ω was varied decoherence was suppressed in all cases as ω was increased, thus the scenario considered is in the worst-case regime.

One important consideration for the LMG interaction, in contrast to the Ising interaction, is that the induced decoherence is non-trivially dependent on the initial qubit state. This means that the purity for a given initial state can have significantly different behavior to the average purity, and indeed can be unity when the average purity is not. It is interesting in the following results that we observe the aver-

[3]We note that in this scenario the qubit cannot be spectroscopically isolated from the bath ensemble.

age purity oscillating away from and back to unity, indiciating universal rephasing at certain times for any given initial qubit state. The evolution is also entanglement breaking for certain periods, which is shown in the following results using the quantity $\mu(t)$ discussed in Sec. 8.2.4.

8.4.1 Single link, $k = 1$

In Fig. 8.6(a) we have plotted the average purity for the qubit connected via a single link to an isotropic bath ($\gamma = 1$) with an interaction strength $\epsilon = h$. For the LMG interaction the average purity is not equal to unity in the normal phase for an isotropic bath, but instead we observe approximate revivals with a rephasing time τ_r that is independent of intra-bath coupling strength λ. The rephasing time increases rapidly with interaction strength and is almost independent of bath anisotropy, as shown in Fig. 8.6(b). The interaction is never entanglement breaking for any γ or ϵ in this phase.

As for the Ising interaction, we observe approximate revivals in the broken phase for all γ and ϵ. The rephasing time τ_r behaves in a similar fashion to the Ising case with a single link: it is almost independent of γ; increases with interaction strength up to $\epsilon = h$ where it is asymptotic at criticality (see Fig. 8.6(c)); and decreases at higher interaction strengths. In Fig. 8.6(d) we have plotted the maximum value of $\mu(t)$ within a time $t \leq 10/h$ for various bath anisotropies. We observe that the induced decoherence is periodically entanglement breaking in time for $\gamma > 0.1$ and interaction strengths $\epsilon > 8h$.

For the LMG interaction we again find that the average purity is independent of bath size for large N. Thus, not only would we observe revivals in the thermodynamical limit, but interestingly they will occur after periods when the induced decoherence is entanglement breaking.

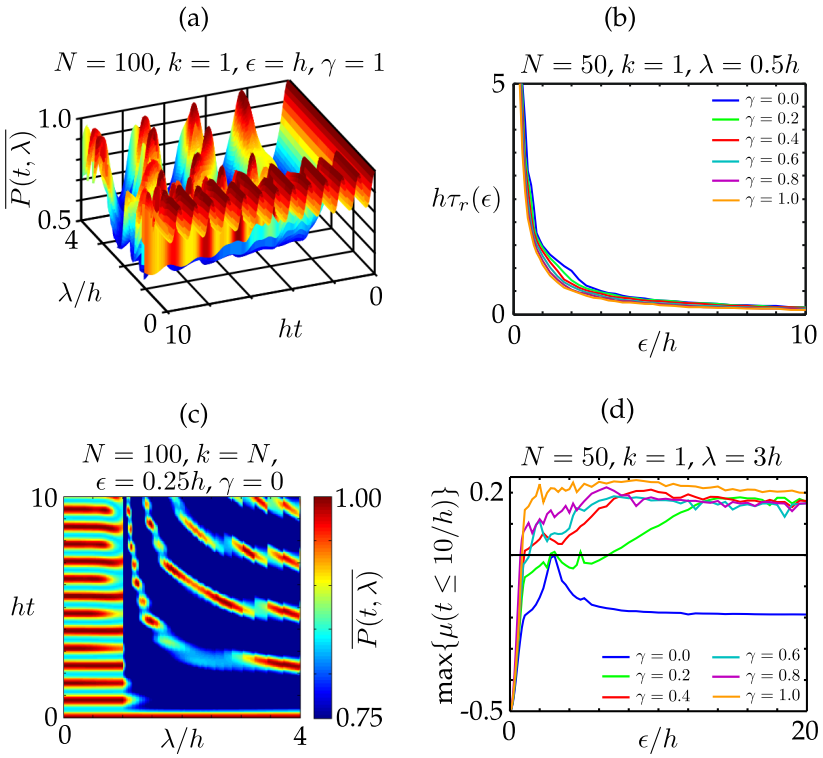


Figure 8.6. LMG interaction, single link ($k = 1$): (a) the average purity plotted against λ and t for $\gamma = 1$. (b) The rephasing time τ_r for the bath in the normal phase ($\lambda = 0.5h$), as a function of ϵ and for various values of γ. (c) A color map of the average purity plotted against λ and t for $\epsilon = h$. The map has a threshold at $\overline{P} = 0.75$ to improve clarity. (d) The maximum value of $\mu(t)$ within $t \leq 10/h$ at $\lambda = 3h$, as a function of ϵ and for various values of γ. Values above zero indicate that the evolution is entanglement breaking.

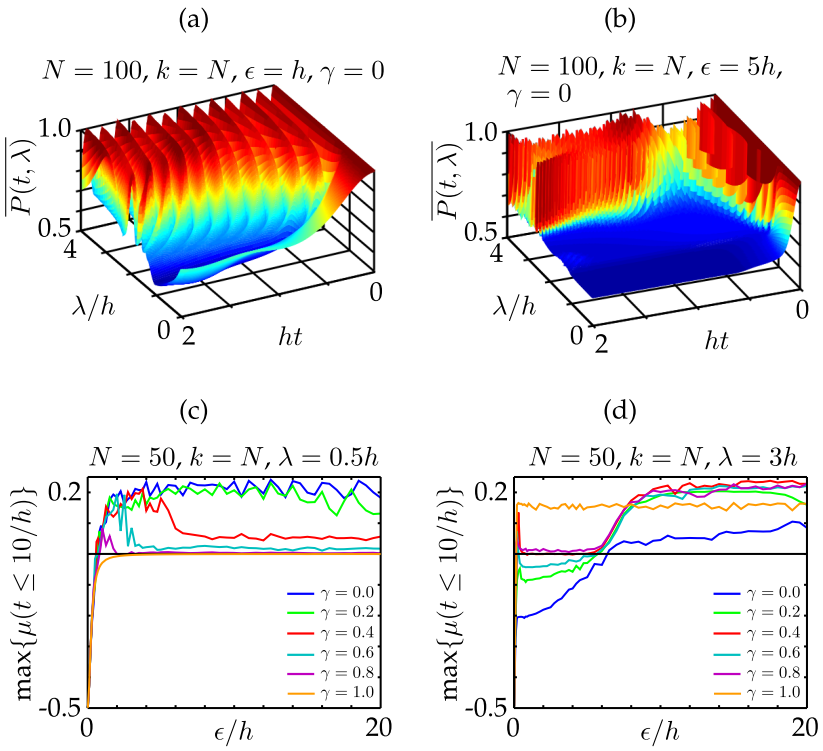


Figure 8.7. LMG interaction, completely connected ($k = N$): (a) and (b), the average purity plotted against λ and t for $\gamma = 0$ and interaction strengths $\epsilon = h$ and $\epsilon = 5h$ respectively. (c) and (d), the maximum value of $\mu(t)$ within $t \leq 10/h$ at $\lambda = 0.5h$ and $\lambda = 3h$ respectively, as a function of ϵ and for various values of γ. Values above zero indicate that the evolution is entanglement breaking.

8.4.2 Completely connected, $k = N$

Figures 8.7(a) and 8.7(b) show the average purity, as a function of intra-bath coupling strength and time, for a completely connected qubit with $\gamma = 0$ and interaction strengths $\epsilon = h$ and $\epsilon = 5h$ respectively. For this bath anistropy there is a decay of the average purity in the normal phase even at low interaction strengths. Note that the decay also occurs at $\lambda = 0$ for which the bath spins do not interact with each other, and extends across criticality into the broken phase at high interaction strengths $\epsilon \gtrsim h$. Rephasing only occurs on short-time scales in the limit $\gamma \to 1$, with the rephasing time τ_r independent of bath size for large baths, $N \gtrsim 100$. The

interaction is now entanglement breaking in this phase on short-time scales except in the limit $\gamma \to 1$, as shown in Fig. 8.7(c).

Approximate revivals occur in the broken phase away from criticality with a frequency much greater than that of the corresponding single link scenarios. Contrary to the Ising case, the rephasing time τ_r increases with interaction strength and converges less rapidly towards a finite value with increasing bath size. Therefore, the rephasing time can only be considered independent of bath size for very large baths, $N \gtrsim 1000$. Figure 8.7(d) shows that the induced decoherence is now periodically entanglement breaking on short-time scales for all γ above $\epsilon \sim 6h$ in this phase. However, at higher interaction strengths this is no longer the case; for $\gamma = 0$ the decoherence is not entanglement breaking for $\epsilon > 23h$ (see Fig. 8.8(d)).

8.4.3 Multiple links

As was the case for the Ising interaction, for the dissipative LMG interaction we observe a change in the qubit's behavior as we move from a single link to fully connected to the bath. In this subsection we discuss how this transition occurs as we vary the link number k for $\gamma = 0$. For this bath anisotropy approximate rephasing occurs on short-time scales in both phases for a single link, but is suppressed in the normal phase for $k = N$. Also, the decoherence is never entanglement breaking for $k = 1$ with $\gamma = 0$, but is at high interaction strengths for $k = N$. We consider intra-bath coupling strengths away from criticality of $\lambda = 0.5h$ for the normal phase and $\lambda = 3h$ for the broken phase.

Figures 8.8(a) and 8.8(b) show the maximum value of the average purity for rephasing within $t \leq 10/h$ with a bath of $N = 50$ spins. Both figures are qualitatively similar to Fig. 8.5(a) for the Ising interaction; approximate rephasing occurs for a single link at any interaction strength, whilst the maxima in the average purity

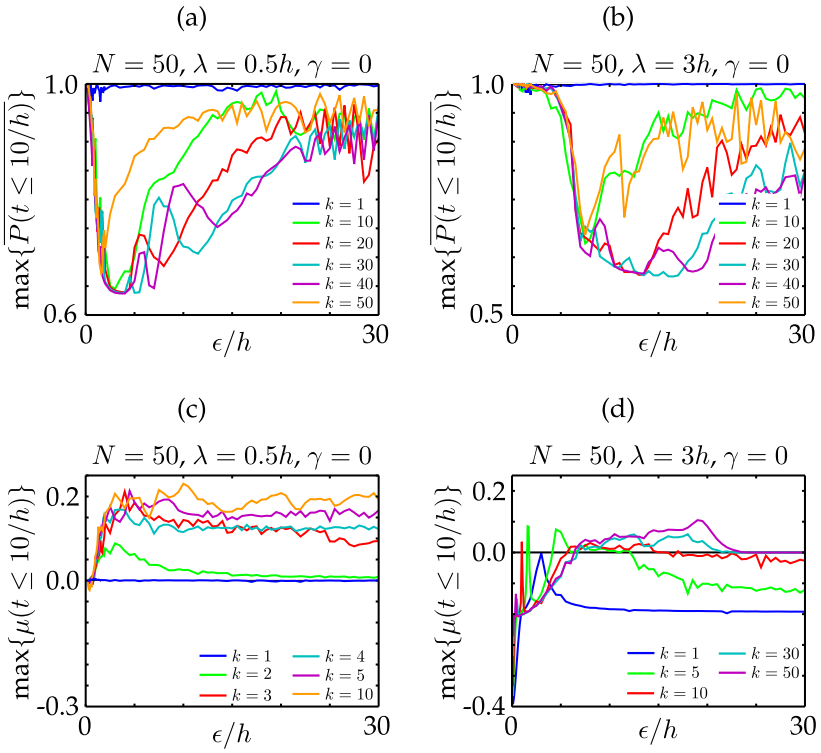


Figure 8.8. LMG interaction: (a) and (b), the maximum value of the purity at $\lambda = 0.5h$ and $\lambda = 3h$ respectively, for rephasing within a time $t \leq 10/h$, as a function of interaction strength ϵ and for various values of k. (c) and (d), the maximum value of $\mu(t)$ within $t \leq 10/h$ at $\lambda = 0.5h$ and $\lambda = 3h$ respectively, as a function of ϵ and for various values of k. Values above zero indicate that the evolution is entanglement breaking.

are suppressed at high interaction strengths for greater link numbers. In the broken phase, high average purities of $\overline{P} > 0.98$ are achieved for any link number below $\epsilon \sim 4h$, whilst in the normal phase this isn't the case and there is an immediate decay of the average purity above $\epsilon = 0$ for $k \neq 1$. As for the Ising interaction, the suppression of maxima is reduced as the interaction strength is further increased, with the rate of increase slowest for link numbers $k \sim$ 30-40. This suggests that our analysis discussed in Sec. 8.3.3, where the induced decoherence was limited by the size of the subspace required to describe the partitioned bath states, has a broader applicability than the Ising interaction alone. Rephasing depends on the number of significant Fourier components for, in this case, the average purity. This quantity is reduced in the limits $\epsilon \ll h$ and $\epsilon \gg h$ for which the interaction term is a small perturbation on the bath Hamiltonian and vice versa respectively.

In Figs. 8.8(c) and 8.8(d) we have plotted the maximum value of $\mu(t)$ within $t \leq 10/h$ for the normal and broken phases respectively. In the normal phase entanglement breaking occurs for $k \neq 1$ at interaction strengths $\epsilon > 0.8h$, whilst in the broken phase the induced decoherence is entanglement breaking for $k \neq 1$ within the range $h < \epsilon < 23h$. It is only the case of coupling via a single link that the qubit is immune to entanglement breaking within the period $t \leq 10/h$.

8.5 Conclusions

To summarize, we have investigated the quantum evolution of a single qubit coupled to a Lipkin-Meshkov-Glick bath as a model for decoherence in solid state quantum memories. The bath, which exhibited a second-order quantum phase transition, was highly symmetric and allowed for exact calculations of the system dynamics for large system sizes, $N \sim 100$ spins. Further, partitioning of the bath was possible without significantly increasing the computational complexity, which allowed us to determine

the effect of increasing exposure of the qubit to the bath spins. Decoherence of the qubit was quantified using the average purity and determining if and when the evolution destroys any entanglement the qubit may have with an external subsystem.

For the qubit interacting via an Ising interaction with just a few bath spins, we observed zero dephasing in the normal phase and almost complete revivals of qubit coherence in the broken phase. The rephasing time, which was sensitive to criticality in the bath, was independent of bath size for large baths and thus faithful qubit storage would be possible in the thermodynamical limit. In general, as the number of links was increased the revivals in the purity were suppressed, which was discussed in terms of the number of components in the Fourier Transform of the decoherence factor. Decoherence was suppressed by the restrictive size of the subspace required to describe the partitioned bath states, which was smallest for just a few links. Further, it is likely that revivals were observed in certain scenarios, even in the thermodynamical limit, because the symmetry of the bath constrained the dynamics to a subspace whose dimension grows only linearly with system size. Such revivals could possibly occur in other systems possessing exchange symmetry that are not as easily amenable to analysis as the LMG model. However, they may be difficult to observe experimentally due to a potential lack of the required bath symmetry in real samples.

In contrast to the Ising interaction, for the dissipative XY-type (LMG) interaction between the qubit and the bath, decoherence was dependent on the energy difference between the two levels of the qubit and additionally was observed in both bath phases. Revivals were found to occur for certain parameter regimes and just a few links between the qubit and the bath. These were once again suppressed as the link number was increased, broadening our analytical discussion for the case of the Ising interaction in terms of the restrictive size of the bath's Hilbert space. Interestingly, the revivals occurred after periods when the evolution was entangle-

ment breaking, indicating a constant transfer of quantum information back and forth between the qubit and bath. Our results were based on a worst-case regime in which the qubit was subjected to an identical transverse field to the bath and in general was found to be less robust against decoherence than the Ising interaction. Thus, systems with Ising interactions coupling only to a small neighborhood of the environment would perform better as quantum memories.

Acknowledgments

This work was supported by the UK EPSRC through projects QIPIRC (GR/S82176/01) and EuroQUAM (EP/E041612/1).

8.A Quantum Operations Formalism and the Jamiolkowski Isomorphism

A powerful tool for considering the evolution of a quantum system is the quantum operations formalism [134]. If the initial state of the quantum system is described in terms of a density operator ρ, the subsequent evolution causes a transformation to a final state given by the mapping $\rho \to \varepsilon\{\rho\}$. The linear, completely positive map ε is known as a quantum operation. For a closed system that implements a particular unitary operation U, the quantum operation is simply $\varepsilon(\rho) = U\rho U^\dagger$. In the same context, the evolution of an open quantum subsystem interacting with some environment R, e.g. a single spin-1/2 interacting with an LMG spin bath, can be described as

$$\varepsilon(\rho) = \mathrm{Tr}_R[U_T(\rho \otimes \rho_R)U_T^\dagger], \tag{8.18}$$

where we consider the total system as closed and obtain the final reduced density operator for the principal subsystem by tracing out the state of the environment

(note that we assume an initial product state for the subsystem and environment).

Although an elegant description, calculating the final state in the above way is often computationally difficult due to the large size of the total Hilbert space. We can instead express Eq. 8.18 explicitly in terms of the principal subsystem's Hilbert space $\mathcal{H}$ as

$$\varepsilon(\rho) = \sum_{i=1}^{d^2} A_i \rho A_i^\dagger, \tag{8.19}$$

where the A_i, which act on $\mathcal{H}$, are known as Kraus operators and d is the dimension of $\mathcal{H}$. Once the Kraus operators are known for a particular type of evolution, one can easily obtain the final state of the open subsystem given any initial state. Importantly, the Kraus operators reveal the nature of the noise induced by the coupling to the environment. For a unital map, which is always the case for the noise described by the coupling to an environment, the Kraus operators satisfy $\sum_i A_i A_i^\dagger = \mathbf{1}$.

An equivalent description of the evolution in Eq. 8.19 can be made in terms of a superoperator Λ. To explain this more fully, consider the Hilbert space $\mathcal{H}$ spanned by basis states $\{|i\rangle \mid i = 0, \cdots, d-1\}$. We can expand any density operator ρ for the system in the operator basis $\{|i\rangle\langle j| \mid i, j = 0, \cdots, d-1\}$, with its corresponding matrix elements ρ_{ij} contained in a d^2-dimensional vector. The superoperator Λ can then be described by a $d^2 \times d^2$ super-matrix with elements

$$\Lambda = \sum_{kl=0}^{d-1} \Lambda_{ij,kl} |k\rangle\langle l|. \tag{8.20}$$

Note that Λ can be inferred from the Kraus operators and vice versa via

$$\Lambda = \sum_{i=1}^{d^2} A_i^* \otimes A_i. \tag{8.21}$$

The Jamiolkowski isomorphism [177] exploits an initial setup of two copies of the

principal subsystem, such that the subsequent evolution transfers all the information about Λ to the final quantum state. The two copies a and b are prepared in the maximally entangled state $|\Psi^+\rangle = \frac{1}{\sqrt{d}}\sum_{i=0}^{d-1}|i\rangle\otimes|i\rangle$ and the superoperator Λ is applied to b as

$$(\mathbf{1}\otimes\Lambda)\{|\Psi^+\rangle\langle\Psi^+|\} = \frac{1}{d}\sum_{ij=0}^{d-1}|i\rangle\langle j|\otimes\Lambda|i\rangle\langle j| = \rho^{\Lambda}. \tag{8.22}$$

The matrix elements of the resulting density operator ρ^{Λ} are related to those of Λ by $d\rho^{\Lambda}_{ikjl} = \Lambda_{ijkl}$, where

$$\rho^{\Lambda} = \sum_{ijkl=0}^{d-1}\rho^{\Lambda}_{ikjl}|i\rangle\langle j|\otimes|k\rangle\langle l|. \tag{8.23}$$

Thus, using the Jamiolkowski isomorphism, it is sufficient to calculate ρ^{Λ} to determine the superoperator Λ, and then trivially the Kraus operators A_i, for any quantum operation $\varepsilon(\rho)$.

8.B The Loschmidt Echo for a single link and an isotropic bath

The GS of an isotropic, ferromagnetically coupled bath is the Dicke state $|N/2, M\rangle$, where $M = N/2$, $\lfloor hN/2\lambda\rceil$ in the normal and broken phases respectively. For $N \gg 1$ the latter can be approximated as $M = hN/2\lambda$. When we partition the bath into a single and $N-1$ spins the Dicke state $|N/2, M\rangle$ decomposes into two terms

$$\begin{aligned}\left|\tfrac{N}{2}, M\right\rangle = c_{1/2}\left|\tfrac{1}{2}, \tfrac{1}{2}\right\rangle\otimes\left|\tfrac{N}{2}-\tfrac{1}{2}, M-\tfrac{1}{2}\right\rangle \\ + c_{-1/2}\left|\tfrac{1}{2}, -\tfrac{1}{2}\right\rangle\otimes\left|\tfrac{N}{2}-\tfrac{1}{2}, M+\tfrac{1}{2}\right\rangle,\end{aligned} \tag{8.24}$$

where the Clebsch-Gordon coefficients are given by

$$c_{1/2} = \left\langle \tfrac{1}{2}, \tfrac{1}{2} \right| \otimes \left\langle \tfrac{N}{2} - \tfrac{1}{2}, M - \tfrac{1}{2} \middle| \tfrac{N}{2}, M \right\rangle = \sqrt{\tfrac{1}{2} + \tfrac{M}{N}}, \tag{8.25}$$

$$c_{-1/2} = \left\langle \tfrac{1}{2}, -\tfrac{1}{2} \right| \otimes \left\langle \tfrac{N}{2} - \tfrac{1}{2}, M + \tfrac{1}{2} \middle| \tfrac{N}{2}, M \right\rangle = \sqrt{\tfrac{1}{2} - \tfrac{M}{N}}. \tag{8.26}$$

Evolution of the GS under the perturbed bath Hamiltonians $H_\pm = H_R \pm \epsilon\sigma_1^z$ for this scenario is restricted to the two states on the RHS of Eq. 8.24. Using these states as a basis, the action of $H_\pm$ on the Dicke state $|N/2, M\rangle$ can be summarised by the matrix equation

$$H_\pm \left| \tfrac{N}{2}, M \right\rangle = h \begin{pmatrix} \alpha \pm \epsilon/h & \beta \\ \beta & \alpha + \zeta \mp \epsilon/h \end{pmatrix} \begin{pmatrix} c_{1/2} \\ c_{-1/2} \end{pmatrix}, \tag{8.27}$$

where

$$\alpha = -\frac{\lambda}{2hN} \left\{ (N-1)^2 - (2M-1)^2 \right\} - 2M, \tag{8.28}$$

$$\beta = -\frac{\lambda}{h} \sqrt{1 - \frac{4M^2}{N^2}}, \tag{8.29}$$

$$\zeta = \frac{4\lambda M}{hN}. \tag{8.30}$$

For $N \gg 1$, the latter two quantities become

$$\beta = -\frac{\lambda}{h} \sqrt{1 - \frac{h^2}{\lambda^2}}, \tag{8.31}$$

$$\zeta = 2. \tag{8.32}$$

By firstly diagonalizing the matrix representations of $H_\pm$ in Eq. 8.27, we can find similar representations for $e^{-iH_\pm t}$ in this basis, given by

$$e^{-iH_\pm t} = \frac{e^{-i(\alpha+1)ht}}{\eta_\pm} \times \begin{pmatrix} \eta_\pm \cos(\eta_\pm t/2) + 2i(h \mp \epsilon)\sin(\eta_\pm t/2) & -2i\beta h \sin(\eta_\pm t/2) \\ -2i\beta h \sin(\eta_\pm t/2) & \eta_\pm \cos(\eta_\pm t/2) - 2i(h \mp \epsilon)\sin(\eta_\pm t/2) \end{pmatrix}, \tag{8.33}$$

where $\eta_\pm = 2\sqrt{\lambda^2 + \epsilon(\epsilon \mp 2h)}$. The LE for the broken phase ($\lambda > h$) can now be calculated by multiplying the matrix forms of $(e^{-iH_+ t})^\dagger$ and $e^{-iH_+ t}$, and taking the expectation value with respect to the GS, i.e.

$$L(t) = \left| \left(c_{1/2}, c_{-1/2}\right) \left[e^{-iH_+ t}\right]^\dagger e^{-iH_- t} \begin{pmatrix} c_{1/2} \\ c_{-1/2} \end{pmatrix} \right|^2. \tag{8.34}$$

The resulting expression for the LE is complicated and need not be written here explicitly. Importantly, we can see revivals of full qubit coherence occur at times $t = l\tau_c$ that satisfy both $\eta_-\tau_c = 2l_-\pi$ and $\eta_+\tau_c = 2l_+\pi$, where l, l_- and l_+ are all integers; at these times the matrices $e^{-iH_\pm t}$ in Eq. 8.33 and are both equal to the identity. In the limit $\epsilon \ll h$ the two frequencies are approximately equal and the coherence time is $\tau_c = \pi/\lambda$.

Chapter 9

Conclusion

In this thesis we have investigated the physics of systems of cold atoms in optical lattices, in particular in the context of simulation of quantum spin Hamiltonians. Here, we summarise the main results of this work:

- In chapter 2 of this thesis we examined numerical methods for calculating maximally localised generalised Wannier functions for optical lattice systems. These functions provide a complete, orthonormal basis in terms of individual lattice sites, from which one can calculate the microscopic hopping and interaction parameters, and thus reduce the many-body Hamiltonian to one containing only local interactions. Importantly, generalised Wannier functions are required when the bands are degenerate. We presented modifications to an algorithm devised by Marzari and Vanderbilt [71] for minimising the total spread of the generalised Wannier functions via steepest-descent, which in our experience suffered from initialisation issues resulting in the procedure becoming trapped in local minima of the spread functional. Specifically, our method involves pre-processing the input Bloch eigenstates using an algorithm based on that of Souza *et al.* [72] to vastly reduce the spread of the initial configuration, thus allowing the steepest-descent procedure to find the global

minimum without fail. Moreover, our method requires no prior knowledge of the form of the maximally localised generalised Wannier functions and is therefore easier to apply in comparison with the initialisation step in Ref. [71]. We also discussed common scenarios for optical lattice systems for which an iterative minimisation can be avoided. Instead, the maximally localised Wannier functions can be obtained directly by appropriately adjusting the phases of the Bloch eigenstates during a single pass through the Brillouin zone.

- In chapters 3 and 4 we applied these methods to optical lattice systems in one- and two-dimensions. We presented results for the hopping and interaction parameters for a variety of geometries, including hexagonal and Kagomé, which have degenerate lower bands. We showed that these systems realise the Bose-Hubbard model where hopping occurs between neighbouring potential minima, and further demonstrated in chapter 5 that the superfluid-Mott insulator transition can be achieved in a rhombic optical lattice at fixed lattice depth by adjusting the acute angle of the unit cell. We also showed that generalised Wannier functions, which are generated by mixing states between bands, can provide a more optimal basis for the purposes of reducing the Hamiltonian to one including only local interactions, even when the bands are not degenerate. Our results suggested that this is true when the potential exhibits multiple minima of similar depths per lattice unit cell corresponding to vanishing band gaps between the bands.

- In chapters 7 and 8 we investigated two spin-1/2 systems with long-range interactions as paradigm examples of the models that can be simulated using optical lattices loaded with dipolar molecules. Using the infinite density matrix renormalisation group method we calculated the critical properties of a 1D spin-1/2 Ising chain possessing exponentially decaying interactions as

the range of the interactions was increased. We observed a diverging critical point indicating that an increasing coordination number stabilises the ferromagnetic phase against the effect of a transverse field. Moreover, the critical point was found to converge towards the mean-field value indicating a smooth approach to the classical limit. In chapter 8 we employed the infinite-ranged Lipkin-Meshkov-Glick model as an environment for a single spin-1/2 in order to study decoherence in solid state quantum memories. We observed revivals of the initial qubit state in certain parameter regimes, which may become independent of the bath size for large baths. This was likely a result of the high degree of symmetry of the bath causing the dynamics to be constrained to a subspace whose dimension grows only linearly with system size.

Finally, we would like to discuss possible directions for future research:

- Our work on calculating maximally localised generalised Wannier functions has opened up a wide variety of optical lattice geometries for detailed investigation. In this thesis we demonstrated our methods using a selection of one- and two-dimensional systems, however, these methods work equally well for three-dimensional systems. For example, generalised Wannier functions for lattice structures such as face-centred-cubic and body-centred-cubic, which are prominent in condensed matter physics, could easily be calculated. Optical lattices systems with these structures can be generated as discussed in Ref. [28], and could lead to observations of rich quantum phases similar to those expected for two-dimensional geometries such as triangular and Kagomé.

- Our results for the two-dimensional geometries have shown that the generalised Wannier functions exhibit the same symmetry as the underlying lattice and therefore differ significantly from the Gaussian functions that are assumed in other works. Therefore, it would be interesting to re-evaluate the microscopic

parameters determined in these works, for example as was calculated in Ref. [31] for a trimerised Kagomé lattice.

- For the two-dimensional geometries with degenerate bands examined in this thesis we observed that a specific gauge exists such that the Berry curvature of each band is zero, and therefore the band-diagonal part of the spread for each band can also be made to be zero. This in agreement with the conjecture in Ref. [71] that the set of maximally localised generalised Wannier functions are always real. We expect a rigorous mathematical proof may exist to account for these observations, however, we were not able to determine one in this work. Such a proof may allow for a more direct approach in determining the maximally localised generalised Wannier without the need for iterative calculations.

- Through our work in examining quantum spin systems with long- and infinite-ranged interactions we observed a variety of interesting phenomena, notably a smooth approach to a mean-field regime via increasing the range of the interactions, and revivals of qubit coherence that are expected to persist in the thermodynamic limit. While these systems may be difficult to realise with current technology, the recent progress towards optical lattices with dipolar molecules opens the possibility of simulating long-ranged spin systems for which these results could provide relevant theoretical understanding. We look forward to future experiments and further progress in this line of research.

Bibliography

[1] M. Lewenstein, A. Sanpera, V. Ahufinger, B. Damski, A. Sen(De), and U. Sen. Ultracold atomic gases in optical lattices: mimicking condensed matter physics and beyond. *Advances in Physics* **56**(2), 243–379 March (2007).

[2] H.J. Metcalf and P. van der Straten. *Laser Cooling and Trapping*. Springer, New York, (1999).

[3] M.H. Anderson, J.R. Ensher, M.R. Matthews, C.E. Wieman, and E.A. Cornell. Observation of bose-einstein condensation in a dilute atomic vapor. *Science (New York, N.Y.)* **269**(5221), 198–201 July (1995).

[4] K. Davis, M. Mewes, M.R. Andrews, N. van Druten, D.S. Durfee, D.M. Kurn, and W. Ketterle. Bose-Einstein Condensation in a Gas of Sodium Atoms. *Physical Review Letters* **75**(22), 3969–3973 November (1995).

[5] L. Pitaevskii and S. Stringari. *Bose-Einstein Condensation*. Oxford University Press, Oxford, (2003).

[6] M.R. Andrews, C.G. Townsend, H.-J. Miesner, D.S. Durfee, D.M. Kurn, and W. Ketterle. Observation of Interference Between Two Bose Condensates. *Science* **275**(5300), 637–641 January (1997).

[7] I. Bloch, T.W. Hansch, and T. Esslinger. Measurement of the spatial coherence of a trapped Bose gas at the phase transition. *Nature* **403**(6766), 166–70 January (2000).

[8] J. Denschlag, J.E. Simsarian, D.L. Feder, C.W. Clark, L.A. Collins, J. Cubizolles, L. Deng, E.W. Hagley, K. Helmerson, W.P. Reinhardt, S.L. Rolston, B.I. Schneider, and W.D. Phillips. Generating Solitons by Phase Engineering of a Bose-Einstein Condensate. *Science* **287**(5450), 97–101 January (2000).

[9] M.R. Matthews, B.P. Anderson, P. Haljan, D. Hall, C.E. Wieman, and E.A. Cornell. Vortices in a Bose-Einstein Condensate. *Physical Review Letters* **83**(13), 2498–2501 September (1999).

[10] J.R. Abo-Shaeer, C. Raman, J.M. Vogels, and W. Ketterle. Observation of vortex lattices in Bose-Einstein condensates. *Science (New York, N.Y.)* **292**(5516), 476–9 April (2001).

[11] B. DeMarco and D.S. Jin. Onset of Fermi Degeneracy in a Trapped Atomic Gas. *Science* **285**(5434), 1703–1706 September (1999).

[12] G. Roati, F. Riboli, G. Modugno, and M. Inguscio. Fermi-Bose Quantum Degenerate K40-R87b Mixture with Attractive Interaction. *Physical Review Letters* **89**(15), 150403 September (2002).

[13] D. Jaksch, C. Bruder, J.I. Cirac, C.W. Gardiner, and P. Zoller. Cold Bosonic Atoms in Optical Lattices. *Physical Review Letters* **81**(15), 3108–3111 October (1998).

[14] M. Greiner, O. Mandel, T. Esslinger, T.W. Hänsch, and I. Bloch. Quantum phase transition from a superfluid to a Mott insulator in a gas of ultracold atoms. *Nature* **415**(6867), 39–44 January (2002).

[15] E. Altman, E. Demler, and M. Lukin. Probing many-body states of ultracold atoms via noise correlations. *Physical Review A* **70**(1), 013603 July (2004).

[16] S. Fölling, F. Gerbier, A. Widera, O. Mandel, T. Gericke, and I. Bloch. Spatial quantum noise interferometry in expanding ultracold atom clouds. *Nature* **434**(7032), 481–4 March (2005).

[17] D. Jaksch and P. Zoller. The cold atom Hubbard toolbox. *Annals of Physics* **315**(1), 52–79 January (2005).

[18] D. Schrader, I. Dotsenko, M. Khudaverdyan, Y. Miroshnychenko, A. Rauschenbeutel, and D. Meschede. Neutral Atom Quantum Register. *Physical Review Letters* **93**(15), 150501 October (2004).

[19] D. Jaksch, H.-J. Briegel, J.I. Cirac, C.W. Gardiner, and P. Zoller. Entanglement of Atoms via Cold Controlled Collisions. *Physical Review Letters* **82**(9), 1975–1978 March (1999).

[20] T. Calarco, H.-J. Briegel, D. Jaksch, J.I. Cirac, and P. Zoller. Quantum Computing with Trapped Particles in Microscopic Potentials. *Fortschritte der Physik* **48**(9-11), 945–955 September (2000).

[21] G. Brennen, C. Caves, P. Jessen, and I. Deutsch. Quantum Logic Gates in Optical Lattices. *Physical Review Letters* **82**(5), 1060–1063 February (1999).

[22] G. Brennen, I. Deutsch, and P. Jessen. Entangling dipole-dipole interactions for quantum logic with neutral atoms. *Physical Review A* **61**(6), 62309 May (2000).

[23] T.D. Ladd, F. Jelezko, R. Laflamme, Y. Nakamura, C. Monroe, and J.L. O'Brien. Quantum computers. *Nature* **464**(7285), 45–53 March (2010).

[24] I. Bloch, J. Dalibard, and W. Zwerger. Many-body physics with ultracold gases. *Reviews of Modern Physics* **80**(3), 885–964 July (2008).

[25] M.P.A. Fisher, G. Grinstein, and D.S. Fisher. Boson localization and the superfluid-insulator transition. *Physical Review B* **40**(1), 546–570 July (1989).

[26] B. Paredes, A. Widera, V. Murg, O. Mandel, S. Fölling, J.I. Cirac, G.V. Shlyapnikov, T.W. Hänsch, and I. Bloch. Tonks-Girardeau gas of ultracold atoms in an optical lattice. *Nature* **429**(6989), 277–81 May (2004).

[27] Z. Hadzibabic, P. Krüger, M. Cheneau, B. Battelier, and J. Dalibard. Berezinskii-Kosterlitz-Thouless crossover in a trapped atomic gas. *Nature* **441**(7097), 1118–21 June (2006).

[28] K. Petsas, A. Coates, and G. Grynberg. Crystallography of optical lattices. *Physical Review A* **50**(6), 5173–5189 December (1994).

[29] C. Becker, P. Soltan-Panahi, J. Kronjäger, S. Dörscher, K. Bongs, and K. Sengstock. Ultracold quantum gases in triangular optical lattices. *New Journal of Physics* **12**(6), 065025 June (2010).

[30] J. Struck, C. Ölschläger, R. Le Targat, P. Soltan-Panahi, A. Eckardt, M. Lewenstein, P. Windpassinger, and K. Sengstock. Quantum simulation of frustrated classical magnetism in triangular optical lattices. *Science (New York, N.Y.)* **333**(6045), 996–9 August (2011).

[31] L. Santos, M. Baranov, J.I. Cirac, H.-U. Everts, H. Fehrmann, and M. Lewenstein. Atomic Quantum Gases in Kagomé Lattices. *Physical Review Letters* **93**(3), 030601 July (2004).

[32] J. Ruostekoski. Optical Kagome Lattice for Ultracold Atoms with Nearest Neighbor Interactions. *Physical Review Letters* **103**(8), 080406 August (2009).

[33] S. Peil, J. Porto, B. Tolra, J. Obrecht, B. King, M. Subbotin, S.L. Rolston, and W.D. Phillips. Patterned loading of a Bose-Einstein condensate into an optical lattice. *Physical Review A* **67**(5), 051603 May (2003).

[34] B. Vaucher, S.R. Clark, U. Dorner, and D. Jaksch. Fast initialization of a high-fidelity quantum register using optical superlattices. *New Journal of Physics* **9**(7), 221–221 July (2007).

[35] J. Billy, V. Josse, Z. Zuo, A. Bernard, B. Hambrecht, P. Lugan, D. Clément, L. Sanchez-Palencia, P. Bouyer, and A. Aspect. Direct observation of Anderson

localization of matter waves in a controlled disorder. *Nature* **453**(7197), 891–4 June (2008).

[36] G. Roati, C. D'Errico, L. Fallani, M. Fattori, C. Fort, M. Zaccanti, G. Modugno, M. Modugno, and M. Inguscio. Anderson localization of a non-interacting Bose-Einstein condensate. *Nature* **453**(7197), 895–8 June (2008).

[37] M. White, M. Pasienski, D. McKay, S.Q. Zhou, D. Ceperley, and B. DeMarco. Strongly Interacting Bosons in a Disordered Optical Lattice. *Physical Review Letters* **102**(5), 055301 February (2009).

[38] B.P. Anderson and M.A. Kasevich. Macroscopic Quantum Interference from Atomic Tunnel Arrays. *Science* **282**(5394), 1686–1689 November (1998).

[39] O. Morsch, J. Müller, M. Cristiani, D. Ciampini, and E. Arimondo. Bloch Oscillations and Mean-Field Effects of Bose-Einstein Condensates in 1D Optical Lattices. *Physical Review Letters* **87**(14), 140402 September (2001).

[40] S. Inouye, M.R. Andrews, J. Stenger, H.-J. Miesner, and W. Ketterle. Observation of Feshbach resonances in a BoseEinstein condensate. *Nature* **392**, 151–154 (1998).

[41] E. Timmermans, P. Tommasini, M. Hussein, and A. Kerman. Feshbach resonances in atomic BoseEinstein condensates. *Physics Reports* **315**(1-3), 199–230 July (1999).

[42] S.L. Cornish, N.R. Claussen, J.L. Roberts, E.A. Cornell, and C.E. Wieman. Stable ˆ{85}Rb Bose-Einstein Condensates with Widely Tunable Interactions. *Physical Review Letters* **85**(9), 1795–1798 August (2000).

[43] T. Lahaye, C. Menotti, L. Santos, M. Lewenstein, and T. Pfau. The physics of dipolar bosonic quantum gases. *Reports on Progress in Physics* **72**(12), 126401 December (2009).

[44] K. Góral, L. Santos, and M. Lewenstein. Quantum Phases of Dipolar Bosons in Optical Lattices. *Physical Review Letters* **88**(17), 170406 April (2002).

[45] C. Menotti, C. Trefzger, and M. Lewenstein. Metastable States of a Gas of Dipolar Bosons in a 2D Optical Lattice. *Physical Review Letters* **98**(23), 235301 June (2007).

[46] C. Trefzger, C. Menotti, and M. Lewenstein. Ultracold dipolar gas in an optical lattice: The fate of metastable states. *Physical Review A* **78**(4), 043604 October (2008).

[47] A. Sø rensen, E. Demler, and M. Lukin. Fractional Quantum Hall States of Atoms in Optical Lattices. *Physical Review Letters* **94**(8), 086803 March (2005).

[48] R. Palmer and D. Jaksch. High-Field Fractional Quantum Hall Effect in Optical Lattices. *Physical Review Letters* **96**(18), 180407 May (2006).

[49] J. Struck, C. Ölschläger, M. Weinberg, P. Hauke, J. Simonet, A. Eckardt, M. Lewenstein, K. Sengstock, and P. Windpassinger. Tunable Gauge Potential for Neutral and Spinless Particles in Driven Optical Lattices. *Physical Review Letters* **108**(22), 225304 May (2012).

[50] K. Jiménez-García, L. LeBlanc, R.A. Williams, M. Beeler, A. Perry, and I. Spielman. Peierls Substitution in an Engineered Lattice Potential. *Physical Review Letters* **108**(22), 225303 May (2012).

[51] R.A. Williams, S. Al-Assam, and C.J. Foot. Observation of Vortex Nucleation in a Rotating Two-Dimensional Lattice of Bose-Einstein Condensates. *Physical Review Letters* **104**(5), 050404 February (2010).

[52] M. Aidelsburger, M. Atala, S. Nascimbène, S. Trotzky, Y.-A. Chen, and I. Bloch. Experimental Realization of Strong Effective Magnetic Fields in an

Optical Lattice. *Physical Review Letters* **107**(25), 255301 December (2011).

[53] S.R. White. Density matrix formulation for quantum renormalization groups. *Physical Review Letters* **69**(19), 2863–2866 November (1992).

[54] S.R. White. Density-matrix algorithms for quantum renormalization groups. *Physical Review B* **48**(14), 10345–10356 October (1993).

[55] G. Vidal. Efficient Classical Simulation of Slightly Entangled Quantum Computations. *Physical Review Letters* **91**(14), 147902 October (2003).

[56] G. Vidal. Efficient Simulation of One-Dimensional Quantum Many-Body Systems. *Physical Review Letters* **93**(4), 040502 July (2004).

[57] S.M. Barnett and P.M. Radmore. *Methods in Theoretical Quantum Optics*. Oxford University Press, Oxford, (2002).

[58] E.T. Jaynes and F.W. Cummings. Comparison of quantum and semiclassical radiation theories with application to the beam maser. *Proceedings of the IEEE* **51**(1), 89–109 (1963).

[59] S.R. Clark. *Strongly correlated one-dimensional systems of cold atoms in optical lattices*. PhD thesis, University of Oxford, (2007).

[60] C. Cohen-Tannoudji, J. Dupont-Roc, and G. Grynberg. *Atom-Photon Interactions: Basic Processes and Applications*. Wiley, New York, (1998).

[61] I. Bloch. Ultracold quantum gases in optical lattices. *Nature Physics* **1**(1), 23–30 October (2005).

[62] O. Mandel, M. Greiner, A. Widera, T. Rom, T.W. Hänsch, and I. Bloch. Controlled collisions for multi-particle entanglement of optically trapped atoms. *Nature* **425**(6961), 937–40 October (2003).

[63] B. Vaucher, A. Nunnenkamp, and D. Jaksch. Creation of resilient entangled states and a resource for measurement-based quantum computation with optical superlattices. *New Journal of Physics* **10**(2), 023005 February (2008).

[64] C. Maschler and H. Ritsch. Cold Atom Dynamics in a Quantum Optical Lattice Potential. *Physical Review Letters* **95**(26), 260401 December (2005).

[65] N.W. Ashcroft and D. Mermin. *Solid State Physics*. Holt, Rinehardt and Winston, New York, (1976).

[66] G. Wannier. The Structure of Electronic Excitation Levels in Insulating Crystals. *Physical Review* **52**(3), 191–197 August (1937).

[67] J. Li, Y. Yu, A.M. Dudarev, and Q. Niu. Interaction broadening of Wannier functions and Mott transitions in atomic BEC. *New Journal of Physics* **8**(8), 154 August (2006).

[68] Z.X. Liang, B.B. Hu, and B. Wu. Interaction Effects on Wannier Functions of a Bose-Einstein Condensate in an Optical Lattice and Implications for Bose-Hubbard Model. *arXiv:0903.4058* March (2009).

[69] D. van Oosten, P. van der Straten, and H. Stoof. Mott insulators in an optical lattice with high filling factors. *Physical Review A* **67**(3), 033606 March (2003).

[70] F. Haake. *Quantum Signatures of Chaos*. Springer, New York, 3rd edition, (2010).

[71] N. Marzari and D. Vanderbilt. Maximally localized generalized Wannier functions for composite energy bands. *Physical Review B* **56**(20), 12847–12865 November (1997).

[72] I. Souza, N. Marzari, and D. Vanderbilt. Maximally localized Wannier functions for entangled energy bands. *Physical Review B* **65**(3), 035109 December (2001).

[73] A.A. Mostofi, J.R. Yates, Y.-S. Lee, I. Souza, D. Vanderbilt, and N. Marzari. wannier90: A tool for obtaining maximally-localised Wannier functions. *Computer Physics Communications* **178**(9), 685–699 May (2008).

[74] R. Resta. Manifestations of Berry's phase in molecules and condensed matter. *Journal of Physics: Condensed Matter* **12**(9), R107–R143 March (2000).

[75] M.V. Berry. Quantal Phase Factors Accompanying Adiabatic Changes. *Proceedings of the Royal Society A: Mathematical, Physical and Engineering Sciences* **392**(1802), 45–57 March (1984).

[76] J. Zak. Berrys phase for energy bands in solids. *Physical Review Letters* **62**(23), 2747–2750 June (1989).

[77] J. Zak. Band CenterA Conserved Quantity in Solids. *Physical Review Letters* **48**(5), 359–362 February (1982).

[78] H. Büchler, G. Blatter, and W. Zwerger. Commensurate-Incommensurate Transition of Cold Atoms in an Optical Lattice. *Physical Review Letters* **90**(13), 130401 April (2003).

[79] D.J. Griffiths. *Introduction to quantum mechanics*. Pearson Prentice Hall, New Jersey, 2nd edition, (2004).

[80] J. Sebby-Strabley, M. Anderlini, P. Jessen, and J. Porto. Lattice of double wells for manipulating pairs of cold atoms. *Physical Review A* **73**(3), 033605 March (2006).

[81] B. Damski, H. Fehrmann, H.-U. Everts, M. Baranov, L. Santos, and M. Lewenstein. Quantum gases in trimerized kagomé lattices. *Physical Review A* **72**(5), 053612 November (2005).

[82] P.B. Blakie and C.W. Clark. Wannier states and Bose-Hubbard parameters for 2D optical lattices. *Journal of Physics B: Atomic, Molecular and Optical Physics* **37**(7), 1391–1404 April (2004).

[83] G.-B. Jo, J. Guzman, C. Thomas, P. Hosur, A. Vishwanath, and D. Stamper-Kurn. Ultracold Atoms in a Tunable Optical Kagome Lattice. *Physical Review Letters* **108**(4), 045305 January (2012).

[84] W. Krauth. Bethe ansatz for the one-dimensional boson Hubbard model. *Physical Review B* **44**(17), 9772–9775 November (1991).

[85] A.R. Kolovsky and A. Buchleitner. Quantum chaos in the Bose-Hubbard model. *Europhysics Letters (EPL)* **68**(5), 632–638 December (2004).

[86] E. Calzetta, B.B. Hu, and A. Rey. Bose-Einstein-condensate superfluidMott-insulator transition in an optical lattice. *Physical Review A* **73**(2), 023610 February (2006).

[87] K. Sheshadri, H.R. Krishnamurthy, R. Pandit, and T.V. Ramakrishnan. Superfluid and Insulating Phases in an Interacting-Boson Model: Mean-Field Theory and the RPA. *Europhysics Letters (EPL)* **22**(4), 257–263 May (1993).

[88] D. van Oosten, P. van der Straten, and H. Stoof. Quantum phases in an optical lattice. *Physical Review A* **63**(5), 053601 April (2001).

[89] W. Krauth, M. Caffarel, and J.-P. Bouchaud. Gutzwiller wave function for a model of strongly interacting bosons. *Physical Review B* **45**(6), 3137–3140 February (1992).

[90] D. Rokhsar and B. Kotliar. Gutzwiller projection for bosons. *Physical Review B* **44**(18), 10328–10332 November (1991).

[91] W. Zwerger. Mott Hubbard transition of cold atoms in optical lattices. *Journal of Optics B: Quantum and Semiclassical Optics* **5**(2), S9–S16 April (2003).

[92] C. Schroll, F. Marquardt, and C. Bruder. Perturbative corrections to the Gutzwiller mean-field solution of the Mott-Hubbard model. *Physical Review A* **70**(5), 053609 November (2004).

[93] J. Als-Nielsen and R.J. Birgeneau. Mean field theory, the Ginzburg criterion, and marginal dimensionality of phase transitions. *American Journal of Physics* **45**(6), 554 (1977).

[94] B. Capogrosso-Sansone, N.V. Prokof'ev, and B. Svistunov. Phase diagram and thermodynamics of the three-dimensional Bose-Hubbard model. *Physical Review B* **75**(13), 134302 April (2007).

[95] S. Wessel, F. Alet, M. Troyer, and G. Batrouni. Quantum Monte Carlo simulations of confined bosonic atoms in optical lattices. *Physical Review A* **70**(5), 053615 November (2004).

[96] T.D. Kühner, S.R. White, and H. Monien. One-dimensional Bose-Hubbard model with nearest-neighbor interaction. *Physical Review B* **61**(18), 12474–12489 May (2000).

[97] J. Freericks and H. Monien. Strong-coupling expansions for the pure and disordered Bose-Hubbard model. *Physical Review B* **53**(5), 2691–2700 February (1996).

[98] T.D. Kühner and H. Monien. Phases of the one-dimensional Bose-Hubbard model. *Physical Review B* **58**(22), R14741 December (1997).

[99] M. Pino, J. Prior, A. Somoza, D. Jaksch, and S.R. Clark. Reentrance and entanglement in the one-dimensional Bose-Hubbard model. *Physical Review A* **86**(2), 023631 August (2012).

[100] L.-M. Duan, E. Demler, and M. Lukin. Controlling Spin Exchange Interactions of Ultracold Atoms in Optical Lattices. *Physical Review Letters* **91**(9), 090402

August (2003).

[101] J.J. García-Ripoll and J.I. Cirac. Spin dynamics for bosons in an optical lattice. *New Journal of Physics* **5**, 76 June (2003).

[102] E.A. Donley, N.R. Claussen, S.T. Thompson, and C.E. Wieman. Atom-molecule coherence in a Bose-Einstein condensate. *Nature* **417**(6888), 529–33 May (2002).

[103] A. Griesmaier, J. Werner, S. Hensler, J. Stuhler, and T. Pfau. Bose-Einstein Condensation of Chromium. *Physical Review Letters* **94**(16), 160401 April (2005).

[104] J. Stuhler, A. Griesmaier, T. Koch, M. Fattori, T. Pfau, S. Giovanazzi, P. Pedri, and L. Santos. Observation of Dipole-Dipole Interaction in a Degenerate Quantum Gas. *Physical Review Letters* **95**(15), 150406 October (2005).

[105] M. Baranov. Theoretical progress in many-body physics with ultracold dipolar gases. *Physics Reports* **464**(3), 71–111 August (2008).

[106] B. Capogrosso-Sansone, C. Trefzger, M. Lewenstein, P. Zoller, and G. Pupillo. Quantum Phases of Cold Polar Molecules in 2D Optical Lattices. *Physical Review Letters* **104**(12), 125301 March (2010).

[107] C. Trefzger. *Ultracold Dipolar Gases in Optical Lattices*. PhD thesis, Institut de Ciències Fotòniques, (2010).

[108] S. Sachdev. *Quantum Phase Transitions*. Cambridge University Press, Cambridge, (2001).

[109] A. Dutta and J. Bhattacharjee. Phase transitions in the quantum Ising and rotor models with a long-range interaction. *Physical Review B* **64**(18), 184106 October (2001).

[110] F.J. Dyson. Existence of a phase-transition in a one-dimensional Ising ferromagnet. *Communications in Mathematical Physics* **12**(2), 91–107 June (1969).

[111] J.L. Cardy. One-dimensional models with 1/r 2 interactions. *Journal of Physics A: Mathematical and General* **14**(6), 1407–1415 June (1981).

[112] S. Cannas and F. Tamarit. Long-range interactions and nonextensivity in ferromagnetic spin models. *Physical Review B* **54**(18), R12661–R12664 November (1996).

[113] M. Dalmonte, G. Pupillo, and P. Zoller. One-Dimensional Quantum Liquids with Power-Law Interactions: The Luttinger Staircase. *Physical Review Letters* **105**(14), 140401 September (2010).

[114] A.W. Sandvik. Ground States of a Frustrated Quantum Spin Chain with Long-Range Interactions. *Physical Review Letters* **104**(13), 137204 March (2010).

[115] T. Koffel, M. Lewenstein, and L. Tagliacozzo. Entanglement entropy for the long range Ising chain. , 5 July (2012).

[116] K. Kremer, M. Robbins, and G. Grest. Phase Diagram of Yukawa Systems: Model for Charge-Stabilized Colloids. *Physical Review Letters* **57**(21), 2694–2697 November (1986).

[117] S. Hamaguchi, R.T. Farouki, and D.H.E. Dubin. Phase diagram of Yukawa systems near the one-component-plasma limit revisited. *The Journal of Chemical Physics* **105**(17), 7641 (1996).

[118] D.S. Petrov, G.E. Astrakharchik, D.J. Papoular, C. Salomon, and G.V. Shlyapnikov. Crystalline Phase of Strongly Interacting Fermi Mixtures. *Physical Review Letters* **99**(13), 130407 September (2007).

[119] O.N. Osychenko, G.E. Astrakharchik, F. Mazzanti, and J. Boronat. Zero-temperature phase diagram of Yukawa bosons. *Physical Review A* **85**(6), 063604 June (2012).

[120] T. Lahaye, T. Koch, B. Fröhlich, M. Fattori, J. Metz, A. Griesmaier, S. Giovanazzi, and T. Pfau. Strong dipolar effects in a quantum ferrofluid. *Nature* **448**(7154), 672–5 August (2007).

[121] K.-K. Ni, S. Ospelkaus, M.H.G. de Miranda, A. Pe'er, B. Neyenhuis, J.J. Zirbel, S. Kotochigova, P.S. Julienne, D.S. Jin, and J. Ye. A high phase-space-density gas of polar molecules. *Science (New York, N.Y.)* **322**(5899), 231–5 October (2008).

[122] M. Lu, N. Burdick, S. Youn, and B. Lev. Strongly Dipolar Bose-Einstein Condensate of Dysprosium. *Physical Review Letters* **107**(19), 190401 October (2011).

[123] J. Kestner, B. Wang, J. Sau, and S. Das Sarma. Prediction of a gapless topological Haldane liquid phase in a one-dimensional cold polar molecular lattice. *Physical Review B* **83**(17), 1–8 May (2011).

[124] A. Gorshkov, S. Manmana, G. Chen, J. Ye, E. Demler, M. Lukin, and A. Rey. Tunable Superfluidity and Quantum Magnetism with Ultracold Polar Molecules. *Physical Review Letters* **107**(11), 1–5 September (2011).

[125] P. Pfeuty. The one-dimensional Ising model with a transverse field. *Annals of Physics* **57**(1), 79–90 March (1970).

[126] J. Binney. *The Theory of Critical Phenomena: An Introduction to the Renormalization Group.* Clarendon Press, Oxford, (1992).

[127] P. Sen and B. Chakrabarti. Ising models with competing axial interactions in transverse fields. *Physical Review B* **40**(1), 760–762 July (1989).

[128] E. Lieb, T. Schultz, and D. Mattis. Two soluble models of an antiferromagnetic chain. *Annals of Physics* **16**(3), 407–466 December (1961).

[129] K. Wilson and J. Kogut. The renormalization group and the ϵ expansion. *Physics Reports* **12**(2), 75–199 August (1974).

[130] L. P. Kadanoff. Scaling laws for Ising models near Tc. *Physics* **2**, 263 (1966).

[131] S. Drell, M. Weinstein, and S. Yankielowicz. Quantum field theories on a lattice: Variational methods for arbitrary coupling strengths and the Ising model in a transverse magnetic field. *Physical Review D* **16**(6), 1769–1781 September (1977).

[132] I.P. McCulloch. Infinite size density matrix renormalization group, revisited. *arXiv:0804.2509* April (2008).

[133] R. Orús and G. Vidal. Infinite time-evolving block decimation algorithm beyond unitary evolution. *Physical Review B* **78**(15), 155117 October (2008).

[134] M.A. Nielsen and I.L. Chuang. *Quantum Computation and Quantum Information*. Cambridge University Press, Cambridge, (2000).

[135] N. Gisin, G. Ribordy, W. Tittel, and H. Zbinden. Quantum cryptography. *Reviews of Modern Physics* **74**(1), 145–195 March (2002).

[136] H.-J. Briegel, W. Dür, J.I. Cirac, and P. Zoller. Quantum Repeaters: The Role of Imperfect Local Operations in Quantum Communication. *Physical Review Letters* **81**(26), 5932–5935 December (1998).

[137] L.-M. Duan, M. Lukin, J.I. Cirac, and P. Zoller. Long-distance quantum communication with atomic ensembles and linear optics. *Nature* **414**(6862), 413–8 November (2001).

[138] A. Acín, J.I. Cirac, and M. Lewenstein. Entanglement percolation in quantum networks. *Nature Physics* **3**(4), 256–259 February (2007).

[139] S. Broadfoot, U. Dorner, and D. Jaksch. Entanglement percolation with bipartite mixed states. *EPL (Europhysics Letters)* **88**(5), 50002 December (2009).

[140] S. Perseguers, J.I. Cirac, and J. Wehr. Entanglement distribution in pure-state quantum networks. *Physical Review A* **77**(2), 022308 February (2008).

[141] N.V. Prokof'ev and P.C.E. Stamp. Theory of the spin bath. *Reports on Progress in Physics* **63**(4), 669–726 April (2000).

[142] J.M. Taylor, A. Imamoglu, and M. Lukin. Controlling a Mesoscopic Spin Environment by Quantum Bit Manipulation. *Physical Review Letters* **91**(24), 246802 December (2003).

[143] J.J.L. Morton, A.M. Tyryshkin, R.M. Brown, S. Shankar, B.W. Lovett, A. Ardavan, T. Schenkel, E.E. Haller, J.W. Ager, and S.A. Lyon. Solid-state quantum memory using the 31P nuclear spin. *Nature* **455**(7216), 1085–1088 October (2008).

[144] A. Imamoglu, D.D. Awschalom, G. Burkard, D.P. DiVincenzo, D. Loss, M. Sherwin, and A. Small. Quantum Information Processing Using Quantum Dot Spins and Cavity QED. *Physical Review Letters* **83**(20), 4204–4207 November (1999).

[145] L. Childress, M.V. Gurudev Dutt, J.M. Taylor, A.S. Zibrov, F. Jelezko, J. Wrachtrup, P.R. Hemmer, and M. Lukin. Coherent dynamics of coupled electron and nuclear spin qubits in diamond. *Science (New York, N.Y.)* **314**(5797), 281–5 October (2006).

[146] W. Zurek. Environment-induced superselection rules. *Physical Review D* **26**(8), 1862–1880 October (1982).

[147] S. Paganelli, F. de Pasquale, and S. Giampaolo. Decoherence slowing down in a symmetry-broken environment. *Physical Review A* **66**(5), 052317 November

(2002).

[148] H.-P. Breuer, D. Burgarth, and F. Petruccione. Non-Markovian dynamics in a spin star system: Exact solution and approximation techniques. *Physical Review B* **70**(4), 045323 July (2004).

[149] F. Cucchietti, J. Paz, and W. Zurek. Decoherence from spin environments. *Physical Review A* **72**(5), 052113 November (2005).

[150] H. Quan, Z. Song, X. Liu, P. Zanardi, and C. Sun. Decay of Loschmidt Echo Enhanced by Quantum Criticality. *Physical Review Letters* **96**(14), 140604 April (2006).

[151] F. Cucchietti, S. Fernandez-Vidal, and J. Paz. Universal decoherence induced by an environmental quantum phase transition. *Physical Review A* **75**(3), 032337 March (2007).

[152] Y.-C. Ou and H. Fan. Decoherence of a central quantum system coupled to an XY spin chain. *Journal of Physics A: Mathematical and Theoretical* **40**(10), 2455–2461 March (2007).

[153] S. Camalet and R. Chitra. Effect of random interactions in spin baths on decoherence. *Physical Review B* **75**(9), 094434 March (2007).

[154] C.-Y. Lai, J.-T. Hung, C.-Y. Mou, and P. Chen. Induced decoherence and entanglement by interacting quantum spin baths. *Physical Review B* **77**(20), 205419 May (2008).

[155] Z.-G. Yuan, P. Zhang, and S.-S. Li. Loschmidt echo and Berry phase of a quantum system coupled to an XY spin chain: Proximity to a quantum phase transition. *Physical Review A* **75**(1), 012102 January (2007).

[156] L. Tessieri and J. Wilkie. Decoherence in a spin-spin-bath model with environmental self-interaction. *Journal of Physics A: Mathematical and General* **36**(49), 12305–12327 December (2003).

[157] H. Quan, Z. Wang, and C. Sun. Quantum critical dynamics of a qubit coupled to an isotropic Lipkin-Meshkov-Glick bath. *Physical Review A* **76**(1), 012104 July (2007).

[158] Y. Hamdouni and F. Petruccione. Time evolution and decoherence of a spin-12 particle coupled to a spin bath in thermal equilibrium. *Physical Review B* **76**(17), 174306 November (2007).

[159] A. Relaño, J. Arias, J. Dukelsky, J. García-Ramos, and P. Pérez-Fernández. Decoherence as a signature of an excited-state quantum phase transition. *Physical Review A* **78**(6), 060102 December (2008).

[160] D. Rossini, T. Calarco, V. Giovannetti, S. Montangero, and R. Fazio. Decoherence induced by interacting quantum spin baths. *Physical Review A* **75**(3), 032333 March (2007).

[161] J. Vidal, G. Palacios, and R. Mosseri. Entanglement in a second-order quantum phase transition. *Physical Review A* **69**(2), 022107 February (2004).

[162] J. Vidal, R. Mosseri, and J. Dukelsky. Entanglement in a first-order quantum phase transition. *Physical Review A* **69**(5), 054101 May (2004).

[163] J.I. Latorre, R. Orús, E. Rico, and J. Vidal. Entanglement entropy in the Lipkin-Meshkov-Glick model. *Physical Review A* **71**(6), 064101 June (2005).

[164] H. Cui. Multiparticle entanglement in the Lipkin-Meshkov-Glick model. *Physical Review A* **77**(5), 052105 May (2008).

[165] R. Orús, S. Dusuel, and J. Vidal. Equivalence of Critical Scaling Laws for Many-Body Entanglement in the Lipkin-Meshkov-Glick Model. *Physical Review Letters* **101**(2), 025701 July (2008).

[166] A. Osterloh, L. Amico, G. Falci, and R. Fazio. Scaling of entanglement close to a quantum phase transition. *Nature* **416**(6881), 608–10 April (2002).

[167] T. Osborne and M.A. Nielsen. Entanglement in a simple quantum phase transition. *Physical Review A* **66**(3), 032110 September (2002).

[168] L. Amico, A. Osterloh, and V. Vedral. Entanglement in many-body systems. *Reviews of Modern Physics* **80**(2), 517–576 May (2008).

[169] G. Vidal, J.I. Latorre, E. Rico, and A. Kitaev. Entanglement in Quantum Critical Phenomena. *Physical Review Letters* **90**(22), 227902 June (2003).

[170] H.J. Lipkin, N. Meshkov, and A.J. Glick. Validity of many-body approximation methods for a solvable model. *Nuclear Physics* **62**(2), 188–198 February (1965).

[171] J.I. Cirac, M. Lewenstein, K. Mø lmer, and P. Zoller. Quantum superposition states of Bose-Einstein condensates. *Physical Review A* **57**(2), 1208–1218 February (1998).

[172] S. Morrison and A. Parkins. Dynamical Quantum Phase Transitions in the Dissipative Lipkin-Meshkov-Glick Model with Proposed Realization in Optical Cavity QED. *Physical Review Letters* **100**(4), 040403 January (2008).

[173] R. Dicke. Coherence in Spontaneous Radiation Processes. *Physical Review* **93**(1), 99–110 January (1954).

[174] R. Botet, R. Jullien, and P. Pfeuty. Size Scaling for Infinitely Coordinated Systems. *Physical Review Letters* **49**(7), 478–481 August (1982).

[175] R. Botet and R. Jullien. Large-size critical behavior of infinitely coordinated systems. *Physical Review B* **28**(7), 3955–3967 October (1983).

[176] I.I. Guseinov, A. Özmen, Ü. Atav, and H. Yüksel. Computation of Clebsch-Gordan and Gaunt Coefficients Using Binomial Coefficients. *Journal of Computational Physics* **122**(2), 343–347 December (1995).

[177] A. Jamiokowski. Linear transformations which preserve trace and positive semidefiniteness of operators. *Reports on Mathematical Physics* **3**(4), 275–278 December (1972).

[178] P. Zanardi and D. Lidar. Purity and state fidelity of quantum channels. *Physical Review A* **70**(1), 012315 July (2004).

[179] M. Hein, W. Dür, and H.-J. Briegel. Entanglement properties of multipartite entangled states under the influence of decoherence. *Physical Review A* **71**(3), 032350 March (2005).

[180] A. Peres. Separability Criterion for Density Matrices. *Physical Review Letters* **77**(8), 1413–1415 August (1996).

[181] M. Horodecki, P. Horodecki, and R. Horodecki. Separability of mixed states: necessary and sufficient conditions. *Physics Letters A* **223**(1-2), 1–8 November (1996).

[182] A. Peres. *Quantum Theory: Concepts and Methods.* Springer, New York, (1993).